13

Crustal Structure from Teleseismic Bodywave Data

by

John Edward Foley

M.S., Boston College (1984)
B.S., University of Lowell (1981)

Submitted to the Department of Earth, Atmospheric, and Planetary Sciences
in partial fulfillment of the requirements for the degree of

Doctor of Science

at the

MASSACHUSETTS INSTITUTE OF TECHNOLOGY

June 1990

© Massachusetts Institute of Technology 1990
All rights reserved

Signature of Author .....
Department of Earth, Atmospheric, and Planetary Sciences
May 25, 1990

Certified by .....
M. Nafi Toksöz
Professor of Geophysics
Thesis Advisor

Accepted by .....
Thomas H. Jordan
Chairman
Department of Earth, Atmospheric, and Planetary Sciences

MASSACHUSETTS INSTITUTE OF TECHNOLOGY
JUN 05 1990
WITHDRAWN FROM MIT LIBRARIES
LIBRARIES

Crustal Structure from Teleseismic Bodywave Data

by

John Edward Foley

Submitted to the Department of Earth, Atmospheric, and Planetary Sciences
on May 25, 1990, in partial fulfillment of the
requirements for the degree of
Doctor of Science

Abstract

In this thesis we have developed and implemented a series of techniques to determine information about the crustal velocity structure of the earth beneath a network of seismic stations from the analysis of teleseismic P-waveforms. We examined the usefulness of methods which utilize vertical component teleseismic P-seismograms recorded on 2 seismic monitoring networks. The first is located in the northeastern United States and is utilized as a test area for the new methods, and the second is in Larderello, Italy, the site of one of the world's largest geothermal energy production facilities which is currently being explored with a variety of geological and geophysical methods.

The main general conclusion of this study is that the analysis of vertical component teleseismic P-waveforms can provide very useful information about the crustal velocity structure of the earth. It has long been recognized that the delays in travel time of direct P-waves can image the broad lateral velocity variations in the earth. We have demonstrated that the application of a tomographic method based on these observations can provide a good estimation of the lateral extent of the low velocity zone in Larderello. To improve this model of the earth structure we examined the waveforms for primary reflections from deep velocity discontinuities which either have regional extent or are isolated to the vicinity of individual receivers. The measure of the travel times from these phases (although much more difficult to make than the direct arrival) hold valuable information about the crust. We developed two methods to extract this information from the vertical component teleseismic P-waveforms. The first is the application of a simulated annealing technique to the problem of relative travel time determination and works on the premise that within a window in each waveform a wavelet is common to all stations recording the same event. We use this optimization method to locate the Moho in New England and to determine accurate measures of direct arrivals in the Larderello data. The second method relies upon an important data transformation which simplifies and regularizes the waveforms. This transformation is a two-step process, where we first determine the source wavelet common to all receivers for each recorded event and then convert each source into a simple and repeatable zero-phase wavelet. Once transformed, we take advantage of the wide variety of event incidence angles present in the New England and Larderello data sets. Each primary reflection two-way travel time is dependent on the event incidence angle (or ray parameter), and we exploit this dependency

to determine the relative travel times and average velocities to major discontinuities in the crust by using a ray parameter trajectory stacking scheme (called the *rpt* method).

To extract all of the available information about the crustal velocity structure out of teleseismic waveforms, one must incorporate the entire waveform into the analysis. To this end, we have developed and applied a waveform inversion method to refine the details of the velocity model sketched by the previous techniques. This method is based on the calculation of sensitivity functions, or partial derivatives, of the predicted seismogram to changes in each of the parameters which are used in the calculation of the synthetic waveform. This waveform matching scheme uses the misfit to the data and the Frechet kernel to update the model, and with this process we can resolve important velocity features in the crust.

In addition to these general conclusions we have determined a number of specific important and interesting details about the velocity structure of the Larderello geothermal area. The travel time residual inversion yielded information about the size and extent of the low velocity feature in the crust. This intrusive body is about 20 km by 20 km in lateral extent and exists from depths of about 6 km to below 40 km. The strong travel time residual in the area (about 1 second over about 30 km) indicates a region of intense reduced velocity to by at least 20% (melts of igneous rocks are a reduced in velocity by 30 to 40%). The *rpt* method was applied to the Larderello data to help clarify this picture of the crust, and we found that beneath most stations in the region, strong velocity discontinuities exist at depths of 20 to 25 km. This regional feature is interrupted in the central portion of the area where a negative gravity anomaly is strongest and where temperatures are most elevated. This area has a number of more isolated velocity contrasts.

Our waveform inversion technique confirms many of the findings of the previous applications to teleseismic data and supplements them with detailed information about the crustal velocity structure (particularly in the upper 3 to 10 km). This part of the crust is difficult to image with conventional reflection techniques but holds important information about the tectonic evolution of the region as well as information pertinent to geothermal exploration. We were able to demonstrate with this preliminary study of the velocity structure in Larderello that analysis techniques utilizing vertical component teleseismic waveform data (direct arrivals, primary reflections and full P-waveforms) and two data enhancement techniques (simulated annealing and source equalization) can reveal some of the fine details of the velocity structure of the crust.

Thesis Advisor: M. Nafi Toksöz
Title: Professor of Geophysics

Acknowledgments

I would like to thank a few people who provided help, insight and support to me while I was a student at MIT. First and foremost I would like to thank Nafi Toksöz, my thesis advisor and director of the Earth Resource Laboratory, for his help in putting my effort in its proper scientific perspective. With his wide range of experiences and overview of the the geophysical sciences and geophysical community he has been able to teach me a great deal about many important aspects of becoming an effective and productive scientist. I was also quite fortunate to to have had the advice, encouragement and support of John Ebel from Boston College. John is a consummate seismologist and has educated me immeasurably over the years.

While at MIT I was a member of the Earth Resources Laboratory. Being associated with this group has truly rounded my education and prepared me to leave MIT with numerous tangible skills beyond those related to earthquake seismology. Nafi, Roger Turpening and Arthur Cheng have kept this unique and productive environment alive and have provided an excellent facility in which to work. They deserve many thanks. The lab is run by an excellent staff and I thank Sara Brydges, Jane Maloof, Al Taylor, Naida Buckingham, Liz Henderson and Sue Turbak for all their help.

In the Italian part of my research effort I was lucky to have had the help of Fausto Batini of ENEL. His assistance, along with that of the talented group in his Larderello lab, made the geothermal project a pleasure to work on.

The friends I've made while at MIT have made the last 5 years at ERL a very positive experience. In particular I would like to thank Ed Reiter, Bob Cicerone, Chuck Doll, Jim Mendelson, Fatih Guler, Jane Maloof and Delaine Thompson for their constant good nature, proper perspective and friendship.

Most of all I would like to express my thanks to my wife Judy who never let me take myself too seriously.

Contents

Chapter 1

INTRODUCTION

Thesis Objectives

The amplitudes and travel times of seismic body waves are strongly affected by the media through which they travel and can be measured and analyzed to determine the properties of the earth. This study is undertaken in an effort to derive information about the earth's velocity structure from the analysis of teleseismic P-waveforms. There are two main objectives in this research, both of which focus on the crustal velocity structure near seismic recording stations. The first of our goals is to develop and then apply teleseismic waveform and travel time methods to the specific problem of velocity structure characterization of the Larderello Geothermal Field (Figure 1), an area in central Italy. This important geothermal region has been the focus of numerous geophysical and geological studies undertaken in order to develop a more clear understanding of the crustal structure and crustal dynamics of this area. The tectonic setting of this region has a complicated modern expression, and a clear and accurate account of the tectonic evolution of this area is essential to interpret other geophysical and geological observations. With this study, we add a new set of well controlled observations based on the analysis of teleseismic waveforms to the base of information which presently exists for Larderello, and we develop a model from these velocity structure observations which helps to clarify some of the issues that remain for a better tectonic understanding of the Larderello Geothermal Area.

The second objective of this work is to assess the overall usefulness of complementary

seismic velocity analysis techniques aimed at imaging the velocity structure of the crust utilizing vertical component teleseismic P-waveforms recorded on seismic networks. This type of data is quite abundant from numerous seismic networks operating around the world which are generally deployed to monitor local and regional seismic activity. In this research we limit the development and application of waveform analysis techniques to vertical component seismograms in order to maintain the widest possible base of application of the techniques. Generally, vertical P-waveforms have been used primarily in travel time residual studies based on the relative arrival time of the direct P-wave. The timing and amplitudes of phases arriving after the direct P-wave which originate from the structure near the receiver and are recorded on vertical component sensors have not been used to refine crustal velocity structures. We evaluate the potential of this under–utilized set of observations by applying various vertical waveform analyses to seismograms collected on the Larderello Seismic Network and to the seismograms recorded in New England on the North East United States Seismic Network. We test our analysis methods on waveforms recorded in New England since the velocity structure in this area is simpler than in Larderello and is known fron other seismic studies.

Teleseimic Waveform Data

The focus of this thesis is on vertical component teleseismic P-waveform data collected on seismic monitoring networks. Teleseismic P-waves travel from the earthquake source region through the body of the earth and arrive at the recording network generally at steep incidence angles (Figure 2). Because of large epicentral distances, the curvature of the wavefront is small when it arrives at the recording array and can be represented by a plane (Aki and Richards, 1980). This assumption greatly simplies all of the following analyses.

The data used in this research comes from two seismic monitoring networks which were established to monitor local and regional seismic activity. The first is located in Larderello, Italy in southwest Tuscany and is operated by the Ente Nazionale per l'Energia Elettrica (referred to as ENEL), a national energy agency in Italy. It is comprised of 26 stations (Figure 3). The area covered by the network is about 30 by 40 km in extent and the average station spacing is about 6 km. We use 101 teleseismic events recorded during the period

1986-1988 recorded on the Larderello Seismic Network in this study.

The second seismic network is located in the northeastern United States and is referred to as the NEUSSN. This network is operated principally by four separate monitoring groups: Earth Resources Laboratory at the Massachusetts Institute of Technology, Weston Observatory of Boston College, Lamont Doherty Geological Observatory of Columbia University, and the Earth Physics Branch of Canada. The NEUSSN is comprised of about 100 stations over an area roughly 400 km by 200 km in extent (Figure 4) and has a variable station spacing averaging about 40 km. We have collected 148 teleseismic events recorded on the NEUSSN during the period 1985 – 1987 from earthquakes with magnitudes ranging from M_B 4.8 to M_B 7.3. Both of the networks used in this study record teleseismic waveforms with short period, vertical component sensors at most of their stations.

Some Advantages of Teleseismic Data

Traditionally, there have been two conventional ways to examine the crust with seismic waves. The first is with reflection techniques, where energy is put into the earth at the surface and reflected waves, originating from interfaces below, are recorded on the surface at near vertical angles. The second approach is to use refracted waves, where sources on the surface generate waves which are recorded at various distances from the source. Both of these methods are important and have numerous useful applications. However, when the deep crust and upper mantle are being investigated, they both have serious limitations. With reflection methods energy transmission to great depths is problematic, and with refraction methods lateral spatial resolution is generally limited. The use of teleseismic P-wave data, (direct P-wave arrivals, later reverberations from the crustal discontinuities, or the the entire P-waveforms) to determine crustal features avoids some of the limiting complications of both refraction and reflection approaches. Since teleseismic P-waves travel short lateral distances in the crust (on the order of 10 km), regional scale travel path averaging does not occur. This is in contrast to refraction studies where shot-to-receive distance of over 100 km are required to image the lower crust (Jarchow and Thompson, 1989). The use of teleseismic data helps us discriminate between local irregular velocity structures near individual stations and regional trends of the crustal velocity structure. The second advantage comes from the

frequency band of teleseismic waveforms recorded on the NEUSSN and ENEL networks, which is generally in the range of 0.5–3.0 Hz. Teleseismic data has a lower frequency content than typical reflection sources (10 to 50 Hz) and refraction experiments (2-15 Hz). Resolution of fine velocity structures is reduced with teleseismic waveform methods due to the lower frequencies in the data. However, less attenuation occurs at these frequencies and more energy returns to the surface from deep reflectors. Seismic waves in the frequency band used here are more reflective than higher frequency sources used in reflection seismic methods from laminated layers which have been proposed to exist at the base of the crust (Hale and Thompson, 1982).

In order to take advantage of these attributes of teleseismic waveform data, special analysis and signal-to-noise ratio enhancement techniques are needed to overcome some limitations of teleseismic P-wave data recorded on typical seismic networks. For the direct P-wave arrival recorded at teleseismic distances from a typical earthquake with a magnitude of 6.0, the signal-to-noise ratio is generally great enough to allow for accurate measurements of the travel time of the direct arrival. However, later arriving phases originating as reflections from crustal discontinuities beneath a station typically have amplitudes between 0.05 and 0.2 of the direct arrival and have signal-to-noise ratios which are very low (typically at or below 1.0). In addition to the ambient environmental noise we observe a high degree of incoherent scattered energy on most teleseismic waveforms which are due to lateral heterogeneities in the crust (Dainty, 1990). These arrivals produce a scattered coda wave after the direct arrival and often have greater amplitudes than the arrivals from large scale velocity discontinuities in the crust. Without the amplification of the coherent part of the seismograms we are restricted to analysis of the direct arrivals exclusively for determining crustal velocity features. The second major difficulty with teleseismic P-wave data is the lack of knowledge of the source function incident at the base of the crust. The waveforms recorded at a station on a seismic network are affected by the earthquake source, the raypath through the body of the earth, and local crustal effects. If we want to isolate the crustal response beneath a recording site, we must remove the effects in the waveform which come from other sources.

In this thesis, we develop two methods to overcome these difficulties. The first method,

described in Chapter 2, is based on the idea of simulated annealing optimization (Rothman, 1986) and helps to determine travel times in noisy data. The second method, called source equalization, helps us to determine and remove the source and propagation effects in our data. The source equalization method is divided into two parts; the first part is used to determine the source wavelets which are common to all seismograms recorded on a network from a single event, and the second part removes these effects with a modified deconvolution process. This method is described in Chapter 4.

Crustal Structure Applications

In this thesis we apply five different methods to the problem of crustal velocity structure characterization which utilize vertical component teleseismic P-waveforms. These include:

1. Relative travel time residual inversions of the direct P-wave arrivals,
2. Mapping of coherent reflectors beneath New England with the application of a simulated annealing optimization procedure,
3. Scanning source equalized data recorded at *individual* stations for incident angle dependent reflections,
4. Forward modeling source equalized and stacked waveform data and
5. Inverse modeling source equalized and stacked waveform data.

1.2 The Larderello Geothermal Region

The Larderello Geothermal Field is located within the complex structure of the Apennines Mountains which run down the center of the Italian Peninsula (Figure 1). Most Italian geothermal settings lie in the inner Apennines (toward the Tyrrhenian Sea) and are characterized by a complicated tectonic history. Larderello is in southwestern Tuscany and has had a tectonic history similar to that of other geothermal areas which exist in the NW-SE trending tectonic belt (Mt Amiata, Mt. Cimino, Mt. Vesuvious, Mt Etna, for example). Figure 5 (taken from Batini et al., 1983) shows a schematic diagram of the geologic setting of the Larderello Geothermal Field. This area is characterized by 3 main geologic units. From the top down we see a cap rock made up of a sequence of clayey flysch and conglomerates

deposited during the post-Alpine transgressive phase which is underlain by a series of folded and thrusted sedimentary nappes. This complex of tectonic wedges was overthrusted during the Alpine orogeny and is made up of limestones and anhydrites. Beneath this sedimentary pile is a metamorphic basement composed of phyllites and quartzites strongly corrugated during the Hercynian orogeny. The upper sedimentary rocks of this area area have been extensively studied in an effort to understand the processes controlling geothermal production (Batini and Nicolich, 1984). Within the basement metamorphic rocks a dominant seismic marker was discovered which is believed to represent the top of contact aureole associated with Late Apline magmatic intrusive activity (Batini and Nicolich, 1984). This feature (referred to as the **K** horizon) marks a petrophysical change in the rocks and is thought to be a zone of highly fractured rocks filled with steam or hot fluids. A more complete description of the geologic and tectonic background of the Tuscan region as well as a description of other geophysical observation made in Larderllo can be found in Chapter 7 and a detailed discussion is available from Puxeddu (1984) and Boccaletti et al. (1985).

1.3 Introduction to the New England Application

The application of teleseismic waveform analysis techniques to data collected in New England is undertaken in an effort to test the procedures developed in this study and to assess to usefulness of the techniques in typical local earthquake monitoring settings.

This intraplate region was built by a long progression of intense mountain building episodes. The general northeast trend in the geologic features (Merrimack Synclinorium, Bronson Hill Anticlinorium, Gaspe Synclinorium, etc., Figure 6) is due to the large scale compressive forces associated with repeated opening and closing of the proto–Atlantic Ocean (Taylor and Toksoz, 1979; Williams and Hatcher, 1982). The contacts between major provinces are believed to represent individual continental collision sutures (Rast and Skehan, 1983), and from the complicated nature of the surface geology and tectonic history of the NEUSSN, one might expect the deep crustal structure to vary widely across the region. Refraction and reflection results do indicate that the crust in New England is quite heterogeneous. An extensive and well controlled refraction experiment was undertaken in

central Maine in 1984 and a detailed map of Moho topography resulted from this experiment (Luetgert et al., 1987). This region is utilized as a control area in our simulated annealing analysis. This is the only large scale refraction experiment conducted in the New England until 1988, and results from this more recent project are not yet available. A large number of smaller, more passive, and therefore less well controlled refraction experiments have been conducted in the region (Leet, 1941; Linehan, 1962; Katz, 1955; Dainty et al., 1966; Chiburis et al., 1977; Schneck et al., 1976; Mitronovis, 1985). The models of the deep crustal velocity structure vary widely among these studies.

Reflection techniques deployed in the New England area have had difficulty in quantifying deep crustal velocity characteristics (Ando et al., 1984; Brown et al. 1983, Oliver et al., 1983; Mereu et al., 1986; Phinney, 1986; Hutchinson, 1986; and Stewart et al., 1986). Ando et al. (1984) were able to image to depths of only about 15 km in the Adirondacks, for example. The reflectivity of the New England Moho discontinuity can be quite variable. Mereu et al. (1986), for example, observe sharp Moho reflections in the Central Gneiss Belt of southern Quebec but very weak reflections only 100 km to the southwest in the Ottawa Graben.

1.4 Roadmap and Description of Methods

We are interested in studying the structure and tectonic evolution in Larderello and have developed and implemented a number of varied but related methods to help characterize the velocity structure beneath the seismic network operating in that area. We also test these methods on data collected on the NEUSSN to assess the usefulness of these techniques in a more typical seismic monitoring setting. Since the goals of this research are different in the NEUSSN and ENEL applications, each method is applied differently in the two areas, with emphasis always placed on the Larderello case where more dense spatial coverage has the overwhelming advantage of inherently better resolution. The relatively close station spacing in Larderello (about 6 km) as opposed to the spacing in New England (about 40 km) greatly amplifies the applicability of all of the teleseismic techniques.

We describe in the paragraphs below and show in Table 1-1 the outline of this study. In each chapter we present a general introduction to the current topic, the goals of the appli-

cation and the data requirements. We then discuss the theoretical justification of each of the approaches, as well as the key implementation issues whenever applicable. We generally present only a brief discussion of the results from the Larderello applications in the individual method chapters and leave the interpretation and discussions for the last chapter where all of the results are combined.

Simulated Annealing for Teleseismic Phase Selections

In Chapter 2 we look at the problem of teleseismic phase arrival time determination using the simulated annealing optimization approach. With this method we search the waveforms collected on the NEUSSN for Moho reflections arriving in the coda of the direct arrival. In the ENEL application we use this technique to accurately determine relative direct P-wave arrival times. The simulated annealing method recasts the phase identification problem as an optimization problem where we essentially test all possible combinations of network arrival configurations for each event by probabilistically updating the configuration state of the current model.

Travel Time Residual Inversion

In conjunction with the simulated annealing method of Chapter 2, we use the travel time residual observations of 101 teleseismic events recorded on Larderello network to determine the broad nature of the low velocity anomaly which exists in the center of the area. This study is presented in Chapter 3, and the results are fully interpreted in Chapter 7 where all the results from Larderello are gathered. The approach we have taken comes from the well studied Aki et al. (1977) methodology which has been applied in numerous volcanic areas around the world (see Iyer 1988, for a review).

Source Equalization

In Chapter 4 we present a method by which we can overcome many of the limitations associated with vertical component teleseismic P-waveforms. This is accomplished by removing all common source and common propagation effects from each individual trace and re-shaping

each natural source wavelet into a simple and repeatable source pulse. This transformation facilitates cross-event stacking and makes available a number of useful procedures to examine later arrivals in the seismograms.

Ray Parameter Trajectory Stacks

In Chapter 5 we introduce a new method to determine crustal velocity characteristics beneath a single recording station. This technique is called the ray parameter trajectory stacking method (or *rpt* method), and with it we utilize the wide range of event incidence angles (and therefore ray parameters) which arrive at each station. With this technique we scan source equalized waveforms recorded at a single station for coherent arrivals by systematically testing all possible crustal velocity discontinuity configuration states. With this method we are able to determine the two-way travel time to all major reflectors beneath a station and can make estimates of interval velocities from deep layers.

Waveform Modeling

Like the *rpt* modeling of Chapter 5, Chapter 6 utilizes the major simplifications brought about by the source equalization method of Chapter 4. In this final methods chapter we re-cast the time-domain forward waveform matching process as a maximum likelihood inversion procedure. We discuss the development of the teleseismic waveform inverse problem, as well as model parameterization and implementation issues.

Conclusions

The last chapter of this thesis deals with the combination and interpretation of results of the various methods. We pull together all the new information we have determined about the Larderello geothermal area and combine the results with the wide base of information already known about the region. This information is then integrated to produce a model for this dynamical geothermal region. Lastly, we assess the usefulness of teleseismic data to determine crustal velocity structure and present recommendations for future application of the techniques developed in in this study.

TABLE 1: Roadmap of Thesis

Chapter	Description of Application	Data Used	Application Area
2	Simulated annealing optimization method for travel time selections	Deep Crust Arrivals	Synthetic Tests and New England Moho
3	Simulated annealing optimization	Direct P-Arrivals	ENEL; Direct P-Wave Trav Time Residuals
4	Source Equalization; effective source calculations, and generic wavelet transformations	Entire Waveforms	Synthetic Tests New England Data ENEL Data
5	Ray Parameter Trajectory Stacks	Post-Source To Primary Arrivals	Test Data NEUSSN (11 Stations) ENEL (Entire Network)
6	Waveform Modeling	Entire Waveforms	NEUSSN (2 Stations) ENEL (12 Stations)

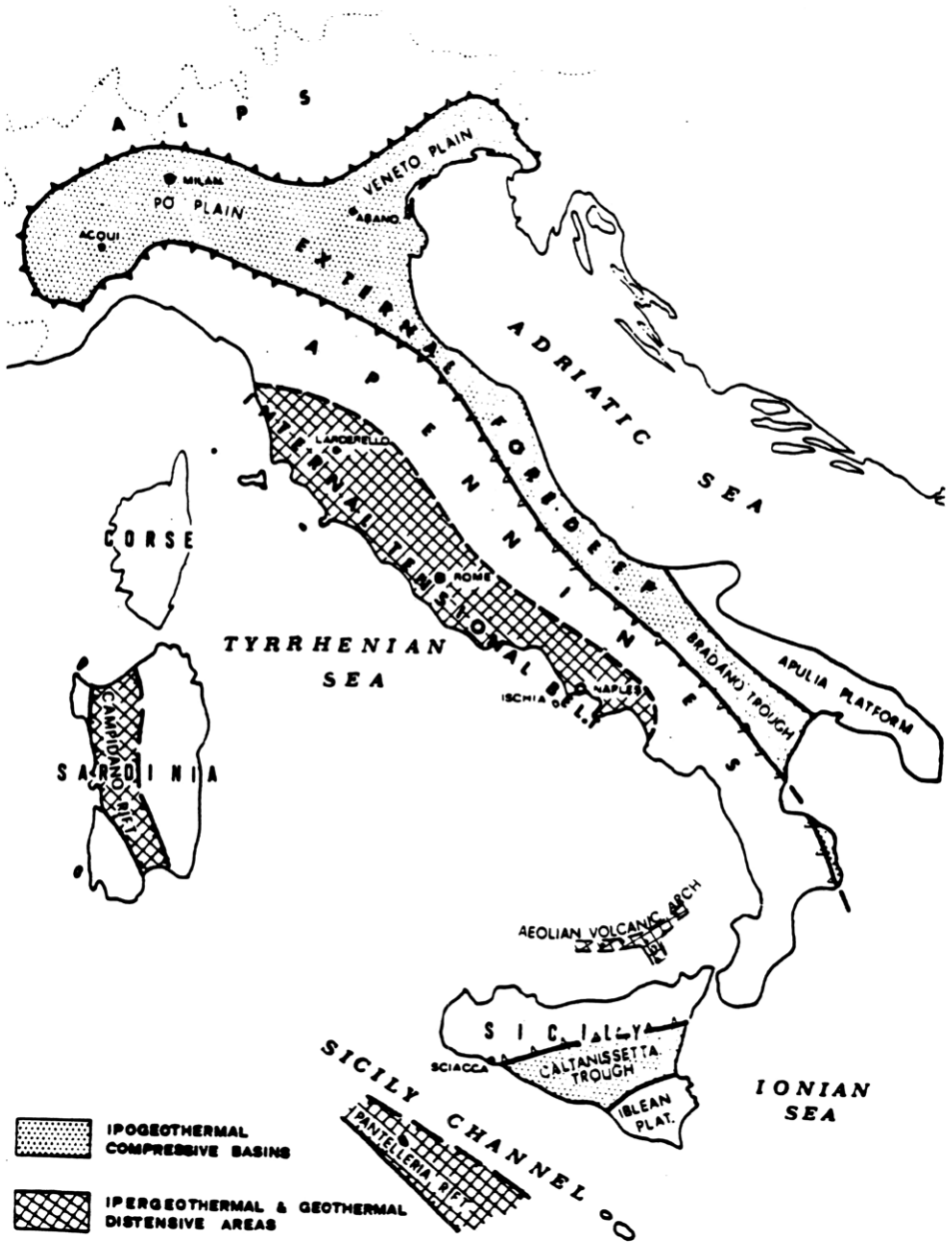

Figure 1: The Larderello geothermal field is located about 100 km south of Florence, Italy and lies within the complex structure of the Apennines which run down the center of the Italian Peninsula. Most Italian geothermal settings lie in the inner Apennines (toward the Tyrrhenian Sea) and are characterized by a complicated tectonic history.

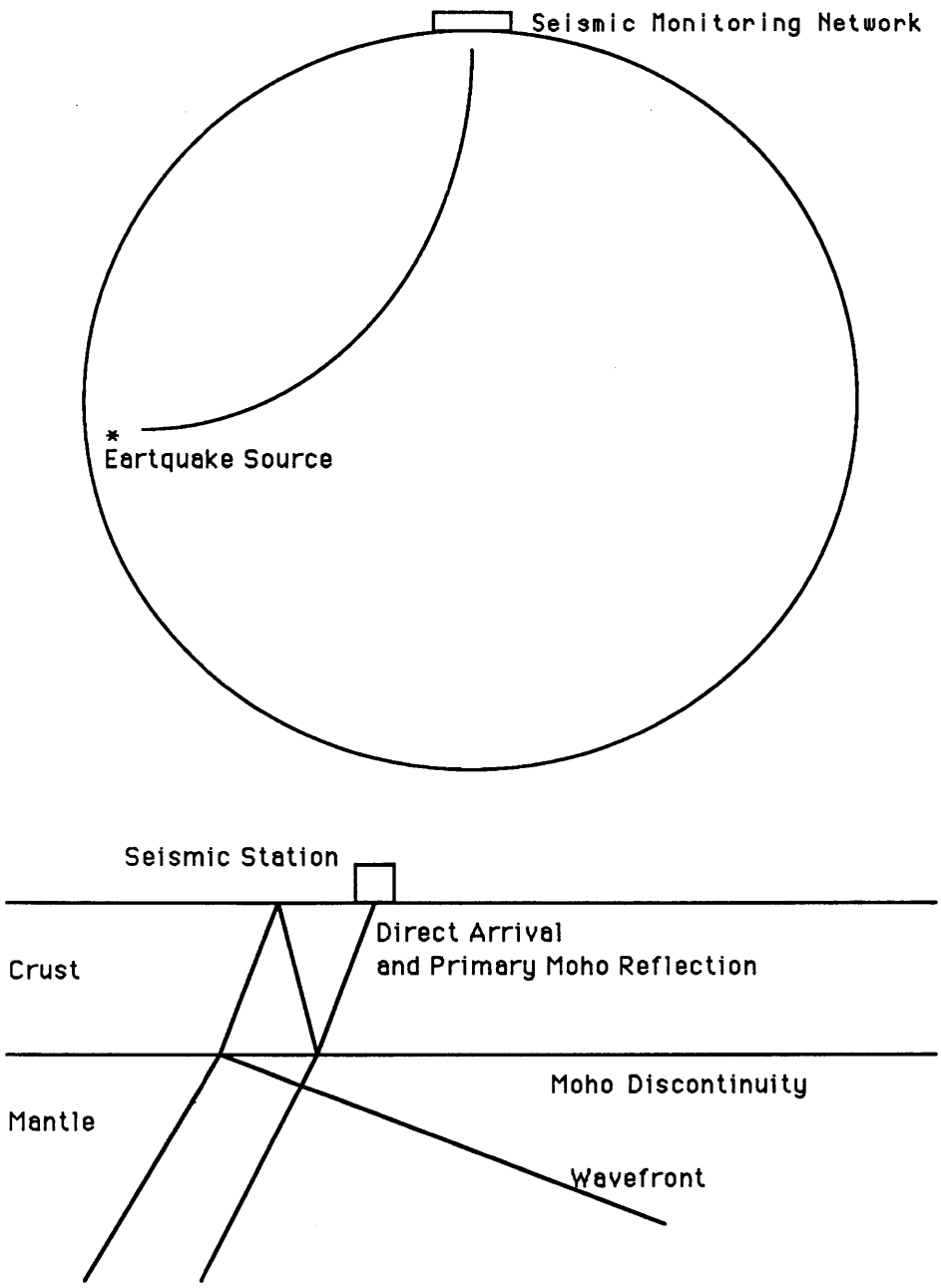

Figure 2: The focus of this thesis is on vertical component teleseismic P-waveform data collected on seismic monitoring networks. Teleseismic P-waves travel from the earthquake source region through the body of the earth and arrive at the recording network generally at steep incidence angles. Because of large epicentral distances, the curvature of the wavefront is small and can be represented by a plane.

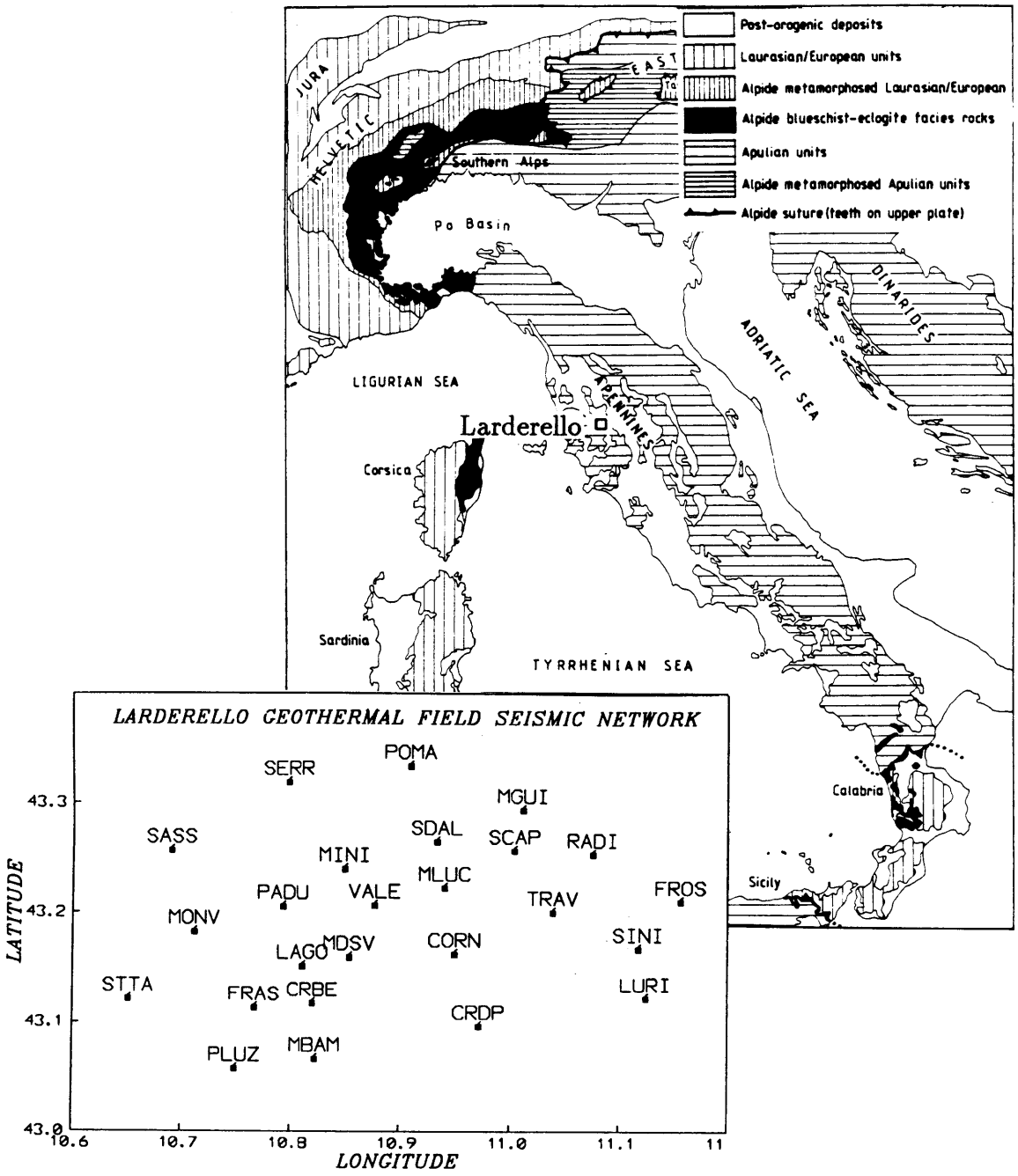

Figure 3: The seismic network at Larderello is operated by the Ente Nazionale per l'Energia Elettrica (ENEL), a national energy agency in Italy, and it has 26 uniform calibrated stations.

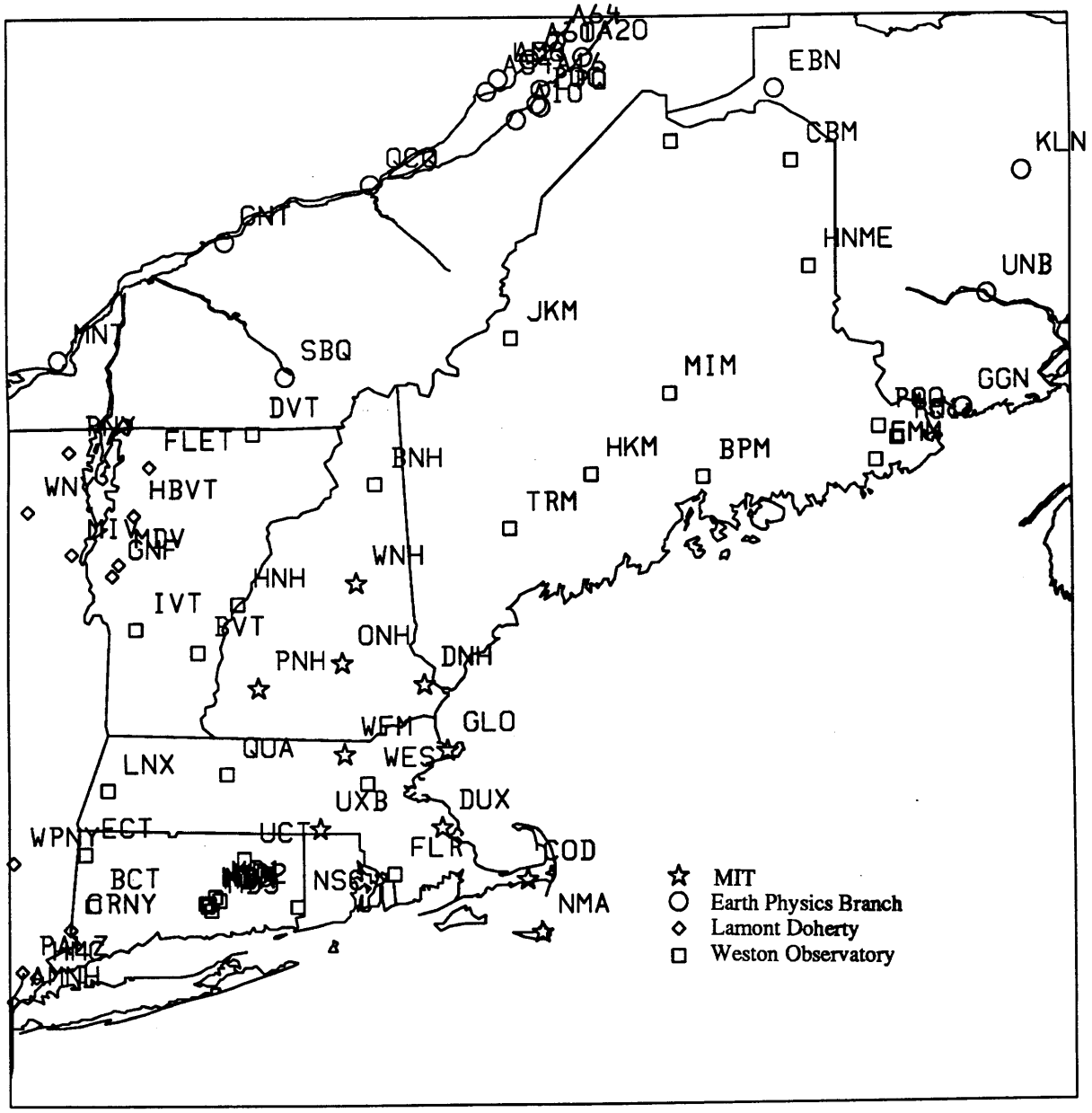

Figure 4: Northeastern United States Seismic Network has about 100 seismic stations and is operated by four separate monitoring groups; Earth Resources Laboratory at the Massachusetts Institute of Technology, Weston Observatory of Boston College, Lamont Doherty Geological Observatory of Cloumbia University and the Earth Physics Branch of Canada.

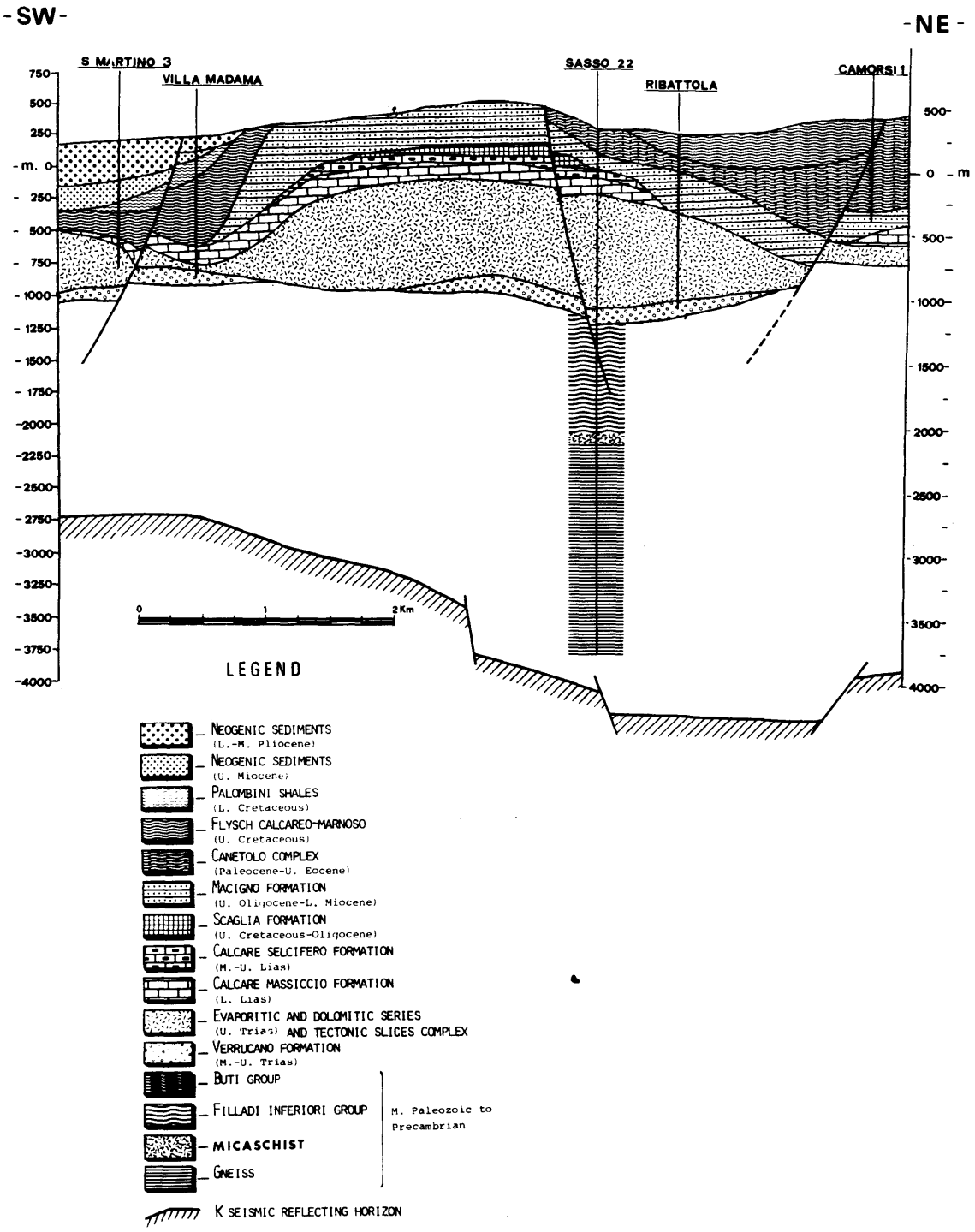

Figure 5: Schematic cross-section of the Larderello Geothermal Field (taken from Batini et al., 1983) is characterized by 3 main units (from top down); a sequence of clayey flysch and conglomerates which is underlain by a series of folded sedimentary nappes. These are in turn underlain by a basement of metasediments. The **K** Horizon is a key petrophysical marker believed to represent the top of an extensive contact aureole.

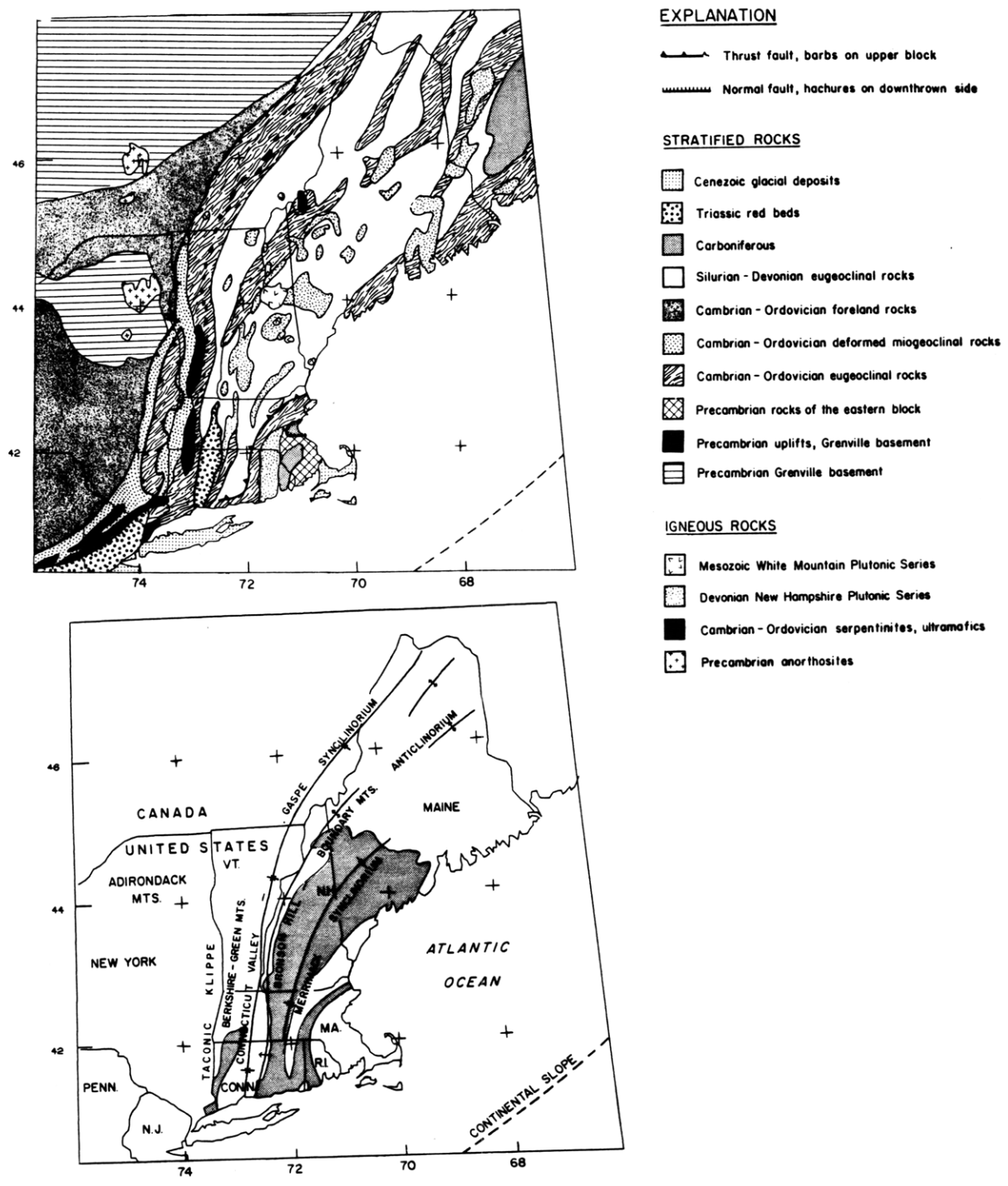

Figure 6: The northeastern United States is an intraplate region built by a long progression of intense mountain building episodes. The general NE trend in the geologic features (Merrimack Synclinorium, Bronson Hill Anticlinorium, Gaspe Synclinorium, etc., Figure 6) is due to the large scale compressive forces associated with repeated opening and closing of the proto–Atlantic Ocean and the contacts between major provinces are believed to represent individual continental collisions sutures. This simplified tectonic map of New England is taken from Taylor and Toksoz (1979).

Chapter 2

SIMULATED ANNEALING WITH TELESEISMIC DATA

2.1 Introduction

We explained in Chapter 1 that one of the basic problems in analyzing earth structure using teleseismic observations is the inherently low signal-to-noise ratio observed on many seismograms. This feature of teleseismic data makes the accurate determination of travel times subject to some uncertainty depending on the impulsiveness, frequency content and amplitude of the arriving signal. In this chapter we present a method which overcomes this liability of teleseismic data through the application of an optimization scheme based on the simulated annealing concept. There are many useful and practical applications which can be employed to determine the nature of the velocity structure of the crust from teleseismic data if we can determine accurate measures of the relative travel times of various teleseismic phases arriving at stations in a seismic network. We develop the method of automated, simulated annealing based phase identification in this chapter and apply this technique to the problem of determining the depth to the Moho in the New England area. In the following chapter we show that the delay times of direct teleseismic P-wave arrivals (derived with the simulated annealing method) can be used to determine important broad features of the velocity structure of the crust and upper mantle beneath the Larderello Seismic Network.

The process of isolating and accurately measuring the arrival time of a particular phase on a vertical component teleseismic P-waveform is subject to inherent uncertainties (Iyer, 1975; Foley and Toksoz, 1987; VanDecar and Crosson, 1990, for example). The source of the difficulty in reading travel times in teleseismic data exists for the following reasons:

1. The signal-to-noise ratio of the direct arrival or a reflected arrival from a velocity discontinuity in the crust is generally low. Relatively weak source pulses and small reflection coefficients of deep crustal reflectors like the Moho, (about 10%), can make direct arrivals and deep reflections subtle features on teleseismic seismograms.

2. Phase arrivals are often emergent, making the exact travel time selection of a phase (once isolated in the waveform) difficult to accurately measure manually or with interactive computer graphics software.

3. The station spacing in most seismic networks is quite variable and is generally greater then one wavelength, limiting the applicability of many array methods (Dainty, 1990). In the NEUSSN Network we have about a 40 km station spacing and in the ENEL Network a 6 km spacing. Based on a 1 Hz wave traveling at 6 $\frac{km}{sec}$, this makes the spacing about 7 and 1 wavelengths, respectively.

For these reasons we are forced to take a statistical approach when dealing with the problem of locating key arrivals in teleseismic data. This is done by recasting the phase identification problem as an optimization problem. We design a function which will be maximized when each of the seismograms recorded on the network from a single event are time shifted by amounts related to the differential travel time of the targeted phase.

In Section 2.2 of this Chapter, we detail the simulated annealing based optimization method for measuring arrival times of teleseismic data and in Section 2.3 show various synthetic data examples using the simulated annealing method. The first real-data application of this technique is presented in Section 2.4 and comes from the New England region where we determine the travel time to the Moho beneath the NEUSSN Network by measuring the differential two-way vertical travel time of the P_MP phase. The second application comes from Larderello where we use the simulated annealing approach to determine the relative

travel times of direct P-waves. These data are used in a travel time residual inversion and provide a broad picture of the anomalous low velocity zone in the center of the region. The ENEL application is presented in Chapter 3 where the inversion study is presented in its entirety.

2.2 Simulated Annealing Method

The application of simulated annealing optimization to the problem of seismic phase arrival identification helps to overcome some of the problems which make the travel time calculations of teleseismic data difficult and unreliable. In particular, the simulated annealing method helps us to quantify the accuracy of phase identifications by defining a probability associated with each travel time selection. As shown below, this method works well when the signal-to-noise ratio is low and when we ordinarily have difficulty pin-pointing emergent arrivals in noisy data. Methods which utilize a probabilistic approach to solve various types of seismic travel time problems have had limited but successful application in the past. Rothman (1986) used the simulated annealing method to solve the problem of station statics corrections in reflection data. Landa et al. (1989) used a generalized simulated annealing technique (Bohachersky et al., 1986) for trace coherency optimization and CMP velocity estimations, Zelt et al. (1987) used a semblance optimization technique to select low amplitude refracted arrivals. VanDecar and Crosson (1990) have recently developed a waveform coherency algorithm to determine the arrival times of direct teleseismic P-wave arrivals recorded on the Washington Regional Seismograph Network.

In the teleseismic travel time applications, we search for a set of trace shifts that maximizes (optimizes) the total energy content of a group seismograms windowed to contain a targeted phase

$$\mathcal{E} = \sum_{i=1}^{N-window} \Big(\sum_{j=1}^{N-traces} d_{i,j}(\tau_j) \Big)^2, \tag{2.1}$$

where $\mathcal{E}$ is defined as the power of the stacked trace, called the *stack power*, which we want to optimize, $d_{i,j}(\tau_j)$ is the i^{th} point in the j^{th} seismogram and τ is the shift of the j^{th} seismogram determined with this procedure. We use this optimization technique to

determine the lags $\tau(i)$ in the data which maximize the stack power of the targeted arrival. Only windowed portions of the full waveforms are used in this process, and these windows are defined for each station by assuming that the arrivals fall within a predetermined range of travel times. These windows only define the portion of the seismogram in time in which the targeted arrival is expected and do not shape or transform the data. We will refer to the stack of these windows as the *annealing stack*. For direct teleseismic arrivals we create windows based on standard reference travel time catalogs. For crustal reflection applications we determine the windows from estimated the two-way vertical travel times which are based on careful qualitative analysis of the waveforms and all available a priori information about the targeted reflector (from refraction results, for example). Tight windowing of the data cuts the computational expense of the method; for an event with 50 seismograms (a typical number recorded on the NEUSSN), each with a 40 point window, there are 40^{50} possible trace alignment states. We use simulated annealing optimization to efficiently maneuver through this 50 dimensional data space in an iterative process to locate the configuration with the maximum annealing stack power.

Simulated annealing is a Monte Carlo optimization procedure which is designed to globally optimize an objective function that contains local minima (Rothman, 1986). The term *Monte Carlo* means that at some point in the process a randomly generated number is used, and as we shall see below, this process is a *Monte Carlo* method because we generate a random number to make selections from probability distributions. The idea of simulated annealing, introduced by Kirkpatrick et al. (1983), is that one can make an analogy between optimization of a function and the physical process of crystal growth (annealing). In this travel time problem, we wish to align all seismograms recorded from a teleseismic event such that the power of the annealing stack is the greatest; this is our objective function. In early iterations we allow traces to be shifted with few constraints. These early iteration are analogous to the high *temperature* state of crystal growth, where a crystal is still mainly liquid and can attain virtually any molecular configuration. Later, the *temperature* of the process is lowered and the range of possible trace shifts becomes limited. Similarly, before a melt solidifies, the motion of individual molecules is not widely constrained, but as the

temperature is lowered (slowly) to the Curie point, the range of motion is reduced until the final crystal lattice is developed.

This optimization can also be thought of as the determination of a set of parameter values (trace shifts) which minimizes a function (1/stack power) which contains local minima. This function has an energy state at each possible combination of trace lags, and simulated annealing finds the lowest energy level. Attempting to locate this global minimum with conventional iterative improvement techniques can lead to solutions which rest in local minima (Tarantola, 1987). We use simulated annealing to insure that the global minimum is reached in each case by iteratively optimizing the function and probabilistically allowing steps which *temporarily* have higher energy levels than previous iterations; we carefully allow for uphill motions on the objective function to avoid local minima. An outline of the simulated annealing procedure described below is shown schematically in Figure 1 and follows the procedure outlined by Rothman (1986).

1. The procedure begins by determining the time window for each trace for the targeted arrival. We use travel time tables of the direct P-wave application, and refraction, reflection and waveform modeling results in the Moho reflection search application.

2. All data are low-pass filtered (corner = 2.5 hz) to make the trace frequency content more uniform across the network.

3. All trace shifts are initially set to zero.

4. The windowed data are summed to produce the *annealing stack* and the stack power is calculated.

5. One seismogram is removed from the annealing stack and a cross correlation is made between that trace and sum of the remaining traces, which we refer to as the *partial stack*. This correlation is referred to as the *trace correlation* below.

6. The trace correlation function is converted into a probability distribution using a temperature conversion factor. The time shifts are weighted by the probability function and a selection is made from this weighted distribution. This time pick is the trace lag for the current iteration.

7. The trace lag is applied to the data and the shifted trace is added back into the partial stack.

8. We return to step 5 until each seismogram in the event is processed for the current iteration.

9. The temperature parameter is lowered to limit the probability of of shifting traces by lags with low trace correlation levels.

10. We return to step 4 for N iterations.

There are a few key points in this procedure:

- At each step in the procedure the data are aligned and summed to produce an annealing stack. This function is a very poor representation of the source wavelet in early iterations, and for the first iteration it is simply a summation of all the prediction windows. No prior knowledge of the source wavelet is needed.

- By the end of the optimization procedure the annealing stack develops into an excellent representation of the source wavelet. Since we can independently determine the source wavelet using the *effective* source technique described in Chapter 4, we utilize the final form of the annealing stack as a measure the reliability of the procedure. This aspect of the optimization is discussed below.

- The trace correlation function is converted into a probability distribution using the relation,

$$PDF(i) = exp(XCOR(i)/T). \tag{2.2}$$

  Here $PDF(i)$ is the probability distribution, $XCOR(i)$ is the trace correlation function and T is the conversion temperature. The *temperature* parameter controls the conversion from trace correlation to probability distribution. High temperatures (early iterations) produce probability distributions which are more uniform, where low correlation values have relatively high probabilities, and low temperatures (late iterations) produce distributions with fewer and greater spikes; see Figure 2.

- A random selection is made from the PDF to determine the shift to be applied to the trace before it is added back into the partial stack. The random nature of this selection makes this a *Monte Carlo* method.

- With this procedure we probabilistically allow for shifts not associated with the maximum trace correlation when defining the optimal trace alignment. This allows us to avoid local minima.

- The procedure is executed for each station in the annealing stack to complete a single iteration. Many iterations are often required with simulated annealing (Rothman, 1986), but in this work stable trace configurations are generally found in as few as 25 iterations. Implications of these values are discussed below.

2.3 Synthetic Examples

To test the performance of the simulated annealing teleseismic phase identification method, we apply the technique to synthetic data contaminated with various levels of noise and attempt to locate the Moho reflection in the synthetic data. We calculate synthetic seismograms for 30 different *random* earth models shown in Figure 3 using the source pulse shown in Figure 4. The *random* nature of the models is controlled to mimic probable crustal velocity profiles found in New England and the number 30 was selected as the minimum number of recording stations used in the New England study. We then test four different cases: first without noise, then with 10, 30 and 80% noise (actual ground noise recorded on the NEUSSN normalized to the peak of the synthetic trace). The synthetic data are presented in Figures 5, 6, 7 and 8.

The procedure outlined above is applied to the synthetic data to determine the relative two-way arrival times of the Moho, and the results of these tests are shown in Table 1. From the first test we see that without noise we can easily isolate the reflection to 0.1 seconds (1 sample). However, we also see that for 2 cases (Traces 29 and 30, which correspond to Models 29 and 30 of Figure 3) we get relatively poor travel time estimates. We conclude that this method has difficulty when the targeted discontinuity is represented as a gradational velocity change; for Models 29 and 30 little or no P_mP energy exists. Figure 9 shows the noise-free data after the final lags are applied to each trace and the P_mP phase is clearly located. We see from the final trace stack (Figure 10a) that in addition to estimating most of

the reflection times, we have also determined the source wavelet used to create the synthetic data (with polarity of the P_mP phase reversed from that of the direct P). As the noise level is increased to 10% (Table 1 and Figure 10b), the results are still good, with only the last two trace lags poorly defined. As we increase the noise to 30% (Figure 10c) and to 80% (Figure 10d) the results are degraded. At 80% the usefulness of the method is questionable, with inaccurate estimates (greater than 0.4 seconds error) in over half of the traces. We conclude that noise levels above 50% can degrade the results to unusable levels. Fortunately, network seismic data are sufficiently abundant that we can select many waveforms with good signal-to-noise levels (below 30%) .

One other obvious limitation of this method is that it requires *some* knowledge of the window (the travel times to the targeted phase in the data) before the method can be applied, ie; we must have a good estimate of the the arrival prediction window to insure that an arrival which is not targeted in the application is not interpreted as the correct arrival. We also must assume that the arrival exists, because this method will find the best possible lag in the prediction window even if there is no actual arrival at all (Trace 29, for example). To overcome these problems, we save the maximum trace correlation level between the prediction window and the annealing stack reached at each station during the procedure as a measure of the performance of the optimization procedure at each station. For example, in the NEUSSN Moho application we apply the simulated annealing method to numerous teleseismic data sets (waveforms recorded on the NEUSSN) and from each data set we derive a Moho travel time estimate at each station. We use the maximum trace correlation values as weighting factors in the final estimate of the Moho travel time at each station. For the synthetic tests, the maximum trace correlation values are included in Table 1 and we see that the final peak trace correlation between the target window and that in a few cases even the *best* stack can be quite variable even when noise is absent. In the noise free-case the peak trace correlations are almost all very good, where we see that only the velocity-gradient cases have peak trace correlation values less than 90%.

To examine the usefulness of the final peak trace correlation value (between the trace window and final annealed stack) as a measure of a parameter estimate *quality factor*, a

quantity we will use below to weight our travel time estimates, for each test model we plot the difference between the actual relative travel time and the predicted relative travel time versus peak trace correlation level. These plots (Figure 11) are shown for the noise free case, as well as the 10, 30, and 80% noise cases. We see that for the noise free example all peak trace correlations from models with strong Moho discontinuities are high (greater the 0.9), but as noise starts to dominate (30% and 80%) we see that the models with high travel time errors generally have smaller trace correlation values. For this reason, in the applications below we weight each Moho travel time estimate by the maximum trace correlation level.

A second weight is applied to the Moho travel time estimates. We use the maximum correlation between the final annealing stack and the *effective* source wavelet for the event (see Chapter 4) to reflect the overall quality of the estimates from each event in the analysis. This correlation level is referred to as the *event correlation* level. When the waveforms are shifted to optimize the power of the annealing stack (the objective function) the resultant wavelet should duplicate the source pulse (inverted due to the negative reflection coefficient). If we assume that the stack of the direct phases represents the source wavelet (discussed Chapter 4), then the event correlation should provide a good event-wide weighting factor. So, as a final estimate of Moho travel times at an individual station we determine the travel time with the simulated annealing procedure and weight this value by the product of the peak trace correlation level and the event correlation level.

2.4 Implementation Issues

- **Event Selection**

  For the New England Moho application, earthquakes were selected with consideration given to epicentral distance, event depth, source signature complexity, source duration and signal-to-noise ratio. We use events with well defined *effective source* signatures (Chapter 4), so that we can evaluate the overall performance of the method for each event by correlating the *effective source* with the wavelet reconstructed from the targeted reflector. All of the events used in both New England and Larderello applications have relatively sharp and simple waveshapes. Many of the available events were not

included in the annealing analysis because of excessively long durations of the source wavelets.

As an example of the data used, we show in Figure 12 waveform data for a typical event recorded on the NEUSSN: the May 1, 1985 earthquake of Peru, hereafter referred to as event 85/05/01. In this plot the natural direct P-wave moveout is removed using the simulated annealing technique. The data show a coherent initial source pulse but little visible similarities in any of the later phases.

- **Phase Selection**

  For events with teleseismic distances in the range of 40-180 degrees, reflections from discontinuities deep in crust generally arrive at a station between 5 and 15 seconds after the direct P-wave and with incidence angles between 50 and 0 degrees from vertical. These arrivals have amplitudes generally less than one tenth of the direct arrival. For a horizontally stratified media, the delay of reflected arrivals is dependent on source-receiver distance, crustal thickness and average crustal velocity. At steep incidence angles (less than 30 degrees from vertical) the P-waves dominate the waveforms, while at shallower angles (greated than 30 degrees) S-energy dominates. (See Chapter 5 for a description of the amplitude and travel time dependence of crustal phases with various incidence angles). To take advantage of this phenomenon we target P-wave reflections for steeply arriving events and converted-phases (one leg of the reflection is a P-wave, one leg is an S-wave) arriving at more oblique angles of incidence.

- **Conversion to Absolute Travel Times**

  The simulated annealing method is applied separately to each event. After a suite of trace shifts which maximize the stack power are determined, we calculate the relative delay for each station included in the event. This procedure is followed for all events and then the results from a particular station are combined and interpreted to produce a single measure of the relative 2-way travel time to the discontinuity beneath each station. To convert the relative times to absolute estimates of 2-way travel time, we select a few stations in the network as control areas where the velocity structure is

well known from previous studies. The relative values are time shifted until they best match the estimates of the inferred vertical two-way travel time of the control areas. For the New England analysis we have good deep crustal information in Central Maine (Leugert, 1985; Kafka and Ebel, 1989) and eastern Massachusetts (Foley 1984; Doll, 1987).

- **Error Analysis**

  With the simulated annealing technique noise-free traces can be aligned to a precision of a single sample, and with the sampling rate set to 10 samples per second, our alignment precision is 0.1 second. For a typical crustal propagation angle of 25 degrees and an average crustal velocity of 6.6 $\frac{km}{sec}$, a 0.1 second error in alignment corresponds to 0.3 km error in interface depth estimation. When noise is introduced, timing accuracy is degraded, so 0.3 km represents the best possible depth resolution of an interface. In the real data applications we make several estimates of the vertical two-way travel time at each station (one for each event in the analysis), and we calculate the average travel time and variance for each station. The variance is used to guide the interpretation of the results and is discussed below. In general, the variances in vertical travel time estimations are about 0.3 seconds, corresponding to a resolution in crustal thickness of about 2 km. Errors in average crustal velocity estimates produce errors in depth estimates when converting travel time estimates to depths. For example, for a ray traveling 25 degrees off vertical, the Moho depth estimate made from a P_mP travel time estimate of 10.0 seconds is in error by 0.5 km when the estimate for average crustal velocity is in error by 0.1 km/sec. Given that the highest frequencies observed in our teleseismic P-waveform data are about 3 Hz, the the shortest wavelengths observed are about 2 km and errors of magnitude 0.5 km cannot be resolved in the data.

- **Conversion Temperature**

  The conversion from cross correlation to probability distribution is very important in the simulated annealing method (Rothman, 1986). We tested three different conversion cases: no annealing ($T = 0$; conventional cross-correlations), steady state annealing ($T = constant$ for all iterations) and temperature varying annealing ($T =$

$T_0 \cdot [1 - cooling\ rate]^{iteration}$). For event 85/05/01 the calculated stack power histories for the three different methods is plotted in Figure 13. The final stack power level for the case where $T = 0$ (no annealing) is lower than both the constant temperature and iteration dependent annealing results. This indicates that the probabilistic approach to teleseismic arrival time selection is an improvement over a simple cross-correlation technique. We also see from the stack power plots that both the steady state and iteration-varying applications reach an equal stack power level and that the temperature varying procedure takes about 5 times as many iterations to reach this level. However, it must be realized the conversion temperature used in the steady state case was determined with a careful and time consuming trial-and-error process. The temperature is a sensitive parameter, and a 10% change in starting temperature can cause the procedure to get trapped in local minima. By implementing a scheme where temperature varies with iteration, a wider range of starting temperatures can be used. We significantly reduce the importance of the starting temperature and therefore automate the process. The tradeoff of this implementation is that the number of iterations necessary for the procedure to converge is increased. We find that in most cases we see convergence within 30-150 iterations. This convergence is quite rapid in contrast to the 3500 iterations Rothman (1986) needed to anneal data for static corrections. The relatively small number of iterations required in this teleseismic application indicates that global minima can be easily reached with the application of this probabilistic approach to travel time picking and that the problem is not strongly contaminated with local minima.

2.5 New England Applications

The topography of the Moho discontinuity beneath the Northeastern United States Seismic Network (NEUSSN) is determined in this section by means of calculating the relative timing of Moho reflections across the region from numerous teleseismic events. We use the simulated annealing technique to determine the delay times of the Moho reflection (P_mP) and to measure the confidence of each travel time selection.

The stations used in the study are plotted in Figure 14. The data used in this analysis are the waveforms from 55 teleseismic events recorded on the NEUSSN. The event locations, magnitudes and geometric information are supplied in Table 2. We plot the average back azimuth and incidence angle of all 55 events used in the New England study in Figure 15. We see that the coverage is not uniform; most of the events come from the northeast, south, northwest or near vertical.

Table 3 shows the final correlation values of each event's reconstructed wavelet with the corresponding *effective* source. The overall level of quality of the travel times determined in the analysis of each event is characterized by its reconstruction of the *effective source*. For the P-phase analysis, the range of reconstruction correlation levels falls between 0.31 (Event 84/05/23) and 0.71 (Event 85/08/27); for the converted-phase analysis the correlations range between 0.29 (Event 87/06/27) and 0.75 (Event 97/06/15). The comparison of *effective* source wavelets and reconstructed wavelets are shown in Figures 16 and 17 for the P-phase and converted-phases, respectively. We see from these plots and from the correlation values that this method can adequately reconstruct the source wavelet, and when the method fails, it is generally due to an inherently low signal-to-noise level in the data.

Data for each individual station are gathered from all events and presented in Table 4. Here we show the results for three cases: the P-phase study, the converted-phase study and the combined results. We present the number of vertical 2-way travel time estimates for each case, the mean value and the standard deviation. We also determine a weighted average of the travel time estimate. Each travel time estimate is weighted by the event *effective* source correlation level (Table 2) as well as the station prediction window correlation. These weighting scheme gives higher weights to the events which reconstruct the *effective* source the best and to individual travel time estimates associated with seismograms with strong prediction window correlation levels. The final weighted estimates range from -1.7 seconds (CBM) to +1.1 seconds (FLR). The standard deviations of these estimates are substantial, ranging from a low of 0.2 seconds (at 5 stations) to 0.6 seconds (MNQ). This rather wide range in these values indicates to us a variable level of success in the application of the method as well as a variable seismic response of the Moho in New England. There are three

explanations for the appreciable spread in the travel time estimate observed at some of the stations. First, we can attribute this to azimuthal variations in the Moho travel time due to lateral heterogeneity in the vicinity of the station. We test this hypothesis by simply plotting the travel time estimates for the stations with large variances on an azimuthal rose diagram. When we see trends in the depth estimates or clusters of different travel time estimates, we can conclude that the Moho is either dipping or disjointed beneath the station. An example of this is at station DNH; here we have a wide variance (0.7 seconds) in the vertical travel time estimate, but the individual prediction window correlation levels are high (average 0.67). A plot of the azimuthal variation in vertical Moho travel time at DNH is plotted in Figure 18, and we see that events from the south tend to have larger positive residuals (above 0.5 seconds indicating a shallower crust) and events from the northwest and northeast tend to have smaller residuals (less than 0.5 seconds indicating a thicker crust to the north).

The second explanation for large variances in Moho travel time estimates is a weak seismic response of the targeted interface. We saw in the synthetic examples that gradational change in velocity does not have a strong seismic signature and that the simulated annealing method finds a *solution* based only on the character of the noise. In these cases we see high variability of the Moho travel time estimates and low prediction window correlations. As an example, the Moho travel time estimates from station ONH are shown in Figure 19. Here the estimates in the Moho two-way travel time residuals are quite random at all azimuths and range from 0.3 seconds to 1.1 seconds.

The third explanation for our results is that the vertical travel time estimates to the Moho can have strong variances if the upper crustal structure is overly complicated and has contaminating effects in the Moho reflection prediction window. Strong near surface discontinuities can trap energy in the crust causing this correlation method to fail. An example of this is in Moodus, Connecticut (MD1-MD5, and HDM) where we have large variances in the data. Through forward modeling of the simplest waveforms recorded in this area we can conclude that the upper crust is quite complex and in general it is difficult to isolate deep crustal phases in the waveforms from these stations.

New England Conclusions

The simulated annealing technique for teleseismic phase arrival identification has enabled us to model the Moho discontinuity beneath the NEUSSN. With this optimization method we have made numerous estimates of relative two-way travel time to the MOHO at 61 stations in the seismic network. We have averaged these estimates, corrected for the incidence angle of each event and weighted by the maximum correlation levels produced during the optimization process, to produce a single estimate of the relative vertical two-way travel time to the Moho at each station. A contour plot of these data is shown in Figure 20. We convert this image of the variation in Moho topography to map of relative Moho depths by using the crustal velocities of Taylor and Toksoz (1979) and then adjusting the depths to match the control areas of central Maine (Leugert et al., 1987; Kafka and Ebel, 1989) and eastern Massachusetts (Foley 1984; Doll, 1987). This map is presented in Figure 21.

There are a number of observations which can be made from these preliminary results. First, we see two major depressions in the Moho in the New England area. One is located in north-central New Hampshire and corresponds to the topographic high of the White Mountains and a strong negative Bouguer gravity anomaly (Figure 22) of about -50 mGals (Kane et al., 1972). The other major Moho depression is in northern Maine where the station coverage is poor and the correlation of the feature to topography or potential fields is more difficult to interpret. Second, we see a relatively flat Moho in coastal and central Maine with a depth of about 32 km which correlates well with the teleseismic waveform modeling results of Lory (1988). Third, we observe a general thickening of the crust from SE to NW. Stations lying near the coast show positive Moho travel time residuals while inland estimates are more less consistent but generally negative. These features will be discussed further in the later chapters.

Table 1: Simulated Annealing Test Results

N	2-Way	Rel-	0 %		10 %		30 %		80 %	
1	Time[1]	ative[2]	Rel[3]	Xcor[4]	Rel	Xcor	Rel	Xcor	Rel	Xcor
1	8.56	0.97	0.90	0.98	0.92	0.90	1.09	0.50	1.17	0.54
2	7.50	2.04	2.00	0.99	2.02	0.94	2.19	0.61	2.47	0.53
3	7.50	2.04	2.00	0.99	2.02	0.93	2.29	0.49	1.97	0.55
4	8.12	1.42	1.30	0.93	1.42	0.85	0.59	0.71	0.37	0.30
5	13.36	-3.81	-3.90	0.98	-3.87	0.75	-3.81	0.62	-3.32	0.59
6	12.93	-3.38	-3.40	0.90	-3.27	0.78	-3.81	0.58	-4.22	0.21
7	10.82	-1.27	-1.20	0.92	-1.17	0.83	-0.91	0.54	-0.92	0.30
8	9.42	0.12	0.00	0.96	0.12	0.80	-0.91	0.40	0.87	0.44
9	9.99	-0.44	-0.50	0.93	-0.37	0.90	-0.01	0.63	-0.22	0.47
10	11.14	-1.59	-1.60	0.94	-1.57	0.82	-1.21	0.57	-2.32	0.28
11	8.55	0.99	1.00	0.95	1.02	0.79	1.29	0.54	1.87	0.43
12	9.09	0.45	0.40	0.97	0.52	0.84	0.69	0.35	1.07	0.49
13	6.24	3.30	3.30	0.95	3.32	0.84	3.99	0.48	3.57	0.62
14	6.95	2.59	2.50	0.95	2.52	0.81	2.89	0.49	1.97	0.56
15	7.18	2.36	2.30	0.98	2.32	0.72	2.49	0.44	2.27	0.68
16	8.99	0.55	0.60	0.91	0.62	0.78	0.69	0.46	0.67	0.60
17	9.36	0.18	0.10	0.97	0.12	0.82	-0.21	0.44	-0.52	0.50
18	11.95	-2.40	-2.50	0.97	-2.47	0.78	-2.21	0.52	-3.32	0.32
19	10.26	-0.71	-0.70	0.98	-0.67	0.92	-1.51	0.57	-0.52	0.35
20	8.20	1.34	1.30	0.95	1.32	0.89	0.69	0.59	0.47	0.49
21	11.06	-1.51	-1.60	0.95	-1.47	0.79	-1.21	0.42	-1.32	0.72
22	11.00	-1.45	-1.50	0.96	-1.47	0.81	-1.51	0.61	-1.02	0.54
23	11.02	-1.47	-1.50	0.96	-1.47	0.96	-1.31	0.84	-2.42	0.30
24	11.14	-1.59	-1.60	0.98	-1.57	0.89	-1.41	0.82	-1.02	0.55
25	8.73	0.81	0.80	0.94	0.82	0.67	0.69	0.47	-0.12	0.49
26	9.45	0.09	0.10	0.94	0.12	0.46	0.49	0.39	0.57	0.54
27	9.39	0.15	0.10	0.94	0.12	0.73	1.29	0.41	0.27	0.29
28	8.28	1.26	2.00	0.84	2.02	0.72	0.89	0.49	1.67	0.51
29	7.41	2.13	2.50	0.78	1.12	0.19	1.29	0.54	2.97	0.47
30	12.72	-3.17	-3.20	0.83	-3.07	0.49	-3.51	0.32	-3.02	0.69

1. Actual 2-way vertical travel time of the Moho P-wave reflection.
2. Actual relative 2-way vertical travel time of all Moho reflections.
3. Relative 2-way vertical travel time via simulated annealing.
4. Peak correlation level.

Table 2: Events Used in NEUSSN Simulated Annealing Application

Event	Lat	Lon	Date	Time	Depth	M_B	Bazm[1]	Angle[2]
840523	-51.95	161.09	05/23/84	05:16	10	5.9	237.2	2.5
840526	49.98	79.06	05/26/84	03:13	0	6.0	18.6	22.8
841004	-9.81	118.79	10/04/84	16:31	34	5.8	341.8	2.1
841025	73.37	54.96	10/25/84	06:29	0	5.9	15.8	32.2
841027	49.95	78.83	10/27/84	01:50	0	6.2	18.7	22.8
841117	-23.27	-67.96	11/17/84	00:27	114	5.5	176.4	29.1
841224	-9.51	-71.34	12/24/84	13:36	545	5.2	179.7	34.4
850413	-9.25	114.19	04/13/85	01:06	99	6.2	349.9	2.0
850501	-9.20	-71.23	05/01/85	13:27	600	6.0	179.6	34.5
850519	53.61	160.53	05/19/85	08:07	63	6.1	330.6	26.4
850525	54.05	160.99	05/25/85	23:29	46	5.9	330.7	26.6
850612	37.25	-116.49	06/12/85	15:15	0	5.5	275.5	41.8
850613	14.73	-90.55	06/13/85	11:42	223	5.0	215.6	42.6
850615	49.89	78.88	06/15/85	00:57	0	6.0	18.7	22.8
850630	49.86	78.70	06/30/85	02:39	0	6.0	18.8	22.8
850704	17.53	-96.99	07/04/85	08:51	70	5.0	227.9	42.2
850706	-9.73	117.67	07/06/85	14:37	86	5.6	343.8	2.0
850720	49.95	78.83	07/20/85	00:53	0	5.9	18.7	22.8
850809	52.38	173.73	08/09/85	13:03	44	5.5	323.5	27.9
850823	-24.09	-66.97	08/23/85	16:35	202	5.4	175.5	28.8
850825	53.71	158.96	08/25/85	10:07	130	5.3	331.5	26.2
850827	-21.46	-67.45	08/27/85	10:44	197	5.2	175.8	29.7
850918	49.64	155.81	09/18/85	01:27	57	5.5	330.8	24.6
851018	46.30	146.29	10/18/85	04:19	291	6.0	334.7	22.4
851024	-31.41	-68.64	10/24/85	01:48	111	5.7	177.4	26.1
860118	51.55	-173.11	01/18/86	01:59	33	5.8	317.0	30.0
860126	-27.07	-70.91	01/26/86	07:48	31	5.7	179.4	27.7
860302	51.68	156.94	03/02/86	03:14	118	5.6	331.3	25.3
860305	-18.81	169.61	03/05/86	15:47	287	5.6	275.4	9.3
860326	-7.13	-71.64	03/26/86	22:06	609	5.8	180.1	35.3
860526	-20.19	178.86	05/26/86	19:06	538	6.4	267.7	11.2

1. Event Back Azimuth
2. Event Incicence Angle

Table 2: Events Used in NEUSSN (Continued)

Event	Lat	Lon	Date	Time	Depth	M_B	Bazm	Angle
860527	-7.07	124.15	05/27/86	08:54	628	5.6	334.5	3.4
860617	53.88	160.39	06/17/86	00:42	33	5.9	330.9	26.4
860625	37.26	-116.50	06/25/86	20:27	0	5.5	275.5	41.8
860717	37.28	-116.36	07/17/86	21:00	0	5.7	275.5	41.9
860905	-37.07	-71.81	09/05/86	06:06	93	5.6	180.2	24.1
861018	-5.63	110.00	10/18/86	22:09	643	5.7	357.5	3.1
861026	53.76	-170.05	10/26/86	04:43	214	5.4	317.8	31.1
870218	51.30	-179.28	02/18/87	00:00	33	6.2	319.4	28.8
870322	-24.08	-70.08	03/22/87	03:23	42	5.9	178.5	28.8
870403	49.90	78.81	04/03/87	01:17	0	6.2	18.7	22.8
870407	-22.99	-66.16	04/07/87	00:51	238	5.4	174.6	29.2
870411	53.37	-167.20	04/11/87	16:22	33	5.0	316.3	31.5
870417	49.85	78.69	04/17/87	01:03	0	6.0	18.8	32.8
870418	61.44	-150.83	04/18/87	02:01	0	5.6	320.8	36.0
870605	41.58	88.75	06/05/87	04:59	0	6.3	14.7	19.3
870615	-19.10	-63.87	06/15/87	21:05	578	5.4	171.8	30.5
870620	49.90	78.73	06/20/87	00:53	0	6.1	18.8	22.8
870627	-14.13	-76.08	06/27/87	09:09	61	5.9	185.2	32.5
870218	51.34	-179.30	02/18/87	05:28	33	5.5	319.5	28.9
070706	53.46	158.34	07/06/87	23:22	149	5.3	331.6	26.0
870708	46.44	149.46	07/08/87	22:56	150	5.5	332.8	22.8
870710	55.05	165.62	07/10/87	18:49	61	6.0	329.1	27.5
870714	49.59	147.82	07/14/87	23:46	591	5.8	335.3	23.6
870715	17.56	-97.18	07/15/87	07:16	67	6.0	228.2	42.2

Table 3: NEUSSN Event Correlations

Event Name	Number Traces	P-Phase Correlation	Converted-Phase Correlation
840523	15	0.312	–
840526	26	0.497	–
841004	42	0.521	–
841025	36	–	0.618
841027	42	0.444	–
841117	16	–	0.342
841224	33	–	0.551
850413	21	0.526	–
850501	76	–	0.762
850519	71	–	0.517
850525	41	0.703	0.654
850612	27	–	0.630
850613	47	–	0.684
850615	51	0.630	0.610
850630	56	0.664	–
850704	36	–	0.461
850706	24	0.316	–
850720	35	0.461	–
850809	19	0.462	0.438
850823	31	0.357	0.434
850825	27	0.595	0.570
850827	41	0.706	0.447
850918	49	0.456	–
851018	67	0.544	–
851024	49	0.592	–
860118	67	0.565	0.545
860126	31	0.517	0.601
860302	71	0.692	0.729
860305	42	0.499	–
860326	65	–	0.640

Table 3: NEUSSN Event Correlations (Continued)

Event Name	Number Traces	P-Phase Correlation	Converted-Phase Correlation
860526	39	0.437	–
860527	44	0.427	–
860617	34	–	0.401
860625	53	–	0.734
860717	39	–	0.587
860905	33	0.518	–
861018	25	0.349	–
861026	40	–	0.604
870218	48	0.476	–
870218	33	0.527	0.504
870322	30	0.444	–
870403	25	0.531	–
870407	27	0.524	0.460
870411	24	–	0.492
870417	37	0.340	–
870418	35	–	0.369
870605	47	0.512	–
870615	47	0.430	0.750
870620	50	0.559	–
870627	28	–	0.294
870706	24	0.497	0.574
870708	35	0.491	–
870710	29	0.434	0.377
870714	45	0.651	–
870715	44	0.459	–

Table 4: NEUSSN Station Results from Simulated Annealing

Name	Lat	Lon	P-Phase			Converted-Phase			All Phases			Weighted
			N	Ave	SD[1]	N	Ave	SD	N	Ave	SD	Average
AGM	47.082	69.023	21	-1.7	0.4	19	-1.5	0.4	40	-1.6	0.4	-1.5
AMNH	40.781	73.974	7	0.4	0.4	8	0.3	0.2	15	0.4	0.2	0.4
BCT	41.493	73.384	25	0.5	0.5	21	0.0	0.5	46	0.3	0.5	0.4
BNH	44.591	71.256	23	-1.9	0.2	23	-1.2	0.2	46	-1.6	0.4	-1.6
BVT	43.349	72.585	31	0.0	0.2	34	0.1	0.4	65	0.0	0.4	0.1
CBM	46.932	68.121	26	-1.9	0.4	19	-1.4	0.4	45	-1.7	0.4	-1.6
CKO	45.994	77.450	22	-1.6	0.2	21	-1.1	0.4	43	-1.4	0.4	-1.2
CRNY	41.312	73.548	6	0.2	0.5	9	0.0	0.5	15	0.1	0.5	0.1
DNH	43.123	70.895	33	0.4	0.4	21	0.2	0.5	54	0.3	0.4	0.4
DUX	42.069	70.768	23	1.3	0.2	14	1.0	0.2	37	1.2	0.2	1.3
DVT	44.962	72.171	26	-1.5	0.2	23	-1.1	0.1	49	-1.3	0.2	-1.4
EBN	47.462	68.242	29	-1.9	0.2	23	-1.4	0.4	52	-1.7	0.4	-1.8
EEO	46.641	79.073	29	0.4	0.5	23	0.2	0.4	52	0.3	0.4	0.3
EMM	44.739	67.489	26	0.5	0.2	25	0.3	0.2	51	0.4	0.2	0.5
FLR	41.717	71.122	19	1.3	0.4	11	1.0	0.4	30	1.2	0.4	1.1
GAC	45.703	75.478	30	-0.9	0.2	23	-0.7	0.2	53	-0.8	0.2	-0.7
GGN	45.117	66.822	27	0.4	0.2	20	0.0	0.2	47	0.2	0.2	0.3
GLO	42.640	70.727	29	1.4	0.2	19	1.0	0.2	48	1.3	0.2	1.2
GNT	46.363	72.372	26	0.3	0.5	19	0.3	0.4	45	0.3	0.4	0.3
GRQ	46.607	75.860	17	-1.0	0.2	15	-0.6	0.2	32	-0.8	0.2	-0.9
GSQ	48.914	67.111	29	0.7	0.5	23	0.3	0.5	52	0.5	0.5	0.5
HBVT	44.362	73.065	6	0.2	0.2	11	0.4	0.5	17	0.3	0.4	0.3
HDM	41.486	72.523	14	0.1	0.4	14	0.6	0.5	28	0.4	0.4	0.4
HKM	44.656	69.641	23	-0.2	0.2	20	0.0	0.2	43	-0.1	0.2	-0.1
HNH	43.705	72.286	22	0.7	0.4	17	0.3	0.4	39	0.5	0.4	0.6
HTQ	49.192	68.394	27	0.6	0.4	19	0.4	0.5	46	0.5	0.5	0.6
IVT	43.522	73.053	26	0.7	0.4	23	0.3	0.4	49	0.5	0.4	0.4
JAQ	53.802	75.721	25	0.7	0.5	19	0.4	0.5	44	0.5	0.5	0.6
JKM	45.655	70.243	13	-1.0	0.2	10	-0.6	0.2	23	-0.8	0.2	-0.8
KLN	46.843	66.372	31	-0.5	0.4	22	-0.1	0.5	53	-0.3	0.5	-0.4
LMN	45.852	64.806	28	0.5	0.5	21	0.4	0.5	49	0.5	0.5	0.4

1. Standard Deviation

Table 4: NEUSSN Station Results (Continued)

Name	Lat	Lon	P-Phase			Converted-Phase			All Phases			Weighted
			N	Ave	SD	N	Ave	SD	N	Ave	SD	Ave
LNX	42.339	73.272	9	0.0	0.4	10	0.6	0.5	19	0.4	0.5	0.5
LPQ	47.341	70.009	28	0.8	0.4	19	0.4	0.5	47	0.6	0.4	0.7
MD1	41.553	72.467	26	0.4	0.5	23	0.3	0.4	49	0.4	0.4	0.3
MD2	41.529	72.436	23	0.2	0.4	19	0.1	0.5	42	0.1	0.4	0.2
MD3	41.506	72.540	23	0.4	0.4	23	0.3	0.4	46	0.3	0.4	0.3
MD4	41.502	72.512	25	0.6	0.5	22	0.2	0.4	47	0.4	0.5	0.5
MD5	41.455	72.495	20	0.5	0.5	20	0.3	0.4	40	0.4	0.5	0.4
MIM	45.244	69.040	24	0.0	0.2	21	0.0	0.2	45	0.0	0.2	0.0
MNQ	50.530	68.770	22	0.3	0.5	14	0.3	0.6	36	0.3	0.6	0.3
MNT	45.502	73.623	29	0.3	0.5	23	0.3	0.4	52	0.3	0.4	0.3
NSC	41.479	71.851	24	0.2	0.2	18	0.3	0.4	42	0.3	0.4	0.2
ONH	43.279	71.506	33	-1.4	0.4	21	-1.2	0.4	54	-1.3	0.4	-1.4
OTT	45.394	75.716	21	-1.0	0.2	17	-0.7	0.2	38	-0.9	0.2	-0.9
PNH	43.094	72.136	28	0.3	0.2	20	0.2	0.2	48	0.3	0.2	0.2
PNY	44.834	73.555	10	0.4	0.4	17	0.0	0.4	27	0.1	0.4	0.2
PQ1	44.904	67.327	26	0.4	0.2	22	0.2	0.2	48	0.3	0.2	0.3
QUA	42.458	72.375	24	0.2	0.4	20	0.2	0.4	44	0.2	0.4	0.2
SBQ	45.378	71.926	26	-0.1	0.2	17	-0.1	0.2	43	-0.1	0.2	-0.1
TBR	41.142	74.222	8	0.3	0.4	10	0.0	0.5	18	0.1	0.4	0.2
TRM	44.260	70.255	22	-0.7	0.2	21	-0.5	0.2	43	-0.6	0.2	-0.6
TRQ	46.222	74.555	23	0.5	0.4	19	0.2	0.4	42	0.4	0.4	0.4
UCT	41.832	72.251	9	0.4	0.4	9	0.7	0.5	18	0.5	0.4	0.5
VDQ	48.230	77.972	16	-1.6	0.2	12	-1.1	0.2	28	-1.4	0.2	-1.3
WBO	45.000	75.275	26	0.3	0.4	21	0.5	0.4	47	0.4	0.4	0.3
WEO	44.019	78.374	28	0.5	0.5	19	0.4	0.4	47	0.5	0.5	0.5
WES	42.385	71.322	25	0.3	0.2	23	0.2	0.2	48	0.3	0.2	0.3
WFM	42.611	71.491	29	0.4	0.2	19	0.1	0.2	48	0.3	0.2	0.3
WNH	43.868	71.400	30	-1.7	0.2	19	-1.3	0.2	49	-1.5	0.2	-1.6
WNY	44.391	73.859	6	0.2	0.4	11	0.0	0.2	17	0.1	0.4	0.1
WPNY	41.803	73.971	7	0.2	0.4	10	0.1	0.4	17	0.1	0.4	0.1

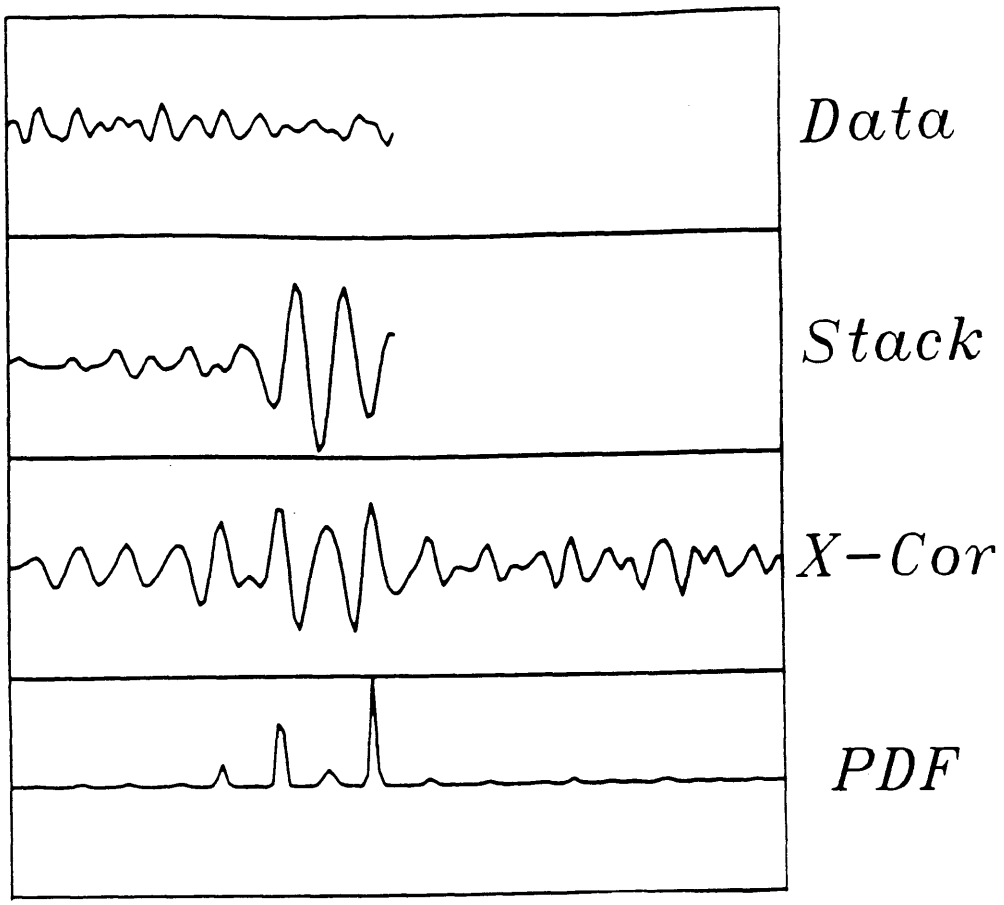

Figure 1: Simulated annealing optimization procedure schematic: A seismogram is windowed to contain the P_mP phase (top). All other stations are added to create the P_mP partial stack (second). A cross correlation is calculated between the windowed seismogram and the partial stack (third) and then converted into a probability distribution (fourth) using the temperature conversion scheme. A random selection is made from the distribution to define the trace shift. The data is shifted and the stack is updated. This procedure is done for each trace defining one iteration.

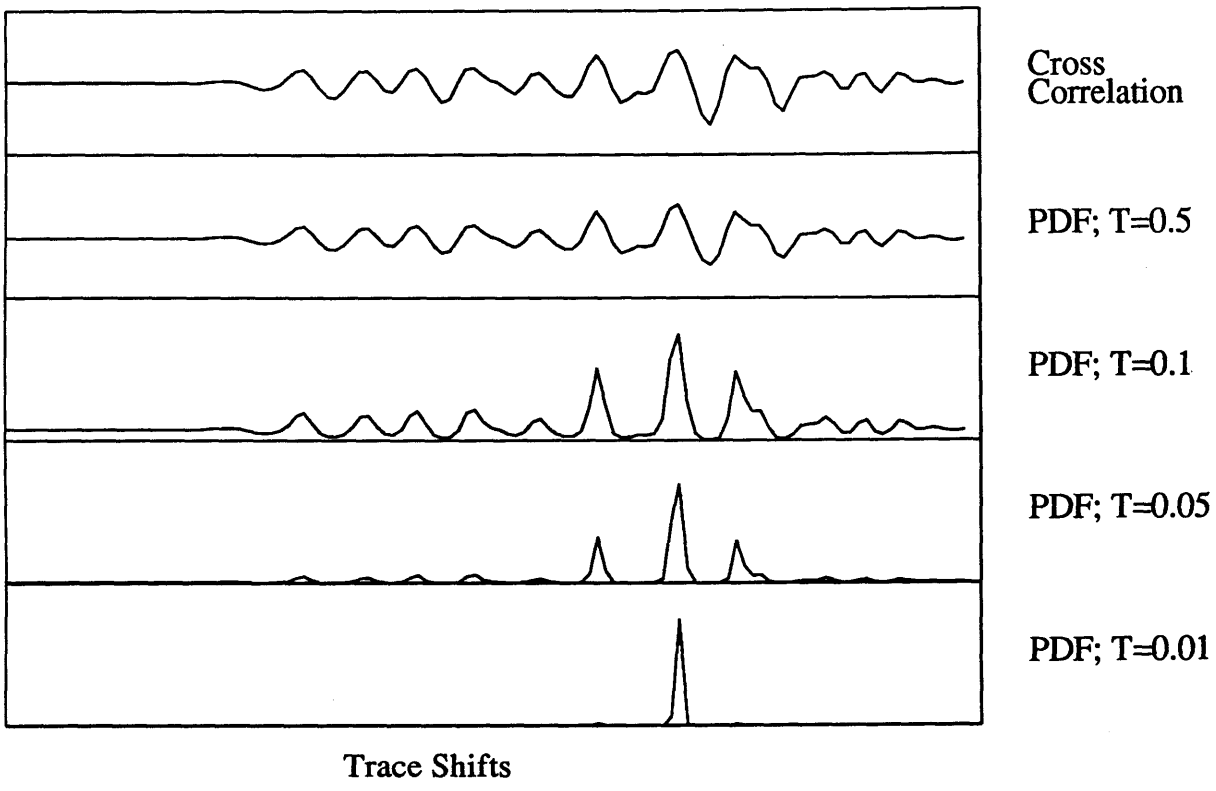

Figure 2: The conversion of cross correlation to probability distribution is dependent on the *temperature* (see text). Top Figure shows a typical cross correlation between a prediction window and a partial stack. Below are the probability distributions for *temperatures* of 0.5, 0.1, 0.05, and 0.01. As the *temperature* is lowered, we limit the probability associated with low correlation lags.

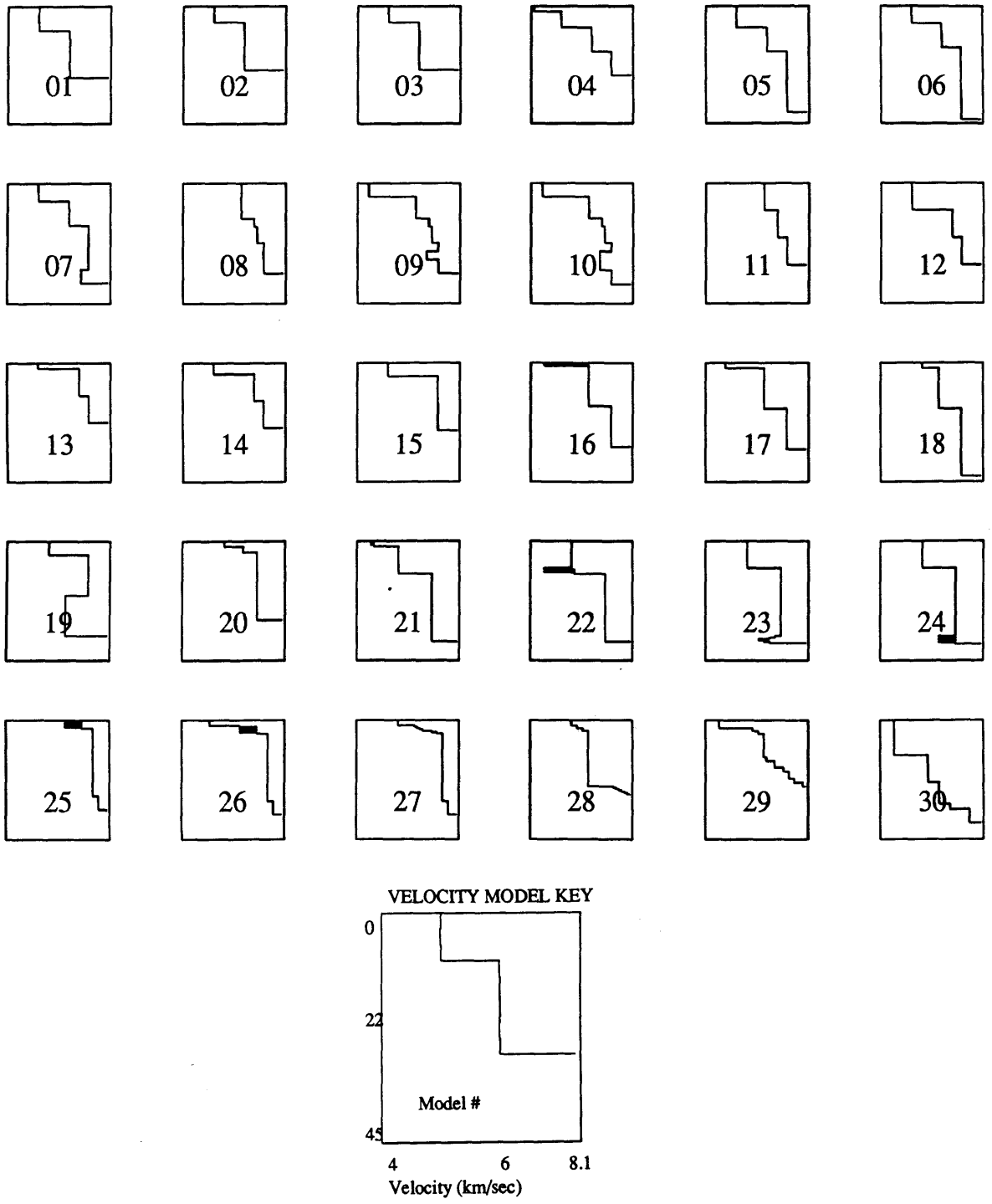

Figure 3: Velocity models used in the synthetic seismogram calculations. All plots range in velocity from 4.0 $\frac{km}{sec}$ to 8.2 $\frac{km}{sec}$ and range in depth from 0 to 45 km.

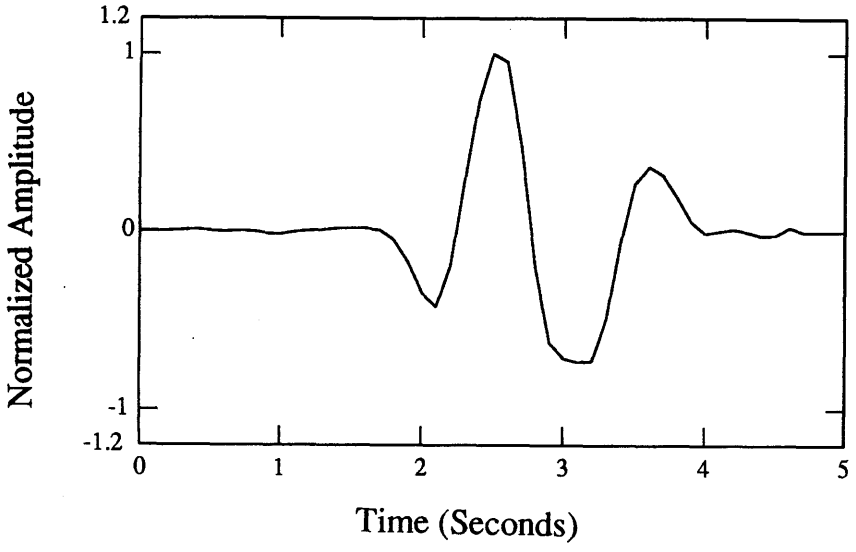

Figure 4: Source wavelet used in the synthetic seismogram calculations. This wavelet comes from event 86/03/02 (Table 2).

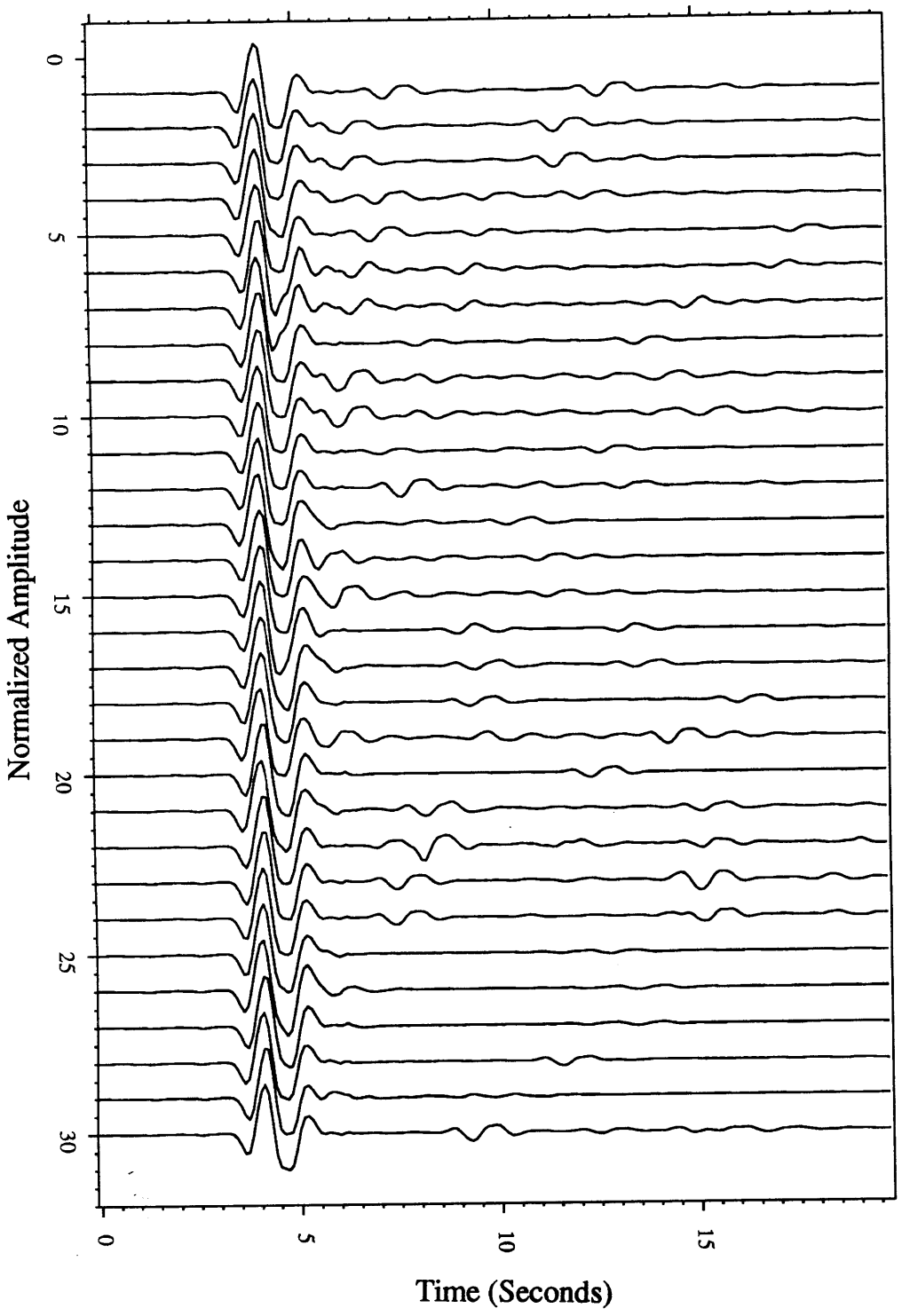

Figure 5: Synthetic data for the 30 models of Figure 3 and the source wavelet of Figure 4. Data are aligned to the direct P-wave before the analysis begins. No noise is added to the data.

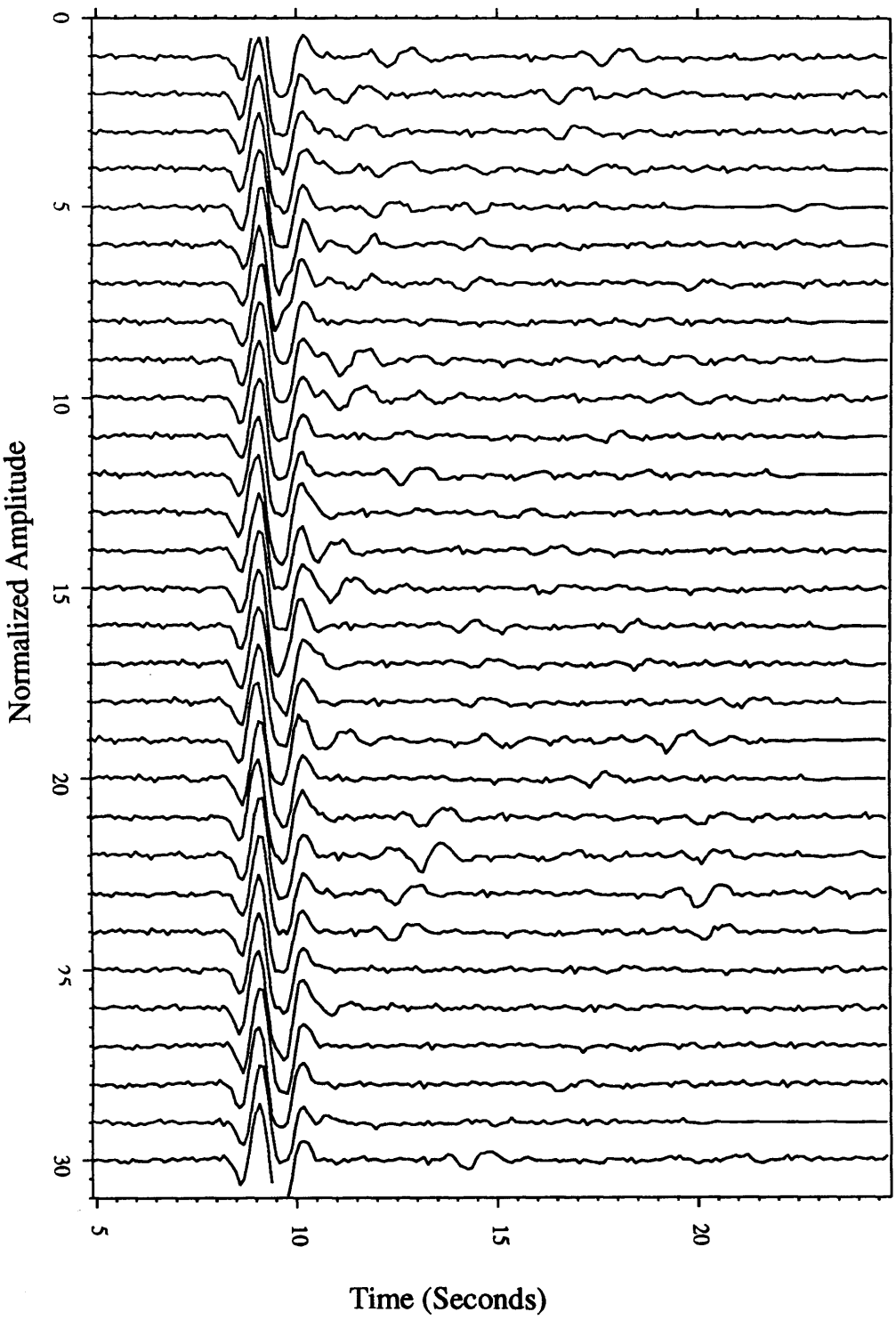

Figure 6: Synthetic data for the 30 models of Figure 3 and the source wavelet of Figure 4. Data are aligned to the direct P-wave before the analysis begins. 10% noise is added to the data.

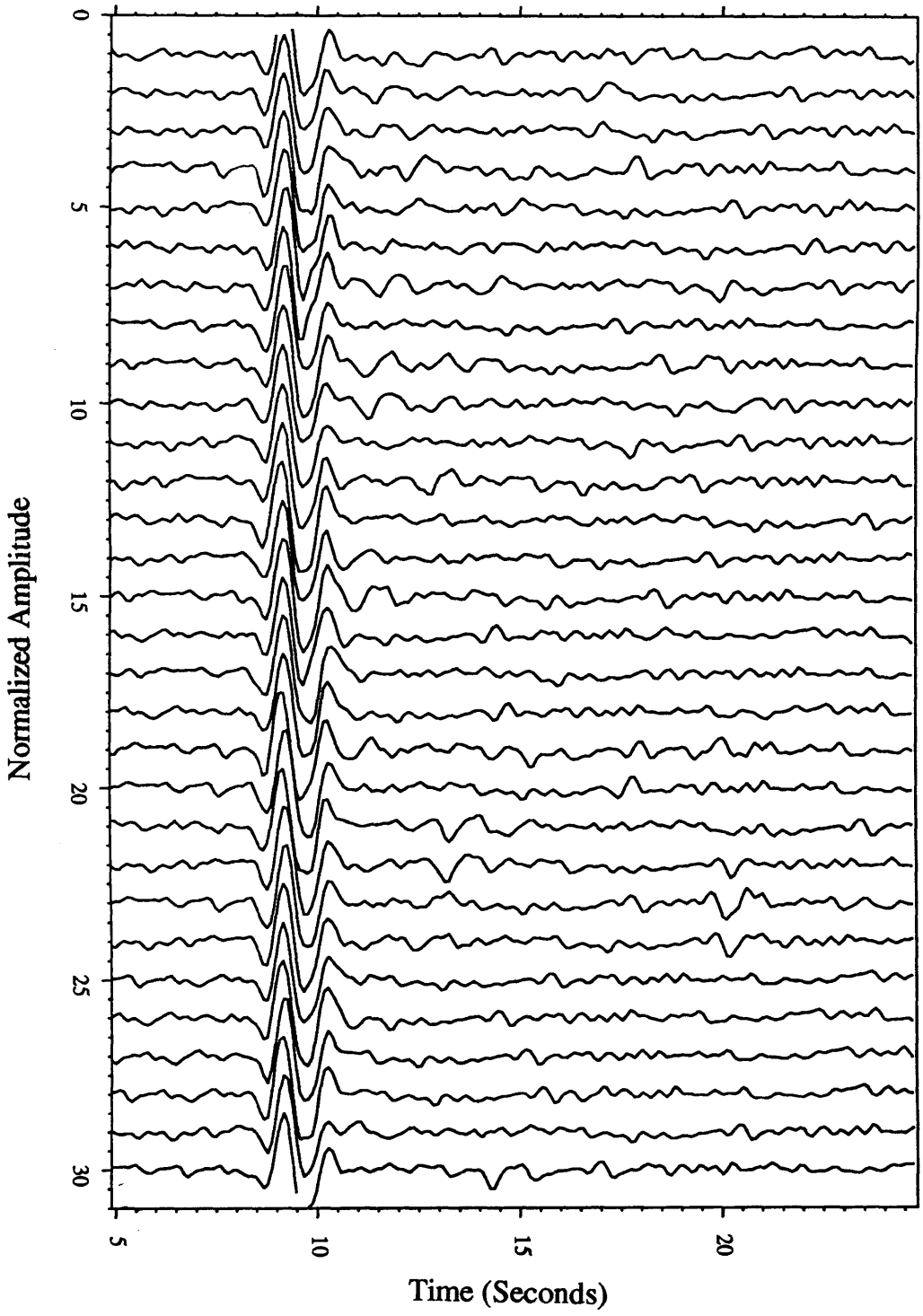

Figure 7: Synthetic data for the 30 models of Figure 3 and the source wavelet of Figure 4. Data are aligned to the direct P-wave before the analysis begins. 30% noise is added to the data.

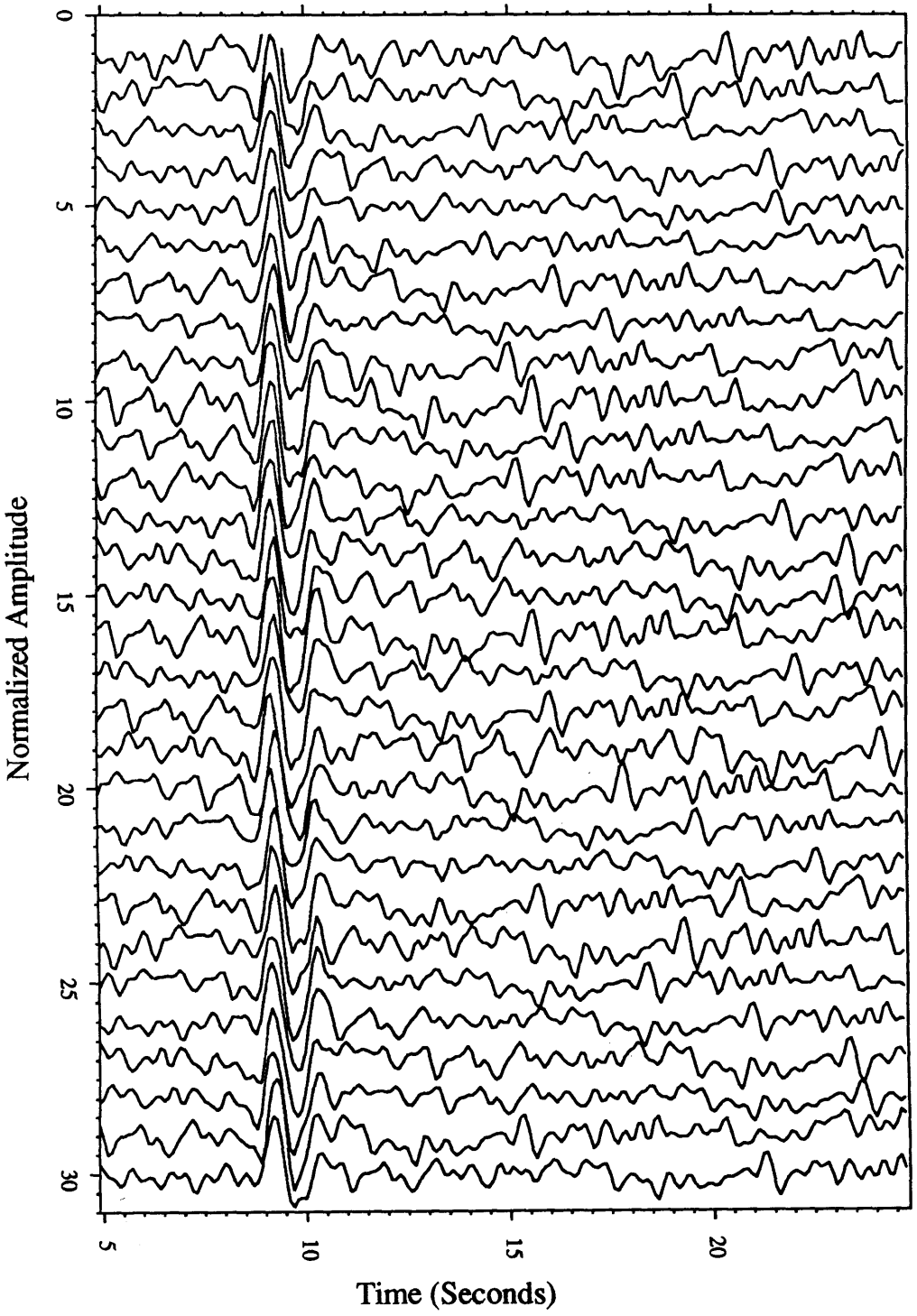

Figure 8: Synthetic data for the 30 models of Figure 3 and the source wavelet of Figure 4. Data are aligned to the direct P-wave before the analysis begins. 80% noise is added to the data.

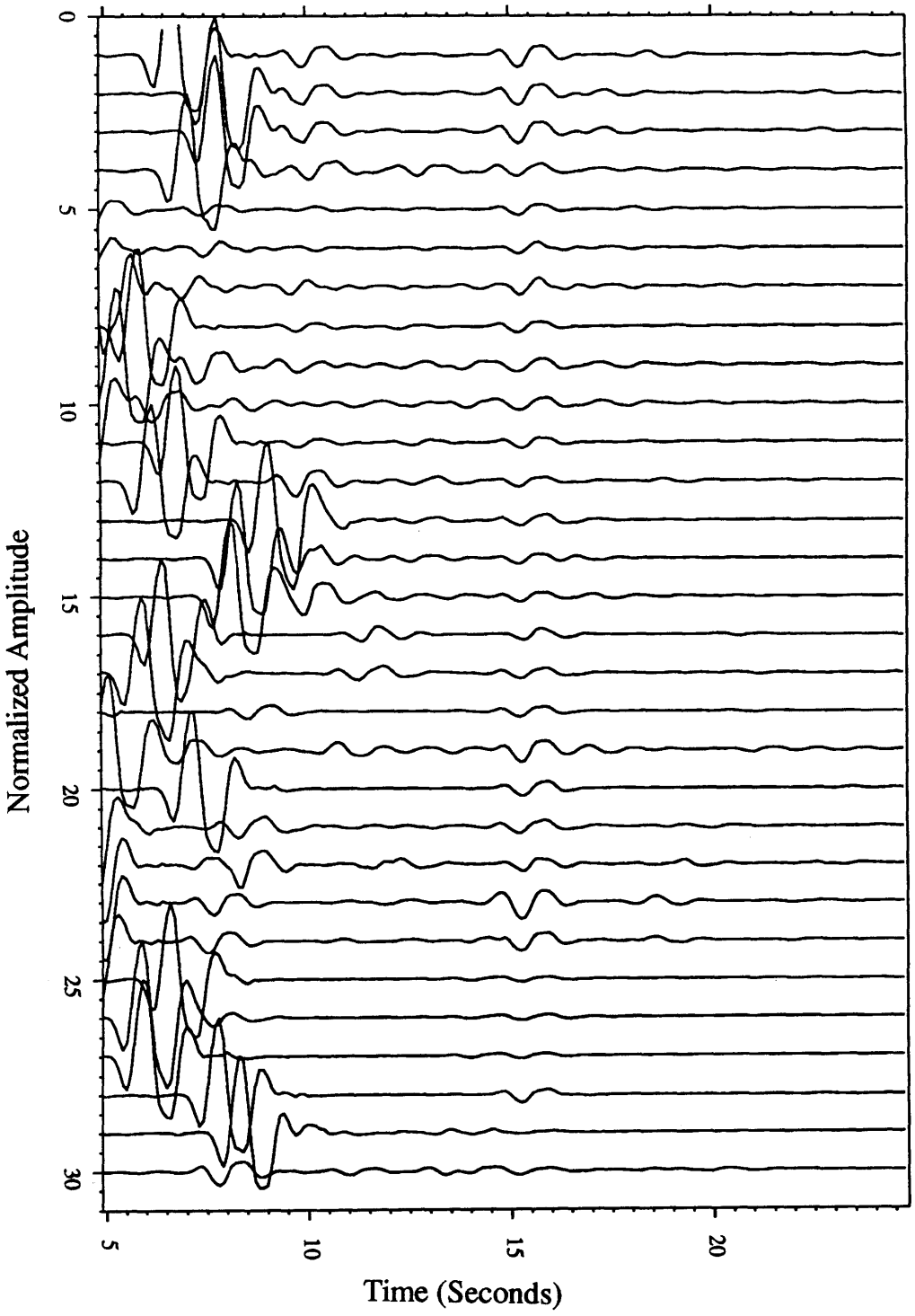

Figure 9: Synthetic data (noise-free) after the best trace configuration has been found. The P_mP phase arrives at 15.2 seconds on this plot.

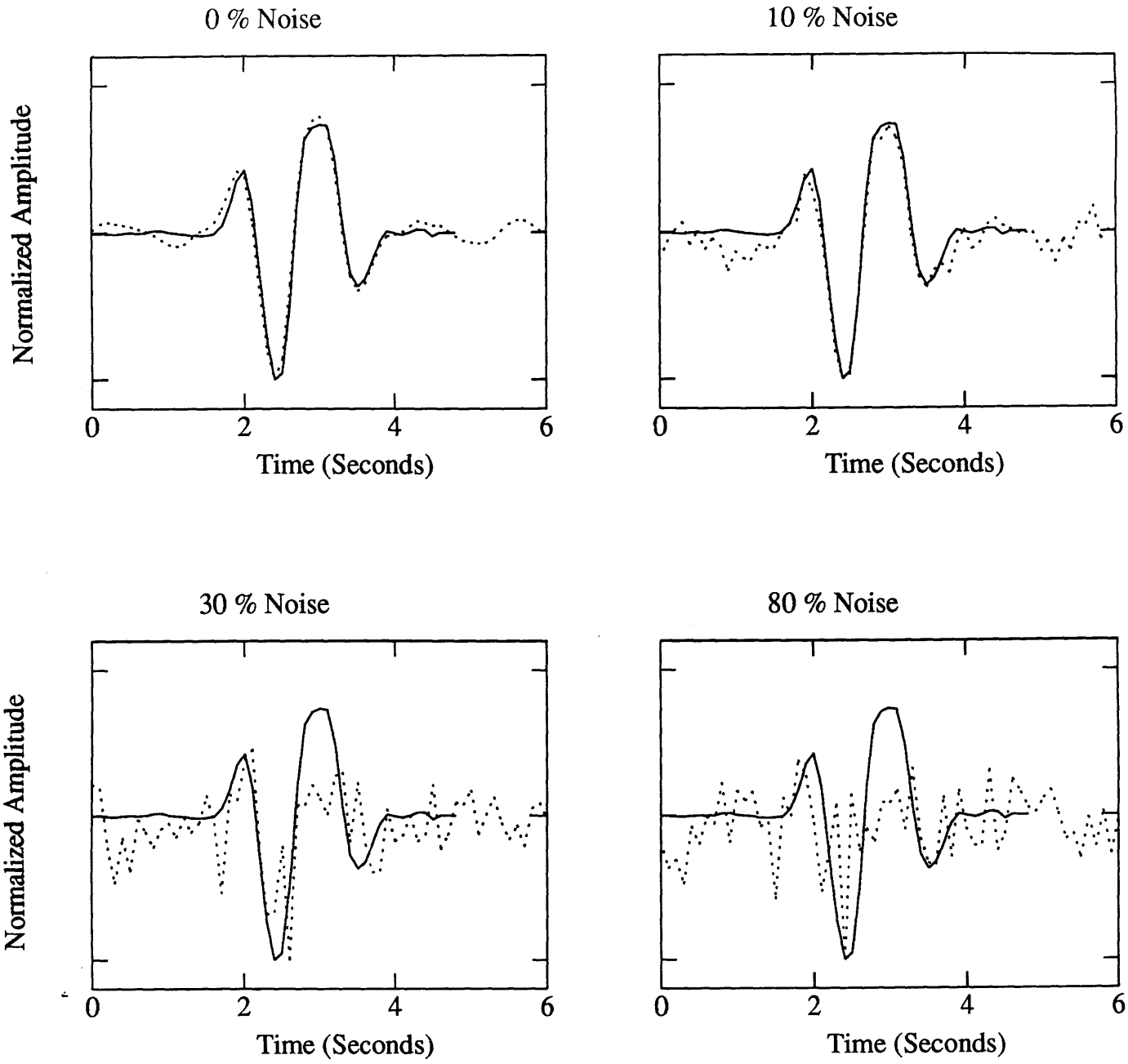

Figure 10: Reconstructed source wavelets for the noise-free, 10, 30, and 80% noise cases. Actual wavelet is solid.

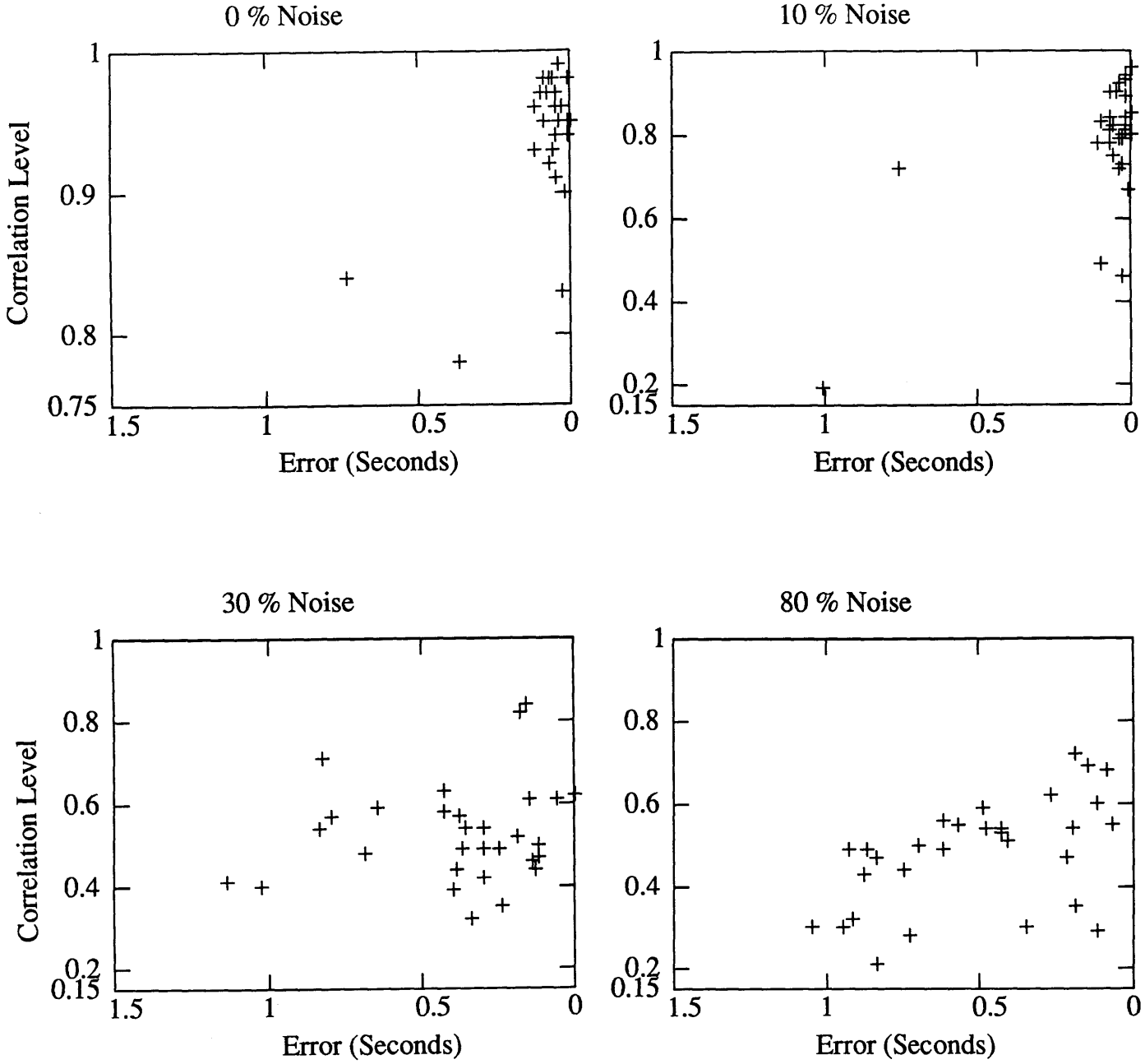

Figure 11: Scatter plots of relative vertical travel time error versus correlation level for the noise-free, 10, 30, and 80% noise cases. Note that the noise-free case has a Y-axis range different than the other cases.

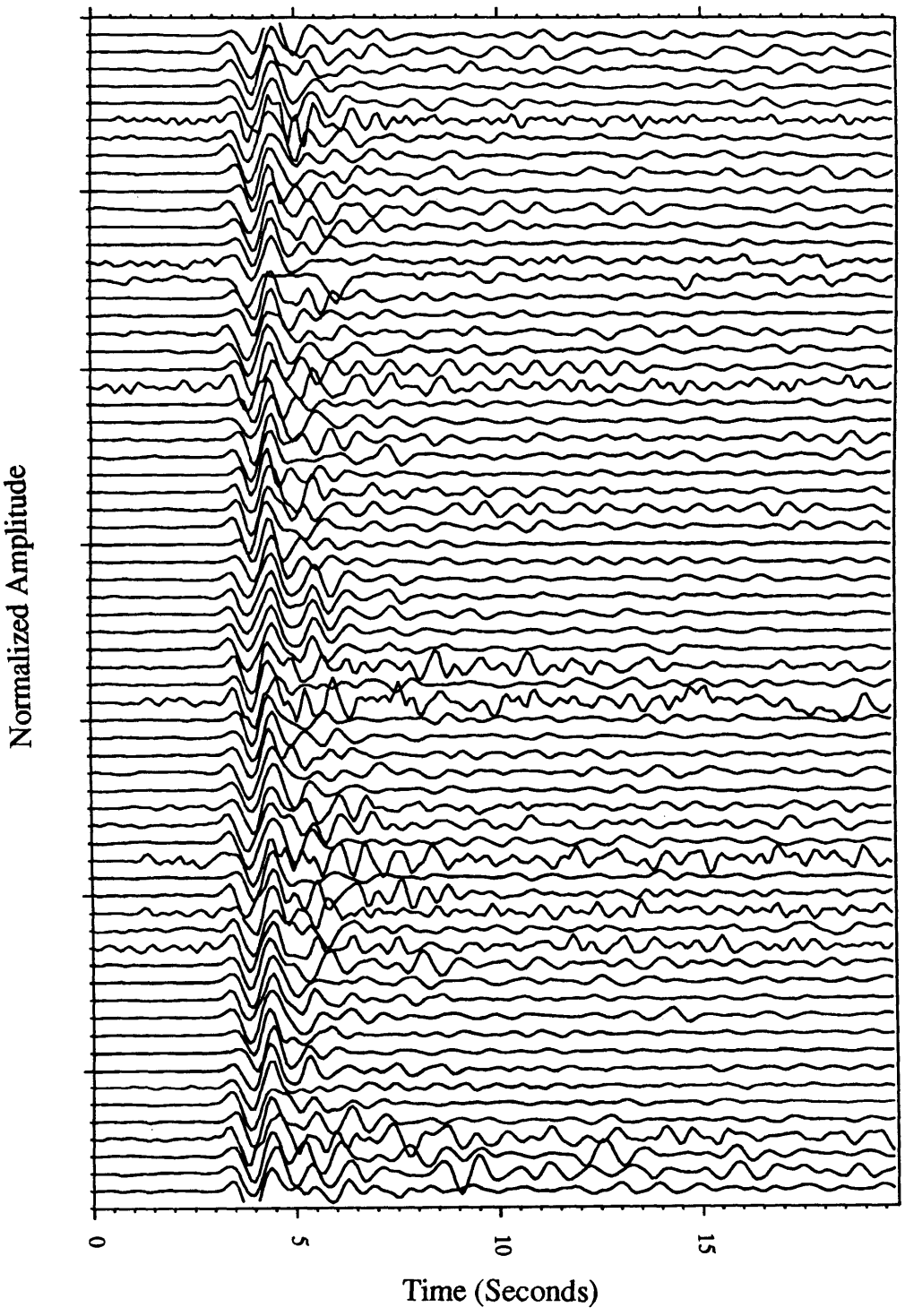

Figure 12: Actual data from Event 85/05/01. Information about this event can be found in Table 2.

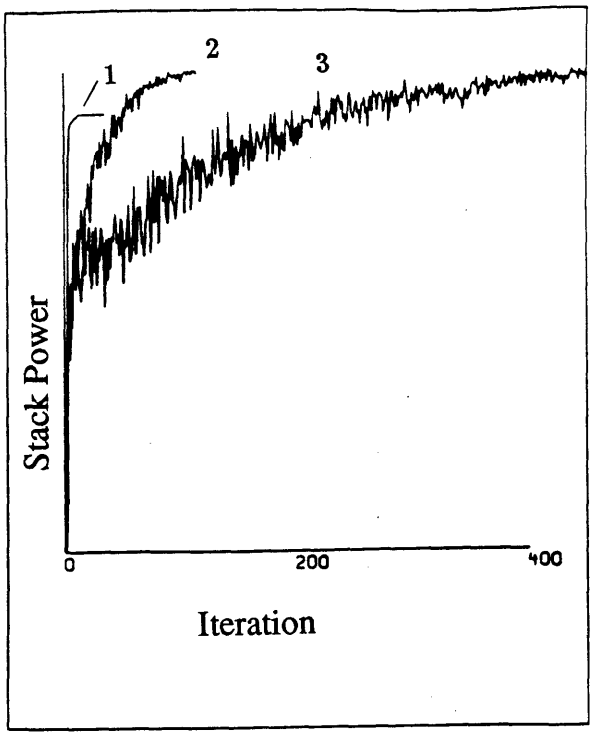

Figure 13: Stack power plot for three separate temperature cases; 1). No annealing ($T = 0$; conventional cross-correlations). 2). Steady state annealing ($T = constant$ for all iterations). 3). Temperature varying annealing: ($T = T_0 \cdot [1 - cooling\ rate]^{iteration}$).

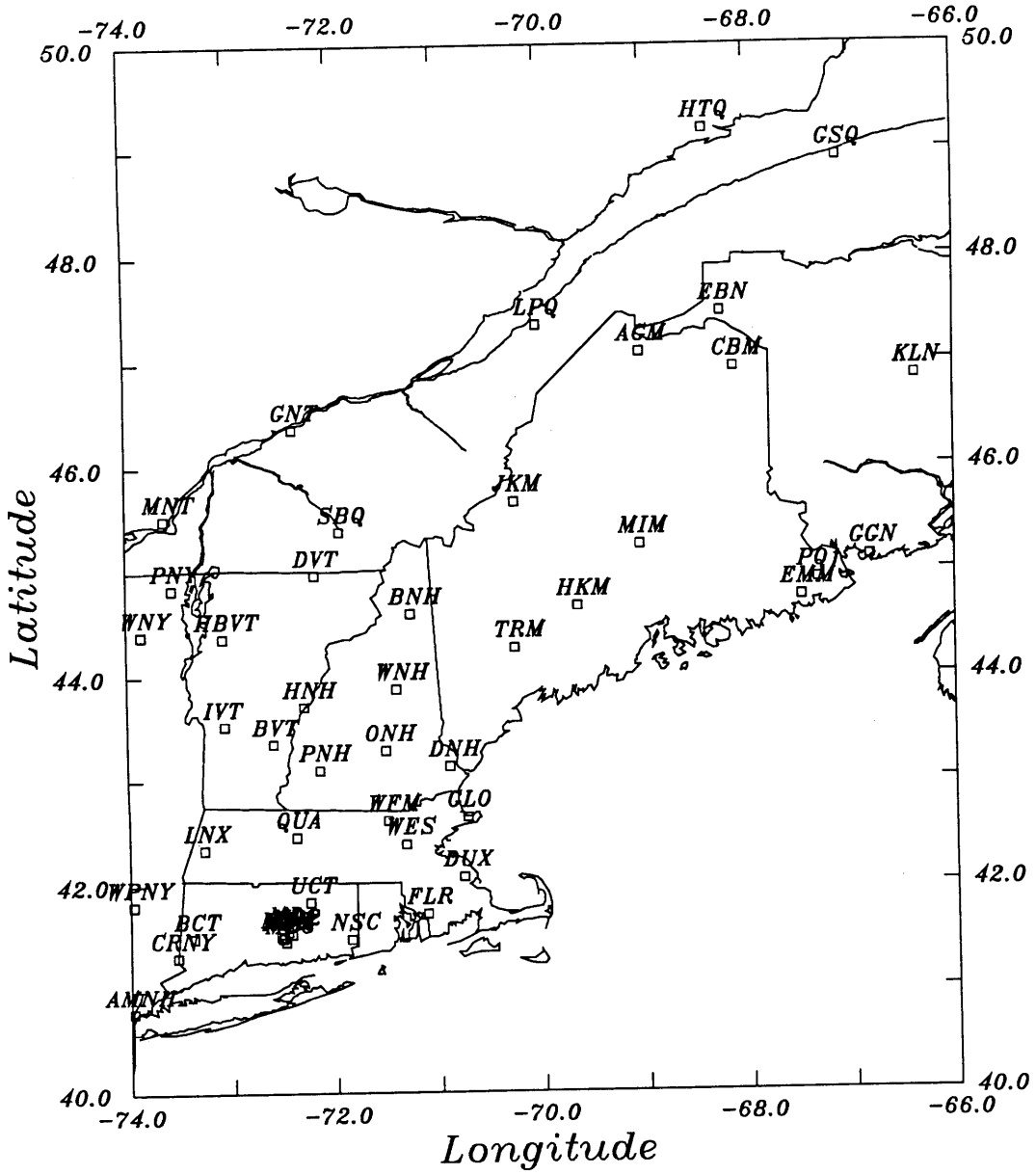

Figure 14: The stations used from the NEUSSN study area (Table 3).

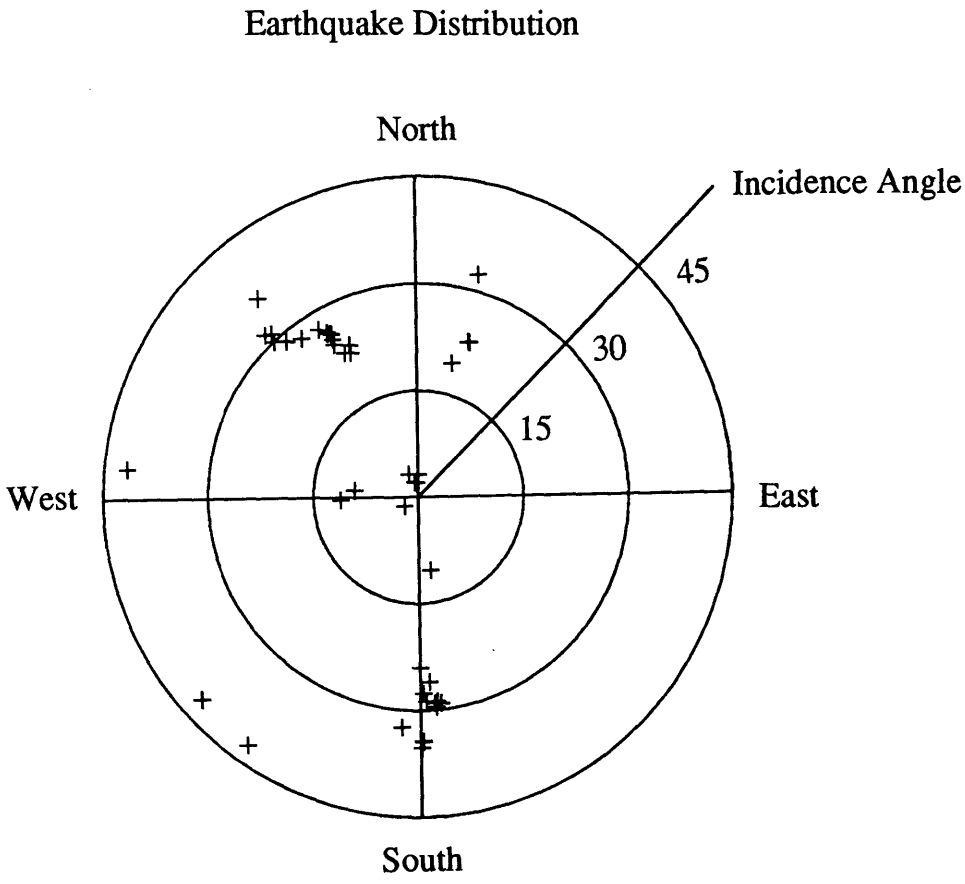

Figure 15: Average back azimuth and incidence angle of all events used in the New England study. This plot has back azimuth represented clockwise from vertical and incidence angle radial from the center. Concentric circles are at incidence angles of 15, 30, and 45 degrees.

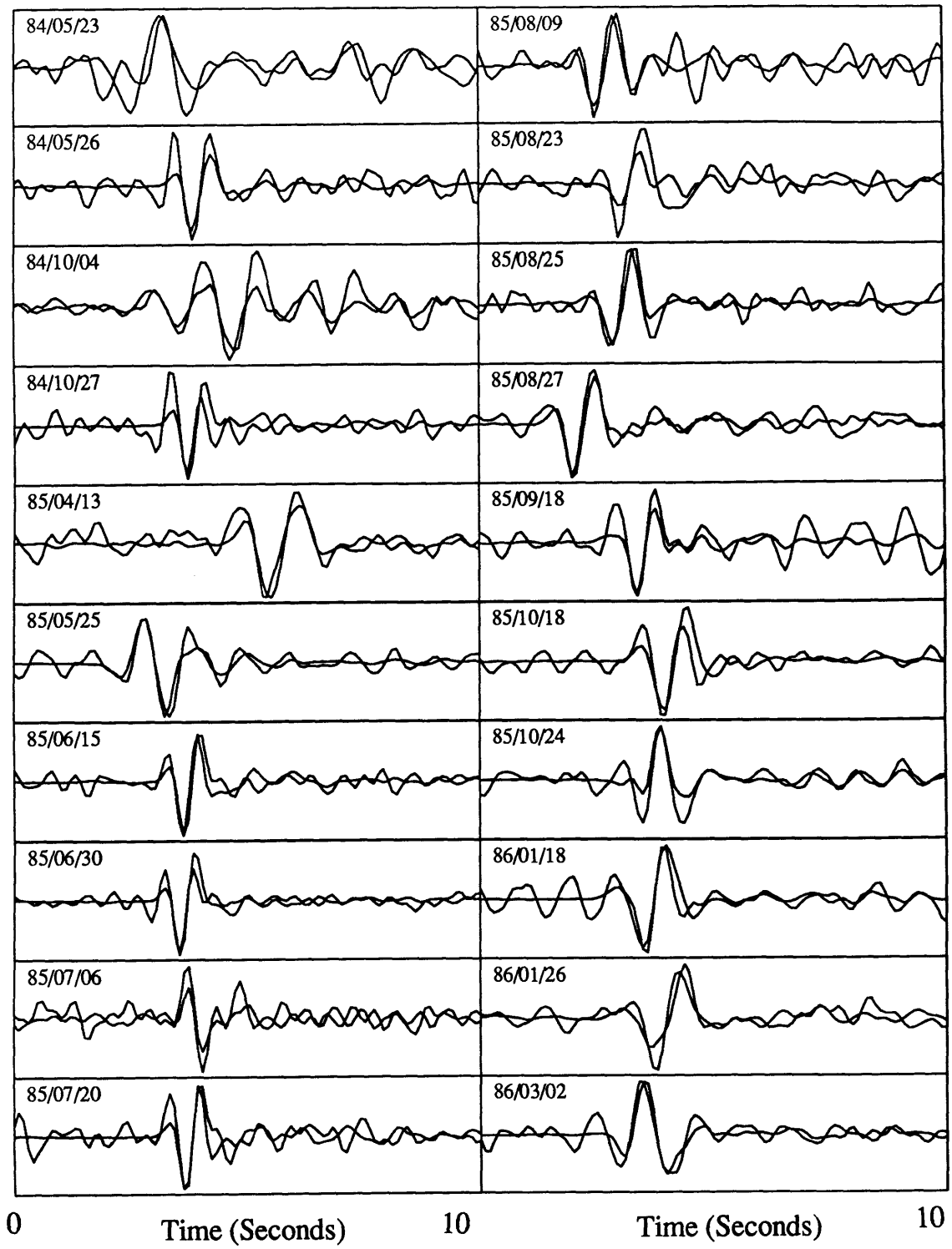

Figure 16: Comparison of the P-phase reconstruction wavelets (dashed) and the *effective* source wavelets for all P-phase events used in the final interpretation.

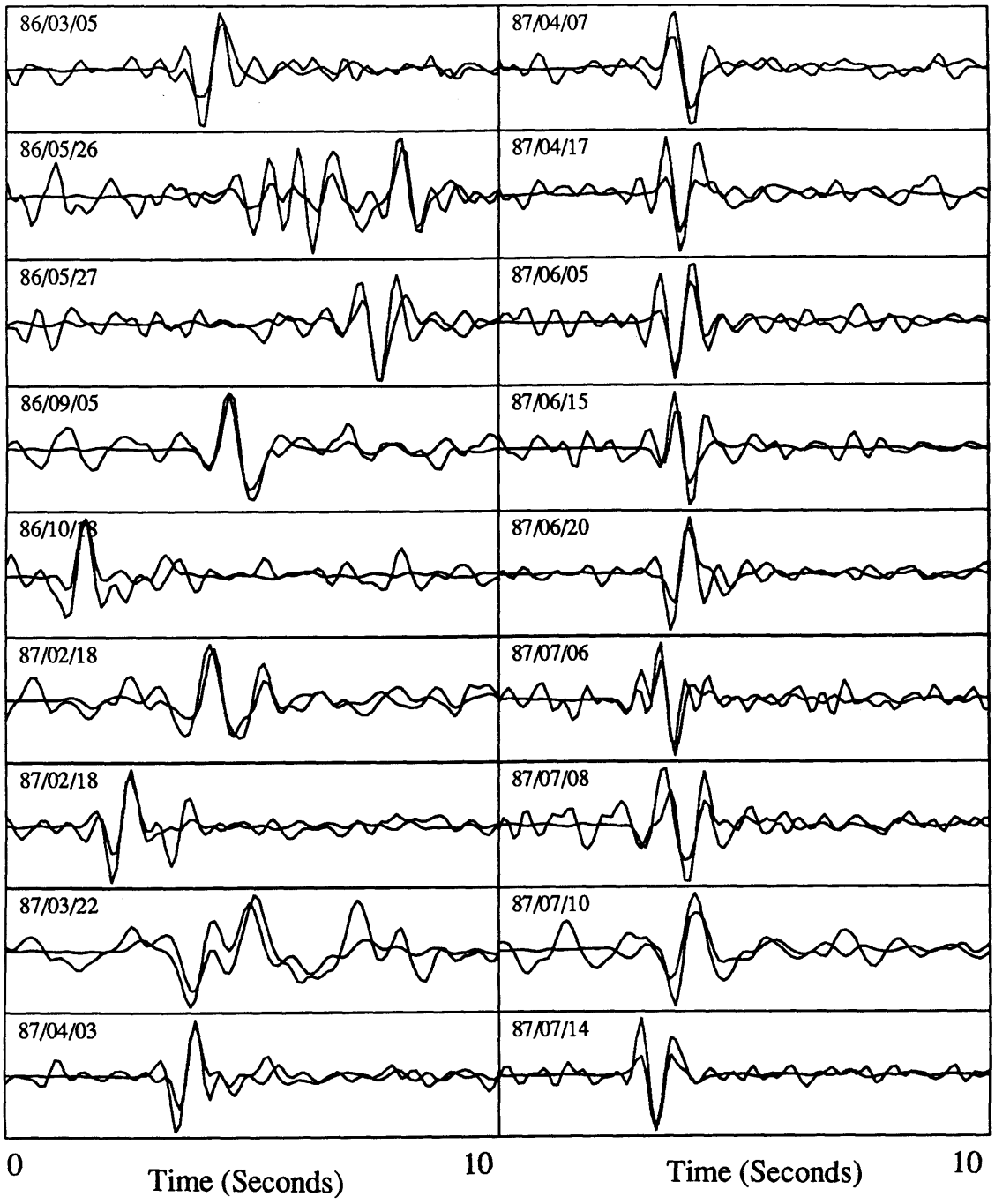

Figure 16 (Continued): Comparison of the P-phase reconstruction wavelets (dashed) and the *effective* source wavelets for P-phase events used in the final interpretation.

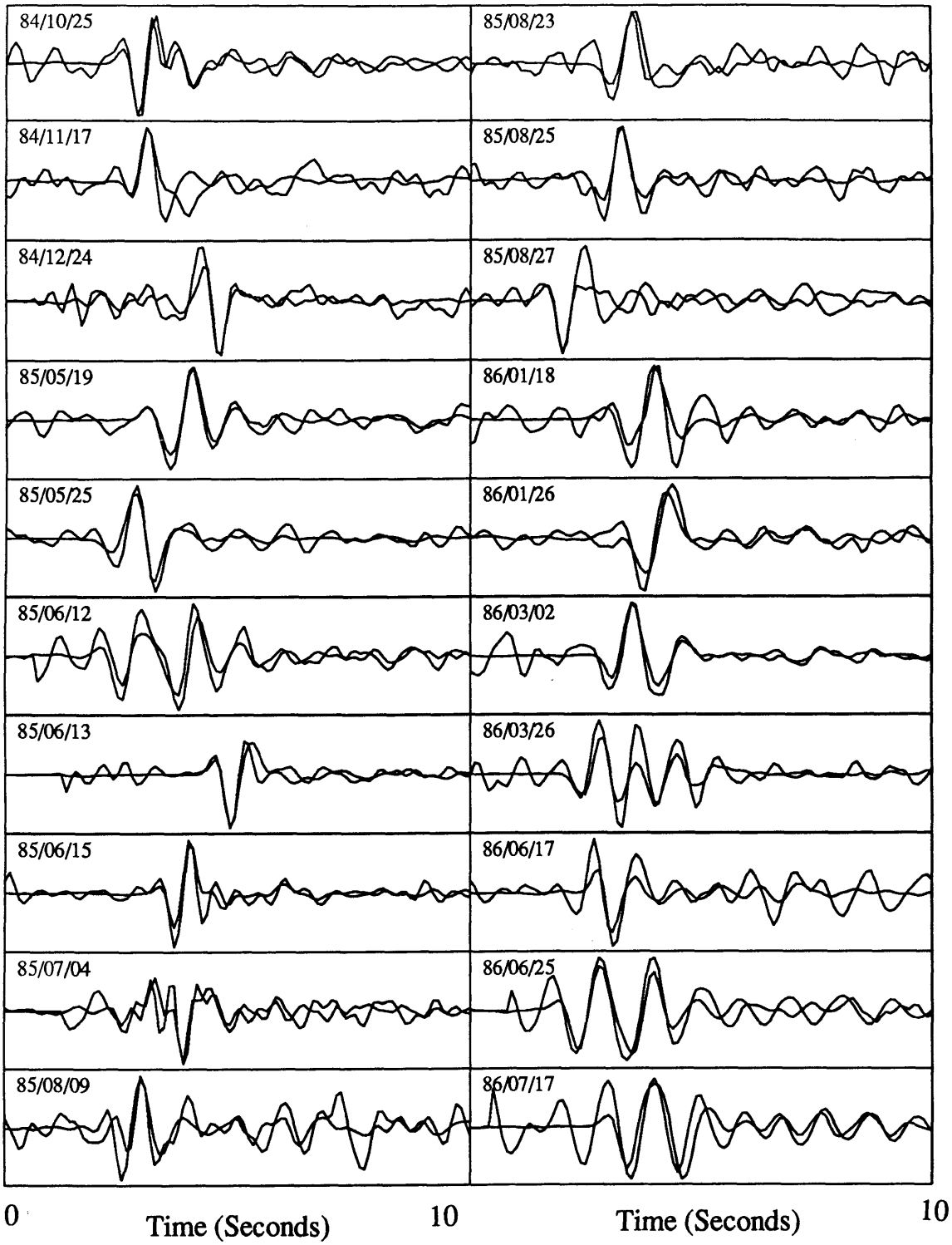

Figure 17: Comparison of the converted-phase reconstruction wavelets (dashed) and the *effective* source wavelets for all converted-phase events used in the final interpretation.

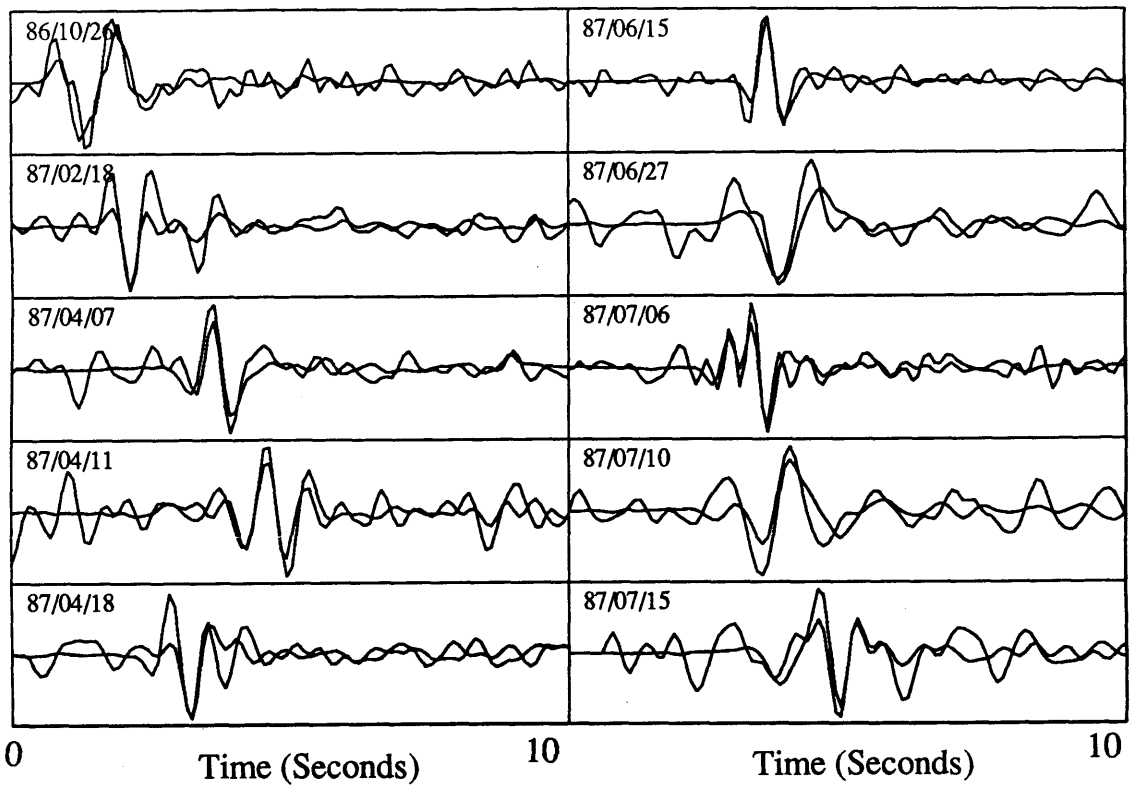

Figure 17 (Continued): Comparison of the converted-phase reconstruction wavelets (dashed) and the *effective* source wavelets for converted-phase events used in the final interpretation.

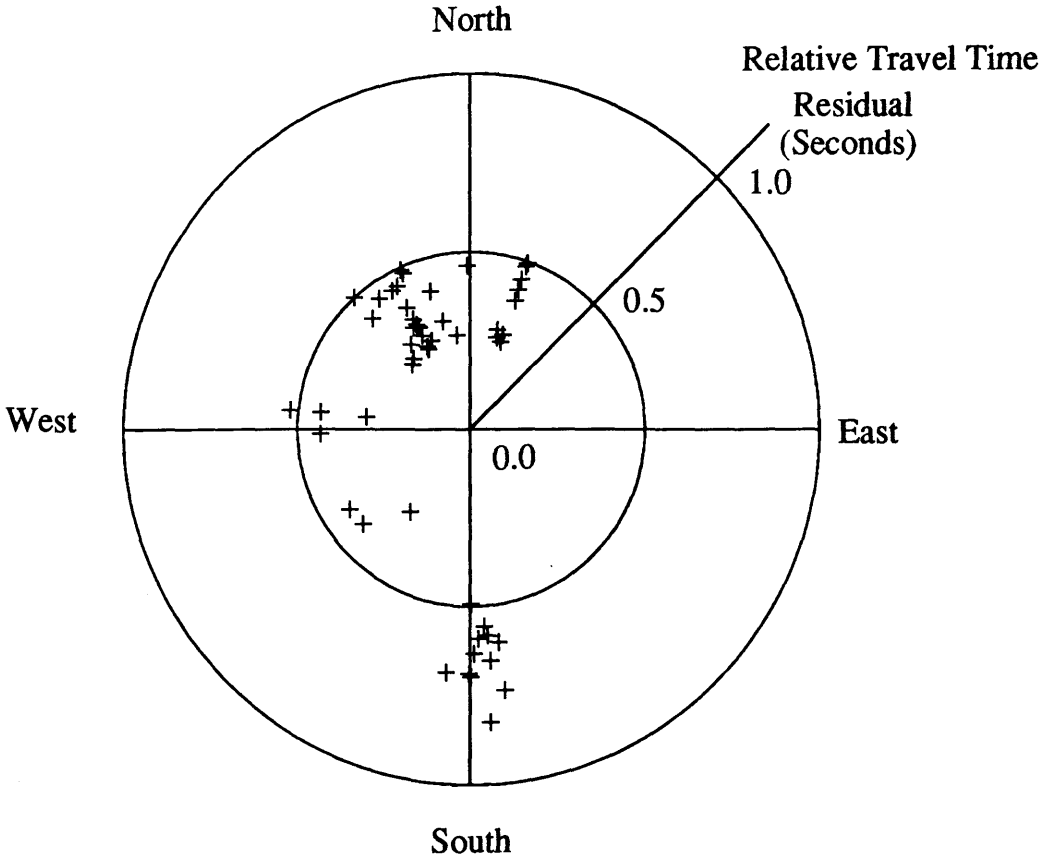

Figure 18: Rose diagram of the event back azimuths and the relative travel time estimate to the Moho for station DNH. We see that events from the south have larger relative travel times than from other azimuths.

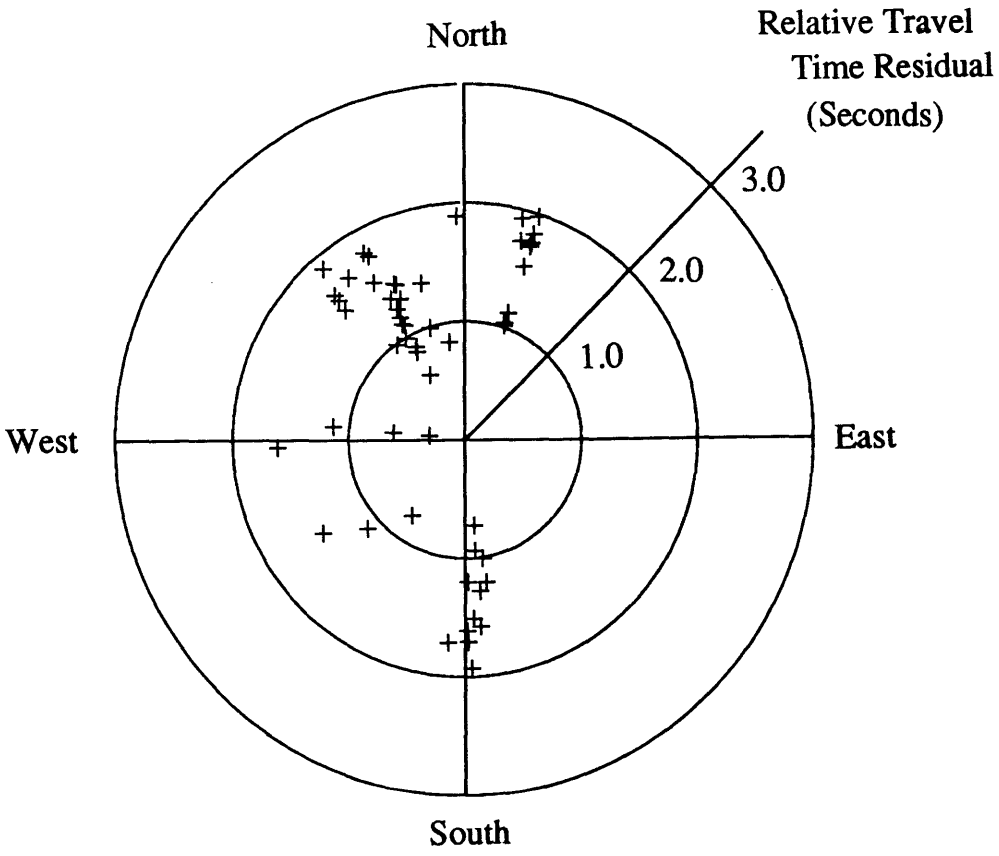

Figure 19: Rose diagram of the event back azimuths and the relative travel time estimate to the Moho for station ONH. We see no azimuthal pattern in the data.

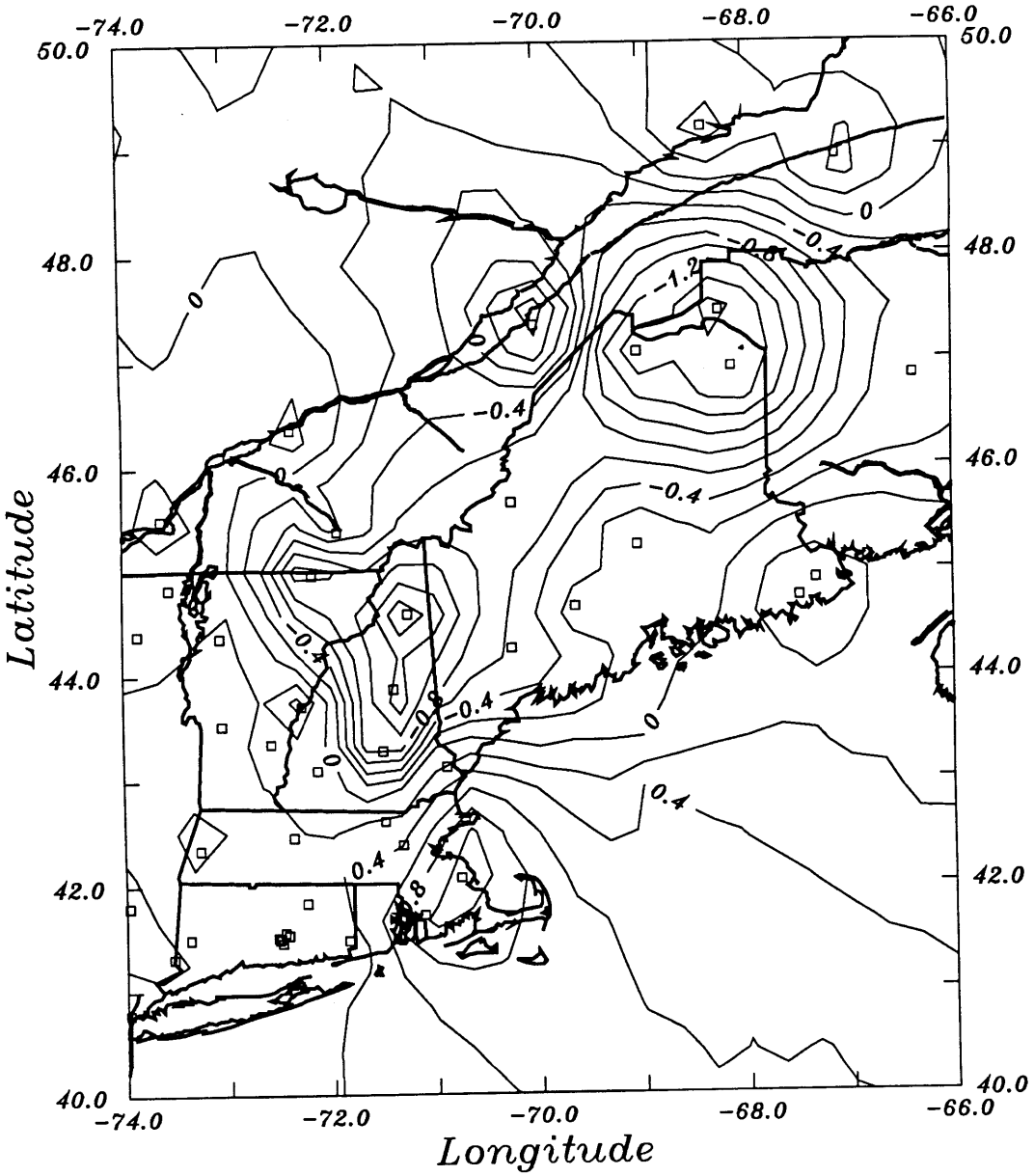

Figure 20: Plot of the final relative vertical 2-way travel times to the Moho for all stations in Table 4. Contour interval is 0.2 seconds.

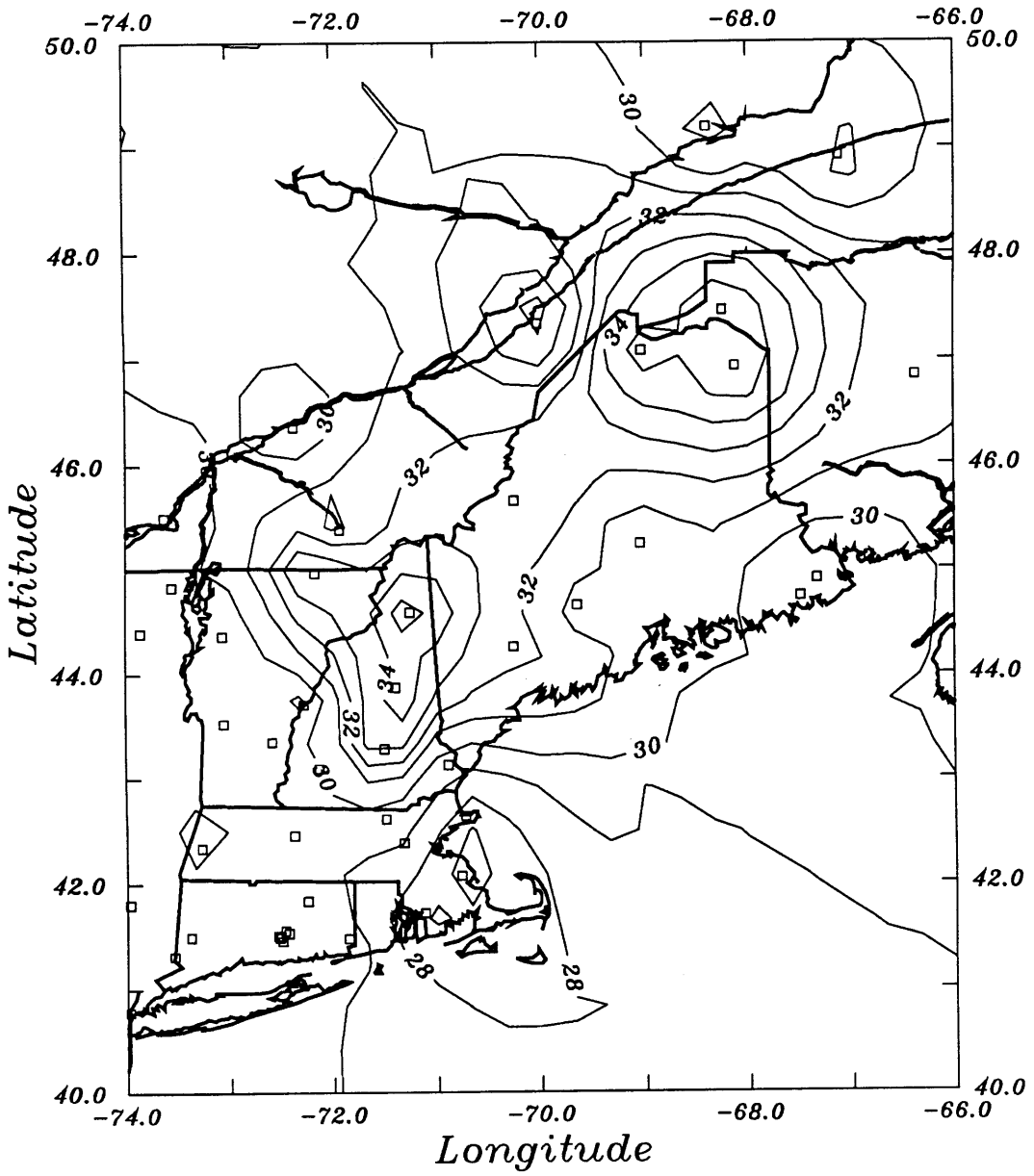

Figure 21: Plot of the NEUSSN Moho depths from relative $P_m P$ travel time residuals derived from the simulated annealing optimization procedure. The reduction velocities used for this figure come from Taylor and Toksoz (1979) and the final depths are adjusted to match the control areas of central Maine and eastern Massachusetts.

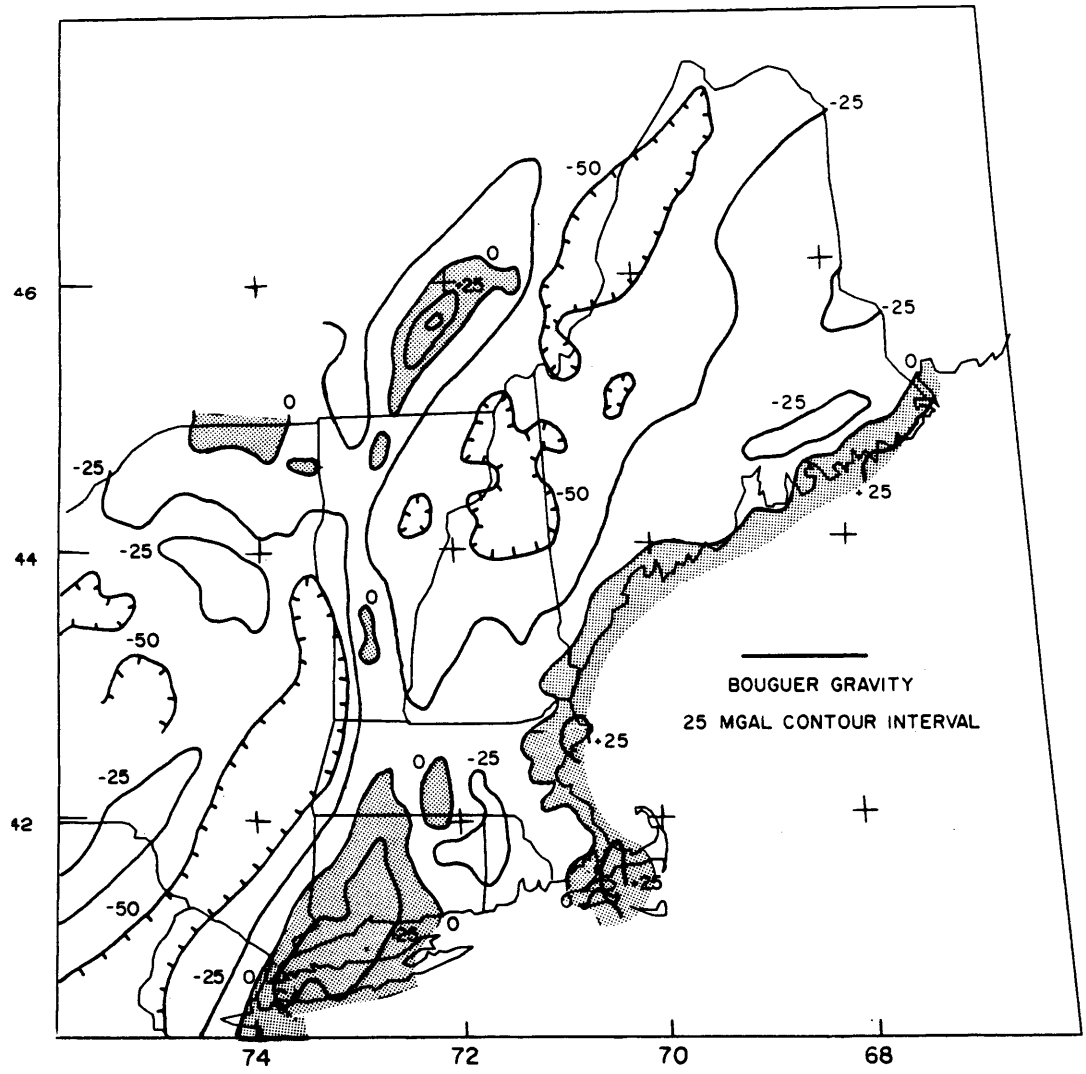

Figure 22: Bouguer gravity map for the northeastern United States. Positive anomaly is shaded (Kane et al., 1972)

Chapter 3

Teleseismic Travel Time Residual Inversion

3.1 Introduction

In this chapter the deep velocity structure of the Larderello geothermal area of central Italy is investigated by inversion of teleseismic P-wave travel time residuals. With the application of the Aki et al. (1977) travel time residual inversion technique we determine the size, extent and magnitude of the low velocity zone within this geothermal region. Information about the velocity structure helps us to understand the regional processes which control this important economic resource and helps to give us insight into the origin of other geophysical anomalies observed in the areas such as teleseismic P-wave amplitude anomalies, temperature anomalies and gravity anomalies.

A wide range of studies of the earth's velocity structure in volcanic and geothermal regions utilizing anomalous travel times and amplitudes of seismic waves have been made. Some examples include: Hawaii (Ellsworth, 1977), Yellowstone (Iyer et al., 1981), The Geysers (Oppenheimer et al., 1981) and Long Valley, California (Sanders, 1984). Many aspects of the teleseismic travel time and amplitude observations made in Larderello are similar to those in these other areas and are discussed below.

The data used in this analysis are the relative travel time residuals from the Larderello

seismic network and are determined through the application of the simulated annealing optimization technique described in Chapter 2. We present the travel time data as well as two reduction schemes implemented to improve the vertical resolution of the inversion results in Section 3.2. We also discuss the general azimuthal distribution of these data in this section. The inversion procedure is outlined and results presented in Section 3.3.

3.2 Travel Time Residual Data

The data for this teleseismic travel time inversion come from the 26 station Larderello Seismic Network (Batini et al., 1985). This ENEL monitoring network (Figure 1-3) began recording digital seismic waveforms in 1978 and in 1985 the network reached its present 26 station configuration (Table 1). Approximately 200 teleseismic events were recorded from early 1985 through June 1988, and we selected 101 of these events to use in this analysis based on the signal-to-noise ratio of the data as well as source complexity and impulsiveness. Information about these events can be found in Table 2.

The simulated annealing technique for teleseismic phase identification was applied to the waveforms of all 101 events in order to determine the relative arrival times of the direct P-wave arrivals. With this automated optimization method (described in Chapter 2) we efficiently calculate a set of relative travel times of the direct P-wave arrival for each event. Elevation corrections are applied to the travel time data and then absolute residuals are calculated using the equation

$$R_{ij}^{H} = T_{ij}^{obs} - T_{ij}^{H} \tag{3.1}$$

where $R_{i,j}^{H}$ is the absolute residual from the Herrin (1968) travel time tables for the i^{th} station and j^{th} event, T_{ij}^{obs} is the observed direct P-wave travel time determined with the simulated annealing technique and T_{ij}^{H} is the theoretical time through the reference earth model. Relative residuals RR_{ij} are calculated using

$$RR_{ij} = R_{ij}^{H} - \frac{1}{N}\sum_{i=1}^{N} R_{ij}^{H} \tag{3.2}$$

where N is the number of stations in event j. See Zandt (1978) for complete details.

Travel time residuals were calculated for all 101 teleseismic earthquakes and nuclear explosions. The azimuthal and incidence angle distribution of these data (Figure 1) can be categorized into 5 groups: events from the north-northeast, northeast, east, west and events arriving with nearly vertical incidence (referred to as PKIKP events). A large gap of 74 degrees in the azimuthal coverage exists from the southwest, however, there is sufficient azimuthal variation in the travel time residual observations to obtain a high degree of variability, or crossfire, of rays through the model. Average station residuals were calculated for the entire data set and for the 5 subdivisions (Table 3).

Two corrections were applied to the relative travel residual data. The first was introduced to reduce the residuals to a reference level of 2 km below sea level. This data reduction is required to remove the effect of back propagating near surface low velocity anomalies into the mid- and lower-crust. This travel time reduction is implemented by utilizing the well defined near surface velocity structure determined from extensive reflection analysis of the region (Batini and Nicolich, 1984). One dimensional, 2–km–deep P-wave velocity profiles for each station are established and the travel time of each ray is reduced to the 2 km level in accordance with that model and the angle of incidence of the event.

After an inversion of the travel time residual data set reduced to 2 km was performed, we found that a second reduction of the data was necessary. The initial inversion of the data referenced to 2 km produced velocity estimates of the upper most layers (defined between 2 and 7 km depth) reduced from the reference velocities by 25 to 40%. However, results from reflection analysis (Batini and Nicolich, 1984) indicate that a strong LVZ in Larderello does *not* exist above the **K** reflection horizon which is found at depths of 3 to 6 km in the Larderello area. In addition, we believe that the LVZ must be located below the level of intense earthquake activity observed over the entire Larderello region. A contour map of the deepest earthquakes recorded in the area (Figure 2) was made by reviewing the Larderello seismicity catalog for the deepest events occurring on a 2 km by 2 km grid across the region. A second datum reduction level of 6 km was selected by examination of the local earthquake depth distribution pattern, where we see earthquakes occurring at depths of 6 to 8 km throughout the area. The second reduction applied to the data lowers the reference datum

deep into the crust and helps reduce upward smearing of residuals into the top layers of the model from the strong, deeper anomalies below. To correct the relative travel time residuals to 6 km we follow the same procedure as in the 2 km reduction and use the deep velocity estimates of Batini and Nicolich (1984).

Figure 3 shows the average station travel time residuals after both reductions are applied to the travel time data. We show the patterns of travel time residuals for the four azimuth groups, the PKIKP events and all the data together. The average travel time residuals and number of observations for each station are listed in Table 3. From these maps we can see that the strongest low velocity area is concentrated in the center of the network. Strong positive residuals (slow) of up to 0.6 seconds are observed there which are in contrast to the negative (fast) residuals up to -0.4 seconds on the periphery. The contour of zero residual is aligned toward the northeast in each case with dimensions of approximately 30 by 40 km. The total travel time differences are about 1.0 second which represents a very strong travel time anomaly for a small region (approximately 25 km between average extremes). This range in average travel time residuals is similar to those found in Geysers – Clear Lake Geothermal field in California (Oppenheim et al., 1981). To produce a one second relative delay for a PKIKP event (near vertical ray) from crustal effects requires a 35% velocity decrease along the entire crustal raypath. Velocities of rhyolite melts (Murase and McBirney, 1973) and dacite melts (Hayakawa, 1957) of about 4 $\frac{km}{sec}$ would represent a 38% velocity reduction of a 6.5 $\frac{km}{sec}$ country rock. This indicates that the low velocity anomaly either exists as a large body of melted magma in the crust or, more likely, that it penetrates the crust into the mantle to depths below 20 km.

Patterns exhibited in Figure 3 indicate that average station travel time residuals calculated for events with rays passing through the center of the network have generally slower raypaths. Those paths which exclude the network center are generally faster. Stations located near the zero–second contour show this effect clearly. For events arriving from the east, stations MGUI and PADU (see Figure 1-3 for station names) have residuals of -0.29 seconds (fast) and 0.28 seconds (slow), respectively. From the west the pattern is reversed; the average residual at MGUI is 0.14 and -0.02 at PADU. Rays arriving at PADU from the

west and MGUI from the east are fast and rays arriving at PADU from the east and MGUI from the west are delayed. This pattern indicates that the first layer stripping procedure has effectively removed the near surface anomalies and that the data represents only mid-crust and mantle effects. It also implies that the velocity contrasts are quite strong and have rapid lateral variations.

3.4 Inversion

Travel time residuals are inverted for velocity perturbations using the method of Aki et al. (1977). This method of inversion has been used quite extensively in the past, particularly for the purposes of magma chamber delineation. See Iyer(1988) for a review of Aki inversions in volcanic and geothermal regions. The details of the inversion are only sketched below; for a complete review of the inverse formulation see Zandt (1978) or Taylor and Toksoz (1979).

An earth model consisting of a set of layers subdivided into right rectangular blocks is established as a starting model. A velocity is assigned to each block and for each event and each station rays are traced through the model in accordance with the event incidence angle. Travel time residuals are distributed in the blocks along the raypath proportional to the length of the ray in each block, and since events are located at various distances and azimuths from each station, a dense mesh of distributed residuals is formed beneath the network. The Aki technique solves the system of equations which characterizes this travel time distribution using a damped least squares technique.

The starting model for the travel time inversion is the five layer model shown in Table 4. The crust is characterized by three layers, each of which is 5 km thick with velocities of 6.0, 6.5, and 7.0 $\frac{km}{sec}$, respectively. The upper mantle is parameterized by two 10 km thick layers at 8.1 $\frac{km}{sec}$. This model is consistent with deep reflection work done in Larderello (Batini et al., 1988) and the refraction model of Giese et al. (1980) developed for southwest Tuscany.

Figure 4 shows the results of the travel time inversion. These plots show the velocity perturbation for each of the five layers in percent of the background velocity as contours of equal velocity perturbation. For the crustal layers (1, 2, and 3; from 6 to 21 km) the region of low velocity is confined to the center of the network in an area 25 by 40 km in extent,

with an elongate pattern to the northeast. This pattern coincides with the region of low amplitude teleseismic P-waves, high heat flow, negative Bouguer gravity anomaly, and the elevated **K** reflection horizon.

Layers 4 and 5 (depth from 21 to 41 km) also have a distinct low velocity pattern in the center of the network. The relative velocity perturbations are still quite large at these depths (10% in the center). The zone of maximum low velocity migrates to the northeast at greater depths and the total area of LVZ increases. Slices through the final perturbed model (Figure 5) show the pattern of the anomalous body in vertical cross section. The southwest to northeast slice shows that strong velocity reductions relative to the reference model (to 18%) are necessary to satisfy the data from depth of about 6 to 16 km. The LVZ in the crustal part of the model is about 20 km wide. Deeper in the crust and in the upper mantle the perturbations are smaller and cover a larger region. However, the results in the lower part of the model may be corrupted by smearing effects in the inversion. This inversion method is a residual redistribution technique which back propagates travel time residuals equally along each raypath. When criss-crossing ray coverage is not sufficient in an area, artificial velocity anomalies can be created. This effect may be accentuating the deep and widespread low velocity area of layers 4 and 5 where velocity reductions of up to 10% are required by the data and the LVZ covers an area about 35 km wide. The northwest to southeast slice shows a more uniform pattern of low velocity, with a reduction of about 10% existing from the top layer (6 km) to a depth of 41 km. The width of the LVZ is about 15 km in the crustal layers and increases at depth. However, resolution of the LVZ is poor to the southeast due to poor data coverage.

To quantify the confidence in the final model, resolution and standard error functions are generated for each model parameter (Zandt, 1978). The resolution values presented here are a measure of how well each block velocity estimate is independently measured. A resolution value of 1.0 indicates a perfectly resolved parameter with no interdependence on other parameters. Lower values of resolution indicate that the final velocity should be thought of as an estimate of an average of the surrounding blocks. The standard error values are a relative measure of how errors on the travel time data affect model parameter

estimates. Figure 6 shows the resolution and error calculations for the southwest to northeast slice. Resolution is best in the center of the model and to the northeast at depth due to good azimuthal and incident angle coverage in that quadrant, and worst from the southwest, where coverage is poor. Because the addition of the damping parameter used to solve the least squares problem discussed above tends to reduce the number of degrees of freedom of the problem, the trade-off between standard error and model resolution must be examined. Through trial and error we find the best trade-off when damping is set to 0.003 $\frac{sec^2}{percent^2}$. A full discussion of the inversion results can be found in Chapter 7.

TABLE 1: Larderello Seismic Network Stations

Station Name	Lat	Lon	Elevation Meters
CLSV	43.23	10.90	671
MINI	43.23	10.85	444
SERR	43.31	10.79	223
POMA	43.33	10.90	231
SDAL	43.26	10.93	380
SCAP	43.25	11.00	360
MGUI	43.29	11.01	341
RADI	43.25	11.07	489
MLUC	43.22	10.94	572
FROS	43.20	11.15	432
SINI	43.16	11.11	350
LURI	43.12	11.12	458
TRAV	43.19	11.03	472
CORN	43.16	10.94	886
VALE	43.20	10.87	782
CRDP	43.09	10.97	816
MDSV	43.15	10.85	754
CRBE	43.11	10.82	442
MBAM	43.06	10.82	342
LAGO	43.15	10.81	319
PADU	43.20	10.79	439
SASS	43.25	10.69	438
MONV	43.18	10.71	445
FRAS	43.11	10.76	220
STTA	43.12	10.65	361
PLUZ	43.05	10.74	156

TABLE 2: Teleseismic Event Information

Event	Lat	Lon	Date	Time	Depth	M_B	Bazm[1]	Angle[2]
001	-21.62	-176.49	Oct 12,85	02:12	157	5.8	18.3	1.8
002	40.32	69.84	Oct 13,85	15:59	33	5.8	72.2	38.1
003	46.30	146.29	Oct 18,85	04:19	291	6.0	29.2	23.2
004	36.72	54.80	Oct 29,85	13:13	33	6.0	85.8	42.1
005	51.77	175.55	Oct 30,85	19:05	33	5.6	9.4	22.5
006	53.26	-166.92	Oct 31,85	19:33	33	5.8	358.6	22.7
007	51.55	-173.11	Jan 18,86	01:59	33	5.8	2.5	22.1
008	-18.81	169.61	Mar 5,86	15:47	287	5.6	43.0	0.7
009	-7.13	-71.64	Mar 26,86	22:06	609	5.8	259.7	20.8
010	54.65	161.58	Apr 1,86	13:40	35	5.7	16.8	24.3
011	43.89	147.57	Apr 16,86	12:52	23	6.3	29.8	22.3
012	51.52	-174.78	May 7,86	22:47	33	6.4	3.5	22.1
013	36.37	70.71	May 7,86	23:25	223	5.6	77.4	37.1
014	51.50	-174.80	May 7,86	23:41	33	5.1	3.5	22.1
015	51.16	-176.57	May 8,86	01:18	33	5.4	4.7	22.0
016	51.16	-176.89	May 8,86	02:04	33	5.5	4.9	22.1
017	51.14	-176.44	May 8,86	04:03	33	5.8	4.6	22.0
018	51.34	-175.36	May 8,86	05:37	18	6.0	3.9	22.1
019	51.46	-174.24	May 9,86	19:04	33	5.8	3.2	22.1
020	51.49	-178.47	May 14,86	04:02	33	5.4	5.8	22.2
021	52.33	-174.50	May 17,86	16:20	26	5.8	3.3	22.4
022	43.68	148.42	May 21,86	05:47	39	6.1	29.4	22.1
023	-21.82	-179.08	May 26,86	18:40	583	6.1	24.4	1.6
024	-20.19	178.86	May 26,86	19:06	538	6.4	27.5	0.9
025	38.00	37.92	Jun 6,86	10:39	10	5.6	95.0	48.0
026	43.27	146.49	Jun 8,86	11:02	56	6.0	30.8	22.3
027	-22.04	-178.93	Jun 16,86	10:48	547	6.3	24.3	1.7
028	-22.04	-178.93	Jun 16,86	10:48	547	6.3	24.3	1.7
029	53.88	160.39	Jun 17,86	00:42	33	5.9	17.7	24.2
030	51.25	-179.75	Jul 5,86	03:01	33	5.6	6.6	22.2
031	10.39	56.83	Jul 7,86	16:26	08	6.4	115.4	34.8
032	29.96	51.58	Jul 12,86	07:54	10	5.7	98.6	41.6
033	16.06	-93.90	Jul 13,86	09:12	80	5.9	291.6	20.7
034	47.26	151.13	Jul 19,86	5:59	141	5.9	26.0	22.9
035	-25.85	-177.49	Jul 27,86	10:43	147	5.8	24.3	1.0

1. BAZM: Back Azimuth from North 2. ANGLE: Average Event Incidence Angle

TABLE 2: Teleseismic Event Information (Continued)

Event	Lat	Lon	Date	Time	Depth	M_B	Bazm	Angle
036	51.60	-174.10	Jul 28,86	04:06	33	5.4	3.1	22.2
037	36.47	71.08	Aug 21,86	01:34	235	5.4	77.1	37.0
038	-23.28	-176.75	Sep 6,86	08:52	122	5.6	20.1	2.3
039	36.71	71.09	Sep 15,86	21:42	89	5.8	76.8	37.1
040	-15.57	167.56	Oct 23,86	02:18	160	5.7	43.0	1.9
041	-14.34	167.68	Nov 12,86	00:26	33	5.3	41.7	2.2
042	51.43	-173.82	Nov 14,86	21:42	33	5.5	2.9	22.1
043	-16.27	167.55	Nov 20,86	13:14	60	5.7	43.7	1.7
044	29.98	51.64	Nov 20,86	20:08	32	5.2	98.5	41.6
045	-15.27	167.35	Nov 22,86	17:08	158	5.8	43.0	2.0
046	-3.34	-77.41	Nov 23,86	01:39	106	6.4	266.4	20.2
047	41.96	81.32	Jan 5,87	22:52	17	5.9	65.7	35.2
048	-19.49	-177.46	Feb 10,87	0:59	395	6.2	19.1	1.0
049	43.17	132.29	Feb 11,87	17:42	499	5.5	39.4	24.4
050	54.72	161.74	Feb 14,87	16:42	33	5.7	16.7	24.3
051	-19.68	168.76	Feb 17,87	4:19	33	5.6	45.3	0.6
052	51.30	-179.28	Feb 18,87	0:00	33	6.2	6.3	22.2
053	-15.85	167.89	Feb 23,87	15:49	234	5.9	42.8	1.8
054	38.10	91.18	Feb 25,87	19:56	26	5.7	65.2	31.9
055	53.03	-162.55	Feb 28,87	23:20	33	4.8	356.0	22.7
056	46.33	152.07	Mar 3,87	1:32	90	5.9	25.8	22.5
057	51.16	179.58	Mar 6,87	13:48	56	5.4	7.1	22.1
058	31.97	131.70	Mar 18,87	3:36	38	6.5	46.9	21.4
059	-14.81	167.24	Mar 19,87	17:14	132	5.3	42.8	2.2
060	-20.31	-176.27	Mar 19,87	22:51	231	5.8	17.0	1.4
061	52.01	-177.44	Mar 21,87	10:41	97	6.0	5.1	22.4
062	51.54	-173.49	Mar 22,87	2:49	22	5.9	2.7	22.1
063	-13.72	167.18	Mar 26,87	16:17	190	5.5	41.9	2.5
064	-22.93	-66.23	Apr 1,87	1:48	224	6.2	244.7	18.3
065	49.90	78.81	Apr 3,87	1:17	0	6.2	56.8	37.1
066	49.85	78.69	Apr 17,87	1:03	0	6.0	56.9	37.1
067	61.44	-150.83	Apr 18,87	2:01	70	5.6	351.0	26.0
068	49.78	78.09	May 6,87	4:02	0	5.5	57.1	37.2
069	-6.35	152.40	May 7,87	1:51	10	5.3	53.9	7.1
070	50.02	156.27	May 12,87	4:03	46	5.4	21.7	23.3

TABLE 2: Teleseismic Event Information (Continued)

Event	Lat	Lon	Date	Time	Depth	M_B	Bazm	Angle
071	49.90	78.73	Jun 20,87	0:53	0	6.1	56.8	37.1
072	54.17	-162.54	Jun 21,87	5:46	33	6.2	356.1	23.1
073	53.43	158.32	Jul 6,87	23:22	149	5.3	29.1	24.2
074	49.87	78.79	Nov 15,87	03:31	0	6.0	56.8	37.1
075	41.36	89.64	Dec 22,87	00:16	22	5.9	62.6	32.9
076	43.29	142.42	Jan 3,88	12:42	177	6.0	33.3	22.8
077	54.78	161.66	Jan 11,88	21:07	43	5.8	16.7	24.4
078	50.81	173.47	Feb 7,88	18:15	33	6.2	10.9	22.3
079	49.95	78.91	Feb 13,88	03:05	0	6.1	56.7	37.1
080	46.66	152.59	Feb 20,88	22:11	54	5.9	25.4	22.6
081	57.27	-142.79	Mar 6,88	22:35	10	6.8	345.7	25.0
082	10.37	-60.58	Mar 10,88	06:17	56	6.2	264.9	27.9
083	54.70	161.61	Mar 12,88	08:38	23	5.7	16.7	24.3
084	49.89	78.96	Apr 3,88	01:33	0	6.0	56.7	37.0
085	10.67	-62.84	Apr 12,88	19:41	98	5.5	266.7	27.4
086	0.95	-30.24	Apr 20,88	04:25	10	5.8	232.6	33.1
087	-23.92	-176.98	Apr 25,88	01:19	127	5.5	21.2	2.4
088	-22.81	170.25	May 3,88	23:22	33	5.9	46.6	0.4
089	11.46	-85.93	May 6,88	14:46	100	5.7	282.9	21.6
090	-13.38	-76.21	May 6,88	16:34	51	5.9	258.2	18.2
091	42.61	143.72	May 7,88	01:59	79	6.1	32.9	22.4
092	73.35	54.47	May 7,88	22:49	0	5.6	19.6	41.0
093	-13.91	166.24	May 16,88	23:07	51	5.9	43.4	2.6
094	52.09	174.24	May 18,88	06:13	33	5.2	10.2	22.7
095	0.76	-30.30	May 21,88	15:15	10	5.5	232.6	33.0
096	50.56	-174.56	May 25,88	14:05	40	5.7	3.4	21.8
097	-7.47	128.36	May 30,88	21:11	66	6.4	76.1	12.1
098	-15.38	167.56	Jun 5,88	18:22	116	5.9	42.8	2.0
099	51.02	-177.60	Jun 18,88	16:15	42	5.1	5.3	22.0
100	-15.23	168.19	Jun 22,88	21:53	53	5.4	41.8	1.9
101	-17.68	-178.88	Jul 6,88	01:10	545	5.6	21.0	0.3

TABLE 3: Average Teleseismic Travel Time Residuals

Station	Lat	Lon	NNE	n	NE	n	EAST	n	WEST	n	PKIKP	n	ALL	n
MINI	43.23	10.85	0.07	16	0.21	14	0.34	15	0.34	6	0.37	21	0.26	72
SERR	43.31	10.79	-0.20	11	-0.24	8	-0.32	10	-0.09	4	-0.23	13	-0.23	46
POMA	43.33	10.90	-0.23	25	-0.24	19	-0.26	20	-0.08	7	-0.19	23	-0.22	94
SDAL	43.26	10.93	-0.13	20	-0.19	15	-0.18	15	0.18	6	-0.13	18	-0.13	74
SCAP	43.25	11.00	-0.24	19	-0.29	13	-0.20	14	0.04	8	-0.25	17	-0.21	71
MGUI	43.29	11.01	-0.25	4	-0.28	3	-0.28	5	0.14	2	-0.26	8	-0.23	22
RADI	43.25	11.07	-0.39	17	-0.43	11	-0.16	12	-0.11	6	-0.30	10	-0.30	56
MLUC	43.22	10.94	0.82	5	0.77	7	0.62	1	0.57	7	0.83	2	0.71	22
FROS	43.20	11.15	-0.27	3	-0.53	2	-0.32	5	-0.47	5	-0.38	3	-0.39	18
SINI	43.16	11.11	0.05	15	-0.02	12	-0.10	8	0.07	6	-0.03	18	-0.00	59
LURI	43.12	11.12	-0.04	11	-0.10	11	-0.08	10	-0.02	6	-0.08	15	-0.07	53
TRAV	43.19	11.03	0.51	21	0.59	12	0.58	12	0.72	5	0.63	18	0.58	68
CORN	43.16	10.94	0.10	11	0.00	11	-0.01	9	-0.04	5	-0.03	14	0.00	50
VALE	43.20	10.87	-0.08	14	-0.11	10	-0.04	13	0.12	7	-0.05	11	-0.05	55
CRDP	43.09	10.97	-0.13	25	-0.20	18	-0.21	18	-0.16	9	-0.21	22	-0.18	92
MDSV	43.15	10.85	0.45	23	0.48	16	0.14	13	0.18	8	0.51	19	0.39	79
CRBE	43.11	10.82	0.24	11	0.28	6	0.26	5	-0.16	1	0.08	8	0.20	31
MBAM	43.06	10.82	0.18	9	0.07	13	0.09	10	-0.03	7	0.05	17	0.07	56
LAGO	43.15	10.81	0.35	13	0.41	16	0.49	19	0.32	4	0.40	23	0.41	75
PADU	43.20	10.79	0.12	5	0.07	9	0.27	7	-0.02	4	0.16	10	0.13	35
SASS	43.25	10.69	-0.35	10	-0.30	12	-0.26	12	-0.36	8	-0.33	17	-0.32	59
MONV	43.18	10.71	-0.20	20	-0.15	19	-0.03	17	-0.29	7	-0.20	19	-0.16	82
FRAS	43.11	10.76	0.05	19	0.07	16	0.12	16	-0.12	8	0.00	15	0.04	74
STTA	43.12	10.65	-0.20	18	-0.23	14	-0.18	16	-0.28	8	-0.28	20	-0.23	76
PLUZ	43.05	10.74	0.08	15	0.09	18	0.10	18	-0.08	10	-0.00	24	0.04	85

Azimuthal Ranges (degrees from North):

NNE: 346 to 16

NE: 17 to 47

EAST: 48 to 116

WEST: 232 to 292

PKIKP: All events with incidence angle less than 10 degrees

TABLE 4: Inversion Starting Model

Layer Number	P-Velocity ($\frac{Km}{Sec}$)	Thickness (Km)	Horiz Dimensions (Km)
1	6.0	5.0	5 by 5
2	6.5	5.0	5 by 5
3	7.0	5.0	5 by 5
4	8.1	10.0	5 by 5
5	8.1	10.0	5 by 5

Net Center: 43 Degrees 14.0 Minutes, 10 Degrees 53.8 Minutes

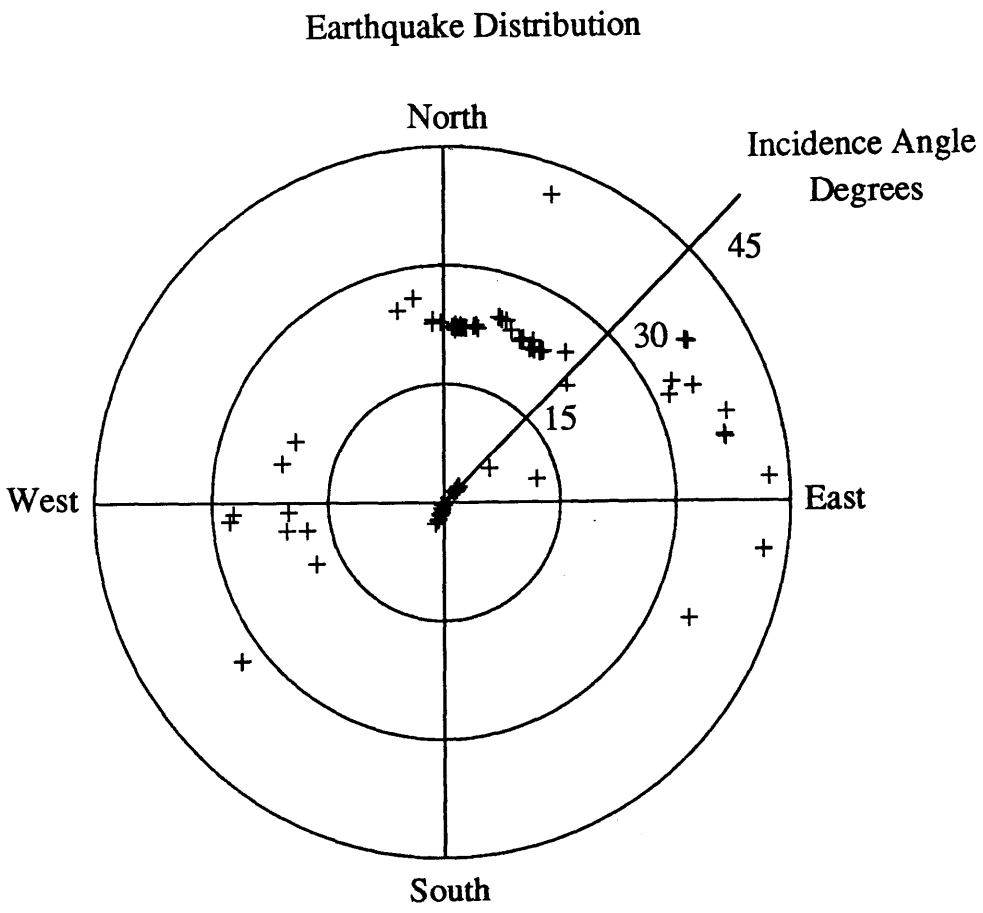

Figure 1: Azimuthal coverage of the 101 events used in the teleseismic travel time inversion. Concentric circles represent 15, 30 and 45 degree of incidence angle. Data are subdivided into 5 groups: North-Northeast, Northeast, East, West, and PKIKP events.

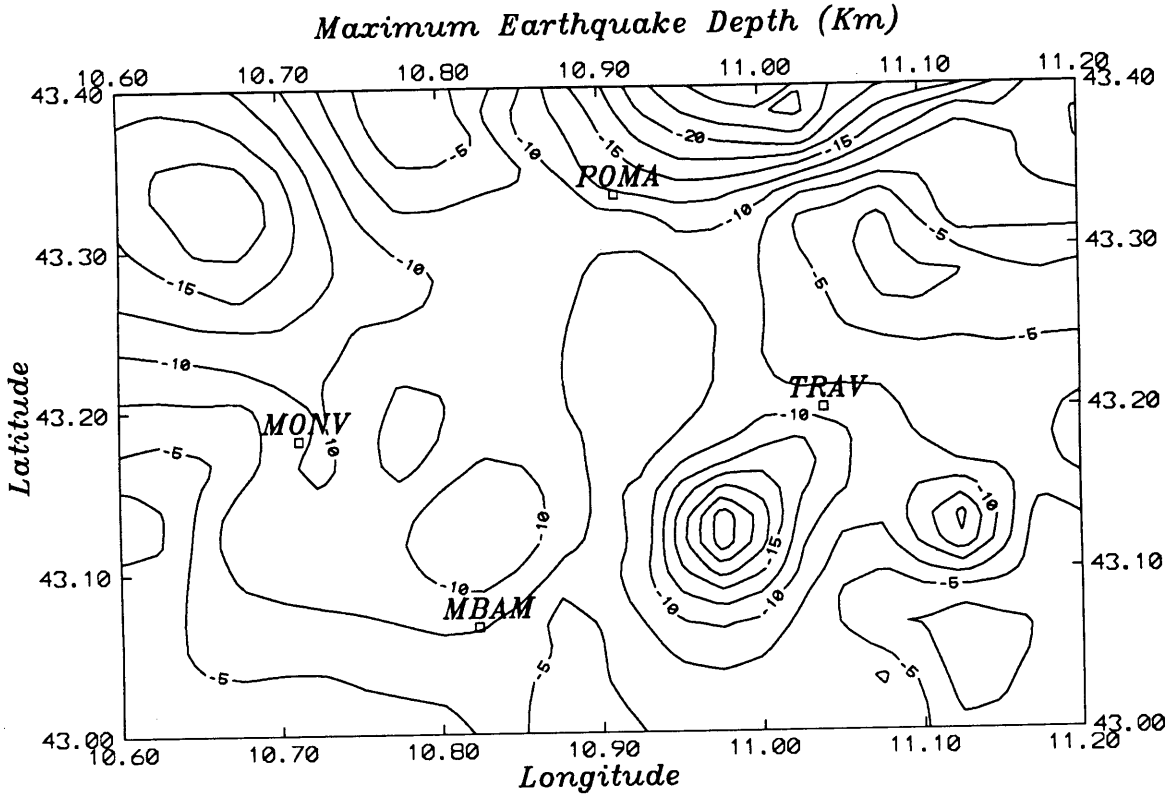

Figure 2: Local earthquake depth distribution beneath the Larderello seismic network. Earthquakes occur throughout the entire region to depths of 6 km and greater.

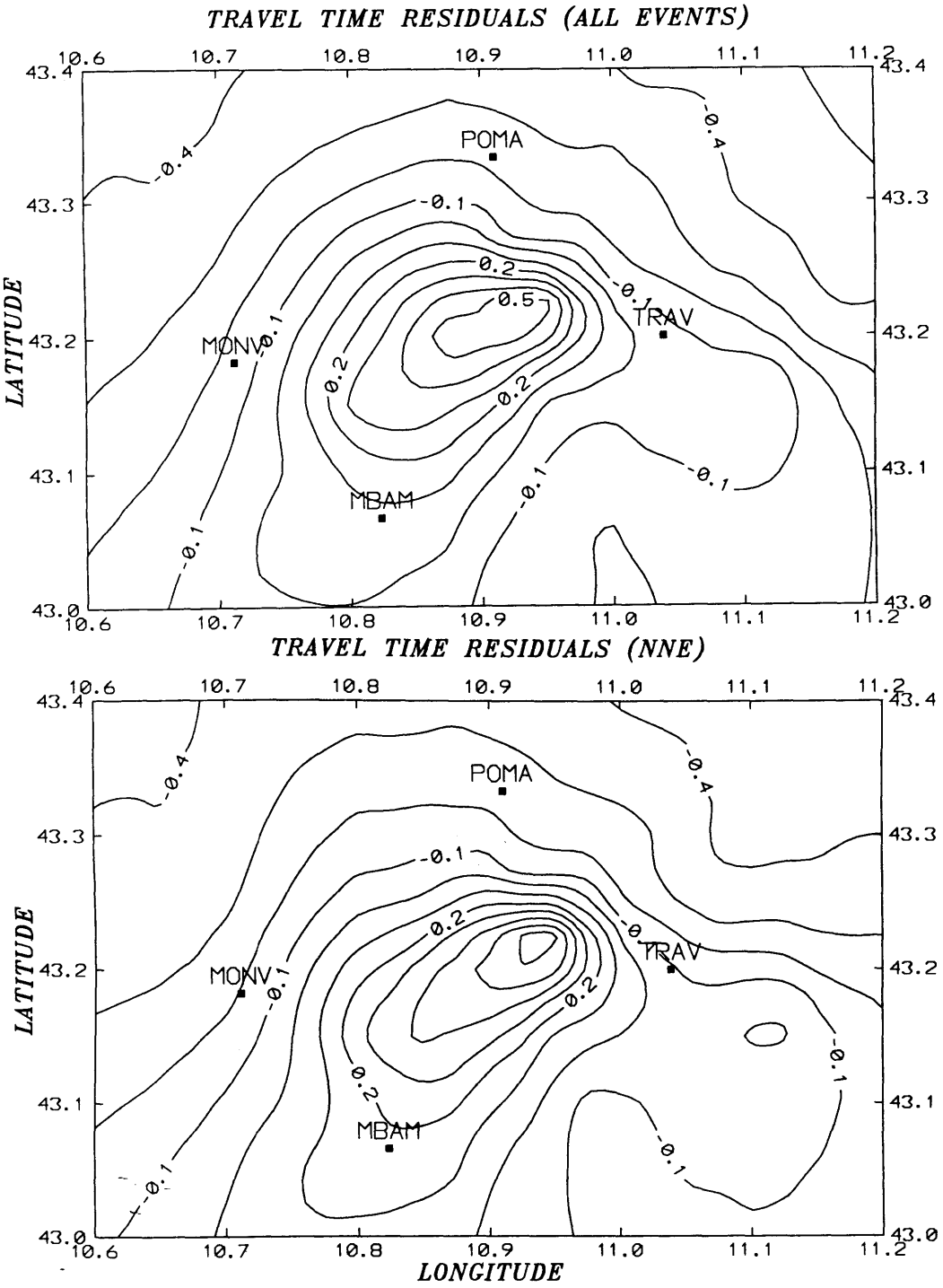

Figure 3: Average travel time residuals recorded on the Larderello seismic network from all 101 events (top). Average travel time residuals for events from the 28 events in the azimuth range of 346 to 16 degrees (north-northeast; bottom). All residuals represent data reduced to 6 km. Contours are lines of equal residual plotted at 0.1 second intervals. See text for description of the residual patterns.

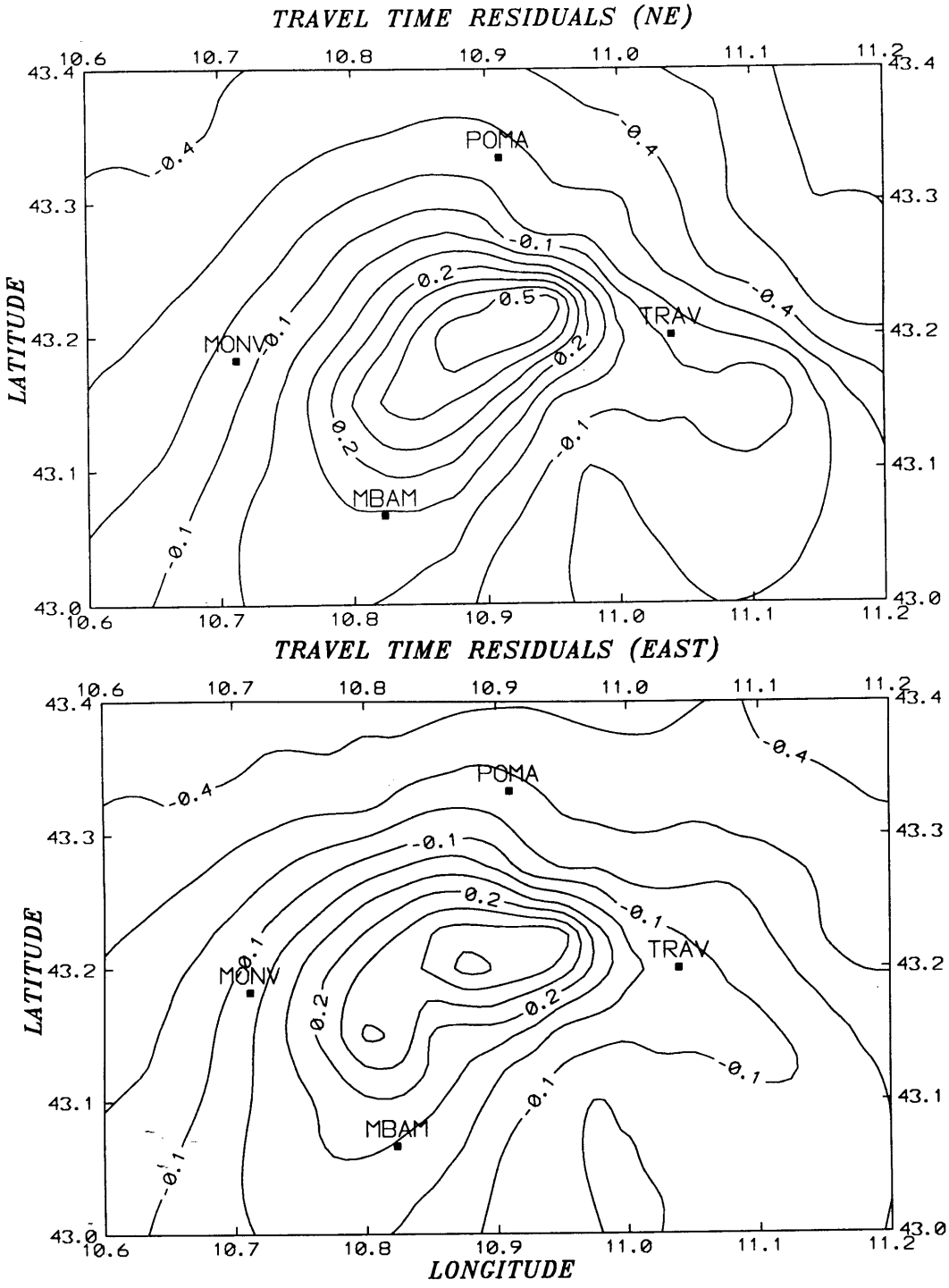

Figure 3: (continued) Average travel time residuals for events from the northeast; 18 events in the azimuth range of 17 to 47 degrees (top). Average travel time residuals for events from the East; 20 events in the azimuth range of 48 to 116 degrees (bottom).

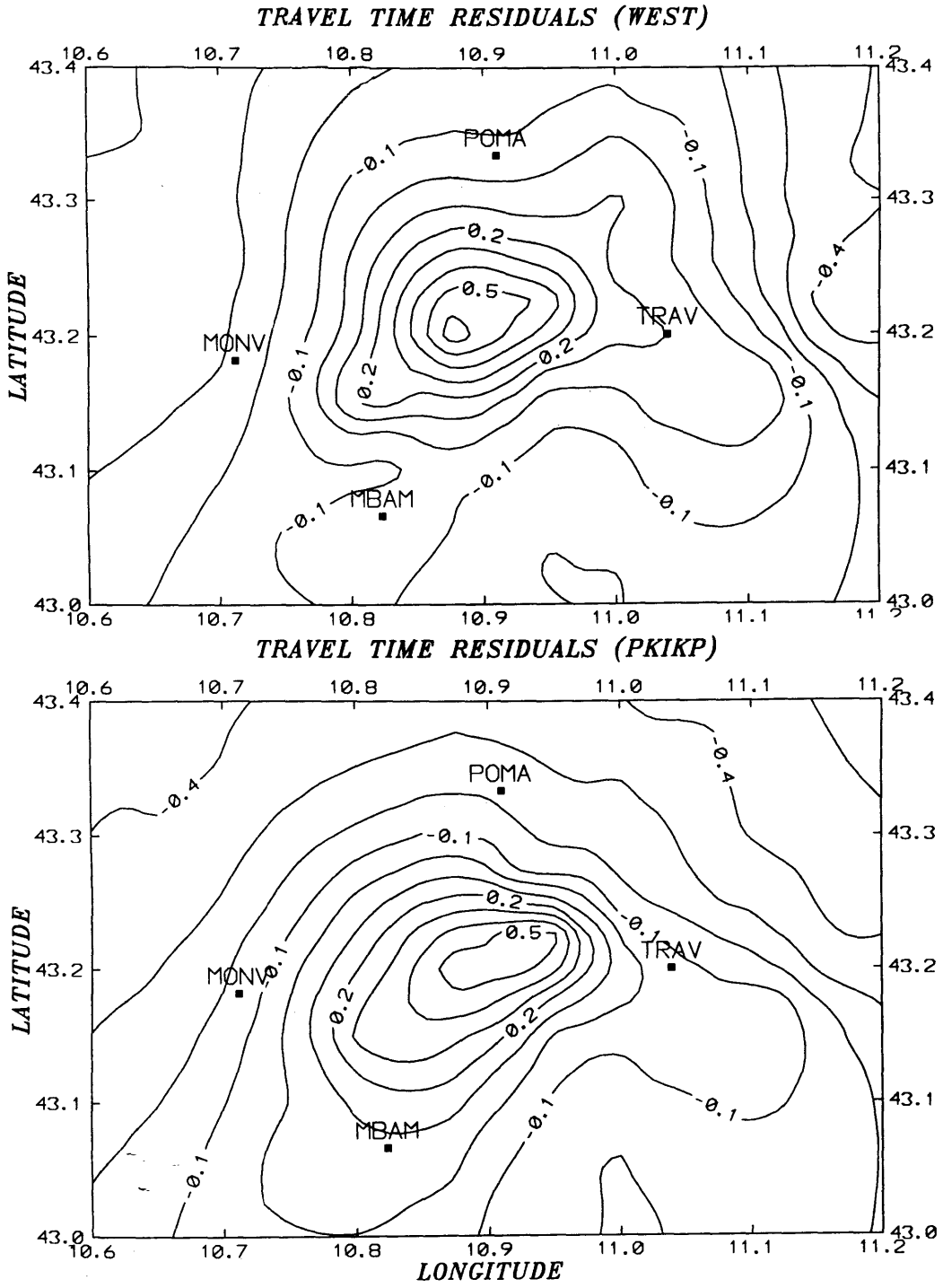

Figure 3: (continued) Average travel time residuals for events from the West; 10 events in the azimuth range of 232 to 292 degrees (top). Average travel time residuals for PKIKP events; 25 events arriving with incidence angles less than 5 degrees (bottom).

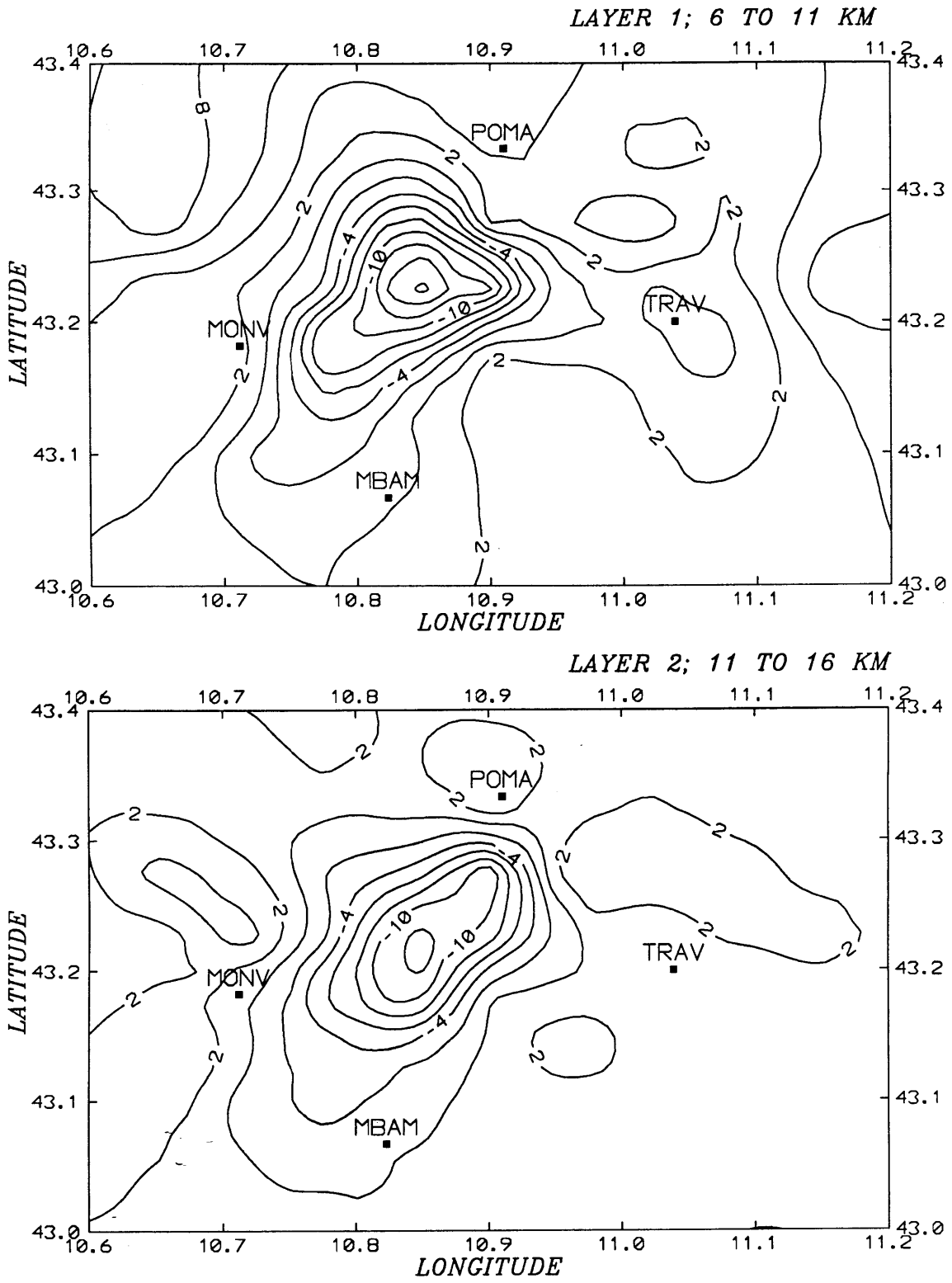

Figure 4a: Inversion results for Layers 1 and 2. Layer 1 represents the crust from 6 to 11 km and Layer 2 from 11 to 16 km. The input model described in Table 4. Plotted are contours of equal velocity perturbation at an interval of 2%. Station locations are plotted for reference.

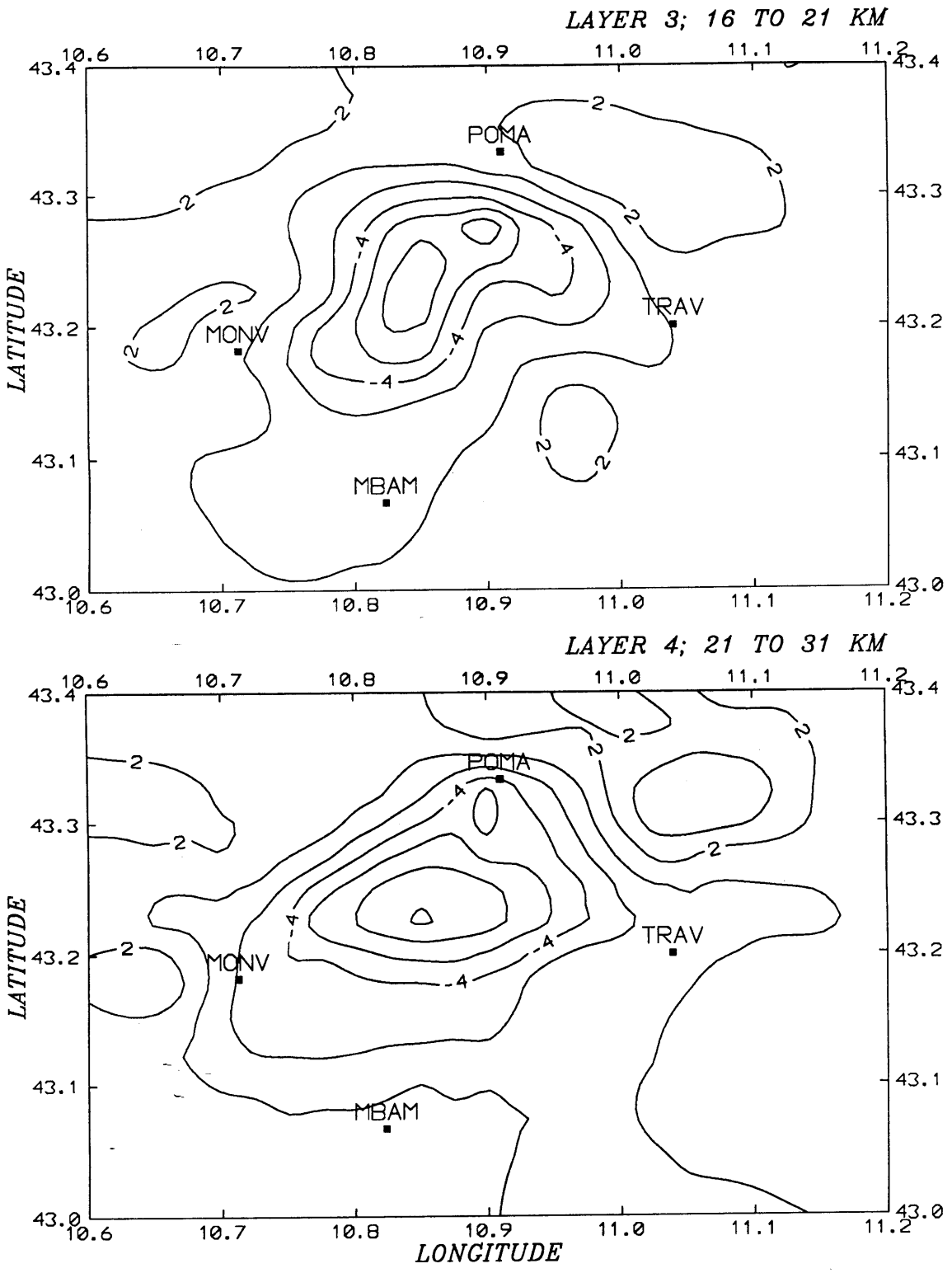

Figure 4b: Inversion results for Layers 3 and 4. Layer 3 represents a depth of 16 to 21 km and Layer 4 from 21 to 31 km.

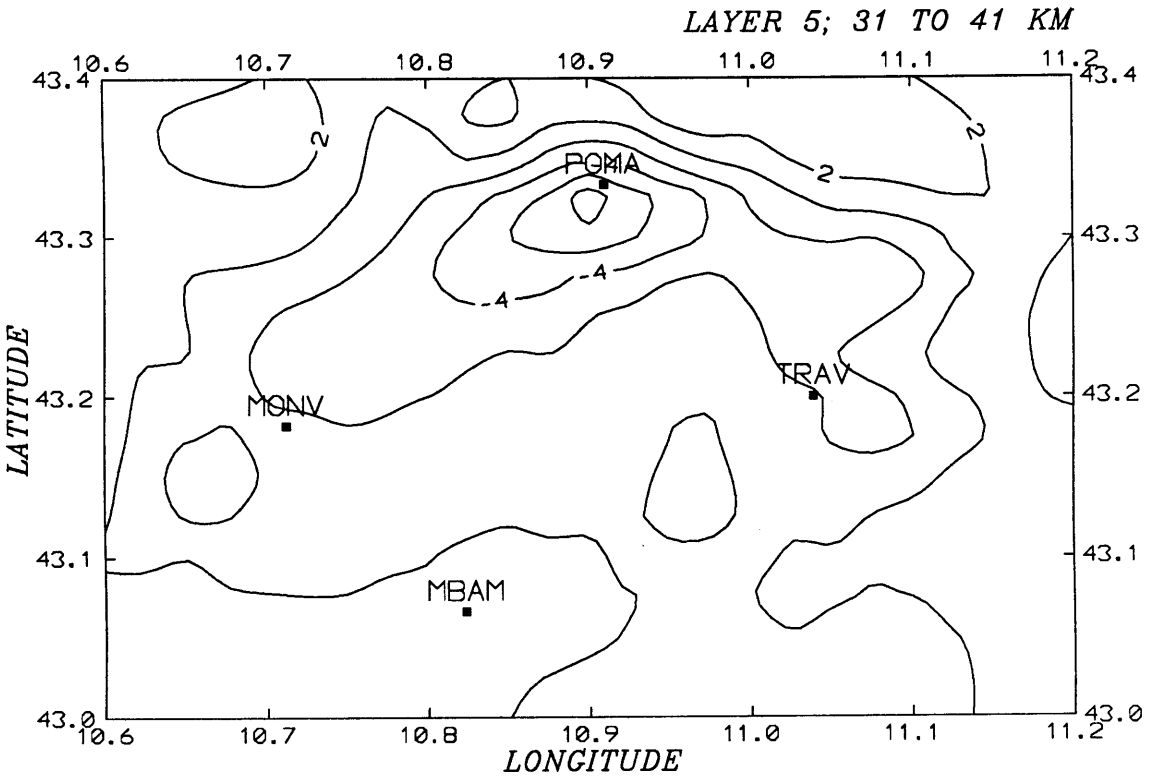

Figure 4c: Inversion results for Layer 5. Layer 5 represents a depth of 31 to 41 km.

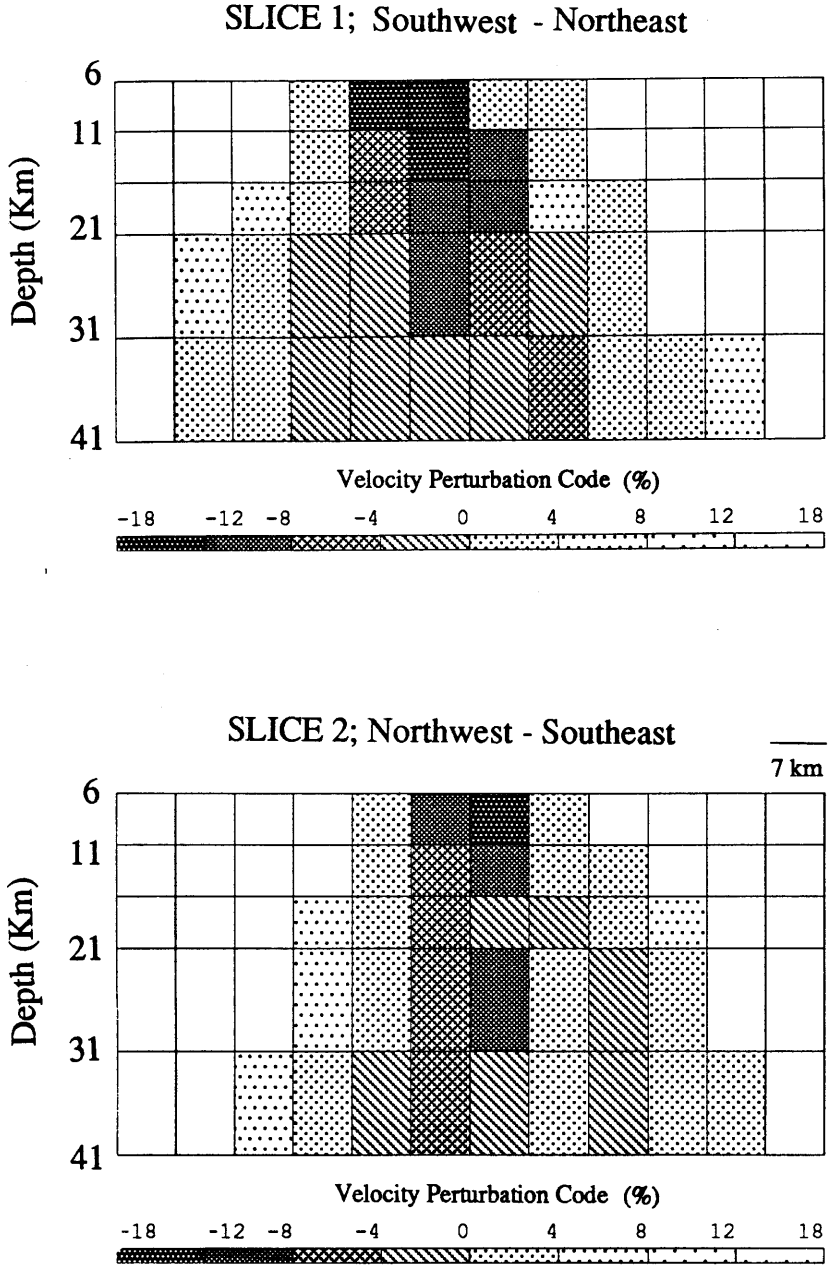

Figure 5 Inversion results for vertical slices through the region. Diagonal slices are from southwest to northeast (top) and northwest to southeast (bottom). All block widths are 7 km. The three crustal layers are 5 km thick and the two mantle layers are 10 km thick. The top of the model represents a depth of 6 km below the surface. The velocity perturbation code is relative to the starting model described in Table 4. Velocity contrasts are depicted with different shade patterns with cross hatched blocks representing velocity decreases and stippled blocks representing regions of increased velocity. Blocks without any pattern represent regions not sampled densely enough (at least 10 rays) for a parameter estimate to be made.

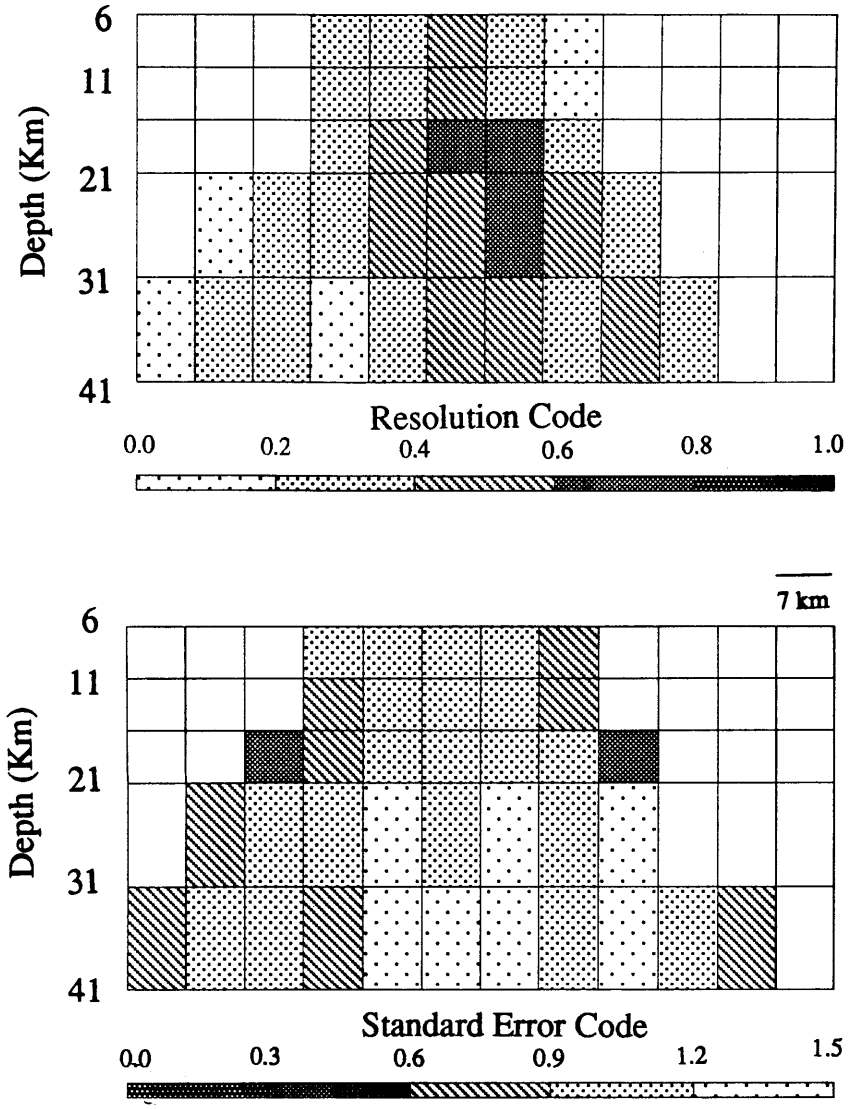

Figure 6: Resolution and error plots of the vertical slice from southwest to northeast. Blocks are all 7 km wide, upper three layer thicknesses are 5 km and the lower 2 layer thicknesses are 10 km. The top of the model represents a depth of 6 km.

Chapter 4

TELESEISMIC SOURCE CHARACTERIZATION

4.1 Introduction

From the previous chapter we saw that the inversion of relative travel time residuals of direct teleseismic P-waves can reveal important information about the relative variations of seismic velocities of the crust. However, it is quite clear that only a small portion of the total information content of the P-waveforms is being utilized to determine the velocity structure of the crust with this inverse method. To get more information about the velocity structure of the crust out of teleseismic waveforms and to improve the resolution of the crustal structure, we must examine the waveforms after the direct arrival. The most fundamental problem with analyzing teleseismic waveforms for crustal receiver structure is the accurate separation of source and receiver-effects in the seismograms. Without a clear understanding of all the near-source effects in the seismogram, it is impossible to remove them from the waveform, and if they are not removed one is left with the dubious task of processing and interpreting source-contaminated data. To help rectify this problem, we present in this chapter a technique to determine the nature of the time-domain source signature recorded on seismic networks at teleseismic distances. These estimates of the source function are called *effective* sources and contain all of the information about the source and propagation effects which are *common*

to each member station in a seismic network.

A second basic problem with using teleseismic waveform data to describe the crustal structure beneath an array of seismic stations is the inherent low signal-to-noise ratio of reflections recorded after the direct arrival. Oftentimes, the important arrivals have a signal-to-noise ratio at or below one. In contrast to exploration techniques where the source signature is repeatable, each earthquake source time history is generally different. This fact makes it inappropriate to use waveforms recorded from different earthquakes in the same analysis; stacking waveforms to improve the signal strength *across* events at a single station produces distorted waveforms. We present a method to solve this problem by means of shaping *effective* sources calculated for each event into a common time domain wavelet. This process of source equalization in conjunction with the calculation of the *effective* source for each event provides a simple and effective means to reduce the inherent limitations of teleseismic waveform data. With the application of this source equalization technique information about the velocity structure of the earth contained in the seismograms beyond the direct arrival is made available.

In Section 4.2 we present the methods of *effective* source calculations and in Section 4.3 we describe our source equalization method.

4.2 *Effective* Source Calculations

The geometry of teleseismic wave propagation problems is sketched in Figure 1-2. Waveforms resulting from the interaction of an incident teleseismic plane wave and the local receiver structure contain numerous reflected and converted phases originating from the structure beneath the station. If we assume that the earth can be approximated as a series of flat lying layers, the simple 3 layer model of the crust shown in Figure 1a produces a simple impulse response $E(t)$, for an earthquake with an epicentral distance of 80 degrees. If this impulse response is convolved with a source pulse $S(t)$, instrument response $I(t)$, and an attenuation operator $A(t)$, one can make an estimate of the waveform expected at the surface.

For the j^{th} teleseismic event recorded on the i^{th} station in a network of N stations we have

$$SS_{i,j}(t) = S(t)_j * E_i(t) * I_i(t) * A_i(t) + \mathcal{N}_{i,j}(t), \tag{4.1}$$

where $SS(t)$ is the synthetic seismogram $\mathcal{N}_{i,j}$ is the noise on each trace and $*$ is the convolution operator. If we represent the source as a simple Blackman pulse (Figure 1b), the seismogram in Figure 1c is generated. In the absence of noise, it is intuitive that this waveform could be used to determine the crustal structure. However, if we replace the simple Blackman pulse with a doublet (Figure 1d) and re-apply Equation 1 while including random noise with an amplitude 10% of the direct arrival, the resultant seismogram (Figure 1e) looses its simplicity and becomes very difficult to interpret. This simple example illustrates the difficulties with using teleseismic data to describe crustal structure; we must know the source function with great accuracy and we must increase the signal-to-noise ratio of the crustal reverberation sequence.

In order to isolate each E_i for the j^{th} event in Equation 1, we define a function called the *effective* source function S_j^e which contains all the contributions of $S(t)_j$, $I(t)$, and $A(t)$ for teleseismic P-waves recorded on a seismic network. To accomplish this, we align each vertical waveform from a single teleseismic event recorded on a seismic network to the direct P-wave arrival, and then stack the shifted data to produce the *effective* source for the entire network:

$$S_j^e(t) = \frac{1}{N}\sum_{i=1}^{N} d_{i,j}^{sh}(\tau) \tag{4.2}$$

where $d^{sh}(\tau)$ are the N shifted seismograms. This function contains all the common source effects and propagation effects, as well as common instrumentation and crustal attenuation effects. If we use Equation 1 to represent the data $d^{sh}(\tau)$, we can rewrite Equation 2 as,

$$S_j^e(t) = \frac{1}{N}\sum_{i=1}^{N} S(\tau)_j * E_i(\tau) * I_i(\tau) * A_i(\tau) + \frac{1}{N}\sum_{i=1}^{N} \mathcal{N}_{i,j}(\tau) \tag{4.3}$$

To be able to use this network-wide stack as a good approximation to each particular *effective* source for any single station which is a member of the stacked set of stations, we must demonstrate the validity of four important assumptions. First, we assume that each of the stations has the same source function. Second, each station must have an equivalent

instrument response. Third, the attenuation functions at each station must be the same. Fourth, we assume that, through the stacking procedure, the sum of vertical component crustal impulse responses approaches a delta function.

The first assumption (equivalent source) is geometrical, and to insure its validity in Equation 2, we exclude stations from the stack which fall outside a 2 degree by 2 degree box of azimuth and distance from the source to the receiver position. This stacking limitation insures that the geometry of the rays to each station in the analysis is similar across the network, and that each station falls on a very similar part of the source focal sphere and is not influenced by azimuthal variations in the source radiation pattern. The second assumption (equivalent instrument response) is generally valid for all stations in the NEUSSN in the frequency band (0.5 to 2.5 hz) used here (Ebel, 1985, Basham et al., 1985; Toksoz and Kadinsky-Cade, 1988) and is quite valid among the ENEL seismic network in Larderello, (ENEL, 1987). However, approximately 25% of the available NEUSSN data was removed from our analysis because of unknown station polarity, unusual station response or weak signal strength. The absolute gain of many of the stations of the NEUSSN is not known, so we normalize each trace recorded on that network to the maximum amplitude of the direct P-wave to remove these effects. The third assumption (equivalent attenuation character of each receiver) is validated deterministically through forward modeling of various $A(t)$ filters (Futterman, 1962) with randomly generated models. We are satisfied that the average $A(t)$ of the cross-network stack represents individual stations adequately and does not contaminate the forward modeling procedure.

The most important assumption of the method is the fourth, namely, that stacking many vertical crustal impulse responses approximates a delta function,

$$\frac{1}{N}\sum_{i=1}^{N} E_i(t) = \delta(t). \tag{4.4}$$

Physically, this assumption means that enough variation exists in the impulses responses of the individual stations in a seismic network to insure that when we sum these functions (assuming that the direct arrival of each impulse response is aligned to a common time point), the phases after the direct arrival will not stack constructively.

If we assume that the first 3 assumptions above hold for teleseismic data, we can rewrite

Equation 3 as

$$S_j^e(t) = \frac{1}{N}\sum_{i=1}^{N} S_j^c(t) * I_i^c(t) * A_i^c(t) * E_i(t) + \frac{1}{N}\sum_{i=1}^{N} \mathcal{N}_{i,j}(t), \tag{4.5}$$

where c denotes a common operator for all seismograms for a given event. We can now rewrite this as

$$S_j^e(t) = S_j^c(t) * I_i^c(t) * A_i^c(t) * \frac{1}{N}\sum_{i=1}^{N} [E_i(t) + \mathcal{N}_{i,j}(t)], \tag{4.6}$$

or

$$S_j^e(t) = S_j^c(t) * I_i^c(t) * A_i^c(t) * \delta(t) + \frac{1}{N}\sum_{i=1}^{N} \mathcal{N}_{i,j}(t). \tag{4.7}$$

If we assume that as N get large we can write

$$\frac{1}{N}\sum_{i=1}^{N} \mathcal{N}_{i,j}(t) = 0, \tag{4.8}$$

Equation 7 becomes

$$S_j^e(t) = S_j^c(t) * I_i^c(t) * A_i^c(t). \tag{4.9}$$

The validity of Equation 4 was rigorously tested with random models and can be shown to be quite strong. Figure 2 shows the results of the first test in which we stack vertical component synthetic seismograms generated from convolving the impulse responses of 30 different *randomly* layered models with the simple Blackman pulse of Figure 1. The *random* nature of the models is controlled to mimic crustal velocity profiles found in New England and the number 30 was selected as a minimum number of recording stations in New England. These models are the same ones used in Chapter 2 (Figure 2-3). The 30 waveforms (Figure 2a) are shifted to the direct arrival (Figure 2b) and stacked to reproduce the test source pulse (Figure 2c). In the second test, we use the same 30 random models but replaced the simple single pulse source with the doublet of Figure 1d. Figure 3a shows the raw synthetic data, the traces shifted to the first arrival (Figure 3b) and then the stacked result (Figure 3c). Again, we recover all of the source information. In the third test we use the complicated source time function shown in Figure 4a, and again the source is completely recovered (Figure 4d). When the crustal models are not *random*, but rather exist as small perturbations of each other, we can bias our representation of the *effective* source. Given the dominant frequency of these teleseismic P-waveforms (about 1.0 hz) and an average

propagation velocity of 6 $\frac{km}{sec}$ in the crust, we would expect to see constructive interference from primary crustal reflections arriving from discontinuities in the crust which exist within depths of about 1.5 km (about $\frac{1}{4}$ of the dominant wavelength). Given the variability of the crustal velocity structure determined from refraction experiments in New England and the variability in structure inferred from reflection and refraction data in Larderello, we conclude that there is enough variation in crustal velocity structure in these region to use this technique.

Next, we must examine the validity of Equation (8) under various noise conditions. We follow the sequence of the previous tests (single Blackman pulse, double Blackman pulse and actual source wavelet) while adding various levels of actual ground noise recorded on the NEUSSN into the synthetic seismogram. Figure 5 shows the final comparison between actual and recovered source pulses for 50% noise. It is evident that with a 30 fold stack we can recover an excellent estimate of the source (cross correlation level of greater that 95%), even when single station noise levels are high (50%). When we have more traces in the stack, we can tolerate greater noise levels. Figure 6 shows source recovery results for 100% noise conditions; we still can recover a fair representation of the source. For 15 fold stacks a 30% noise level produces a source with cross correlation of 91%. We conclude, therefore, that even in the presence of strong background noise, we can characterize the *effective* source using

$$S_e^j(t) = \sum_{i=1}^{N} d_i^j(\tau). \tag{4.10}$$

Two real data examples are tested to confirm the utility of this procedure. The first comes from the May 1st, 1985 (85/05/01) earthquake in Peru and the second for the September 22nd, 1985 (85/09/22) earthquake from the Mid-Atlantic Ridge. The raw data recorded on the NEUSSN network are aligned to the direct P-waves (Figures 7 and 8), and then stacked (Figure 9). The 85/05/01 event is a simple, short duration earthquake of about 4 seconds while the 85/09/22 event has a more complex source signature. It will be shown in the next section that both of these types of source shapes can be utilized in the waveform analysis.

4.3 Source Equalization

While the calculation of the *effective* source allows one to adequately determine the contribution of the source, propagation, instrumentation and attenuation effects at teleseismic distances, it still leaves us with two important problems which limit the usefulness of teleseismic waveform data. The first is the very complicated nature of most of the *effective* sources. A review of teleseismic events recorded on the NEUSSN and ENEL networks reveals that most *effective* sources are quite complex in signature as well as long in duration compared to the two-way travel times of important arrival from discontinuities believed to exist in the crust. Only in cases where the source pulses are short and simple (about 20 events of the 148 in the ENEL study, for example) can the *effective* sources be used directly. In the majority of the data the sources are too long and too complicated to allow for straightforward interpretation of the waveforms. The second difficulty remaining with the data is the strong variation among all of the *effective* sources. Without further processing, we cannot include data from different events in the same analysis.

We need to transform each *effective* source into a simple and repeatable wavelet. The first attempt one may make to regularize the effects between different sources is to deconvolve the *effective* source from each trace which contributes to the cross-net stack (Equation 10) (Clayton and Wiggins, 1976). In theory, this process should transform each seismogram into an impulse response of the earth under the station:

$$E(\omega) = \frac{E(\omega) \cdot S(\omega) \cdot A(\omega) \cdot I(\omega)}{S(\omega) \cdot A(\omega) \cdot I(\omega)} \tag{4.11}$$

$$= \frac{E(\omega) \cdot S_e^j(\omega)}{S_e^j(\omega)}$$

However, due to the band limited nature of the source and instrumentation, to small errors in the assumptions of uniformity of $A(t)$ and $I(t)$ at all stations, and to the presence of noise in the data, deconvolution methods fail to produce high quality estimates of $E(t)$, the impulse response of the earth. An attempt was made to calculate $E(t)$ for each event using the deconvolution process of Helmberger and Wiggins(1971);

$$E_i(\omega) = \frac{d(\omega) \cdot S_e^*}{S_e^j(\omega) \cdot S_e^*(\omega) + \gamma} \tag{4.12}$$

where

$$\gamma = max\left[S_e^j(\omega) \cdot S_e^*(\omega),\ \ \alpha \cdot S_e^j(\omega) \cdot S_e^*(\omega))\right] \tag{4.13}$$

and S_e^* is the complex conjugate of S_e^j and α is the parameter which controls the frequency cut-off level. Various waterlevel parameters γ were tested with with little success. We were unable to remove the effects of S_e^j without introducing appreciable amounts of noise.

To overcome the difficulties which make deconvolution ineffective with these data, we replace the source-removal goal of Equation 12 with an easier and more realizable source shaping objective. We design a filter for each *effective* source which will transform it into a simpler, common time domain pulse. These filters (one for each teleseismic event) can then be applied to each contributing seismogram of that event to transform each trace into a seismogram with one common source shape. To create the generic source wavelet to be the target pulse, we select the 22 simplest *effective* sources, shift them to the direct arrival (Figure 10a), stack them (Figure 10b), and then take the zero phase version of the stack (Figure 10c). This produces a short simple wavelet $S_g^0(t)$, which we refer to as the *generic source wavelet.* In the NEUSSN case, we stack between 40 and 89 seismograms to produce the 22 separate *effective* sources used to construct the generic zero-phase source wavelet. The final source shape represents a stack of over 1000 waveforms.

Once the generic teleseismic shape was designed, we use the following relation to transform each trace $d_{i,j}(t)$ into a simple function which represents the impulse response of the earth convolved with the generic source wavelet,

$$E_i(t) * S_g^0(t) = \frac{d_i(\omega) \cdot S_{e,j}^*(\omega)}{S_{e,j}(\omega) \cdot S_{e,j}^*(\omega) + \gamma} \cdot S_g^0(\omega). \tag{4.14}$$

We see in Figure 11 an example of this process for Station BVT, located in central Vermont. All available data from this station are shown in Figure 11a, and in Figure 11b we show the *effective* source for these events. In Figure 11c we show the source equalized data. These data will be used extensively in the next 3 chapters.

Langston (1978) proposed a method similar to this to isolate the radial earth response beneath calibrated, three-component stations. With his method, one deconvolves the vertical component seismogram from the radial component under the assumption that the vertical

seismogram approximates a delta function response of the earth. Owens (1986) and Owens et al. (1986) used this technique to model the the S-wave velocity structure beneath broadband *Regional Standard Telemetered Network* (RSTN) stations. Although Owens had success with this approach, the method fails when the vertical component has strong crustal arrivals after the direct P-wave, which is generally the case in both the New England and Larderello data sets. The vertical/radial deconvolution method loses its applicability when dealing with the majority of narrow band, vertical-only seismic stations in existence around the world today, many of which are not accurately calibrated.

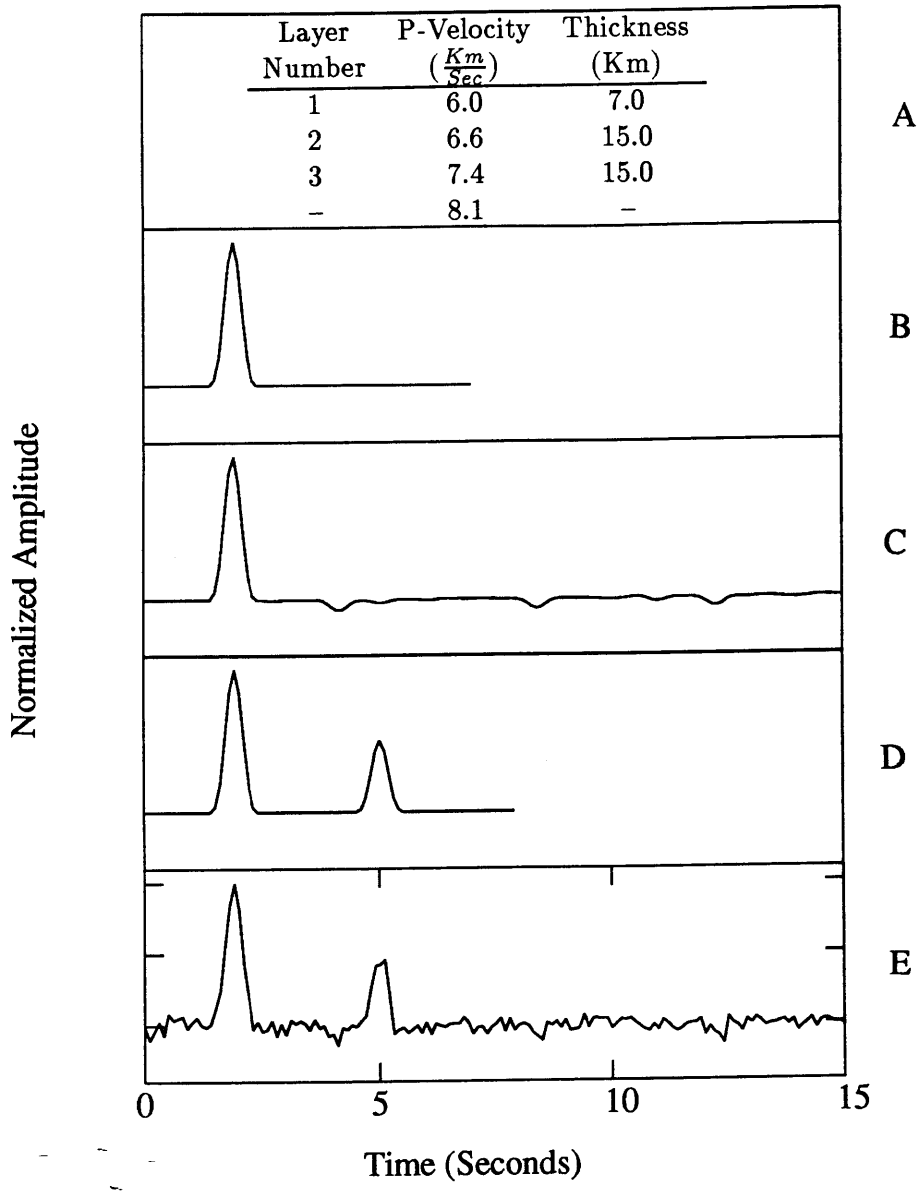

Figure 1: (A). Crustal model used in the following tests. We assume an angle of incidence of 20 degrees. (B). Blackman source pulse. (C). Crustal impulse convolved with Blackman source. (D). Blackman doublet source. (E). Doublet convolved with impulse after addition of 10% noise.

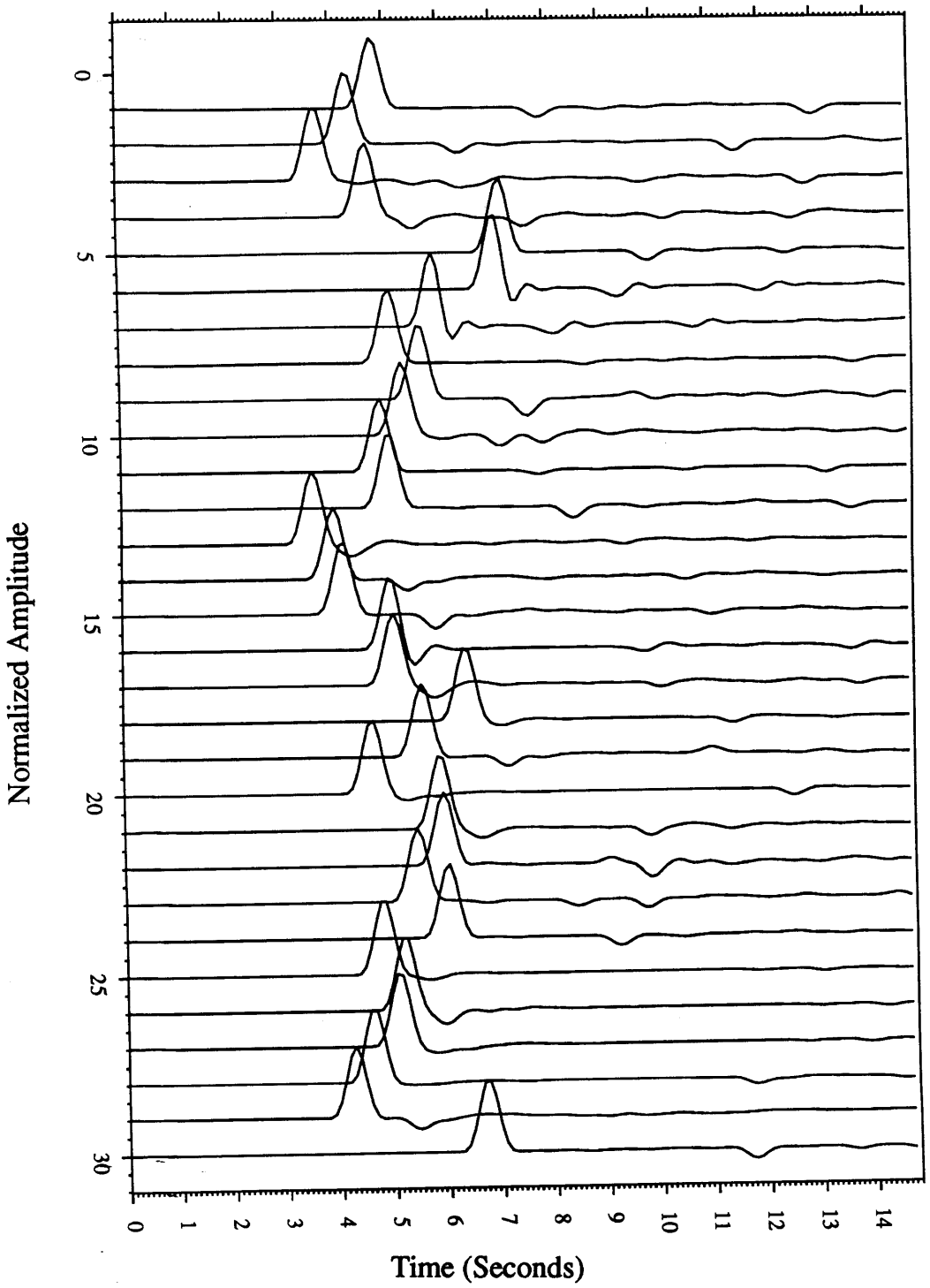

Figure 2a: Seismograms generated from convolution of 30 impulse responses and a simple Blackman source. Models for these seismograms can be found in Figure 2-3.

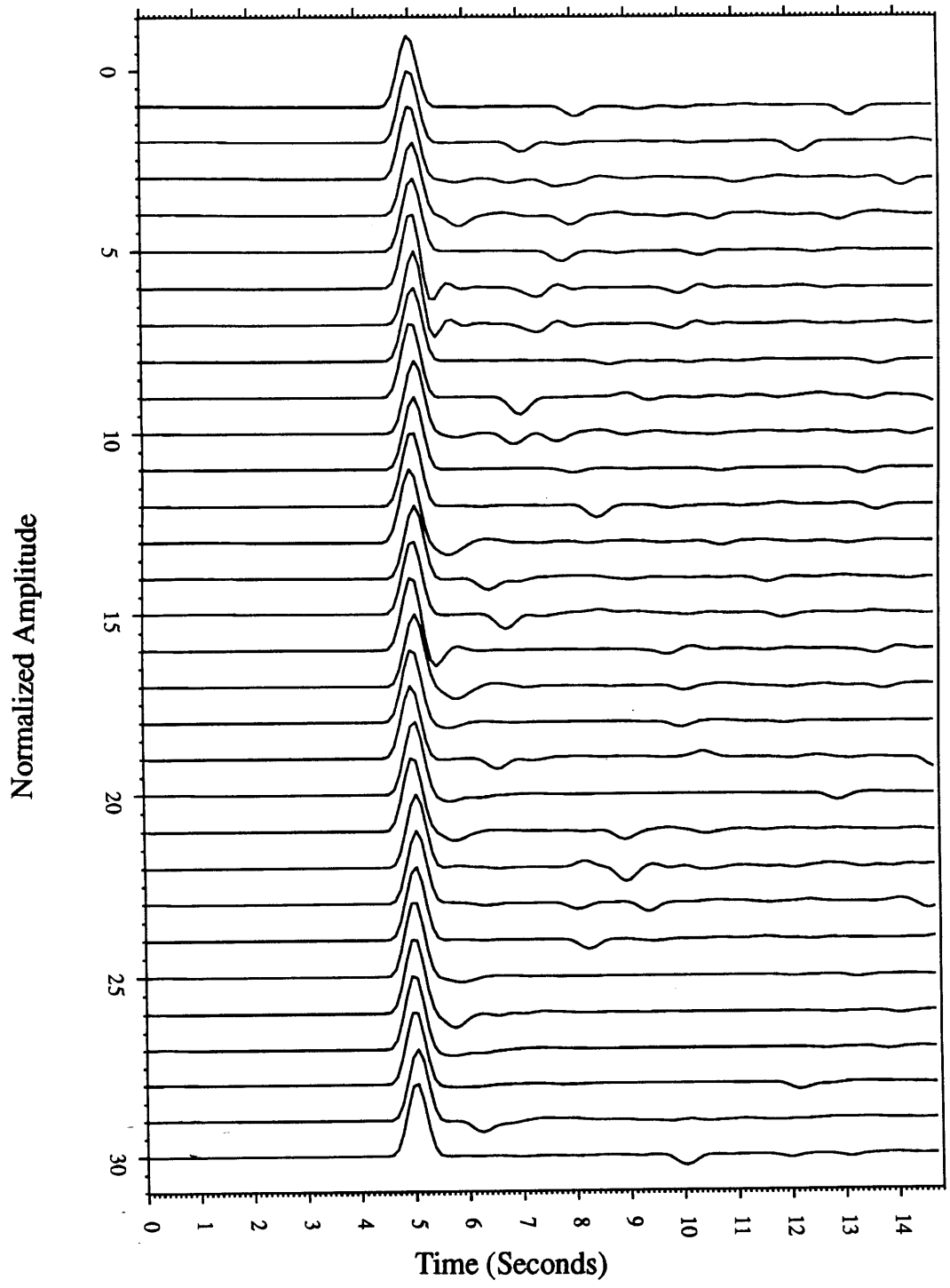

Figure 2b: Seismograms of Figure 2a shifted to common first arrival.

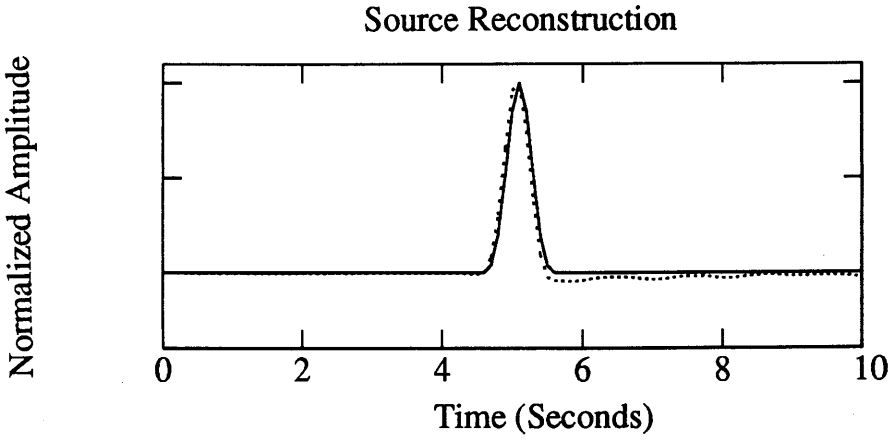

Figure 2c: Stack of 30 simple Blackman seismograms compared with actual source (dashed). We see that we can retrieve the source function quite accurately.

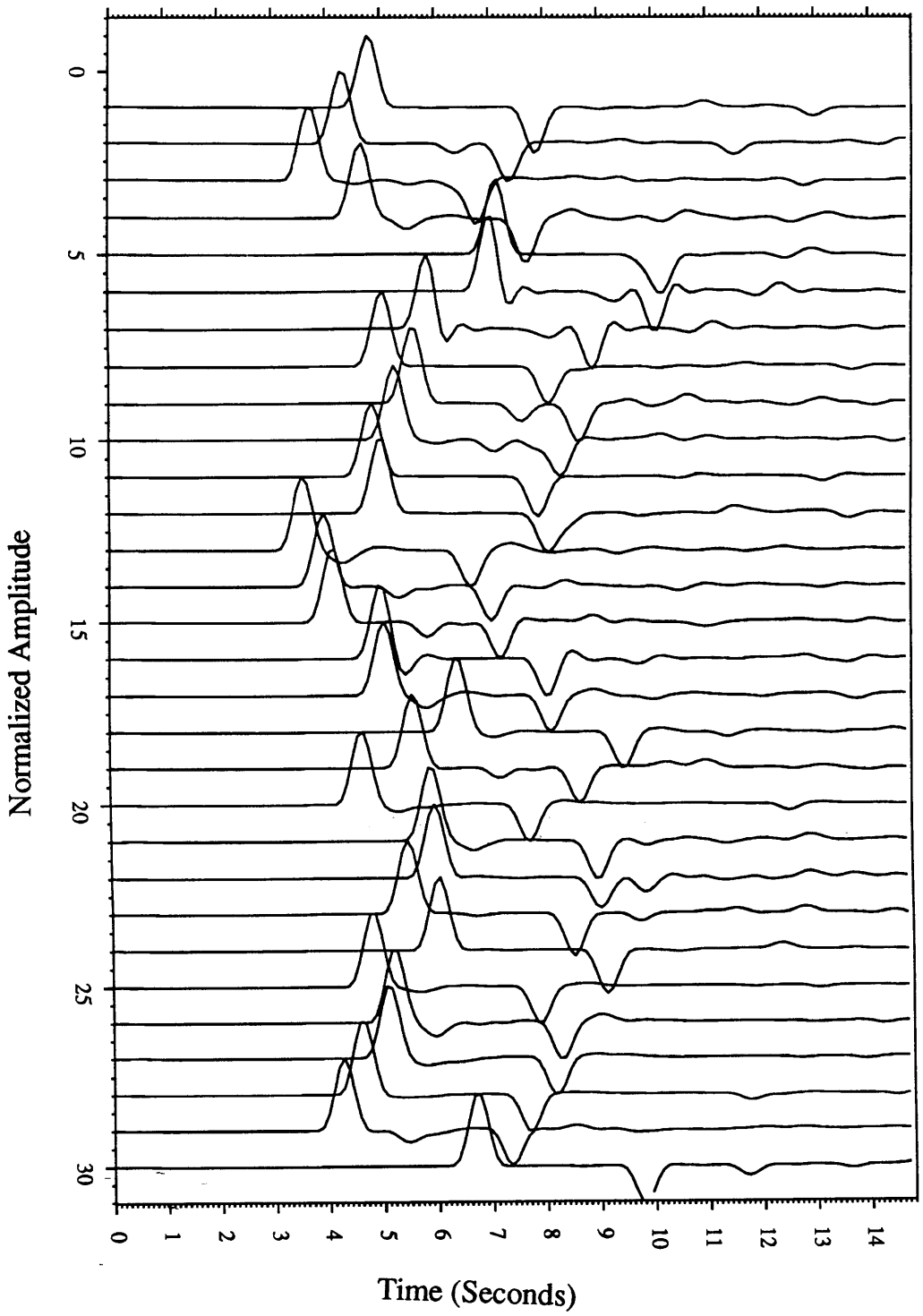

Figure 3a: Seismograms generated from convolution of 30 impulse responses and the Blackman source doublet of Figure 1d.

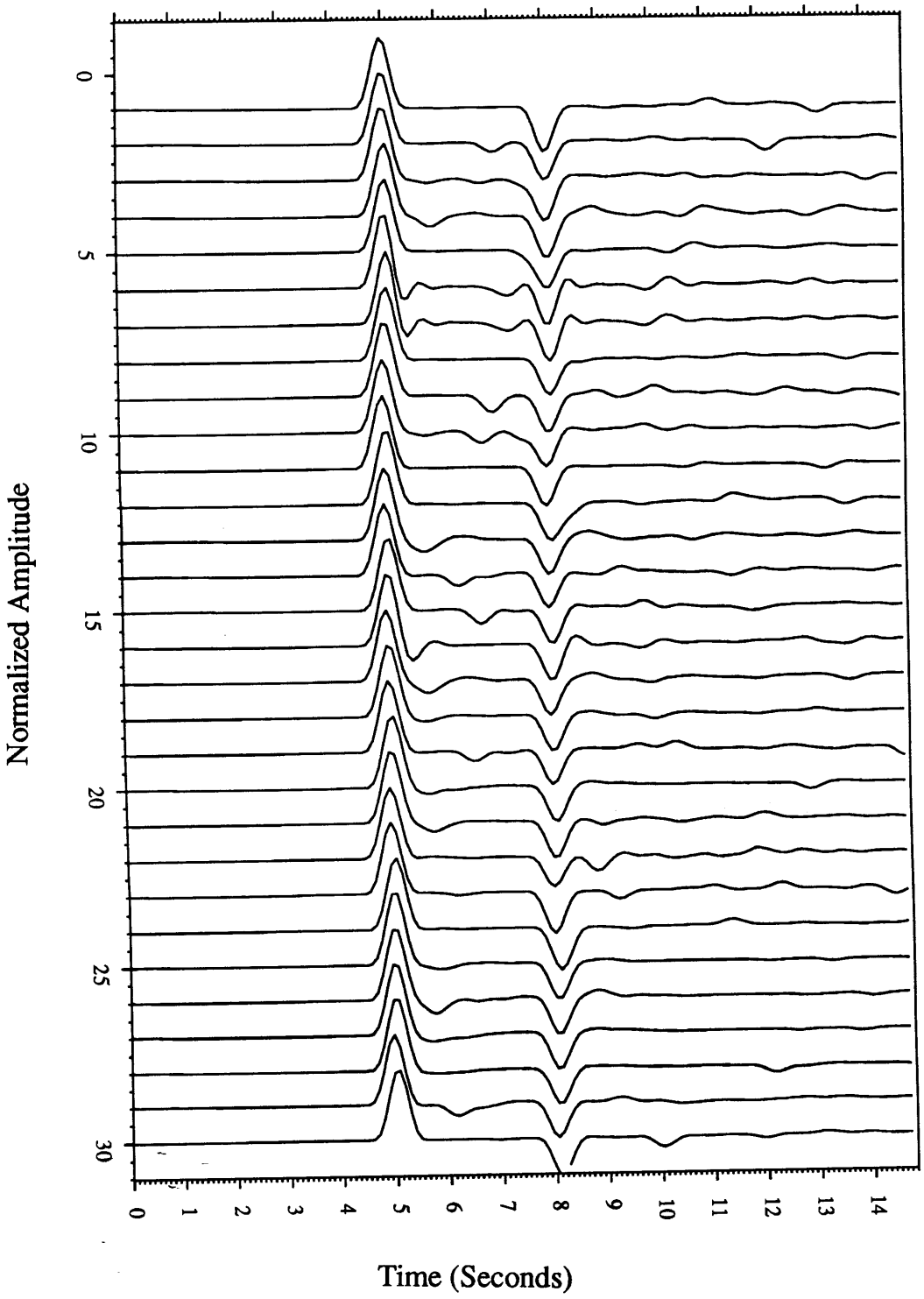

Figure 3b: Seismograms of Figure 3a shifted to common first arrival.

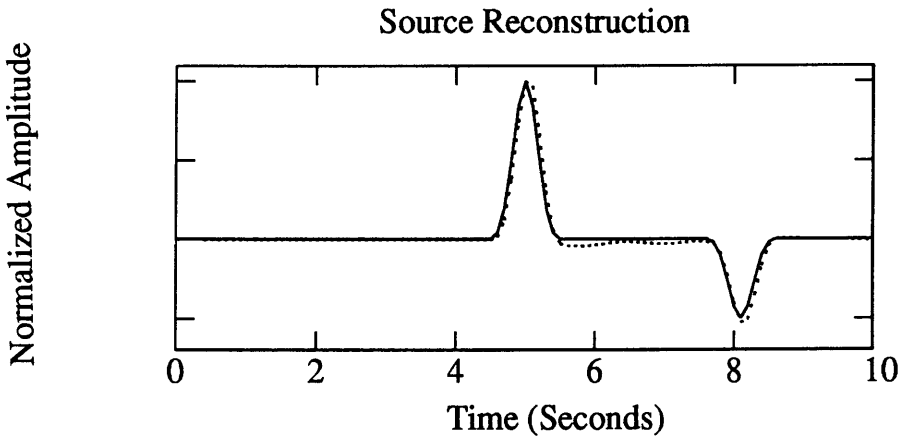

Figure 3c: Stack of 30 Blackman doublet seismograms compared with actual source (dashed).

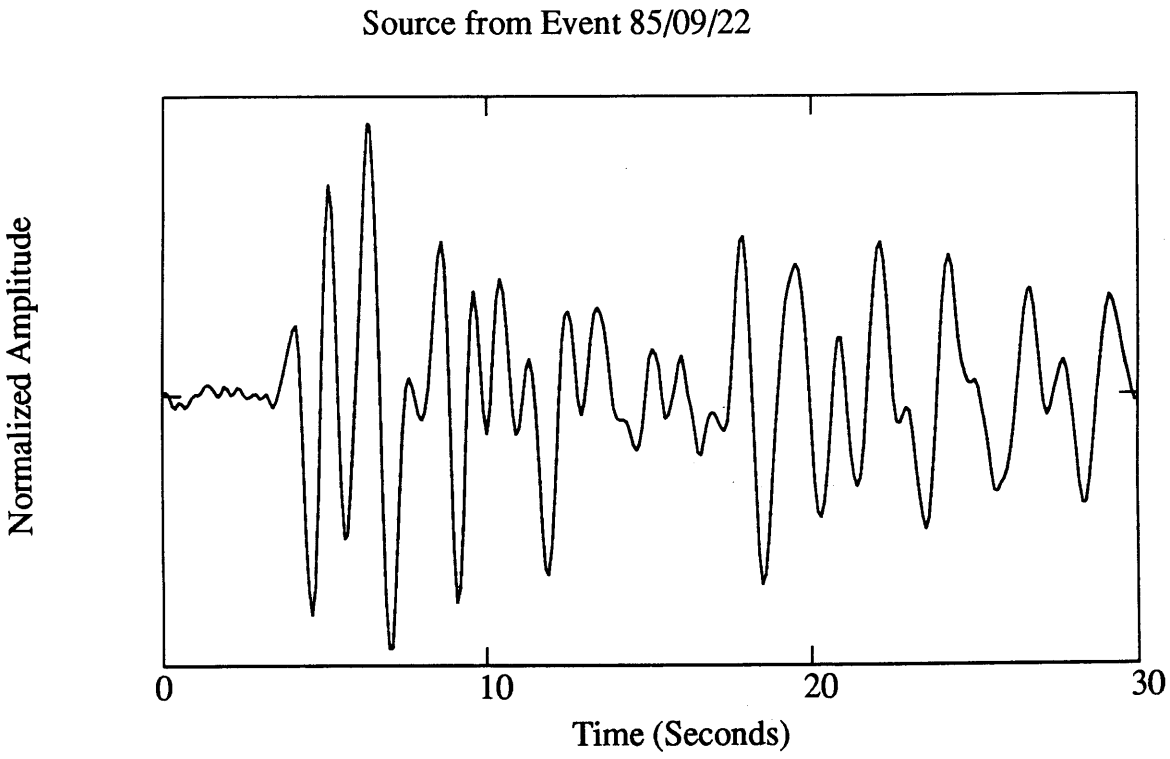

Figure 4a: Actual teleseismic source (Event 85/09/22) from a Mid-Atlantic Ridge earthquake determined by stacking the aligned direct arrival recorded ion the NEUSSN.

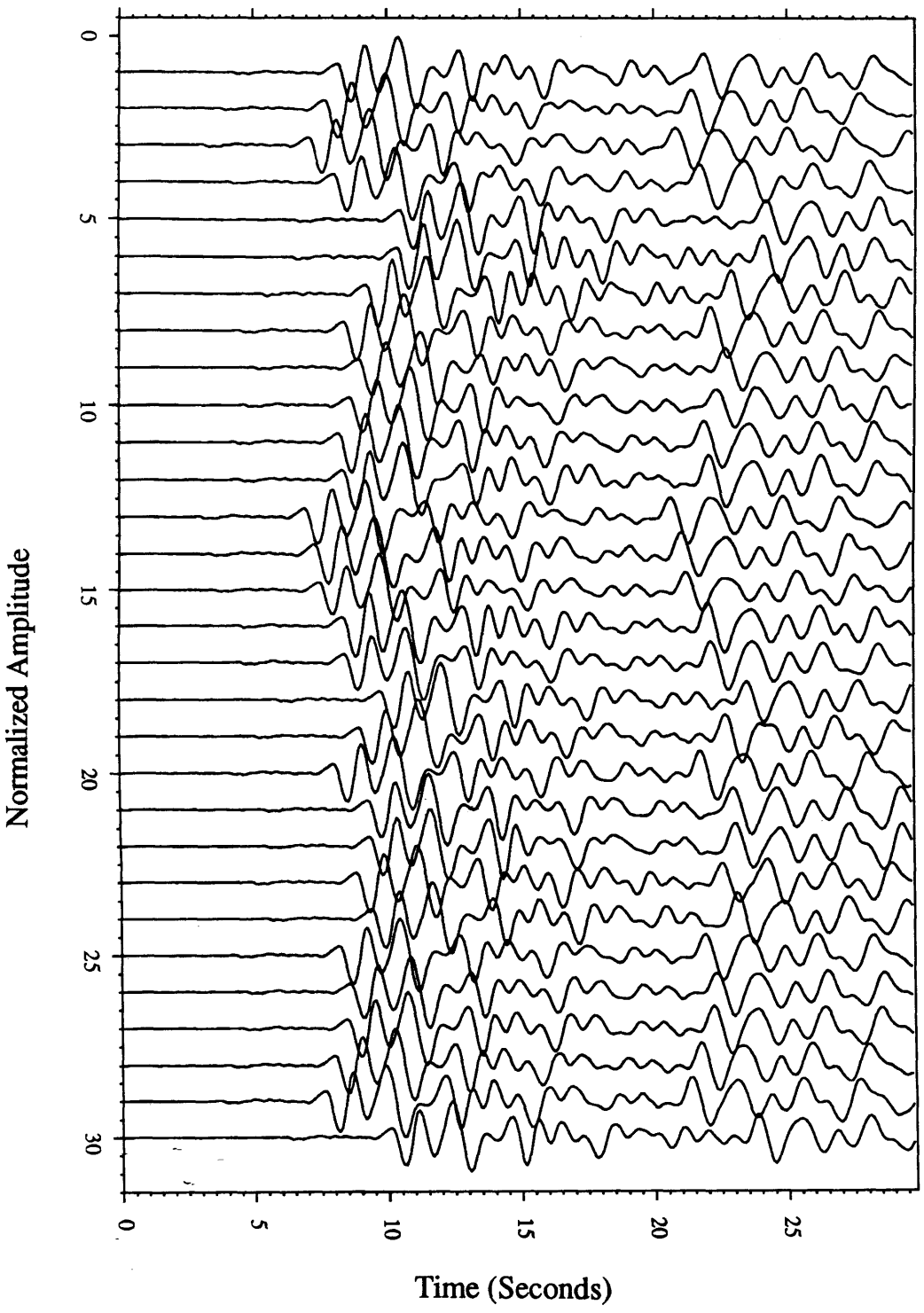

Figure 4b: Seismograms generated from convolution of 30 impulse responses and the actual teleseismic source 85/09/22.

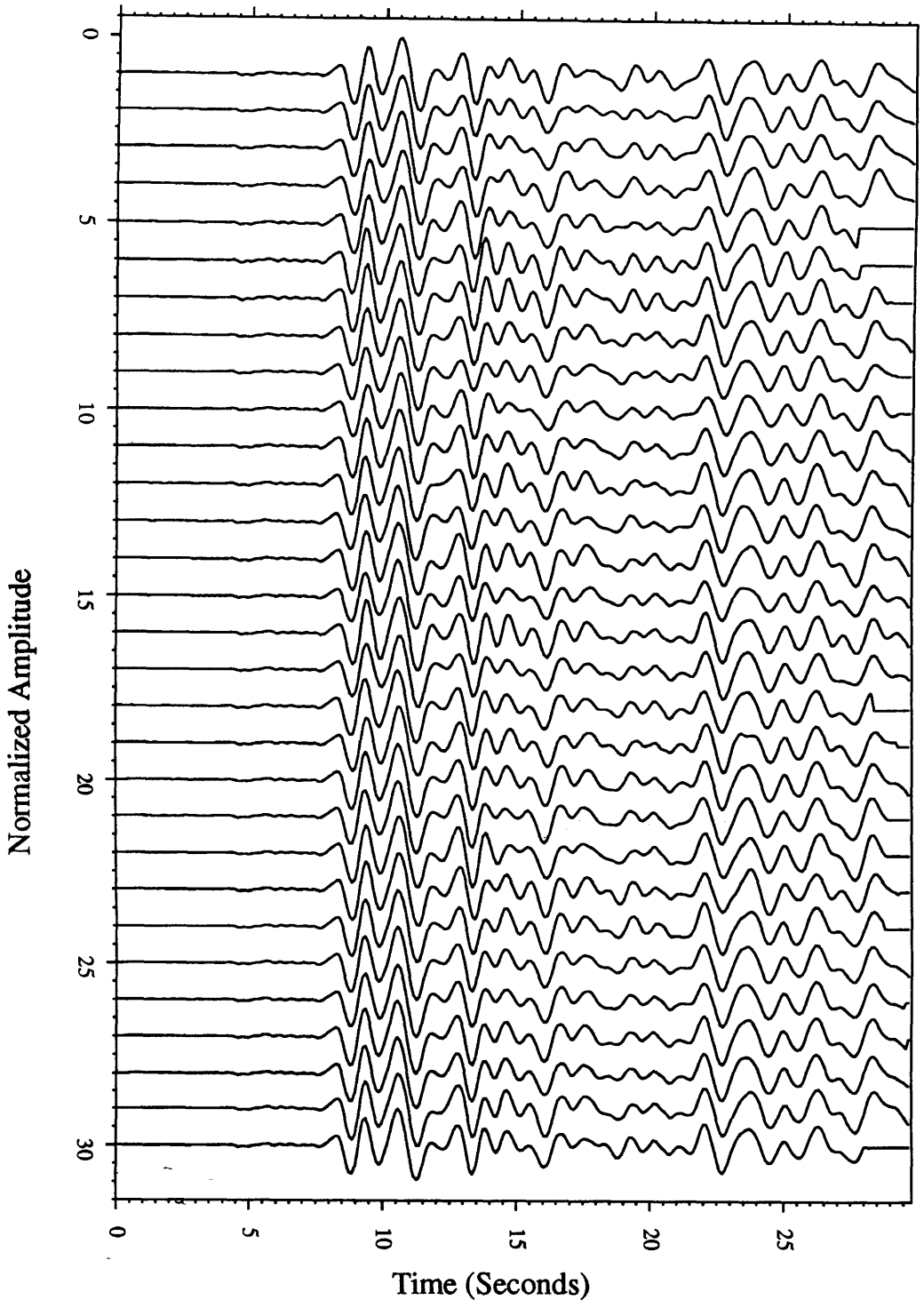

Figure 4c: Seismograms of Figure 4b shifted to common first arrival.

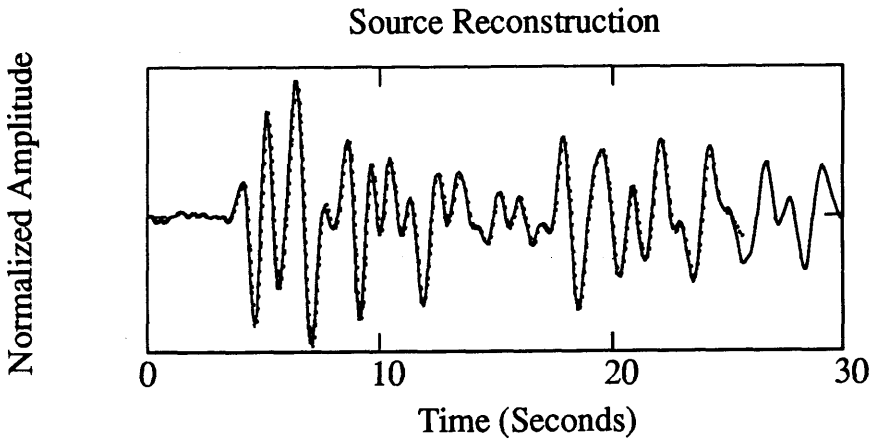

Figure 4d: Stack of 85/09/22 source seismograms compared with actual source function (dashed).

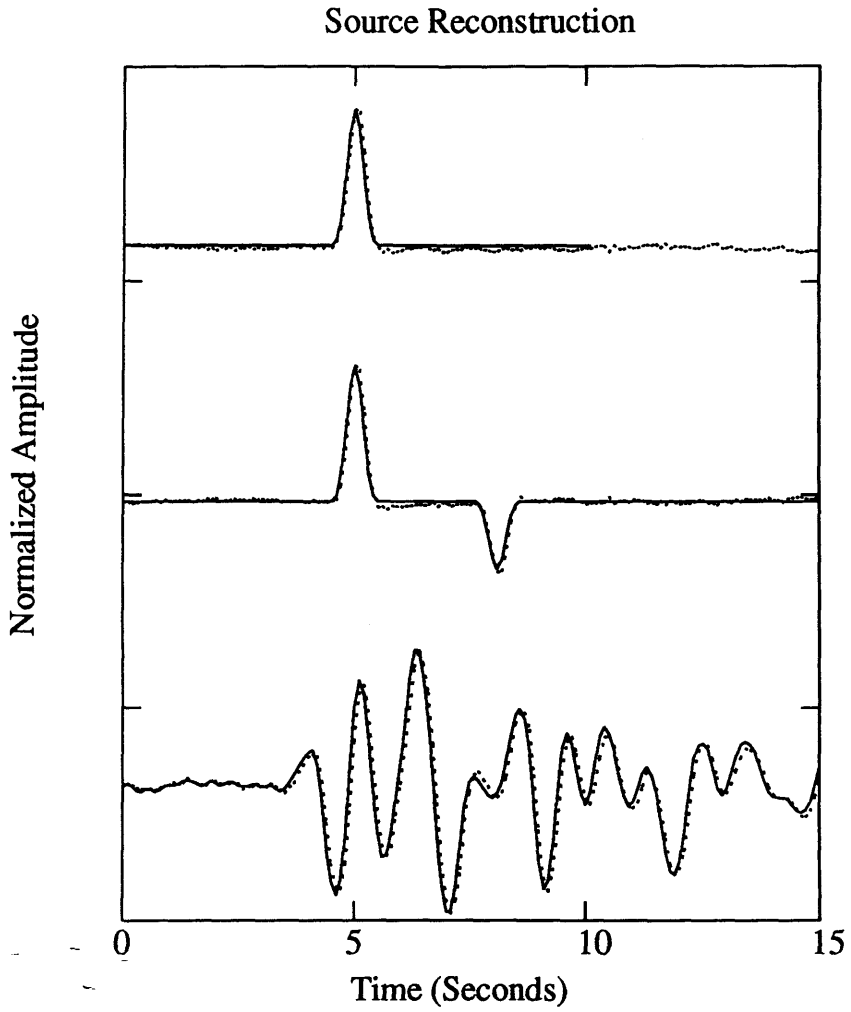

Figure 5: Noise analysis at 50% level, 30 fold stacks. Top: recovery of simple Blackman source. Middle: recovery of Blackman doublet. Bottom: recovery of 85/09/22 source. All actual sources are dashed.

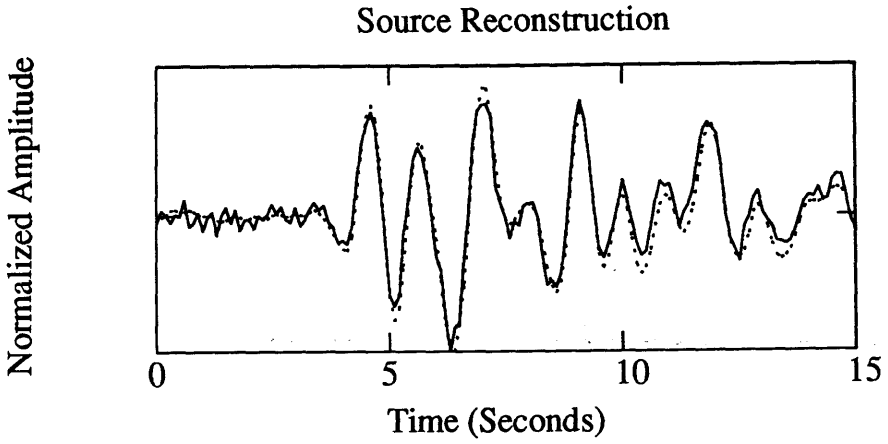

Figure 6: Noise analysis at 100% level; 30 fold stack for the teleseismic source from event 85/09/22. The actual source is dashed.

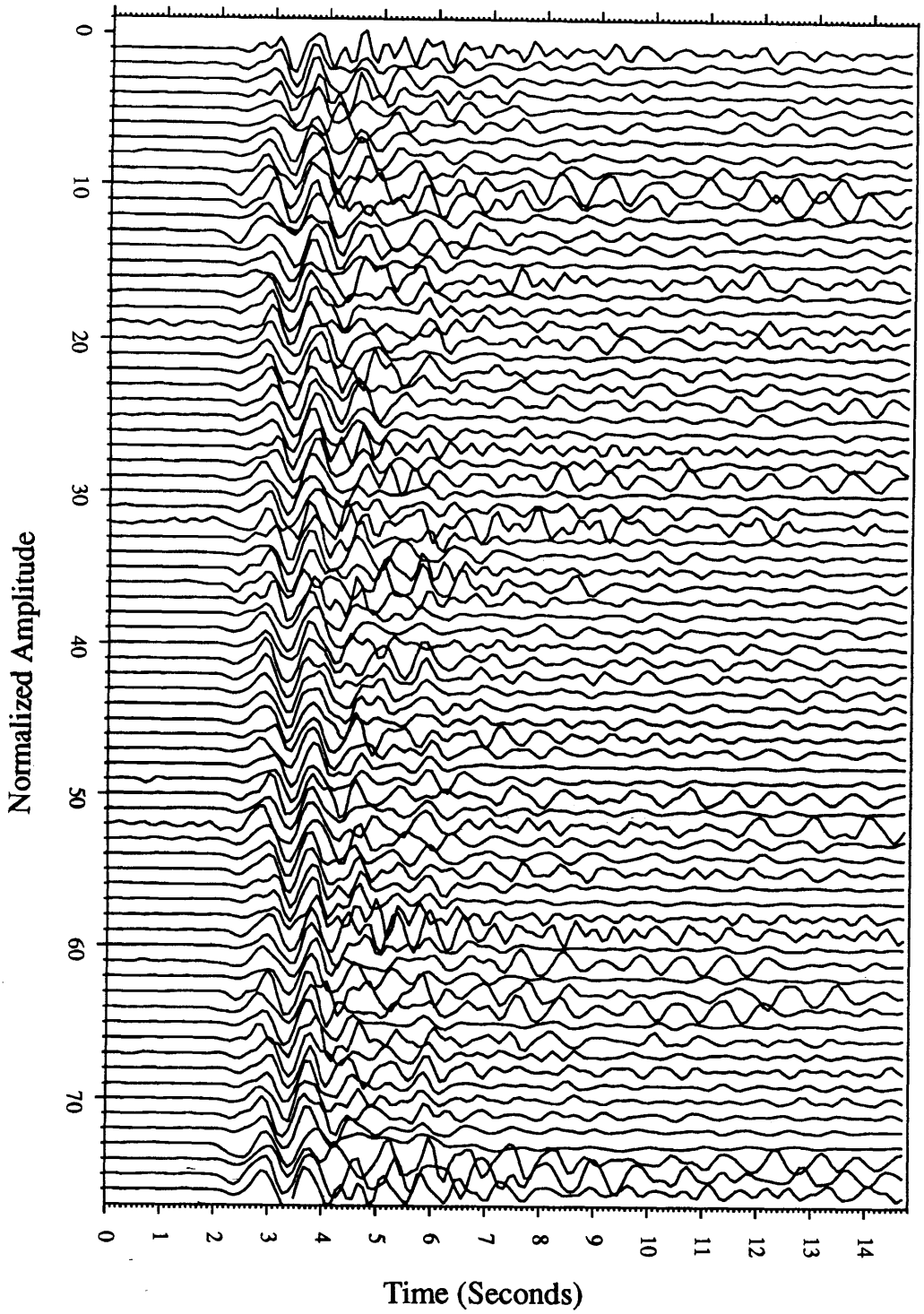

Figure 7: Aligned data from event 85/05/01 recorded on the NEUSSN network.

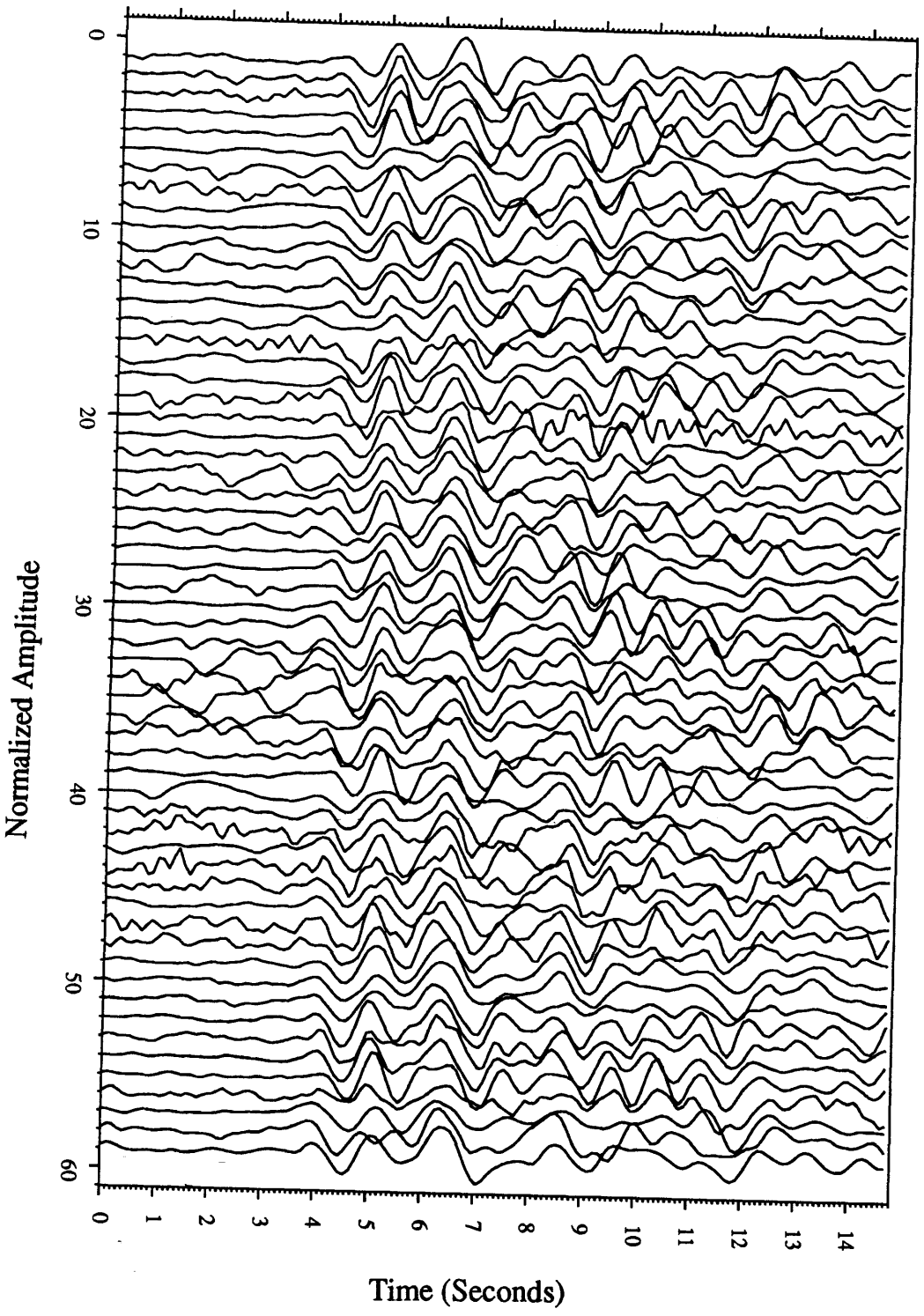

Figure 8: Aligned data from event 85/09/22 recorded on the NEUSSN network.

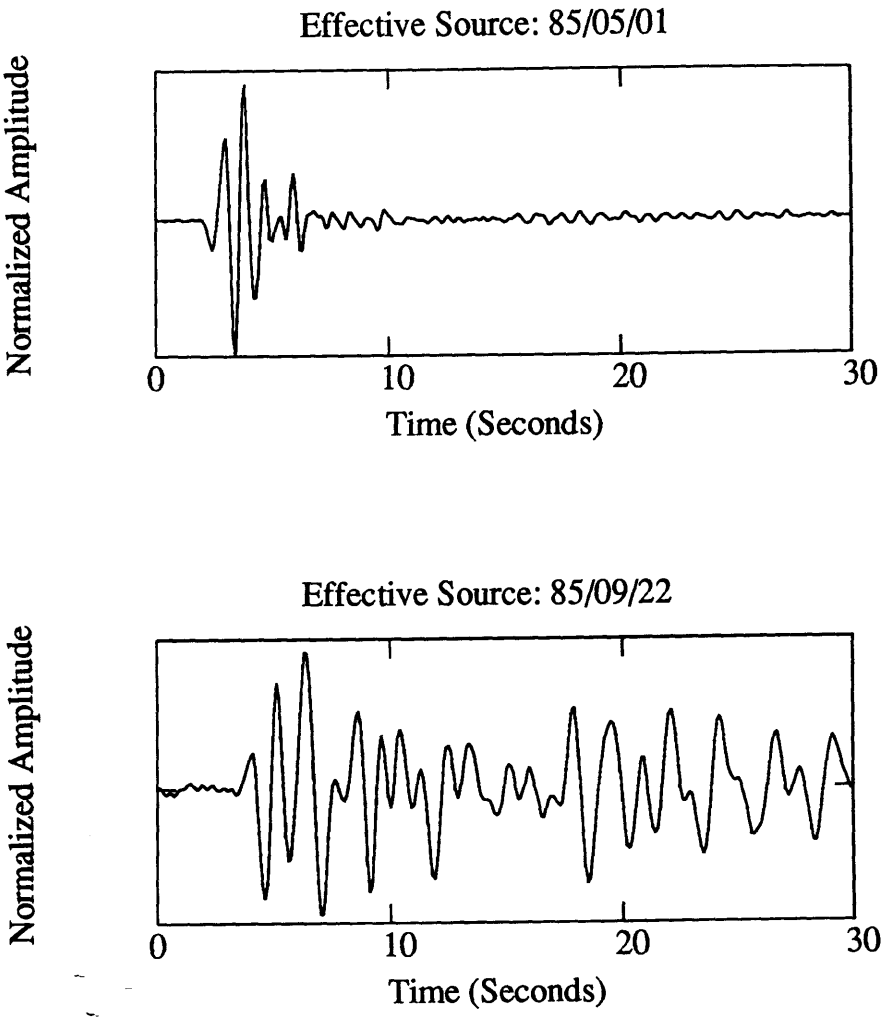

Figure 9: Stack of event 85/05/01 (top) and event 85/09/22 from NEUSSN network.

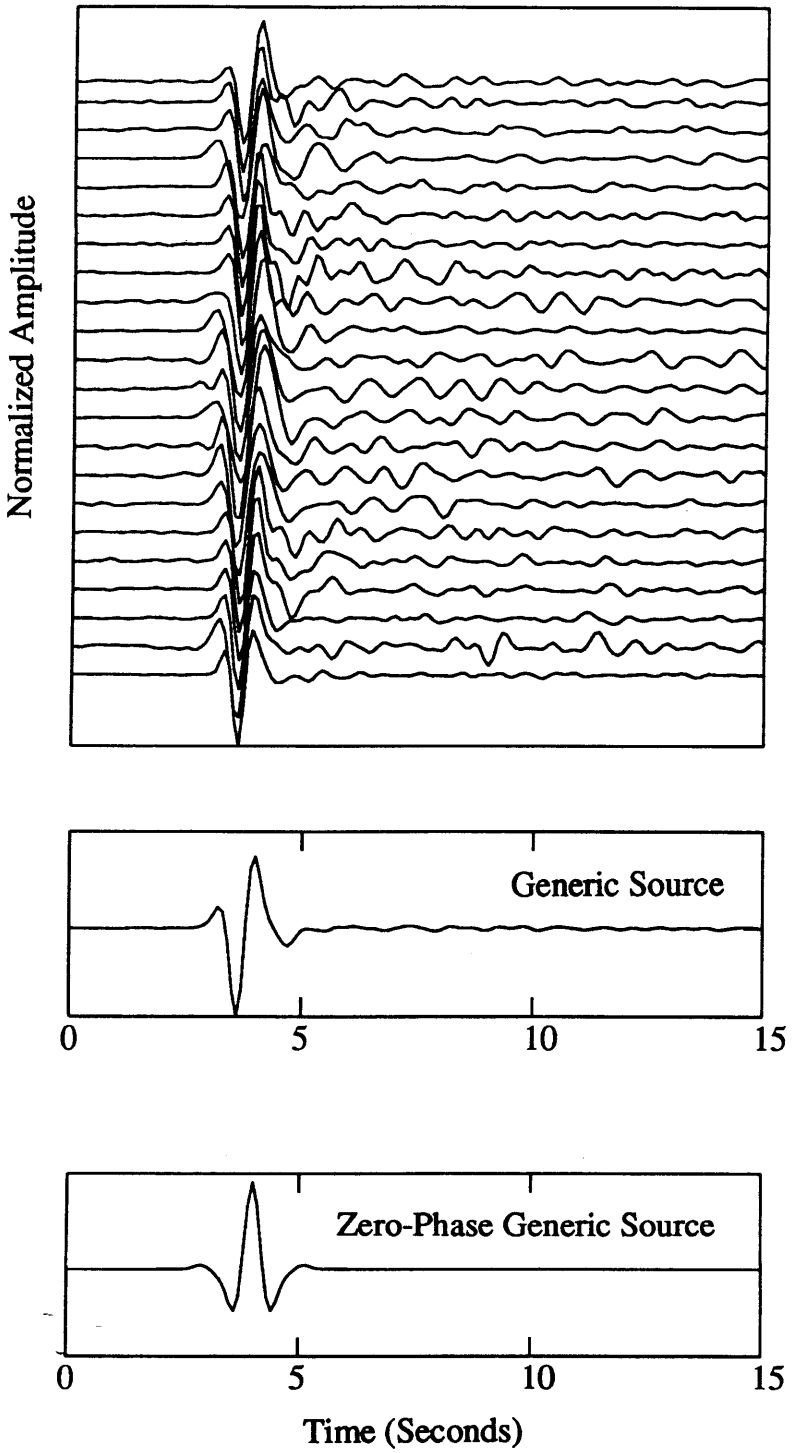

Figure 10: 22 best *effective* sources from the NEUSSN network (top). Stack of the 22 best *effective* sources (middle) and zero-phase representation of *effective* source stack. This becomes the generic source wavelet.

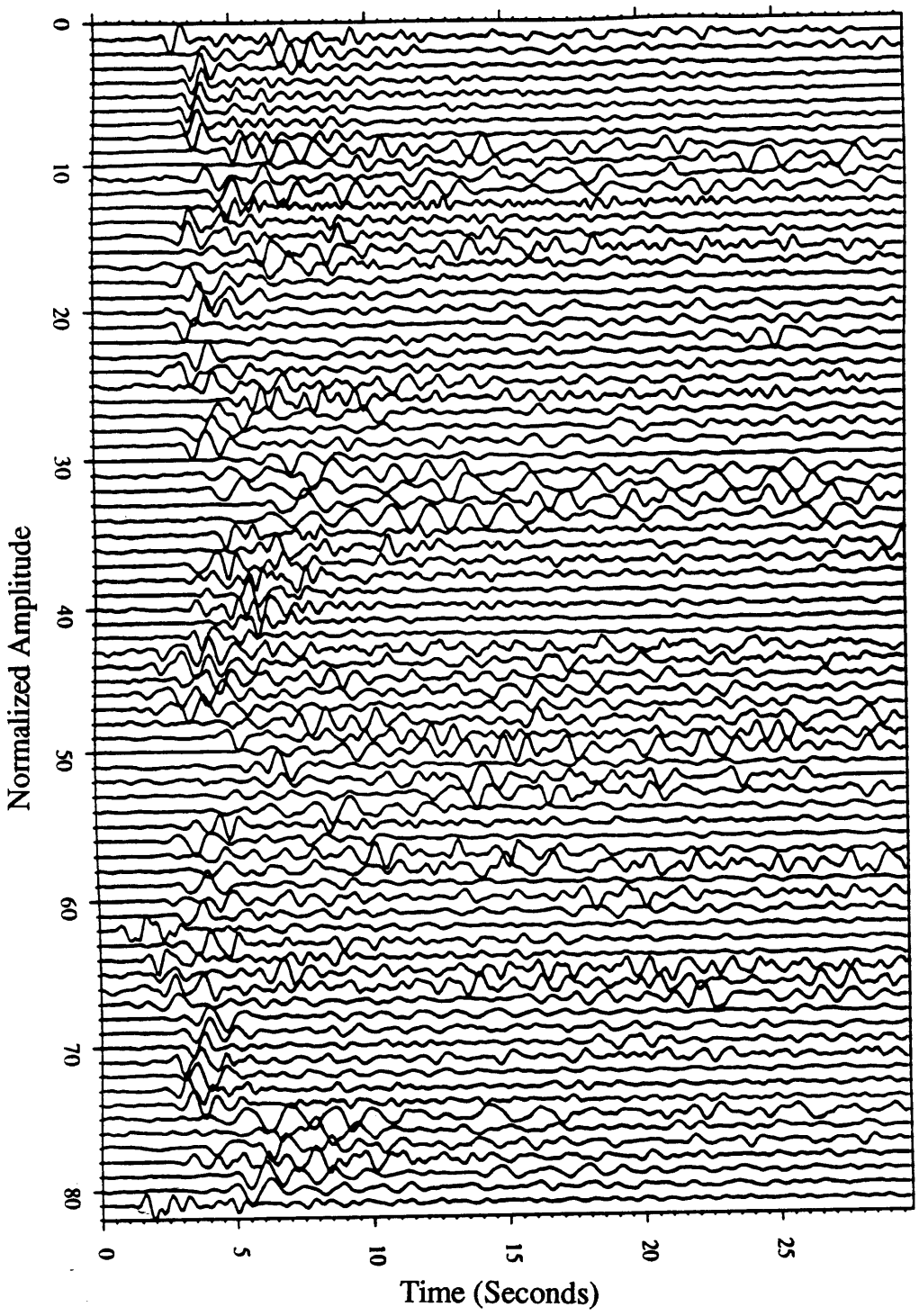

Figure 11a: All available raw data from station BVT, located in central Vermont. This station represents a typical NEUSSN station. This data comes from a 2 year period of recording (1985-1987).

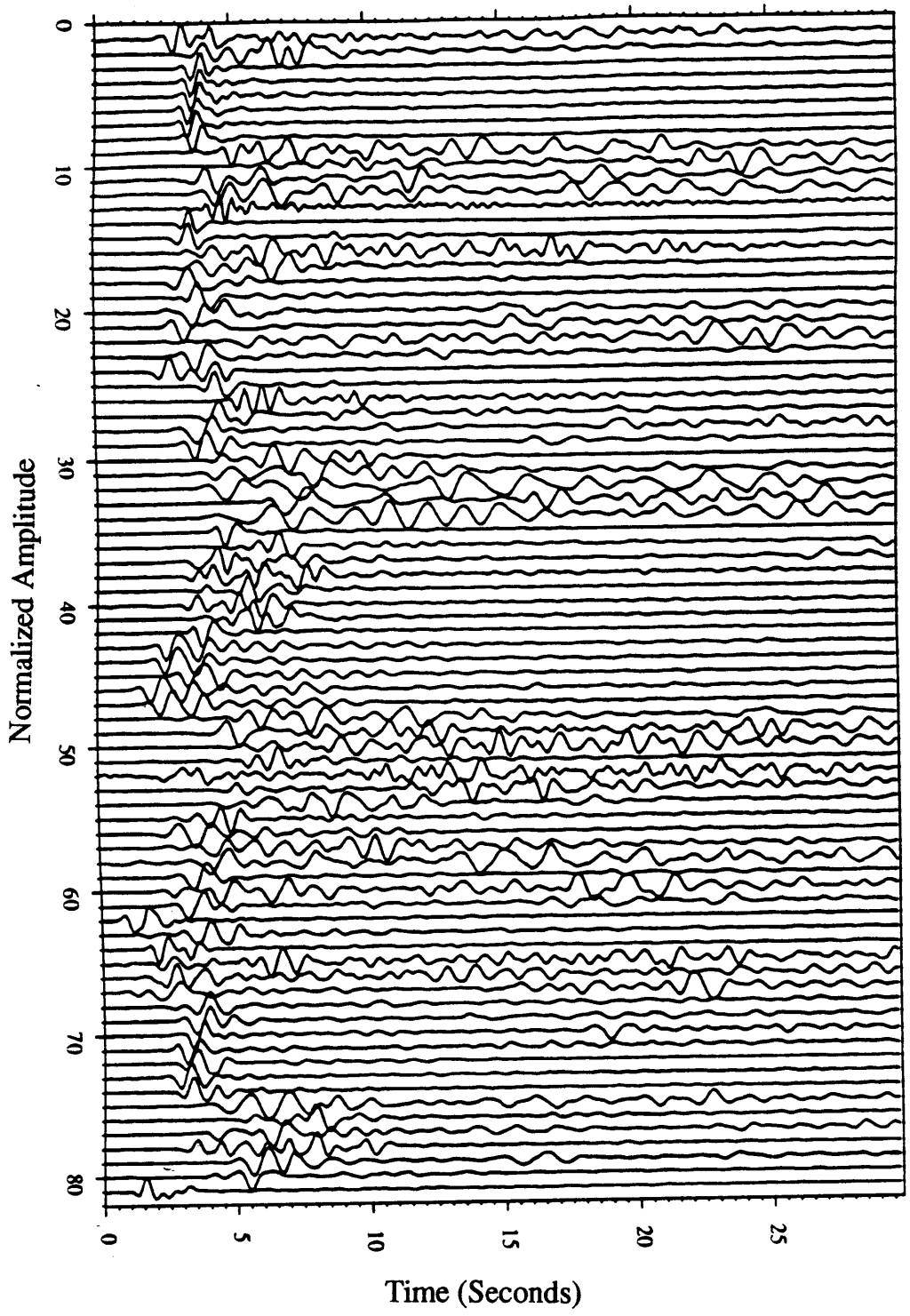

Figure 11b: *Effective* sources for the BVT data. Each *effective* source is made separately to characterize the different source functions arriving at each recording station.

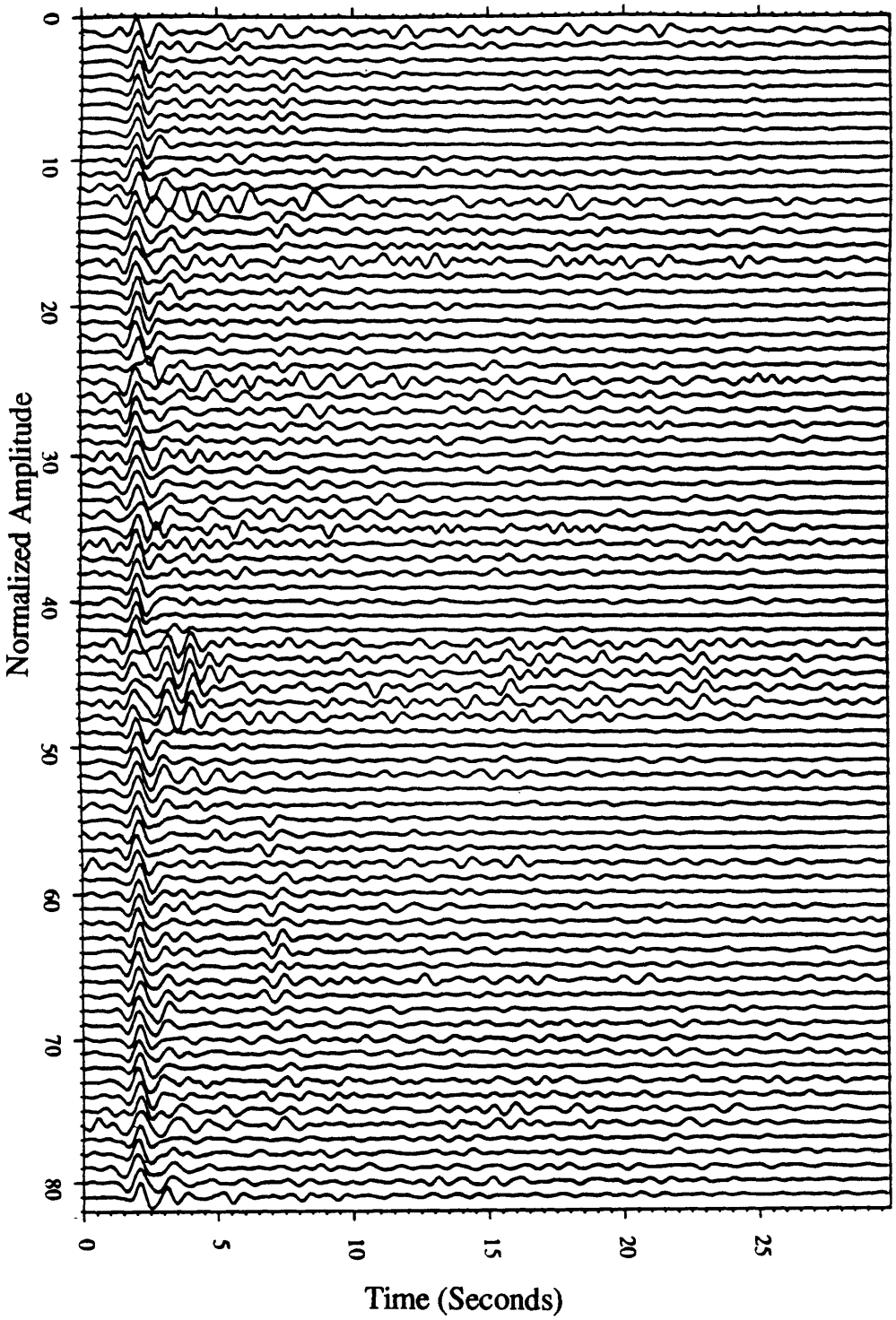

Figure 11c: Transformed BVT data, all natural source shapes have been transformed into a zero-phase wavelet. These data are used extensively in the following chapters.

Chapter 5

RAY PARAMETER TRAJECTORY METHOD

5.1 Introduction

The methods described and implemented in the previous chapters (travel time residual inversion and deep crustal velocity discontinuity determination via simulated annealing) utilize teleseismic waveform data on an event-wide basis and generally have decreasing resolution with depth. In this chapter we develop a new technique which allows us to model deep velocity discontinuities in the crust where conventional teleseismic and exploration methods generally encounter increasingly limited resolution with depth. This approach is different than that of the previous chapters because we now examine many seismograms recorded at a single station to determine the localized structure at a single receiver. In Chapter 2 and Chapter 3 we used all of the seismograms from a single event to characterize regional trends in the structure. We demonstrate that passively collected teleseismic P-waveforms, recorded at a vertical component seismic station which exists as a member of an existing seismic network, can supplement traditional imaging techniques and help to develop a clearer picture of the crustal velocity structure beneath a station.

The method presented here enables us to predict the two-way travel time to velocity discontinuities in the crust by taking advantage of the travel time dependence on the ray

parameter of each event. This technique has a wide base of application because it does not require the use of 3-component data but is designed to work with *vertical* component seismograms only. In addition, this method does not require that station instrument calibration parameters be known to great accuracy. These are important considerations because the vast majority of seismic network data comes from vertical component, poorly calibrated instrumentation. In general, the method describe here can be used with already existing data since teleseismic waveforms are generally abundant from the archives of those seismic networks that have been acquiring digital data for many years. In fact, the analysis presented here uses data from the NEUSSN from 1985, 1986 and the first half of 1987, and from the ENEL network for a period including 1986, 1987, and 1988. This represents only about 20% of the available data for these regions. The method also does not require that the absolute timing of the data be known accurately, which is an important consideration when combining data sets from various networks operated by different institutions at different time periods where there may be absolute time differences between data sets. We use phases which arrive after the direct P-wave and all of the timing is done relative to the P-wave arrival, so we can consider the *common* time base to be that of the time of the direct P-wave recorded at each station.

The ray parameter-trajectory (*rpt*) stacking, described below in Section 5.2, relies upon the *effective* source calculations and generic source transformations described in Chapter 4 to remove the near source and raypath effects. The source transformation process converts all natural source pulses into a common simple wavelet and makes it possible to analyze waveforms from different events at a single station, a capability of great utility with such low signal-to-noise data. The *rpt* method utilizes the wide range of source-to-receiver distances of the 148 events used in the New England study and 101 events recorded at Larderello. Since every seismic signal has its own unique incidence angle (and therefore unique ray parameter), we need to employ a ray parameter dependent stacking procedure to search for coherent energy arriving at a single station. This method is similar to velocity analysis techniques applied to seismic reflection data (Telford et al., 1982; Robinson, 1983) and is applied to the New England and Larderello areas in Section 5.4 and Section 5.5, respectively.

5.2 Method and Synthetic Tests

The ray parameter trajectory (*rpt*) stacking method allows us locate reflectors beneath a recording station by stacking waveforms recorded at a single station from different events along trajectories which are a function of their ray parameter. The *effective* source calculations and the generic source transformations (Chapter 4) allow us to use this cross-event stacking method to search for coherent reflections arriving from various events at an individual station. The *rpt* geometry is schematically illustrated in Figure 1; here we have different teleseismic plane waves arriving beneath a station at different angles of incidence. Each ray which travels to the surface of the Earth and returns back to the receiver as a primary reflection from a given interface has an arrival time which is a function of the event incidence angle. A plane wave can be characterized by its ray parameter

$$p = sin(i)/V, \tag{5.1}$$

where i is the angle of incidence measured from vertical and V is the velocity of the medium. For a given velocity model each incoming plane wave generates the same set of crustal phases arriving after the direct P-wave with arrival times varying as a function of the ray parameter. For horizontal layers the delay time (T_j^d) between the direct P-wave and the primary reflection from layer j is given by

$$T_j^d = \frac{TT_j^v}{cos(\alpha)} \tag{5.2}$$

where TT_j^v is the vertical 2-way travel time to layer j, α is given by $sin^{-1}(p \cdot V_c)$, and V_c is the average velocity of the medium from the surface to the reflector. With this relation we can predict the primary reflection arrival time for any incident plane wave given estimates of the vertical 2-way travel time to the reflector and the average crustal velocity above the reflector. We use this relationship to hunt for reflectors under a station by systematically testing all possible vertical 2-way travel times for various velocity models.

As an example, we show in Figure 2 twenty-six seismograms with different incident angles ranging from 0 to 50 degrees in 2 degree steps, for a 2 layer, 30 km thick crust. The first layer is 9 km thick ($V_p = 6.0 \frac{km}{sec}$) and has a vertical two-way travel time of 3.0 seconds.

The second layer is 20 km thick ($V_p = 7.0 \frac{km}{sec}$) and has a vertical two-way travel time of 8.4 seconds. The mantle velocity used is $V_p = 8.1 \frac{km}{sec}$. There are a few important observations one can make from this synthetic data.

- In the range of incidence angles of 0 to 25 degrees, the primary P-waves dominate the waveforms and the moveout of the important arrivals is small. Deeper reflections ($P_m P$) have more moveout than shallow reflections.

- In the range of incidence angles of 30 to 50 degrees, the waveforms are dominated by converted phases. The dominant arrivals are actually two phases which have equal travel times; each phase has one leg as a P-wave and one leg as a S-wave. We refer to these events as *converted* arrivals.

- In the range of incidence angles of 22 to 36 degrees, the waveforms have both P-wave and converted arrivals. Much of the actual data falls in this more complicated range of angles.

- In general, primary S-reflections are very weak arrivals on vertical component waveforms and are not used in this analysis.

To search for reflector depths in actual teleseismic data, we stack source-transformed data in windows predicted by Equation 2 for different estimates of vertical two-way travel time (TT_i) and various velocity models (referred to as *prediction velocities*). We generate the function $P(i)$, which describes the reflective power of the underlying media at each vertical 2-way travel time for primary P-arrivals and converted-arrivals

$$P_i = \sum_{j=1}^{l} \sum_{k=1}^{N} (d_{j,k}^2), \tag{5.3}$$

where P_i is the i^{th} trajectory stack power, N is the number of traces, and j is the window index (each of length l samples) which is a function of the ray parameter trajectory and controls which part of the seismogram is added to the stack. The stacking window for each seismogram is centered on the travel time estimate (Equation 2) with a fixed number of points. The trajectory stack power $P(i)$ is a maximum when the estimated vertical travel time (TT_j) is the best estimate of the true vertical travel time to the layer.

Figure 3 shows the results for tests when primary P-wave arrivals are targeted. All seismograms are calculated with a ray tracing technique described in Chapter 6. Figures 3a through 3d show the results for window widths of 0.1, 1.0, 2.0, and 3.0 seconds, respectively. In these cases we use the actual velocities of the model as the prediction velocities. We see that we recover the correct 2-way vertical travel time to both velocity discontinuities in the model. The resolution of the peak in the power plots is diminished when the window is too wide due to the inclusion of non-targeted phases in the stack, and as the window is closed to a single point (0.1 second), we see side-lobes adjacent to the peaks in the trajectory stack power which are affects caused by the shape of the source wavelet. When this method is applied to the actual data, we use a window width of 1.1 seconds (the half-width of the generic source wavelet) to minimize the side-lobe effects.

Next, we examine how travel time determinations of crustal discontinuities are effected by changing the velocity estimates used in the stacking procedure. We test the sensitivity of this method to changes in velocity estimates for cases where the prediction velocity is 10% greater than the true model velocity (Figure 3d) and when the prediction velocity is 10% less than the true model velocity (Figure 3e). The changes in velocity (from the true model velocity) cause slight variations in the propagation angles which in turn increase or decrease the path length of rays traveling to the reflector. For the P-wave case, the 10% velocity perturbations cause the peaks in the stack power plots to shift only slightly to compensate for the change in raypaths. However, the amplitudes of the peaks are significantly smaller (35%) when the prediction velocities are inaccurate. We use this information to help us select the most appropriate prediction velocities.

Figures 4a through 4b shows the results of the converted-arrival tests. We show 3 cases: A) the prediction velocity is equal to the true model velocity, B) the prediction velocity is 10% less than the true model velocity, and C) the prediction velocity is 10% greater than the true velocity. Since converted-arrivals are not important for near vertical incident events, we include in the trajectory stacks only events with incidence angles greater than 25 degrees. Again, we recover the correct vertical travel time estimates to the model discontinuities from the converted phases. Figure 4d show the converted-arrival analysis result when *all* incidence

angles are included (0 to 50 degrees). We contaminate the results by including into the stack the primary P-wave reflections (at 3.0 and 8.4 seconds). When the *rpt* method is applied to the actual data, we carefully control the events included in the analysis to avoid these contamination problems.

To test the effect of noise on the *rpt* method, we re-ran the previous tests on synthetic data with actual noise added to the traces. Figures 5 and 6 show the 26 synthetic seismograms of the previous example with noise which is 10% and 30% of the direct P-wave arrival added. Figures 7a and 7b show the power plots of the P-arrival and converted-arrival cases with 10% noise. For reference, the noise-free examples are also plotted on these figures. We see from these plots that the resolution of travel time estimates to the shallow layers is most affected by the noise, but in general, a small amount of random noise does not degrade the results. From the 30% examples (Figures 8a and 8b), we see that we can have numerous false peaks on the stack power plots when noise dominates the seismograms. Overall, we conclude from this analysis that the *rpt* method retains its ability to resolve velocity discontinuities in the presence of realistic noise levels (about 5 to 15% in the actual data).

We showed above that using an *in*accurate prediction velocity degrades the amplitude of the stack power peaks but has little effect on vertical 2-way travel time estimates (particularly for P-waves). We now demonstrate the ability of the *rpt* method to determine accurate crustal velocities. To do this, we analyze the synthetic data for primary P-arrivals and for converted-arrivals for all reasonable half-space velocity models. The layer above the mid-crust discontinuity in our test model has an actual P-wave velocity of 6.6 $\frac{km}{sec}$ and S-wave velocity of 3.46 $\frac{km}{sec}$. The true 1-layer velocity of the crust above the Moho discontinuity in this model has a P-wave velocity of 7.1 $\frac{km}{sec}$ and a S-wave velocity of 4.1 $\frac{km}{sec}$. In Figure 9 we show the primary P-wave power plots for prediction velocities of 4.5 to 7.9 $\frac{km}{sec}$ (in steps of 0.1 $\frac{km}{sec}$). The variation in peak stack power for the 45 tested velocities is shown in Figure 10. We see that the P-wave mid-crust reflections (top) can be used to determine the average crustal velocity as well as the two-way vertical travel time to the discontinuity. The deeper reflections (bottom) have greater trajectory moveout than shallow layers, allowing for more accurate estimates of average velocity at greater depths. Figure 11 shows the S-

wave case for half space prediction velocities of 2.5 $\frac{km}{sec}$ to 5.5 $\frac{km}{sec}$ (in steps of 0.1 $\frac{km}{sec}$), and the variation in peak stack power for the 31 tested velocities is shown in Figure 12. We see that the stronger functional dependence between ray parameter and travel time for the converted-arrivals makes the deep reflection a good indicator of the average crustal velocity.

For real-data applications we want to avoid biasing the answers from events with clustered incidence angle and back azimuth pairs. Often we record events with nearly equivalent source-receiver parameters (nuclear tests, for example). To remove these effects, we weight each seismogram in a stack inversely proportionally to the density (ρ_j) of arriving events within a given azimuth/incidence angle region. Equation 4 now becomes

$$P_i = \sum_{j=1}^{l} \sum_{k=1}^{N} \frac{1}{\rho_j} \cdot (d_{j,k}^2), \tag{5.4}$$

Actual data applications are shown and discussed for the NEUSSN and ENEL networks below.

When the Earth cannot be adequately represented as a series of flat lying layers, the assumptions used in the *rpt* formulation are violated. To examine the extent to which these violations can be tolerated, we simulated various 2-D dipping structures, tested the stacking requirements, and made the following conclusions: 1) When the dip of a deep interface (below 15 km) is greater than 10 degrees, then the primary reflection no longer stacks in phase for rays with incidence angles greater than 10 degrees. 2) For more vertically incident arrivals (less than 15 degrees) the method can tolerate greater dips but suffers from a decreased resolution in velocity due to reduced incidence angle coverage. For more obliquely arriving rays (greater than 30 degrees) the horizontal-layer assumption of the method is more sensitive to sub-horizontal layering and for 10 degree dipping layers Equation 3 is no longer valid. 3) We have found that the *rpt* method does not produce false peaks in the stack power plots; dipping 2-D structures do not map into erroneous 1-D features. We can use this technique, even with the strong geometrical constraints required by the method, in areas where we suspect to see 2 and 3-D effects. 4) Given the problems associated with dipping structures, this method can be used only to infer the existence of horizontal layers and cannot be used to infer the absence of non-horizontal interfaces. This point is discussed below.

5.3 New England Application

In this Section we apply the *rpt* stacking method to 12 stations in the NEUSSN (Figure 13) which represent a good sampling of some of the various tectonic provinces of this area (see Figure 1-6, for example). The group of selected stations trends to the northwest, cutting across the general northeast trend of the geology from southeast New England in the Avalon Terrane through the series of progressively older banded metamorphic terranes which make up the central portions of New England and to southeastern Canada. Station coordinate information can be found in Table 1.

As we described above, all seismograms recorded at an individual station are gathered together and the source equalization process is applied to each trace. This converts the source function of each seismogram into an equivalent wavelet. The data are sorted by increasing incidence angle and then azimuth/incidence angle density functions are calculated. Figure 14 shows the azimuthal and incidence angle distribution of these stations, and we see from this plot that we have excellent coverage in incidence angle from 0 to 45 degrees. The azimuthal coverage is not uniform, with significant gaps from the east. Figure 15 shows all of the data from a typical station in the network station (BVT, located in central Vermont). These data are plotted to demonstrate that some features are visible in the waveforms (between 6 and 9 seconds we see some common arrivals on a number of traces), but in general it is difficult to extract travel time information from these data.

The results of the *rpt* primary P-wave and converted-wave analyses are are presented in Figures 16 through 27. For each station four plots are shown:

1. P-wave *rpt* analysis. Here we plot the relative power of the trajectory stack against two-way vertical travel time. Strong isolated peaks on these graphs indicate coherent reflectors beneath the station with well defined two-way vertical travel times.

2. Converted-arrival *rpt* analysis. These plots are similar to the P-wave plots described above when converted phases are targeted.

3. P-wave velocity analysis. Here we display the relative power of the trajectory stacks for all velocities in the analysis at a particular two-way vertical travel time. We select

the phase which we associate with the Moho reflection for the velocity analysis, and from these graphs we can determine the average velocity of an equivalent 1-layer crust beneath the station.

4. Converted-arrival velocity analysis. As above, we display the relative power stack power for all S-velocities for the associated converted-arrival.

In general we see from these plots that a number of near horizontal velocity discontinuities exist in New England. At nearly every station we see strong and isolated arrivals which indicate that a flat reflector exists beneath the station with appreciable region extent. We see from the velocity analyses that the *rpt* stacking method is sensitive to velocity variations in the crust. We plot the P-wave results on a New England map in Figure 28. We can make a few observations from these data: 1) The crust near each of these stations can be generally described by 2 or 3 dominant interfaces which are are roughly horizontal. A crustal model with a small number of strong discontinuities has been commonly inferred from refraction studies in New England (Luetgert et al., 1987, for example), and these teleseismic results corroborate such a model. 2) Generally, the agreement between the P-wave analyses and the converted-arrival results is not strong. We conclude that the determination of vertical two-way travel times from converted-arrivals is less well controlled than that of the P-wave case because of the oblique angles of incidence of the arrivals (30 to 50 degrees). The converted-arrival travel time estimates are only used to interpret the P-wave stack power plots. 3) There are interesting regional trends in the deep crustal arrivals which are shown in Figure 28. We classify these trends into three broad groups. The first is the southeastern stations (DNH, WFM, WES, GLO and DUX) which all exhibit two-way vertical travel times to a well defined Moho of less than 10 seconds, or at depths in the range of 27 to 33 km. These results match well with forward modeling studies at station WES (Foley and Ebel, 1984; and Doll, 1987) as well as the simulated annealing results of Chapter 2. The second group lies in southern NH and VT (ONH, PNH and BVT) in an area that exhibits a more complicated pattern of crustal reflections than regions to the north or southeast. These relatively closely spaced stations have very different crustal *rpt* responses: BVT has numerous strong arrivals from the mid- and lower crust, while ONH returns very little energy from the lower crust.

A visual inspection of the seismograms which go into the ONH *rpt* analysis indicates that the lack of reflectivity cannot be attributed to a dipping structure, but rather from a weakly reflective transition zone from crust to mantle. This can be inferred from the lack of arrivals at ONH seismograms within the time range of 6 to 15 seconds. In contrast to ONH and BVT, PNH exhibits a simple crust with the Moho at about 35 km. The third regional classification derived from the *rpt* analysis is in northern NH and VT (Stations WNH, BNH and DVT). The crust beneath these stations is thicker than in the other 2 areas, with a Moho depths about 40 km (about 12 second two-way vertical travel times). This is consistent with the travel time residual results of Taylor and Toksoz (1980), who found delayed direct P-wave arrivals at each of these stations, but it is not consistent with the simulated annealing results in Chapter 3 where we see a deeper Moho but one not as accentuated as predicted by the *rpt* analysis. This discrepancy must be studied further.

The main general conclusion we can draw from the *rpt* application in New England is that this modified velocity analysis technique enables us to find the major velocity discontinuities in the deep crust by taking advantage of the incidence angle dependence of primary reflection in the crust. The source equalization method of Chapter 4 makes this type of analysis possible.

5.4 Larderello Applications

The *rpt* stacking method was applied to all but 2 stations of the Larderello Geothermal Field Seismic Network. Stations FRAS and MGUI were removed from the analysis because they recorded very few usable events during the period of interest due to intermittent recording. The event distribution of the earthquakes used in the analysis is shown in Figure 3-1. Unlike the New England case, we do not have a large number of events with incidence angles in the range of 30 to 50 degrees, and for this reason we limit the *rpt* analysis to P-waves which arrive at incidence angles between 0 and 25 degrees. In Figure 29, where we present the P-wave stack power plots and the corresponding P-wave velocity analysis results for all 26 stations. The velocity analysis is based on a single observed arrival (for example the arrival at 6 seconds for station CLSV) which is indicated on each stack power plot. In Figure 30 we

display the results on a map of the network to illustrate the regional distribution of these data. There are a number of observations that can be made from these figures.

1. In general, we see that there are very strong, coherent reflections present at most stations. On the individual station seismogram plots there are few coherent arrivals, and we are unable to determine the vertical two-way travel time to the reflectors without the *rpt* analysis. Even with the relative high quality of these data, the seismograms are dominated by noise and are difficult to study on a single-seismogram basis. The ray parameter dependence of the arrivals make this analysis quite useful for identifying the travel times to all major coherent discontinuities.

2. The stations in the central and southwestern part of the network have a more complicated upper-crustal reflection pattern than stations on the periphery (two-way travel times of less than 5 seconds or about 12 km). Numerous arrivals exist in the stack power plots.

3. The stations on the periphery (SINI, LURI, POMA, SERR, for example) are dominated by very clear, strong and isolated arrivals deeper at about 5.5 seconds two way vertical travel time, or at 16 to 18 km depth. Since deeper arrivals are imaged more effectively than shallow features with this technique, this indicates that the region in the center of the network has a less reflective lower crust than on the periphery; there are fewer isolated and coherent reflectors in the deep crust of significant lateral extent.

4. In the interior region there are several stations with weak arrivals at about 6-7 seconds two-way vertical travel time, at depths of 17 to 22 km. These stations are plotted in cross-section in Figure 31, along with 4 peripheral stations. We interpret this interface as the base of a dominant low velocity zone which exists in the center of the network. Giese et al. (1980), observe a similar feature in the Larderello area using refraction data, and they estimate the low velocity zone to be at a depth of between 18 and 22 km to the southeast of PADU.

5. Of all the stations in the network, only three stations (SASS, MBAM and MLUC) have no significant peaks in the stack power plots after 4 seconds two-way travel time.

From a qualitative review of the seismograms at these stations, we conclude that deep reflectors do exist at each of these stations, but they are not imaged with this technique due to steep dip of the interface. This conclusion is drawn from the existence of numerous arrivals in the seismograms which do not stack along any trajectory based on horizontal layering.

These observations and interpretations are fully discussed in Chapter 7.

TABLE 1: New England Station Information

Station Name	Latitude	Longitude	Elevation (Meters)	P-velocity $\frac{km}{sec}$	S-Velocity $\frac{km}{sec}$
BNH	44.59	71.25	472	6.8	4.0
BVT	43.34	72.58	300	6.3	4.2
DNH	43.12	70.89	24	6.2	4.0
DUX	42.06	70.76	27	6.1	4.0
DVT	44.96	72.17	370	6.6	3.7
GLO	42.64	70.72	15	6.3	3.3
ONH	43.27	71.50	280	6.7	3.6
PNH	43.09	72.13	659	6.3	3.7
SBQ	45.37	71.92	256	6.5	3.8
WES	42.38	71.32	60	6.8	4.1
WFM	42.61	71.49	87	6.0	3.6
WNH	43.86	71.39	220	6.7	4.1

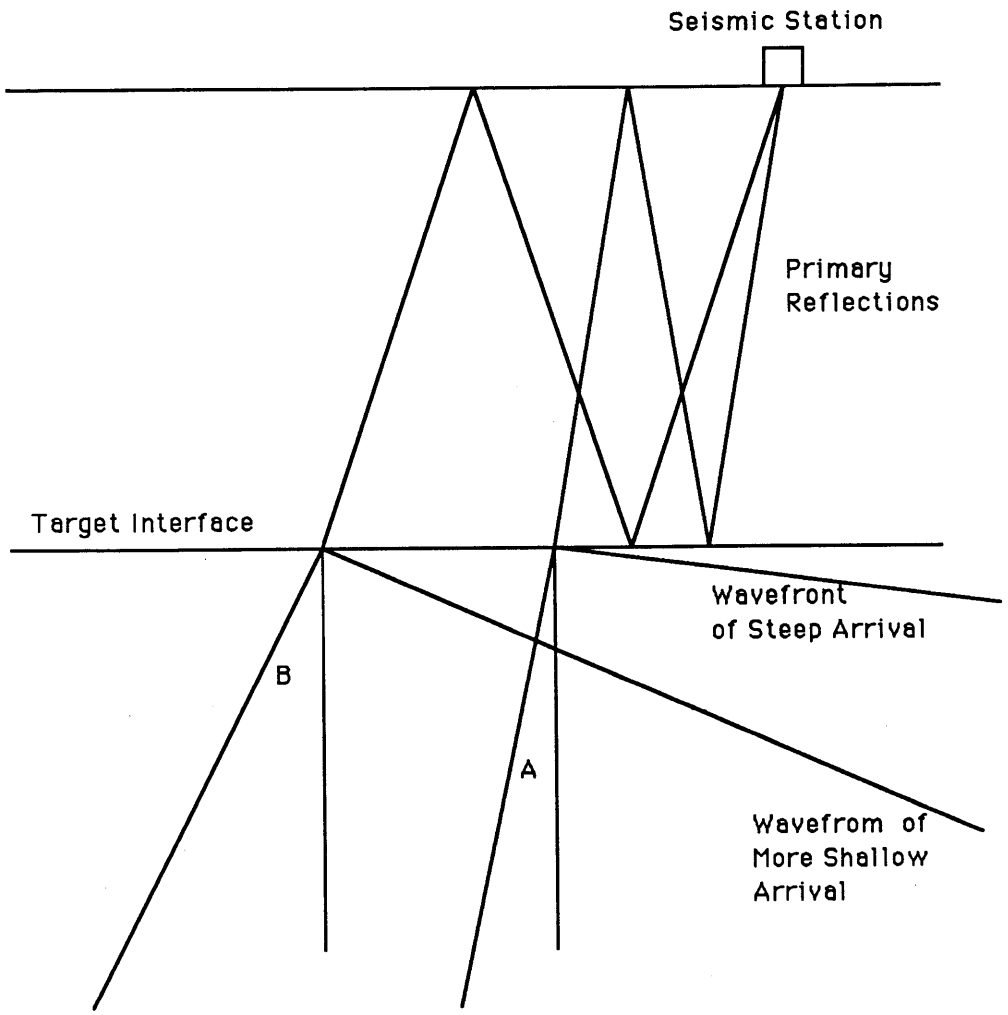

Figure 1: Schematic diagram of the ray-parameter trajectory stacking method. Incoming plane waves arrive with various incidence angles (A and B). The arrival times recorded at the surface of primary reflections from crustal velocity discontinuities are dependent on these angles. We use the differential travel times associated with these phases to determine the vertical two-way travel time to the velocity discontinuities.

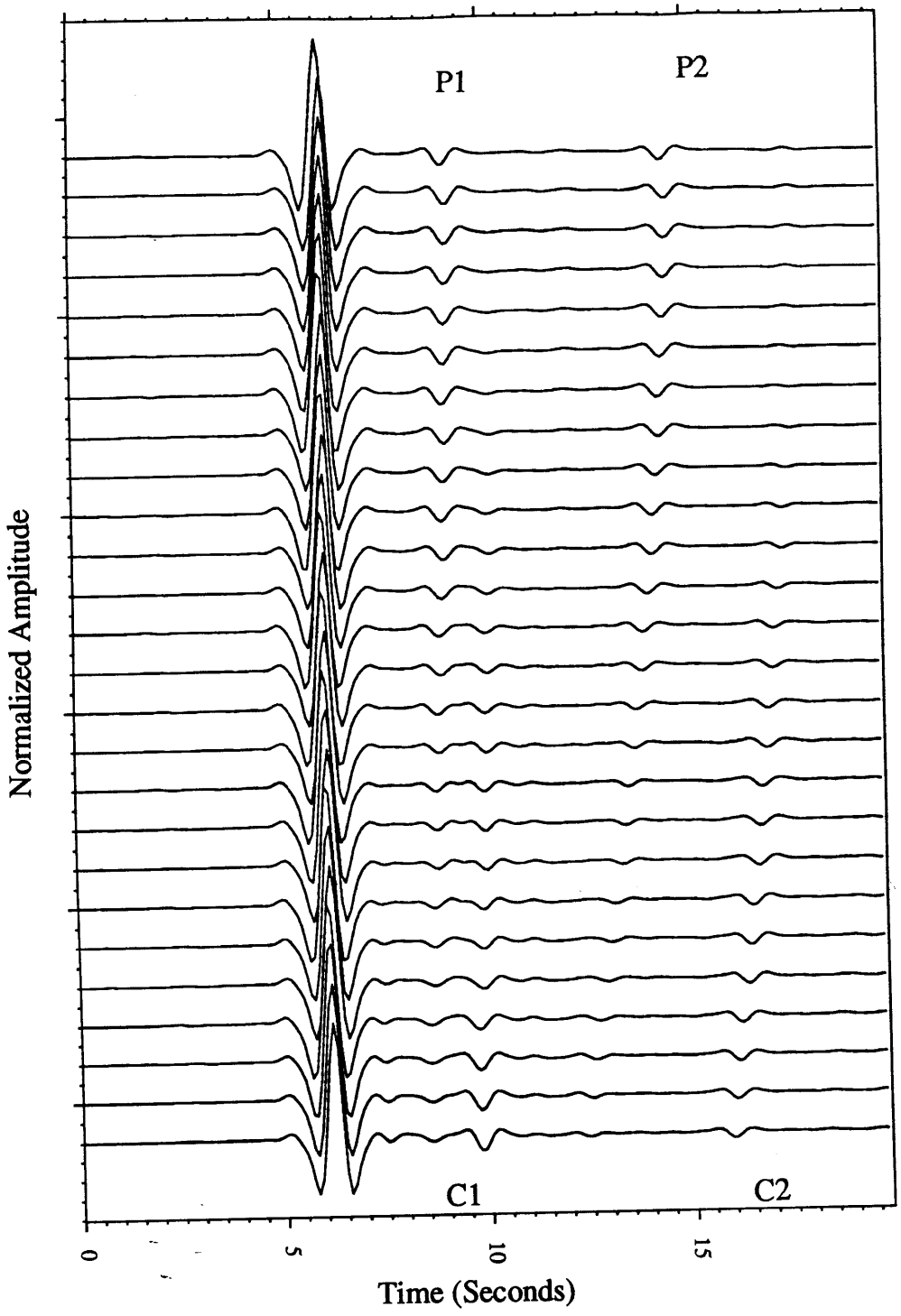

Figure 2: Synthetic data for a 2-layered crust (described in text), for 26 different plane waves. Incidence angles range from 0 degrees (top) to 50 degrees (bottom) in 2 degree steps. The moveout of the 2 primary P-phases (labeled **P1** and **P2**) and 2 converted primary converted-phases (labeled **C1** and **C2**) come from the 2 velocity discontinuities in the model.

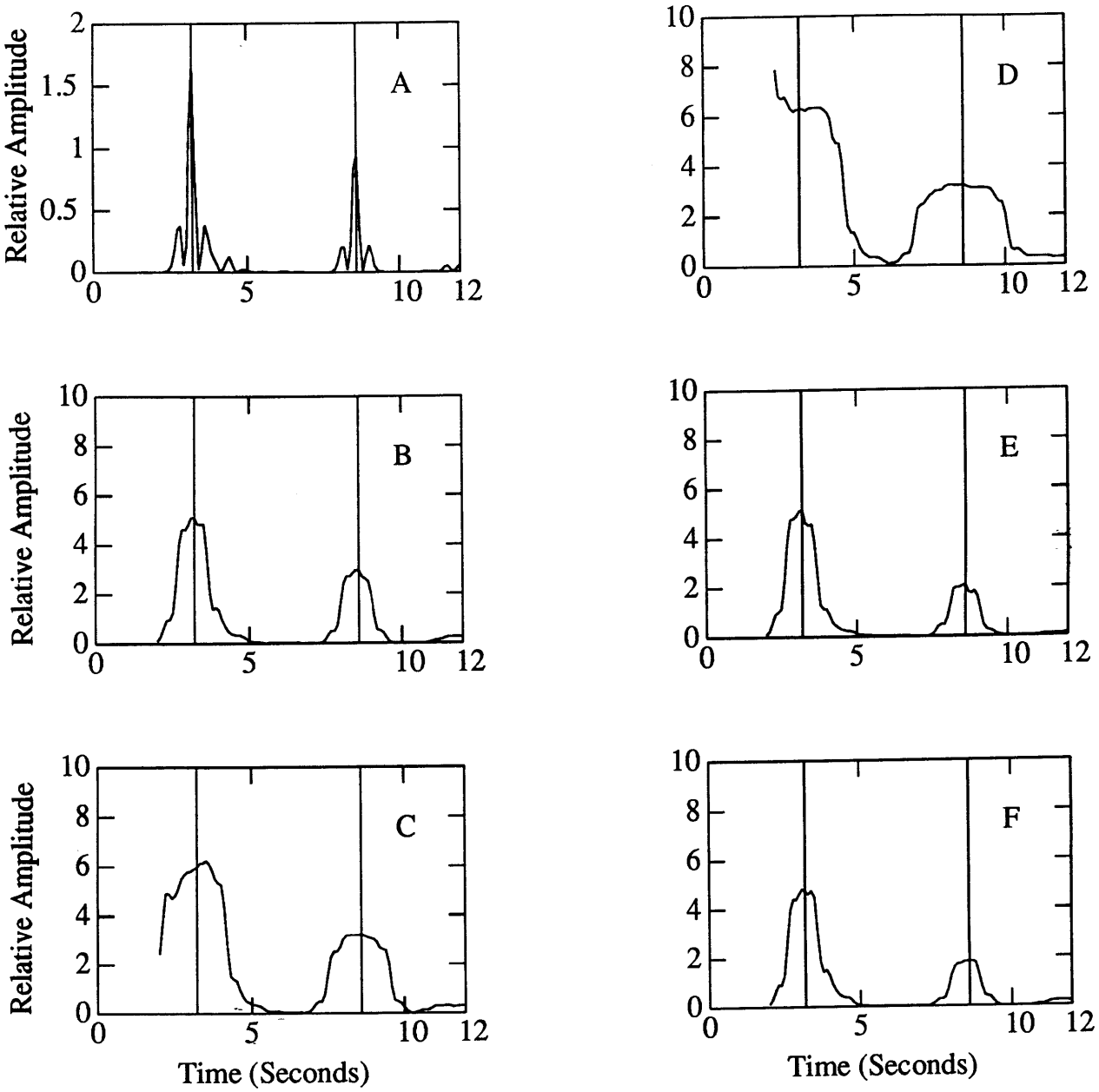

Figure 3: P-wave ray parameter trajectory *(rpt)* stack power plots for the 2-layer model test. Vertical lines are the actual primary arrival times for the 2 layers in the model. Various window widths are tested (A. 0.1 seconds, B. 1.0 sec, C. 2.0 and D. 3.0 sec) as well as perturbations from the actual layer velocity (E. 10% increase and F. 10% decrease).

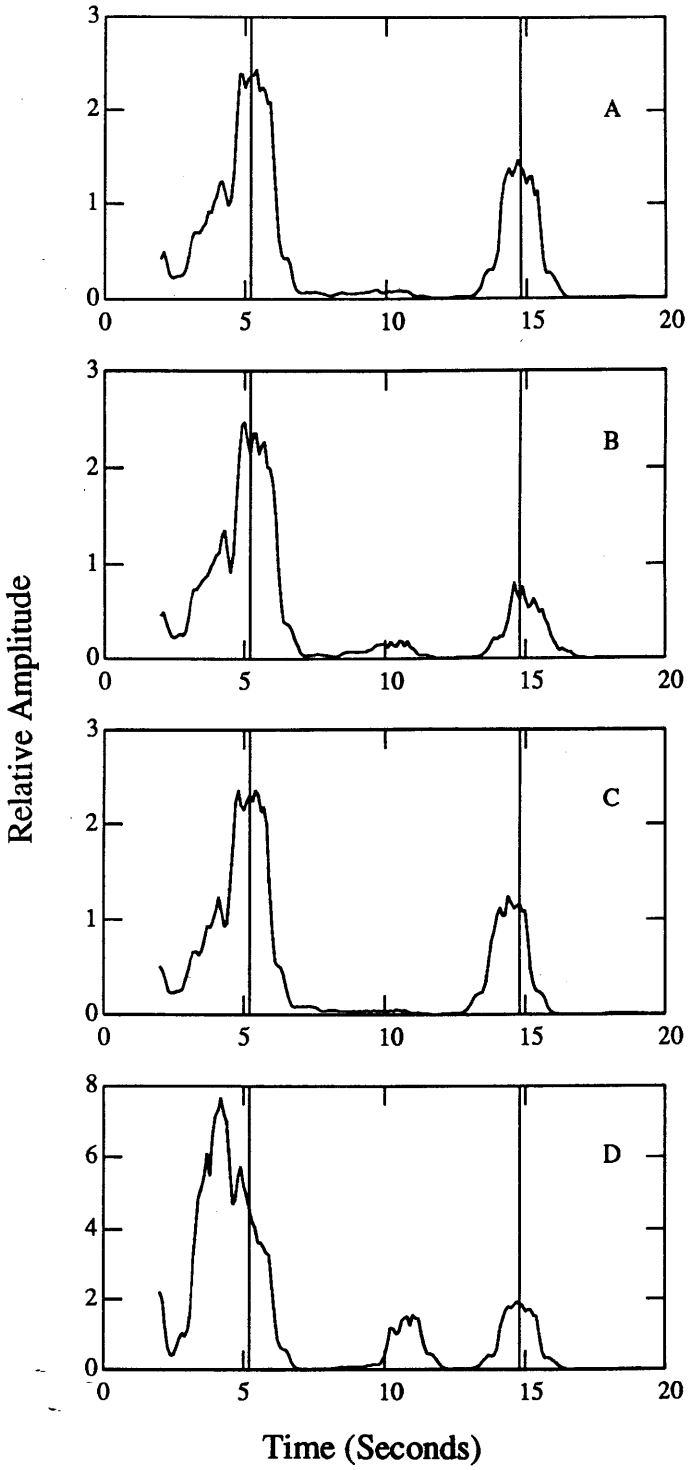

Figure 4: Tests of the *(rpt)* stacking method with converted-arrivals. Power plots for the 2-layer test model: A) prediction velocity equal to true velocity, B) 10% greater than true velocity and C) 10% less than true velocity. Frame D show the case when all incidence angles (0-50 degrees) are included. Vertical lines lines indicate the actual primary reflection arrival times.

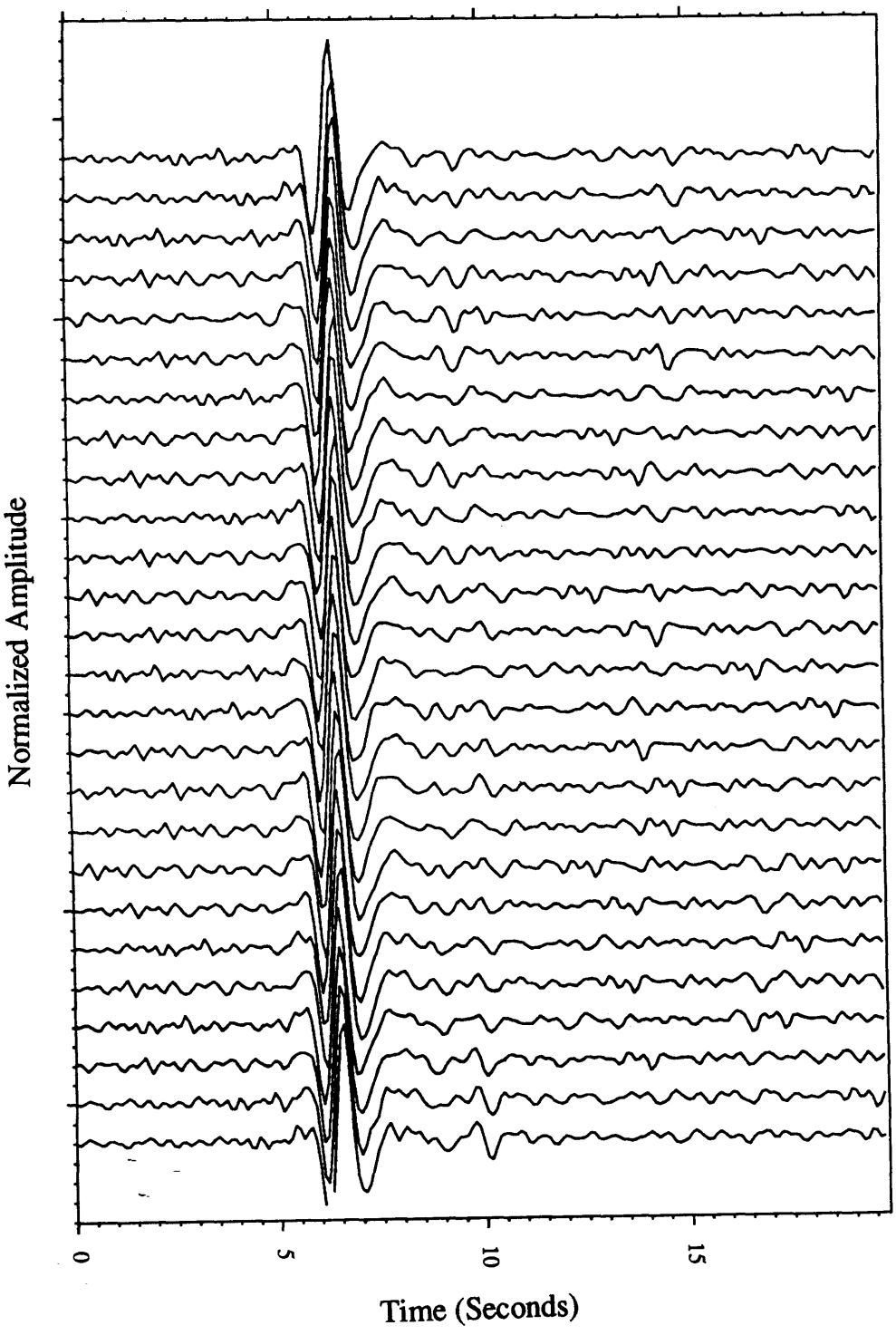

Figure 5: Synthetic data as in the previous example with 10% noise added.

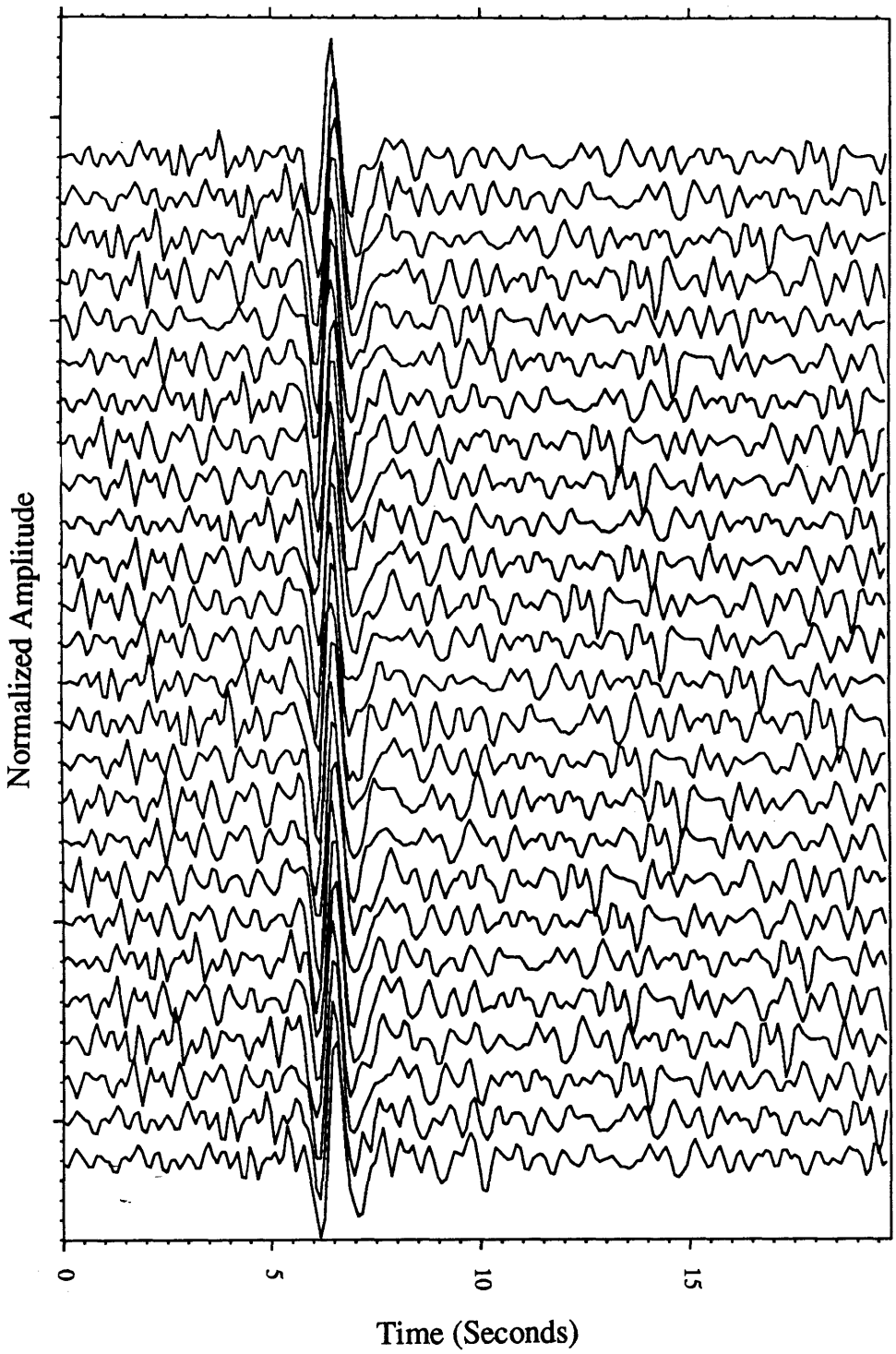

Figure 6: Synthetic data as in the previous example with 30% noise added.

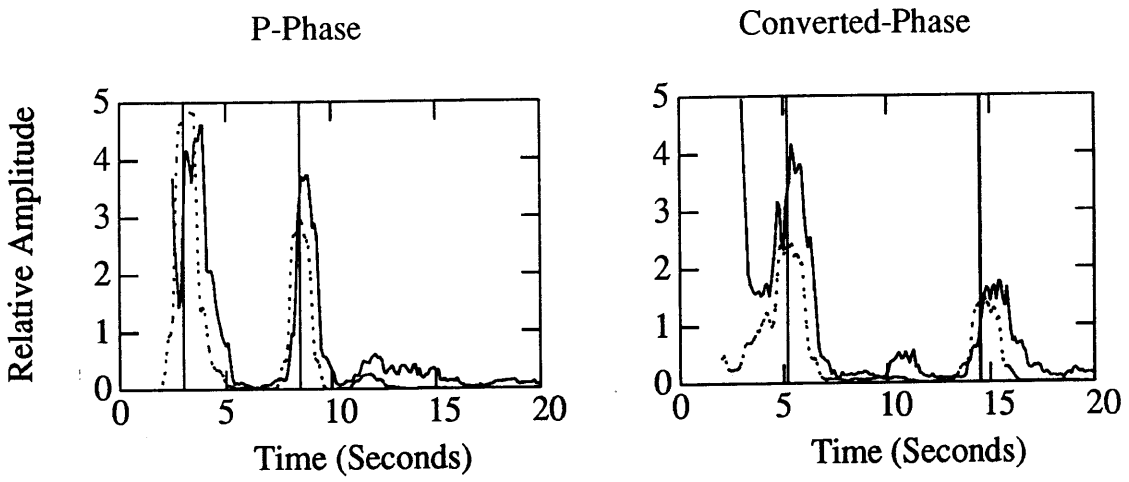

Figure 7: Test result for the 10% noise case: Figure 7a (left) is the P-wave case and 7 (right) is the converted-phase case. For reference, the noise-free examples are also plotted on these figures (dashed).

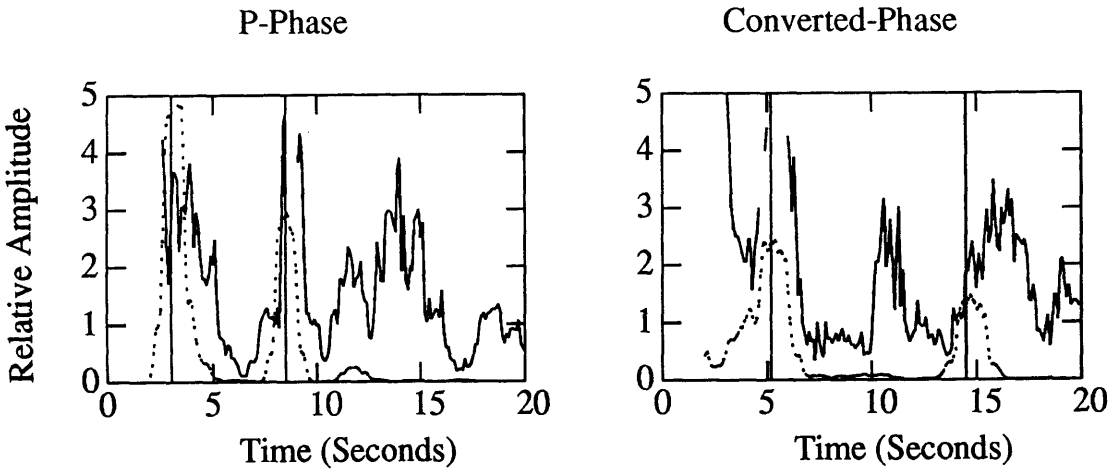

Figure 8: Test result for the 30% noise case. Figure 8a (left) is the P-wave case and 8b (right) is the converted-phase case. For reference, the noise-free examples are also plotted on these figures.

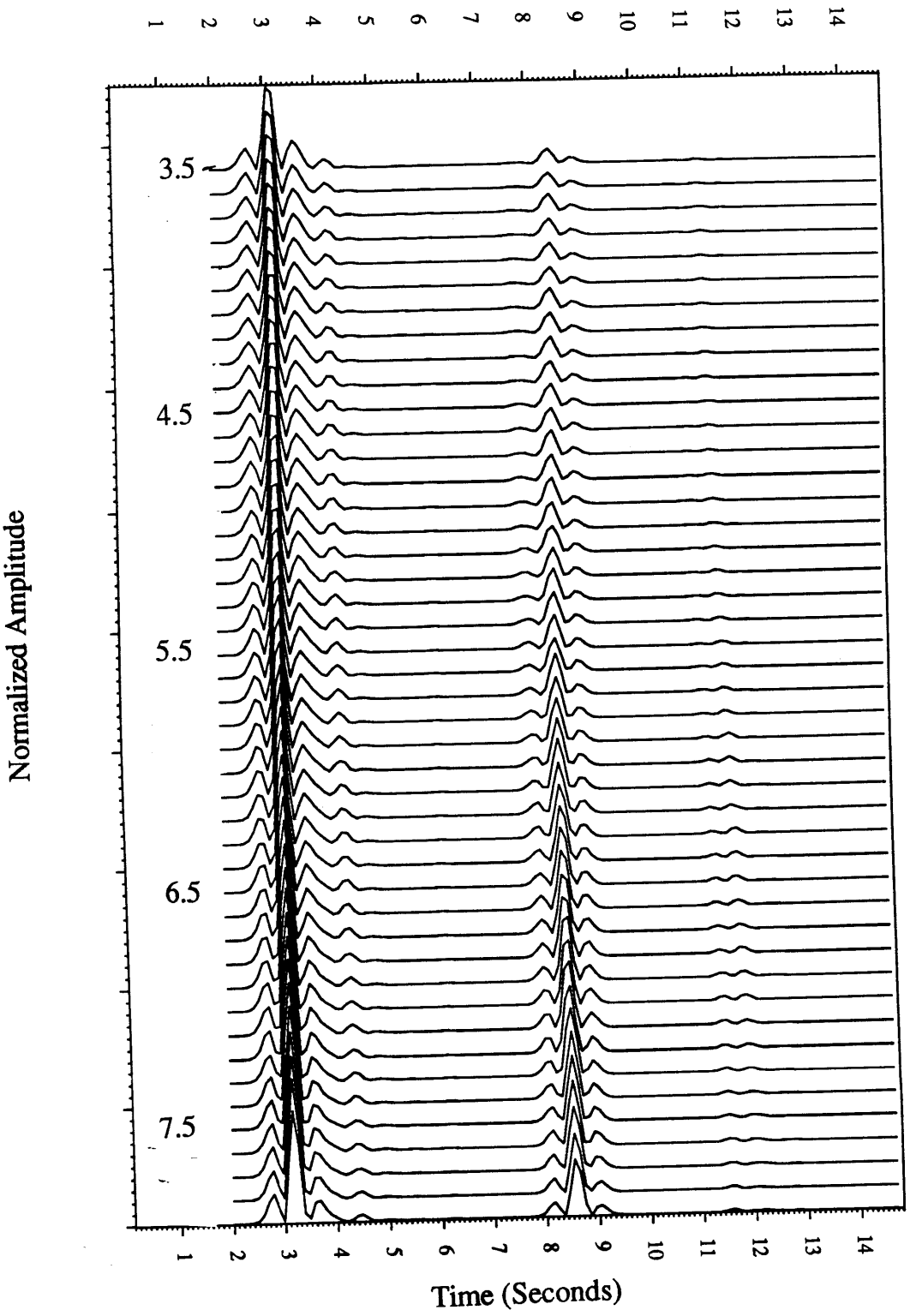

Figure 9: Primary P-wave power plots for prediction velocities of 4.5 to 7.9 $\frac{km}{sec}$ (in steps of 0.1 $\frac{km}{sec}$).

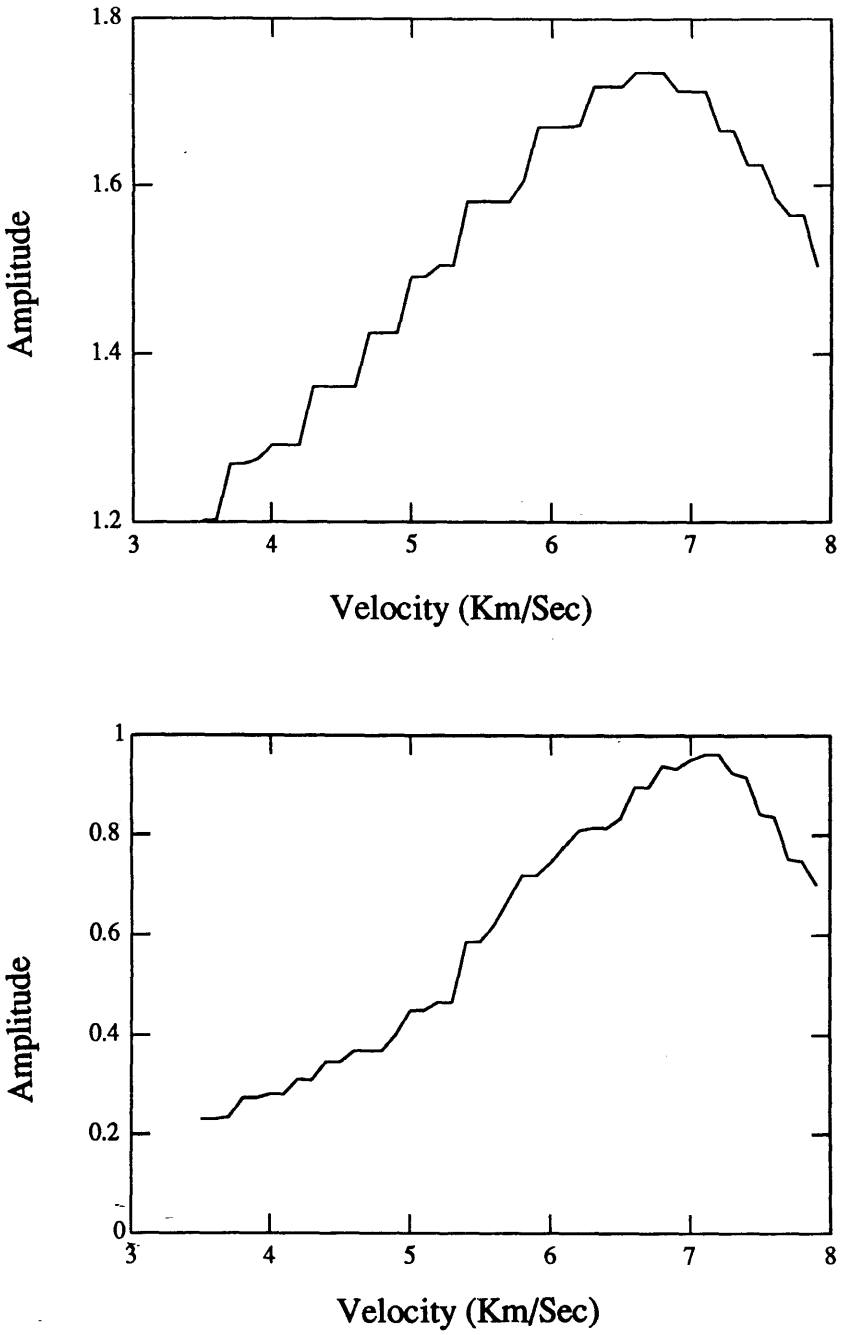

Figure 10: Variation in peak stack power for the 45 tested P-wave velocities for the mid-crust reflections (top) and Moho reflection(bottom).

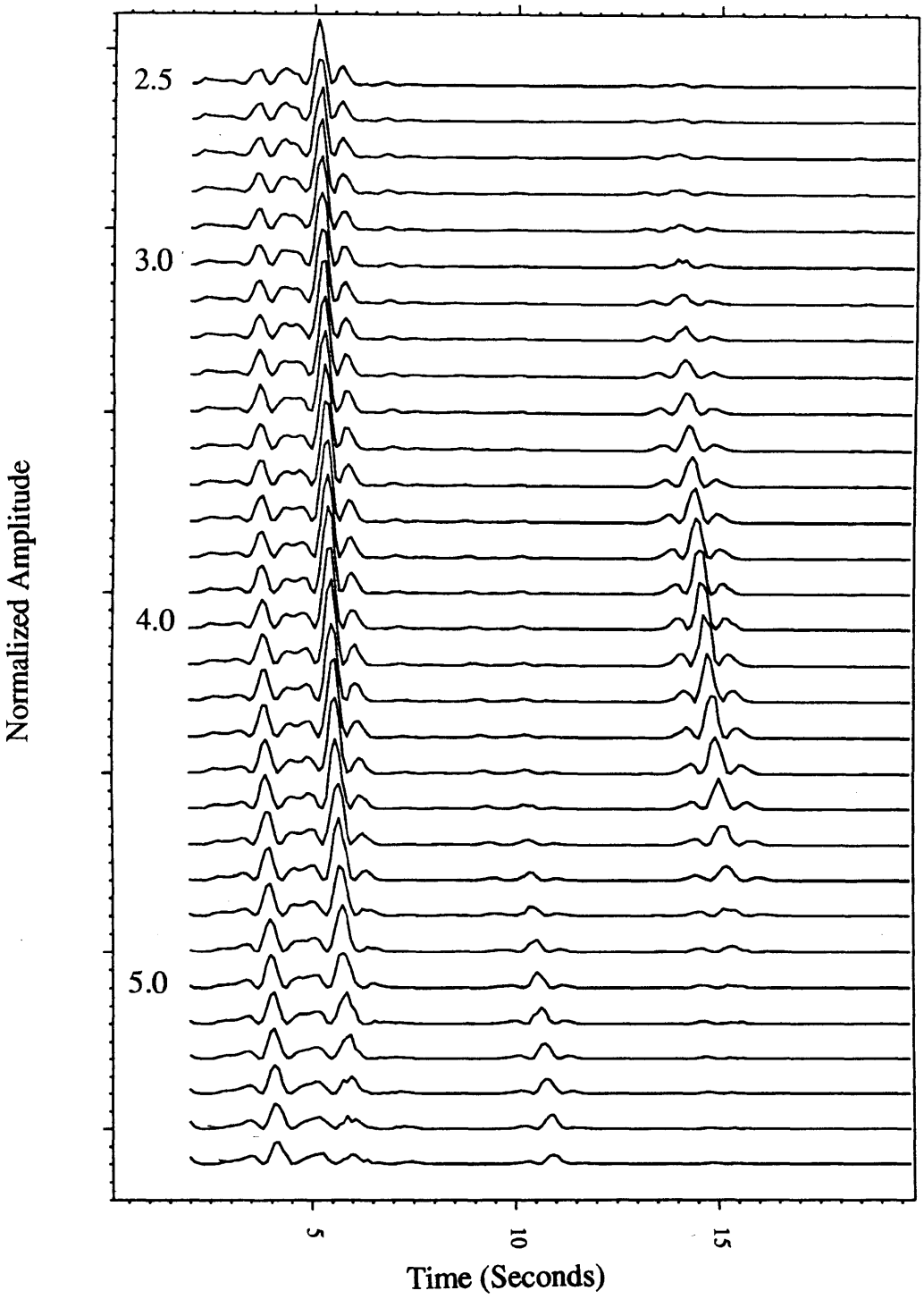

Figure 11: Converted-arrival power plots for prediction velocities of 2.5 $\frac{km}{sec}$ to 5.5 $\frac{km}{sec}$ (in steps of 0.1 $\frac{km}{sec}$).

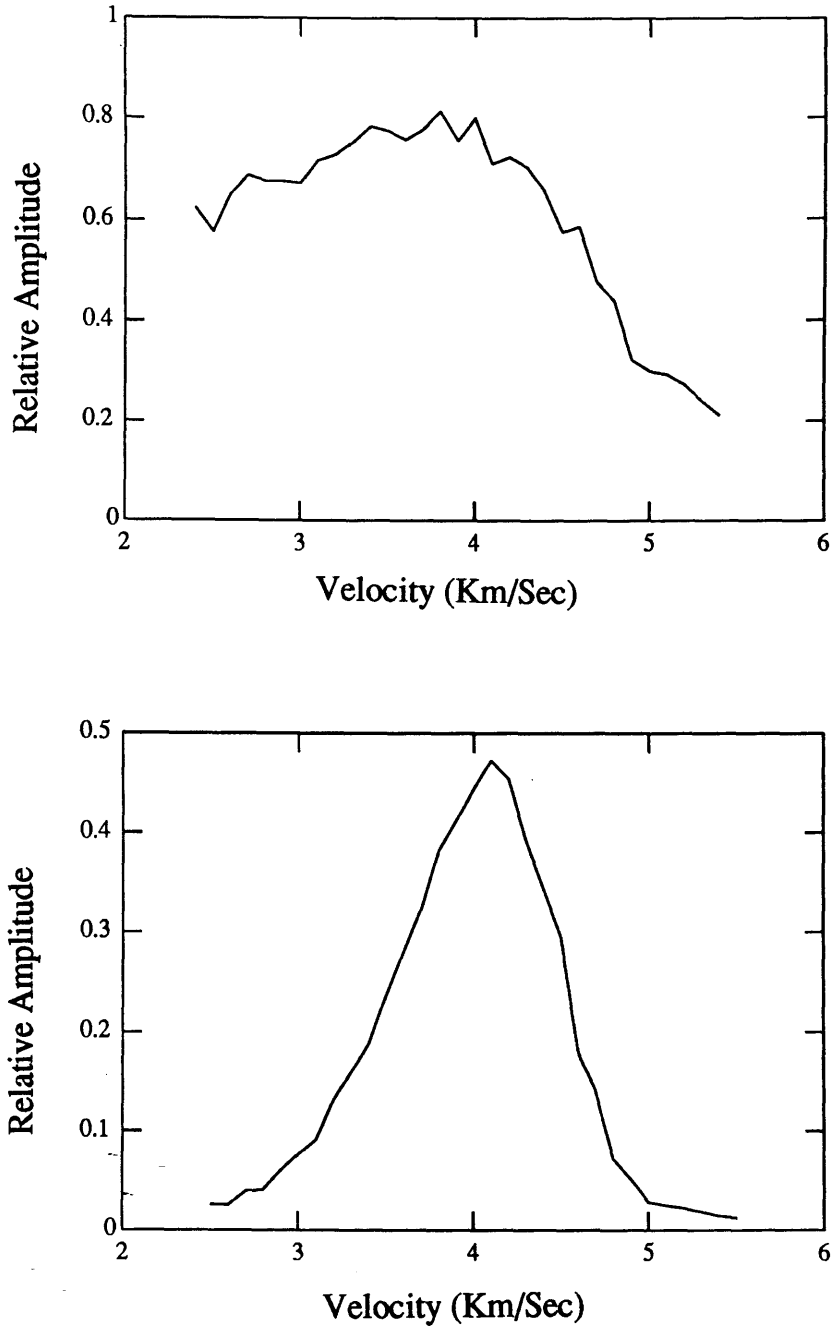

Figure 12: Variation in peak stack power for the 45 tested converted-arrival velocities for the mid-crust reflections (top) and Moho reflection(bottom).

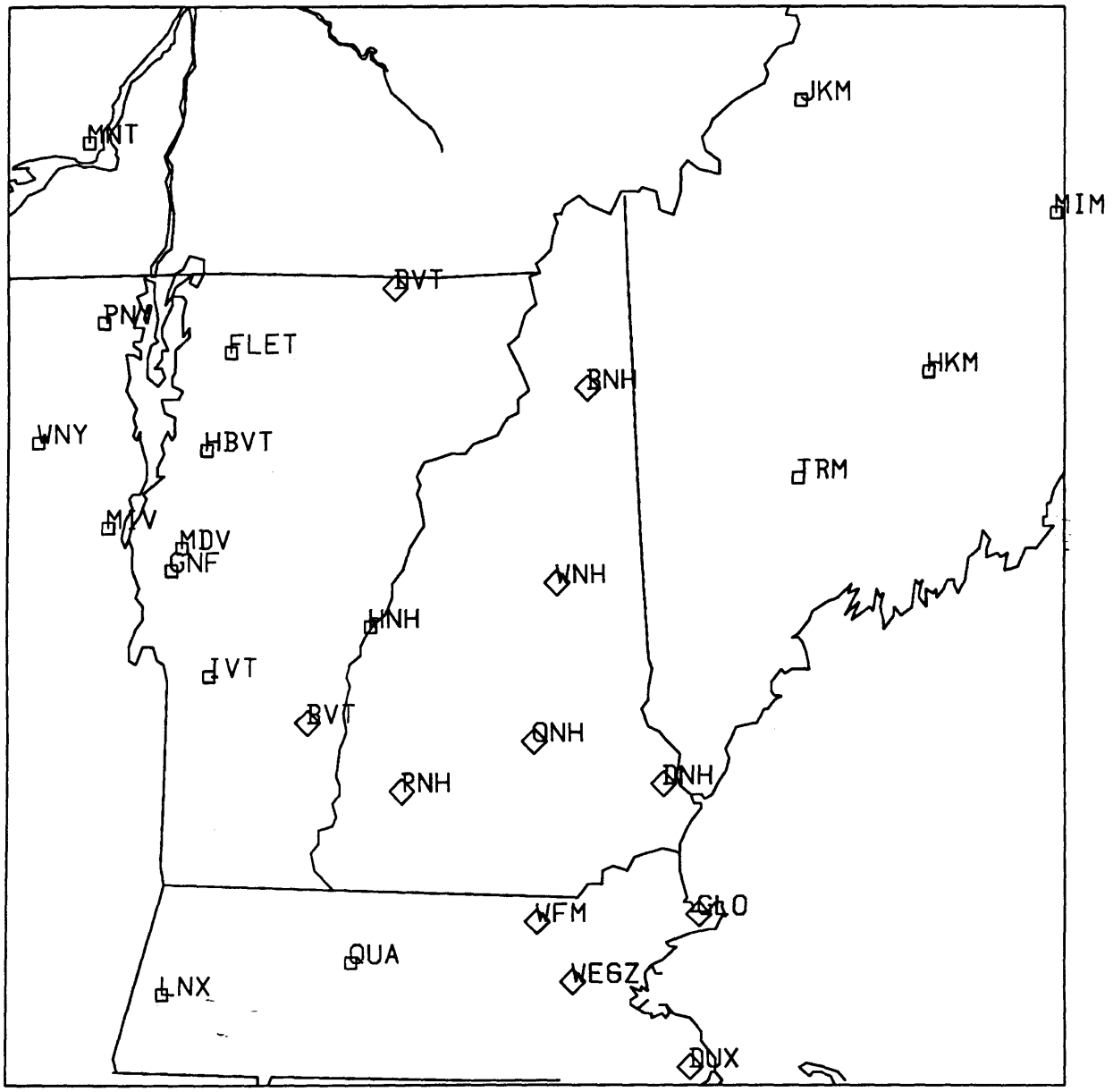

Figure 13: Map showing the distribution of the stations used in the forward modeling. The 12 stations used are represented with diamonds.

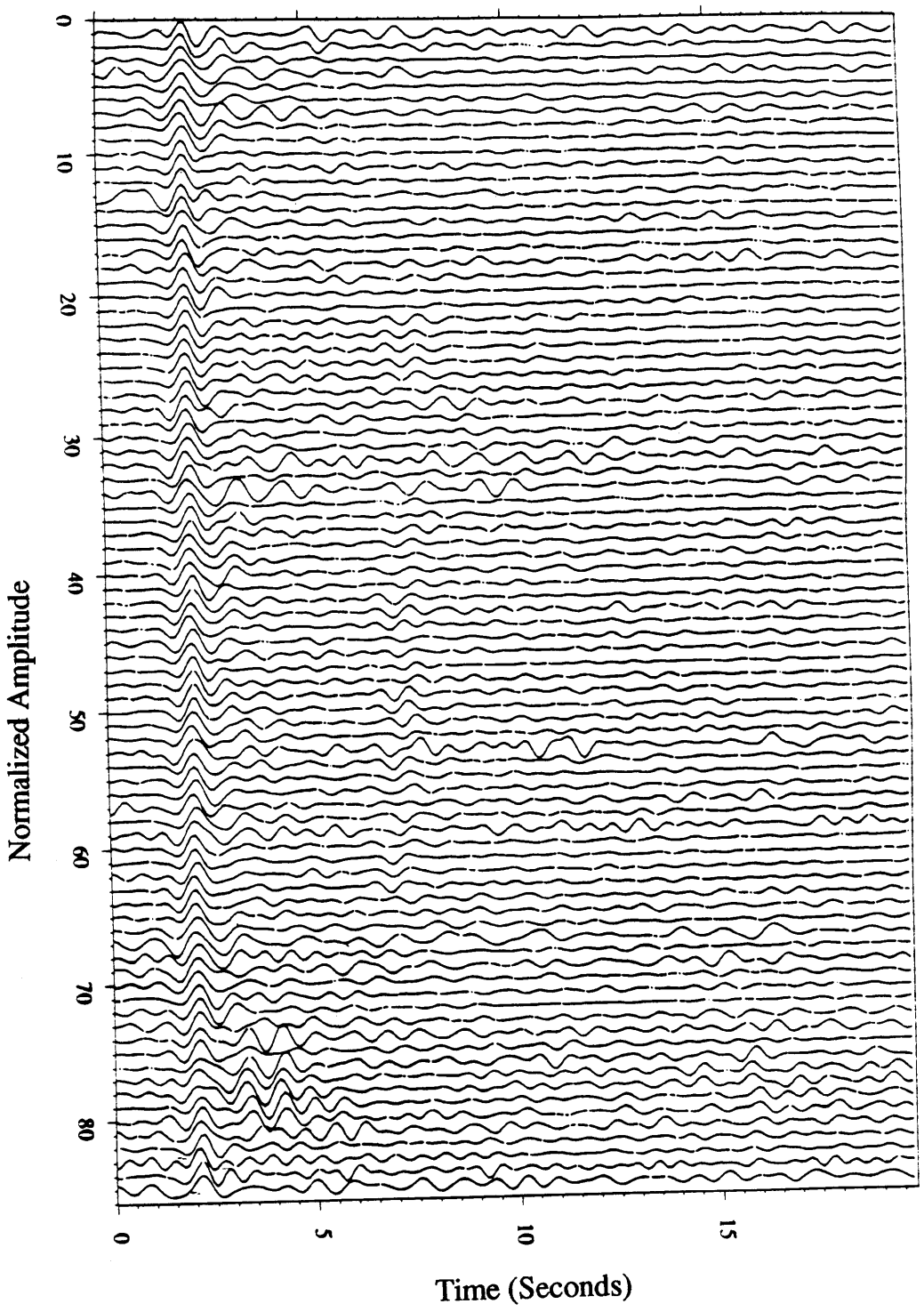

Figure 14: Event distribution for the 12 NEUSSN stations used in the *rpt* analysis.

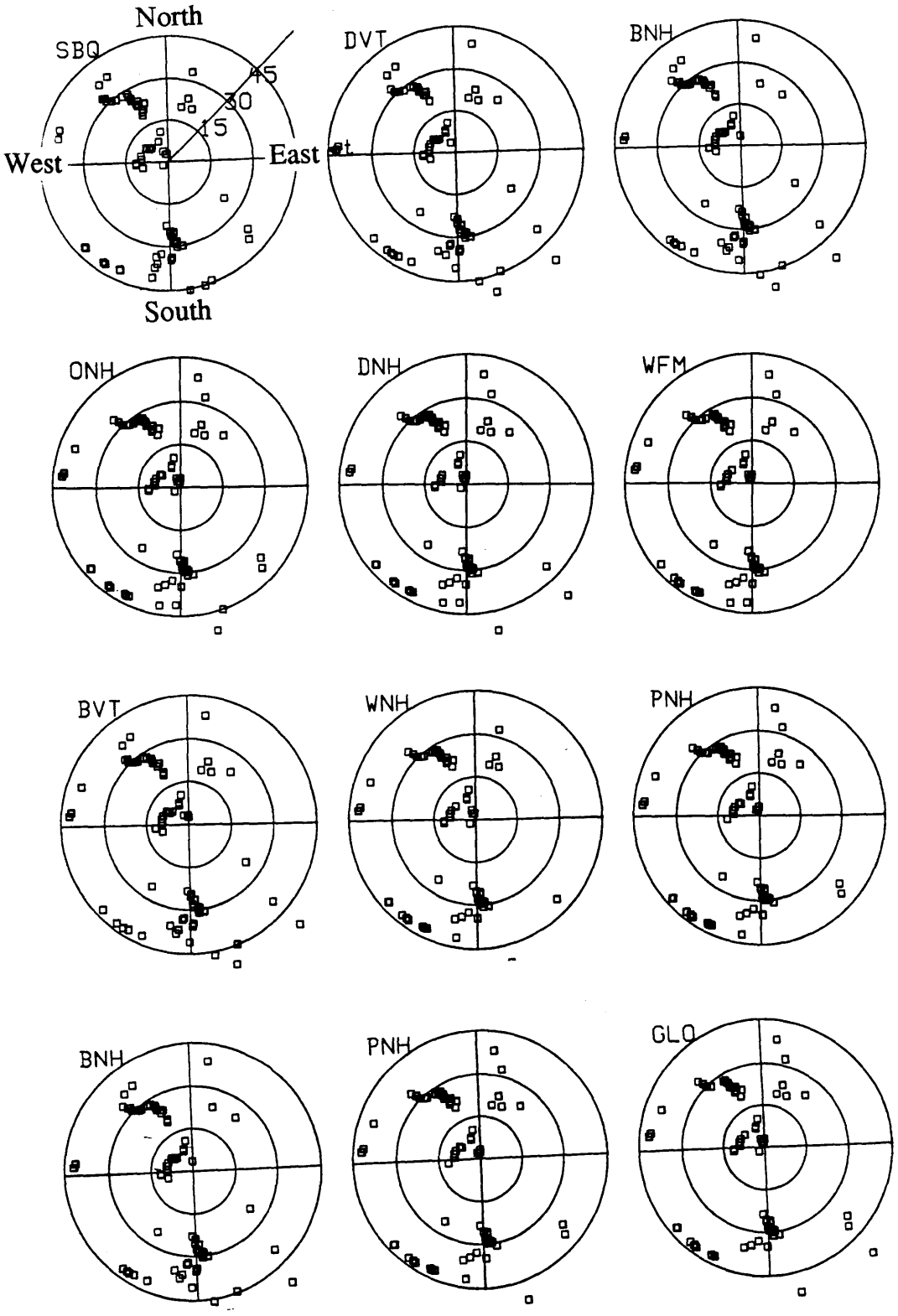

Figure 15: All 85 seismograms available for station BVT. These traces have had their natural source pulses transformed into a common zero phase wavelet. Seismograms are plotted from steepest incidence angle (top, 1.5 degrees) to shallowest (bottom, 51 degrees).

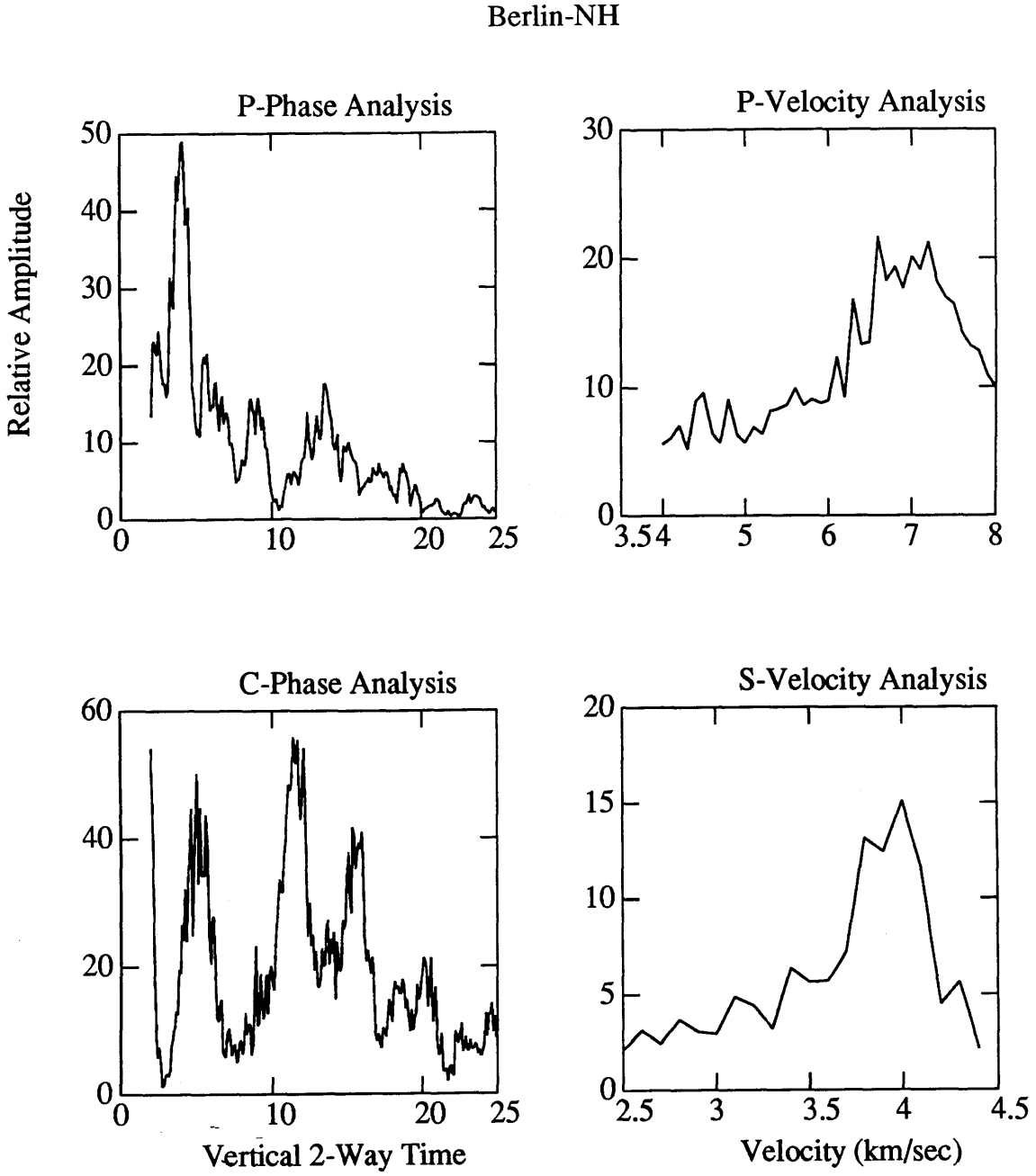

Figure 16: *Rpt* analysis for station BNH. For this and all other stations in the New England analysis we plot the P-wave travel time analysis (top left), the P-velocity analysis (top right), the converted-wave travel analysis (bottom left) and the converted-wave velocity analysis (bottom right).

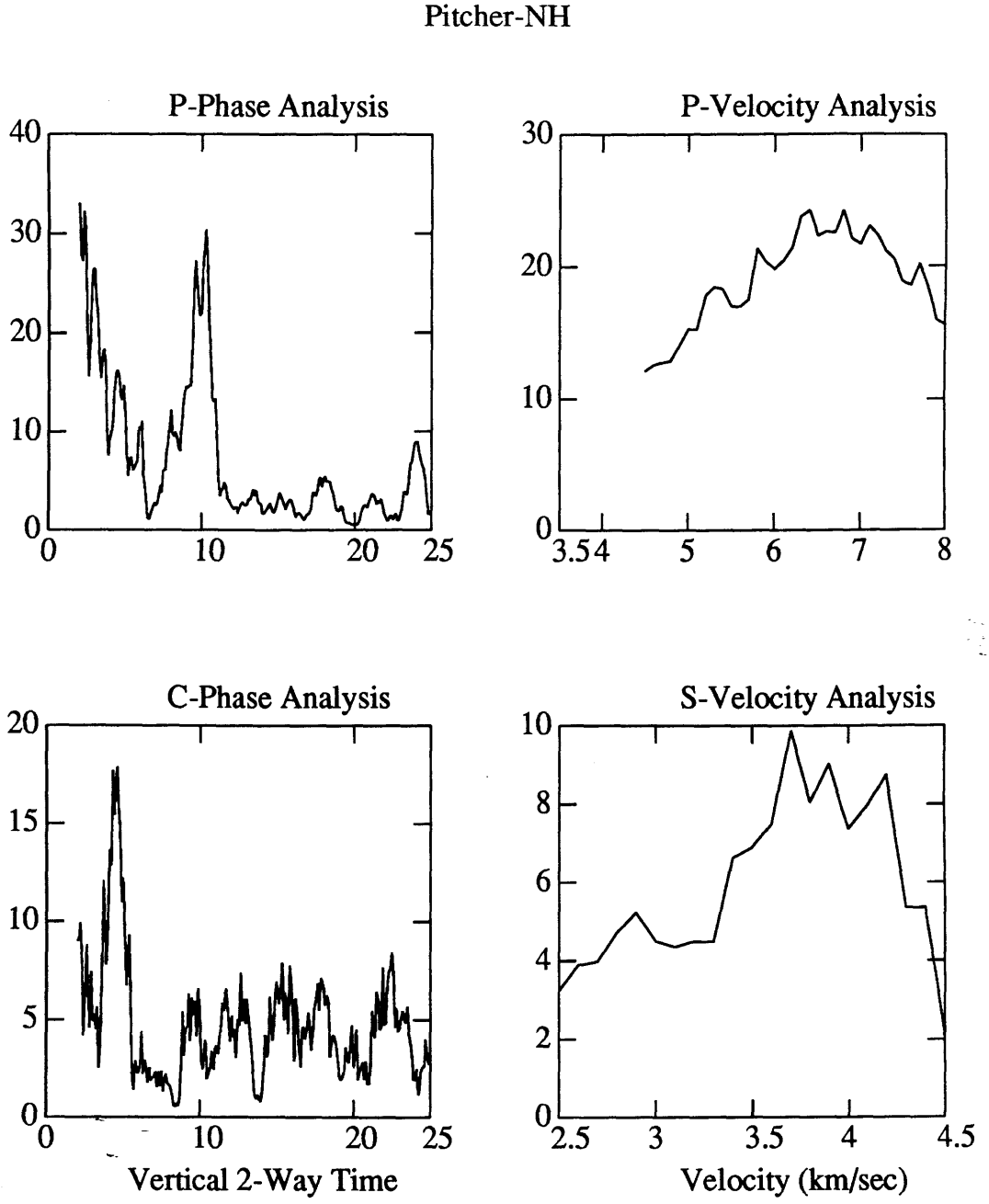

Figure 17: *Rpt* analysis for station PNH.

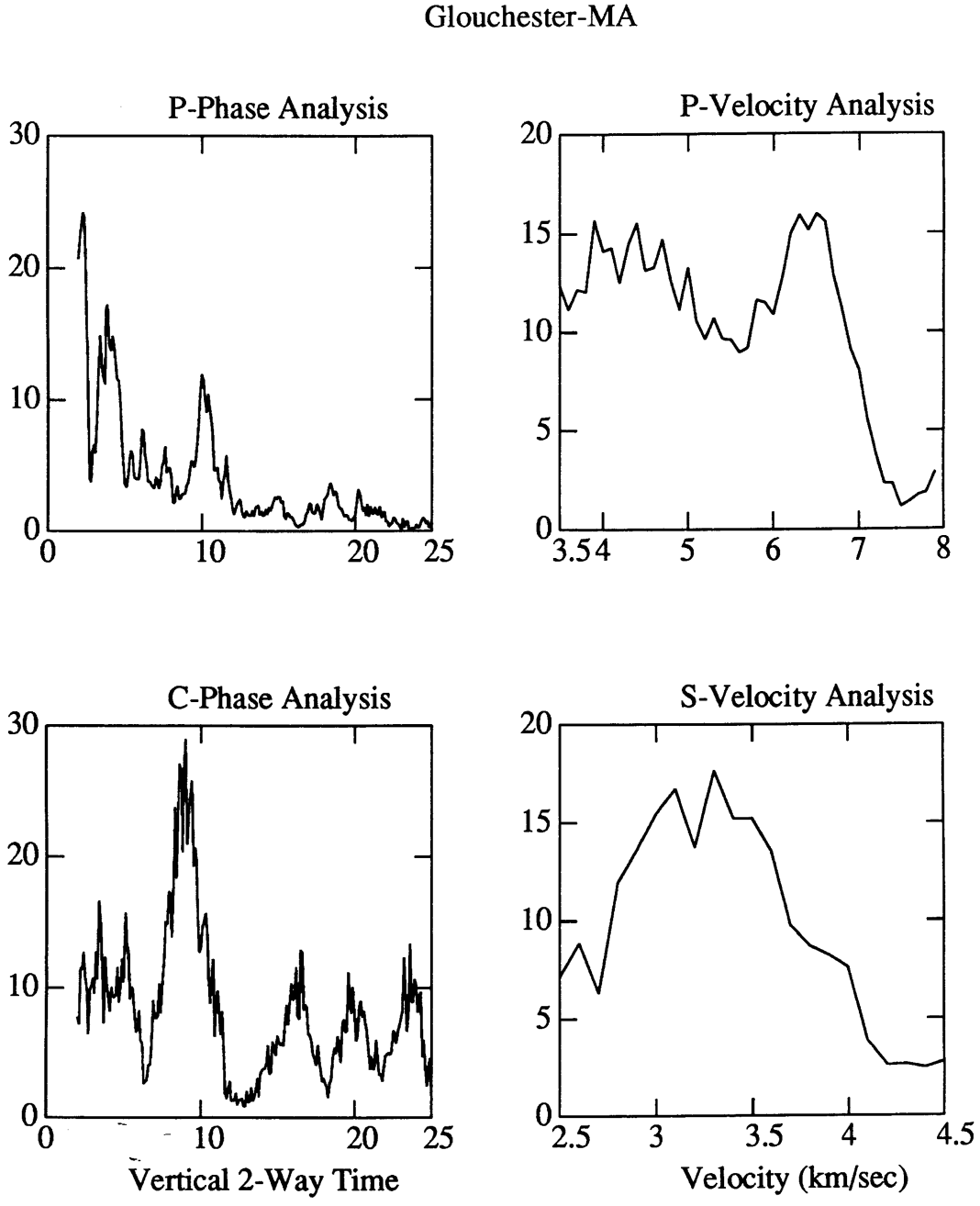

Figure 18: *Rpt* analysis for station GLO.

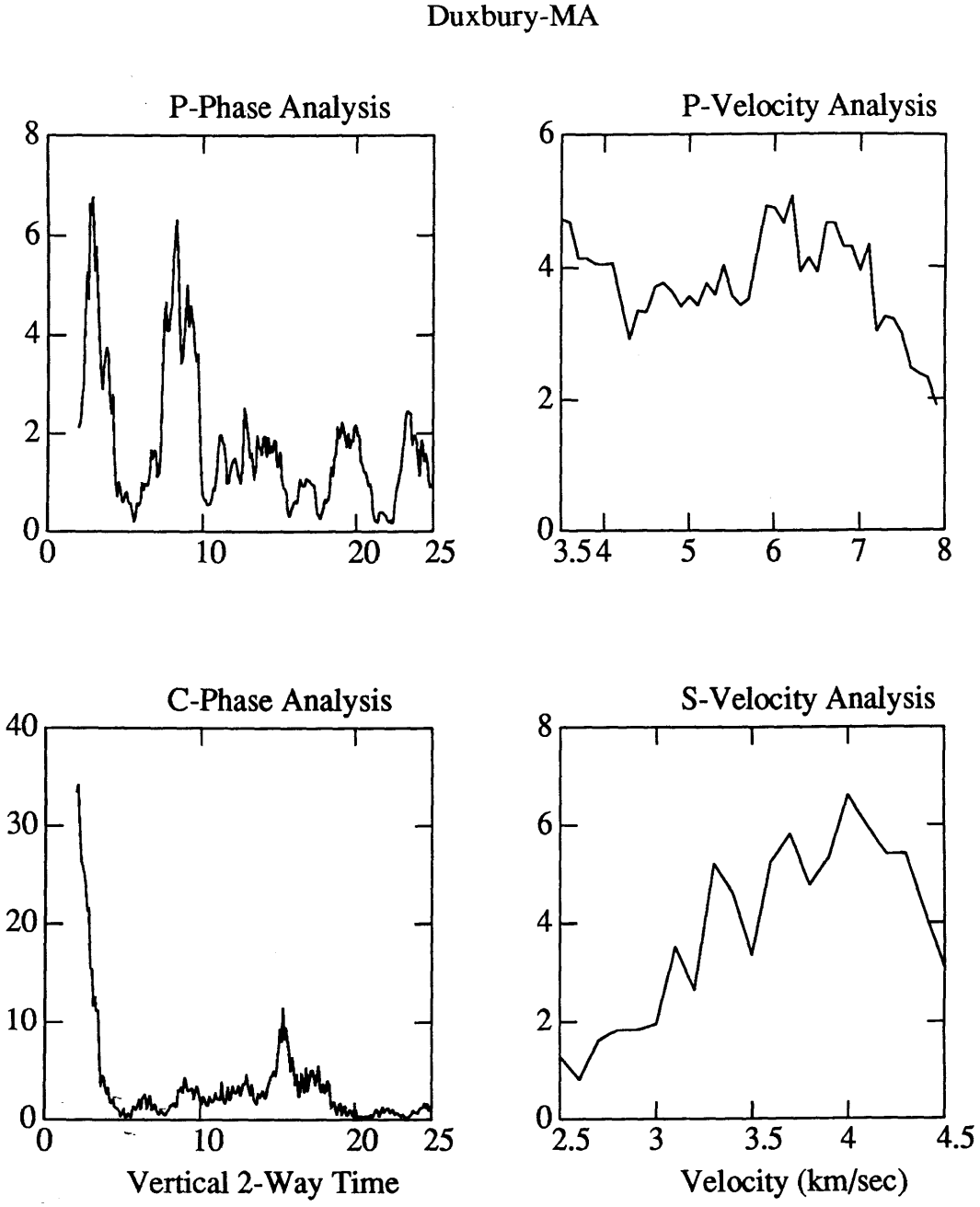

Figure 19: *Rpt* analysis for station DUX.

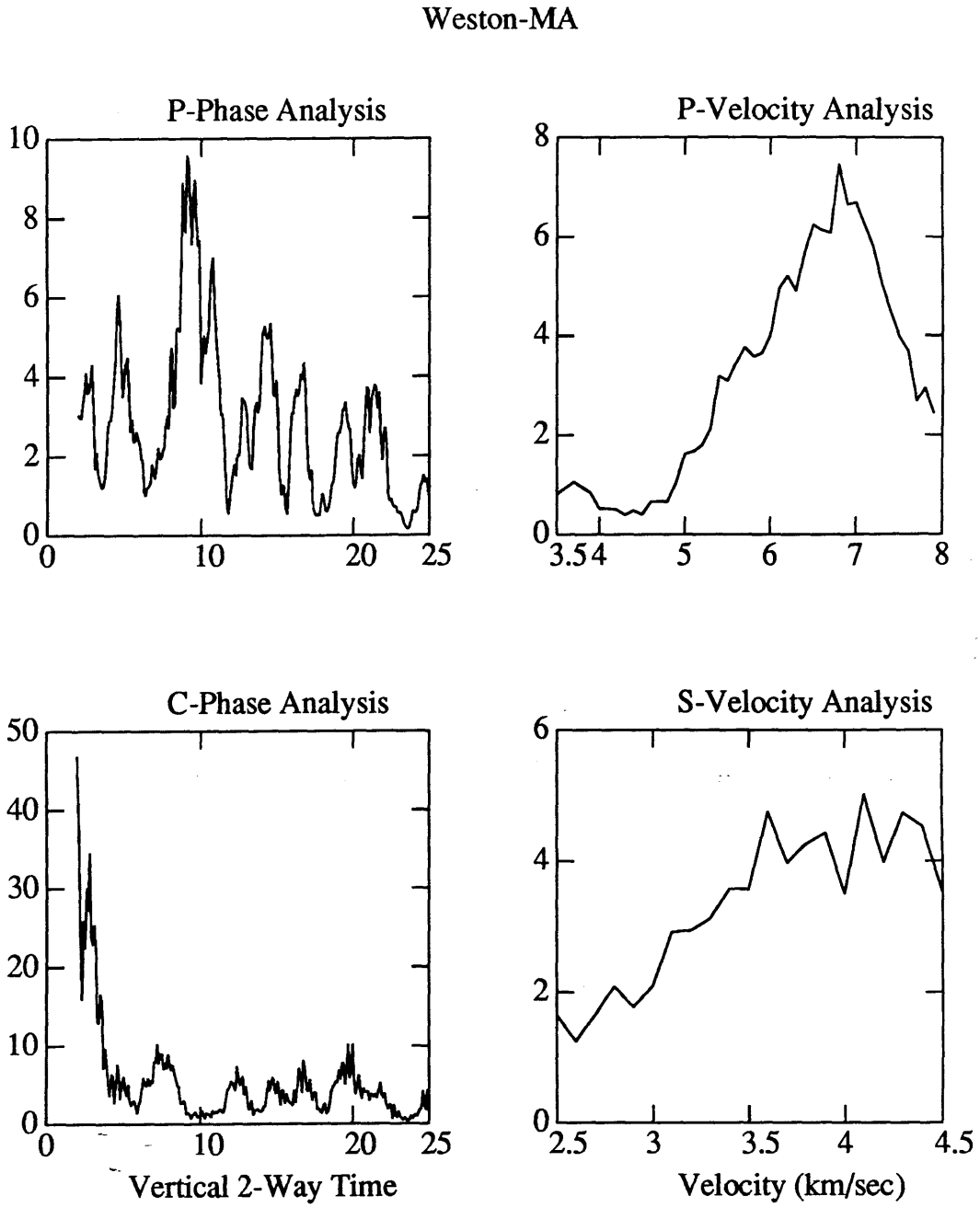

Figure 20: *Rpt* analysis for station WES.

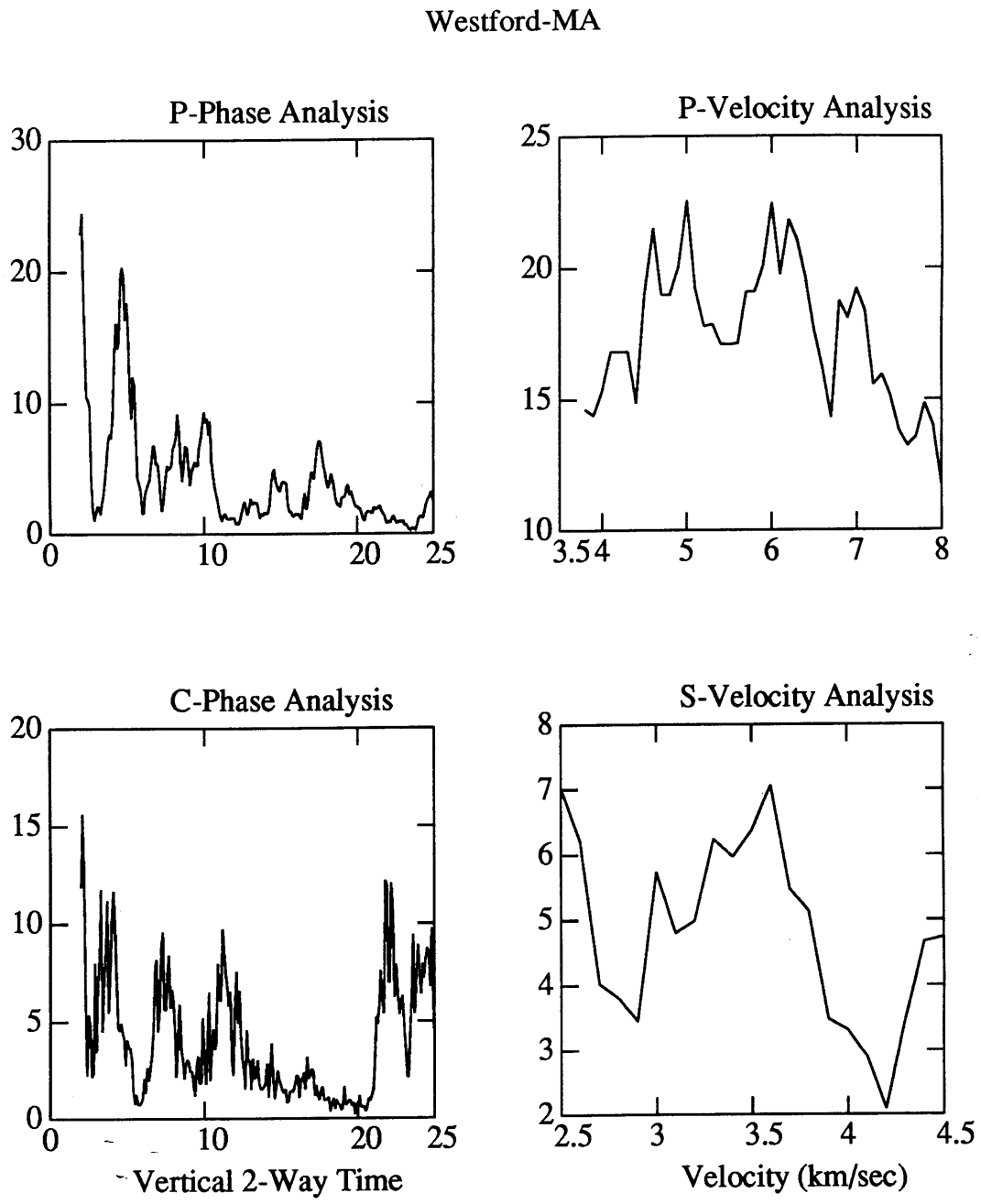

Figure 21: *Rpt* analysis for station WFM.

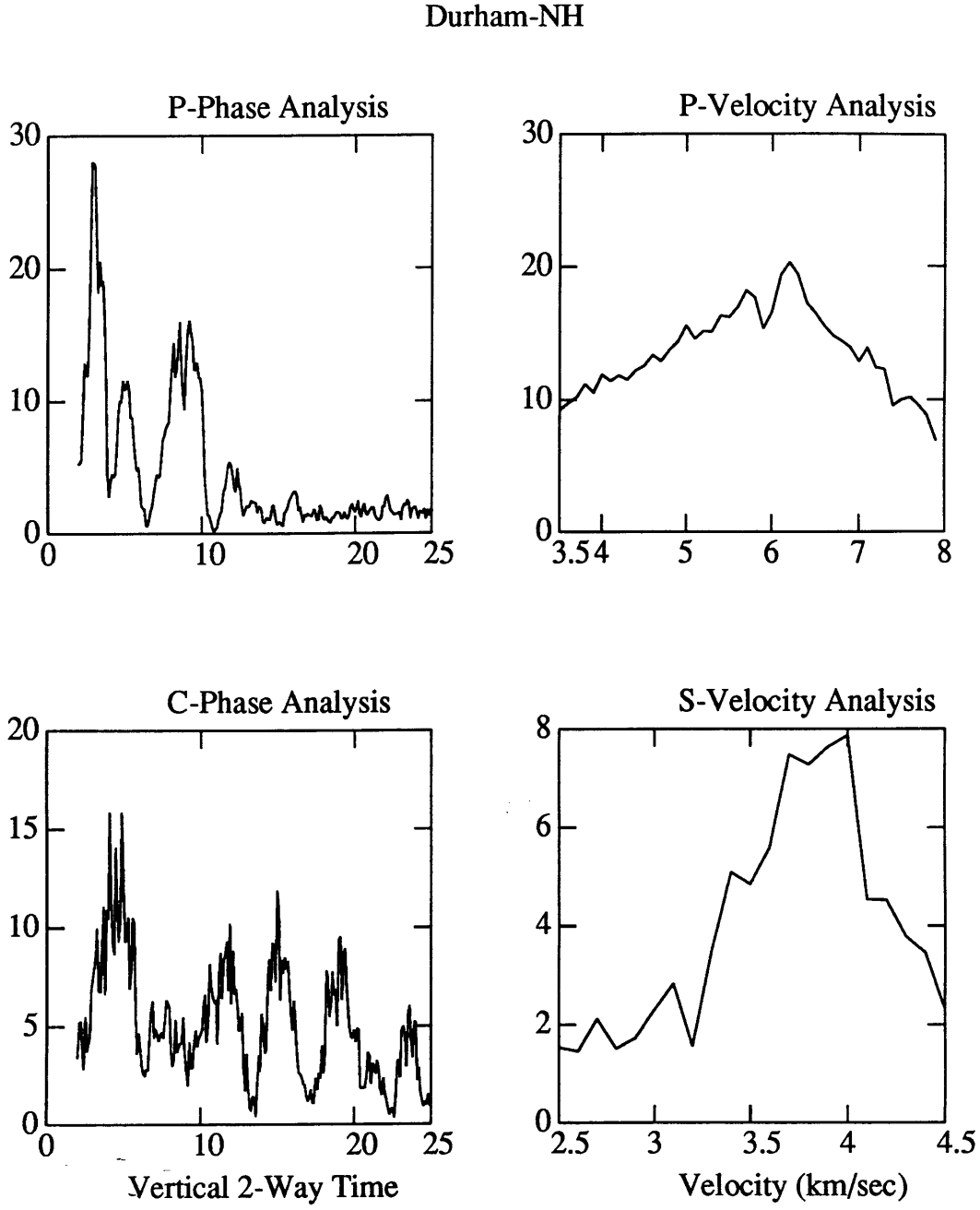

Figure 22: *Rpt* analysis for station DNH.

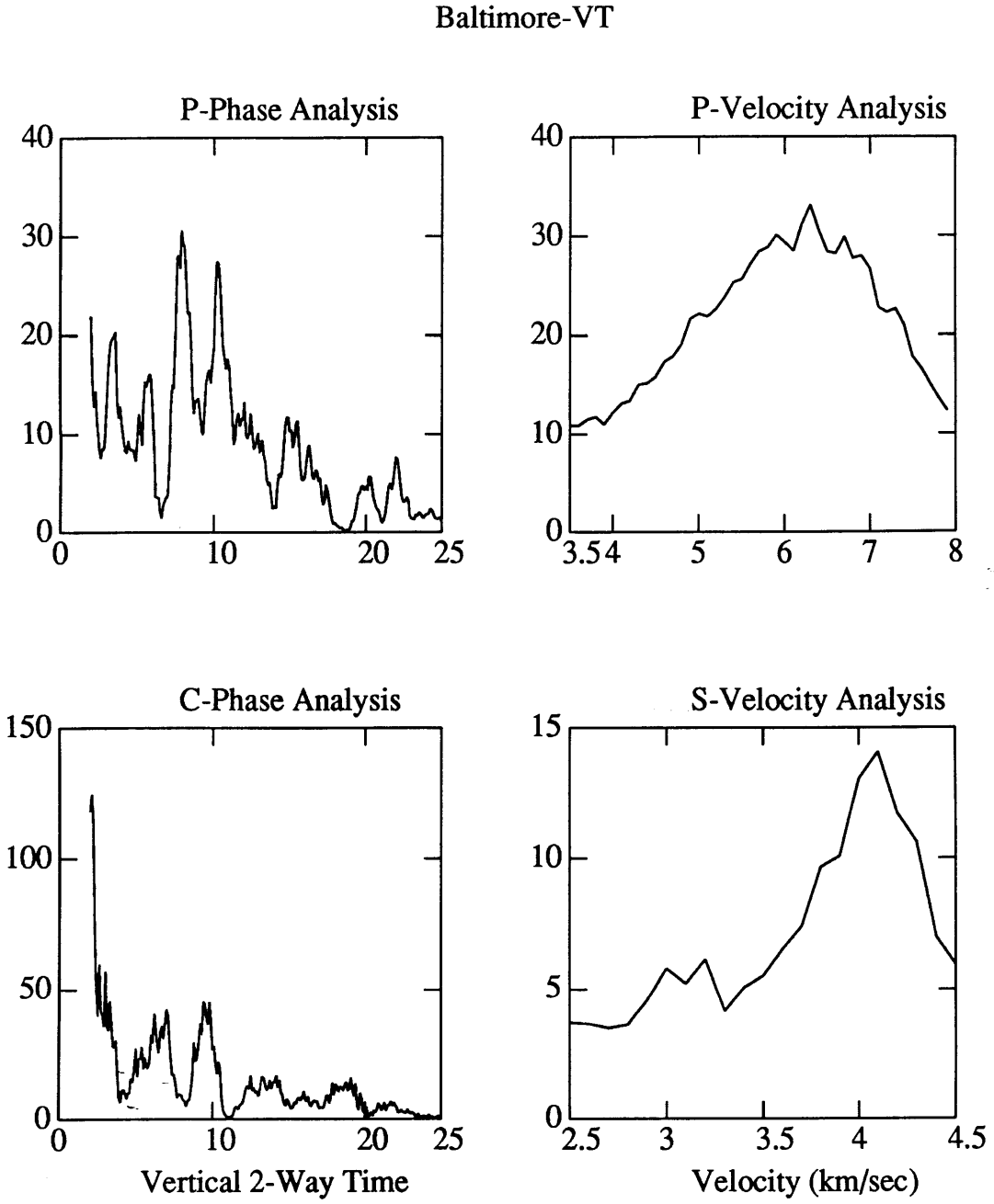

Figure 23: *Rpt* analysis for station BVT.

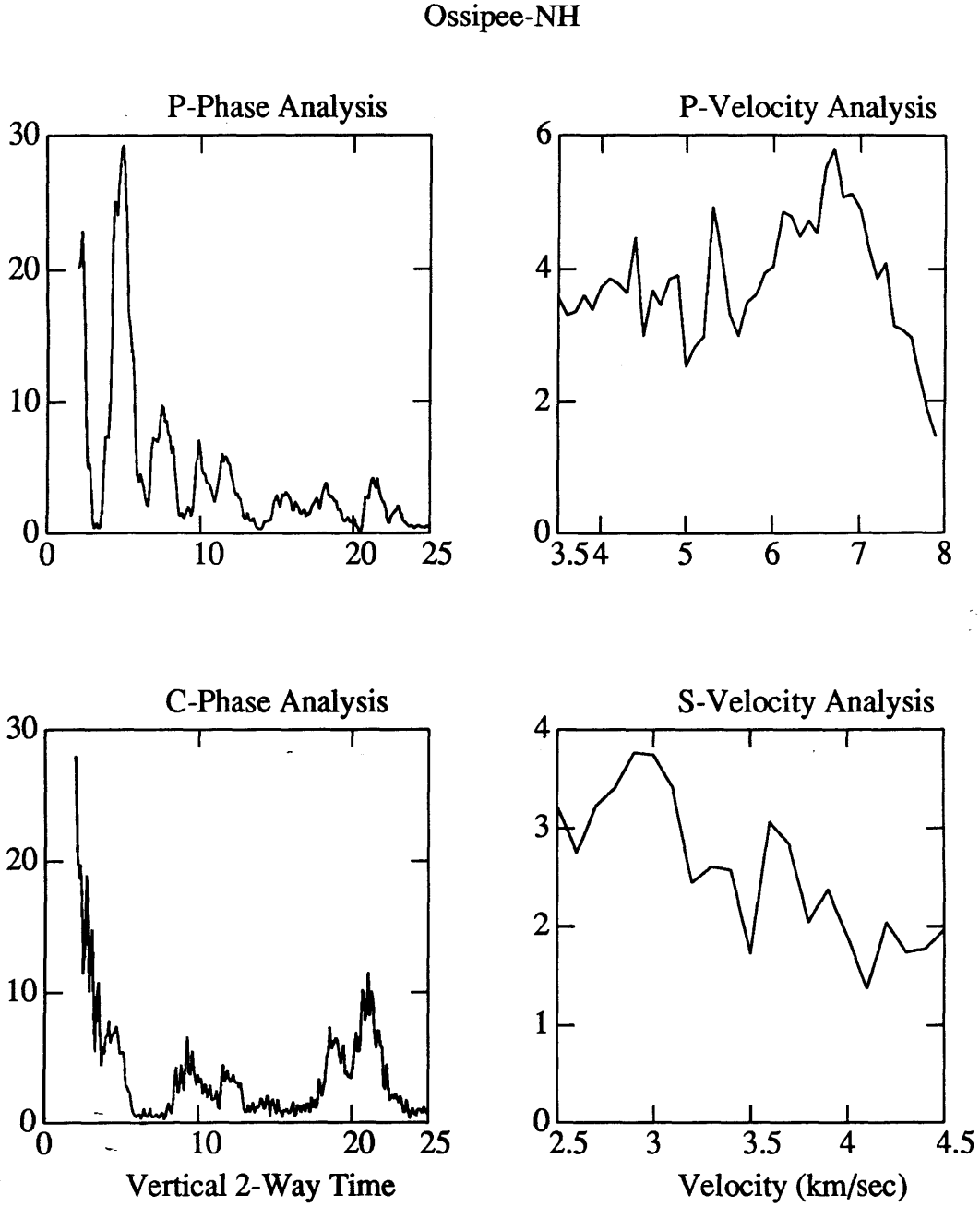

Figure 24: *Rpt* analysis for station ONH.

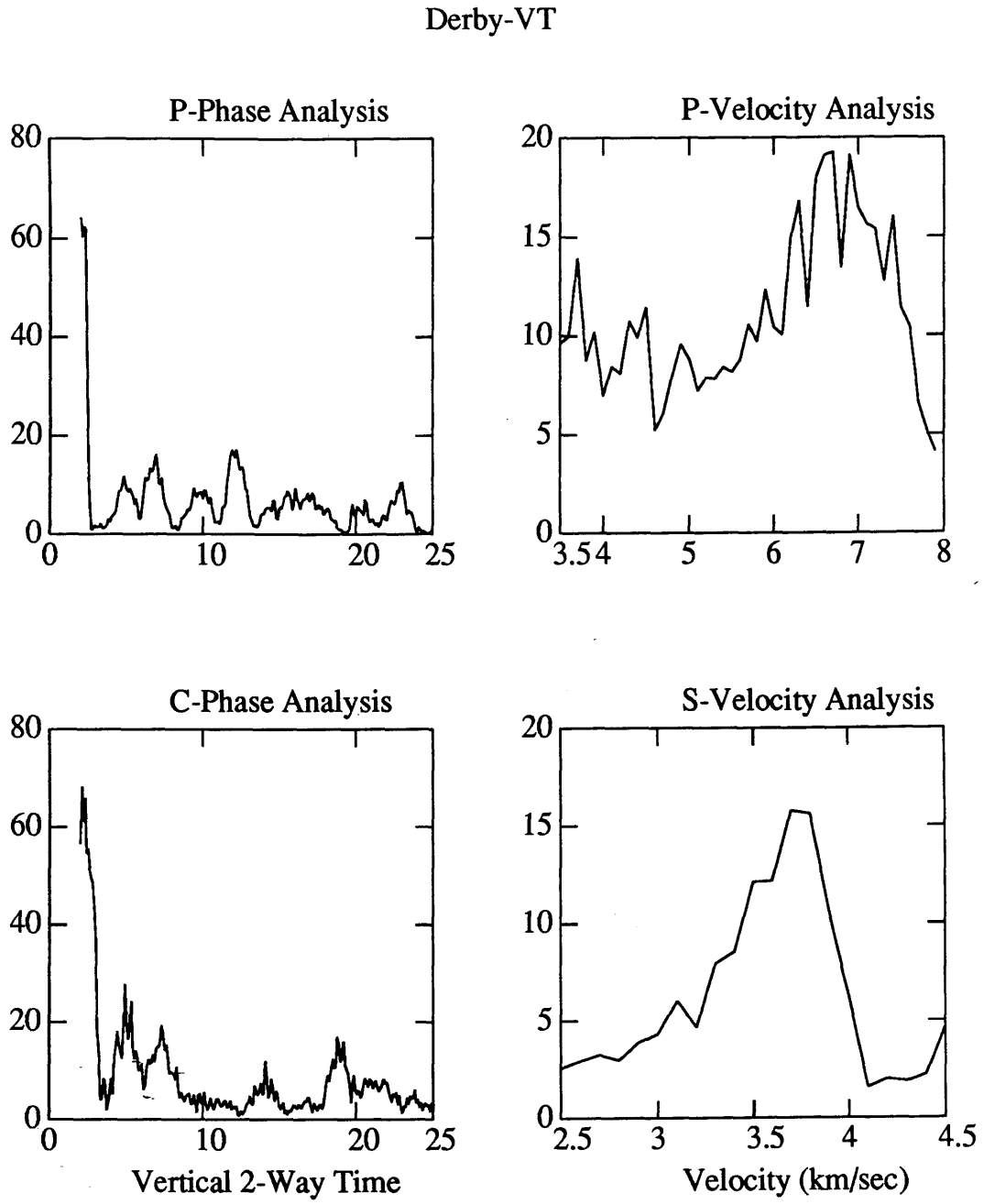

Figure 25: *Rpt* analysis for station DVT.

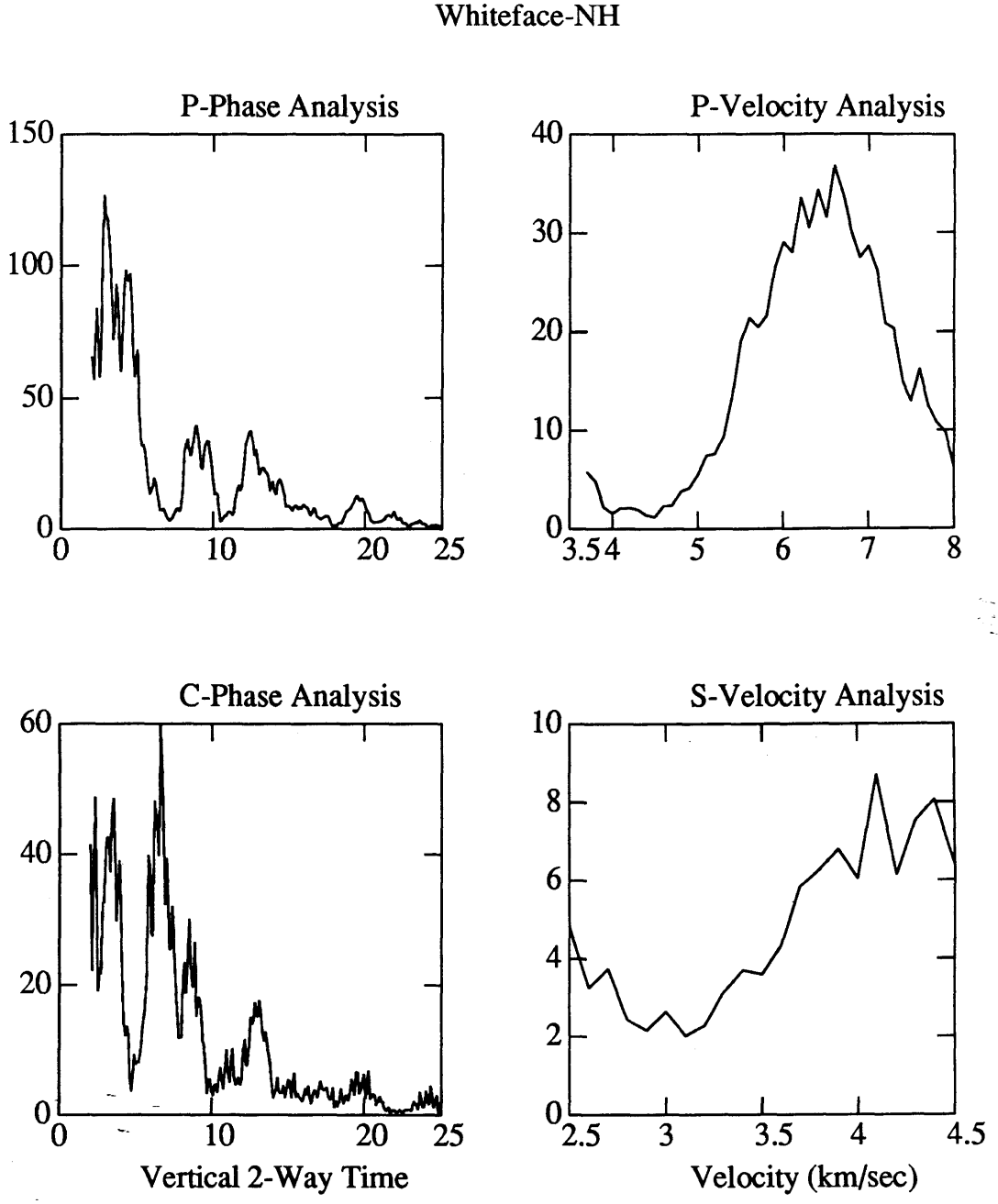

Figure 26: *Rpt* analysis for station WNH.

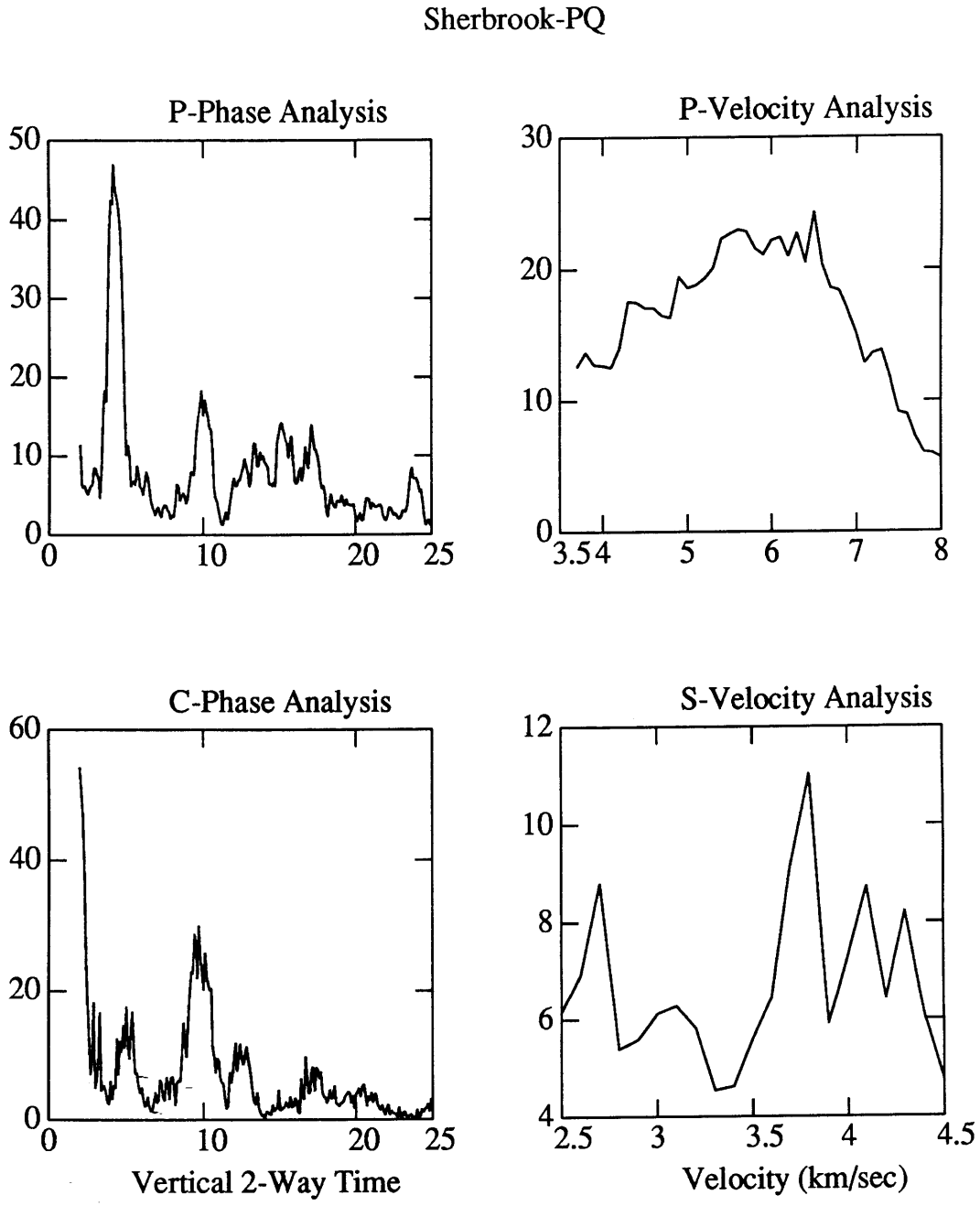

Figure 27: *Rpt* analysis for station SBQ.

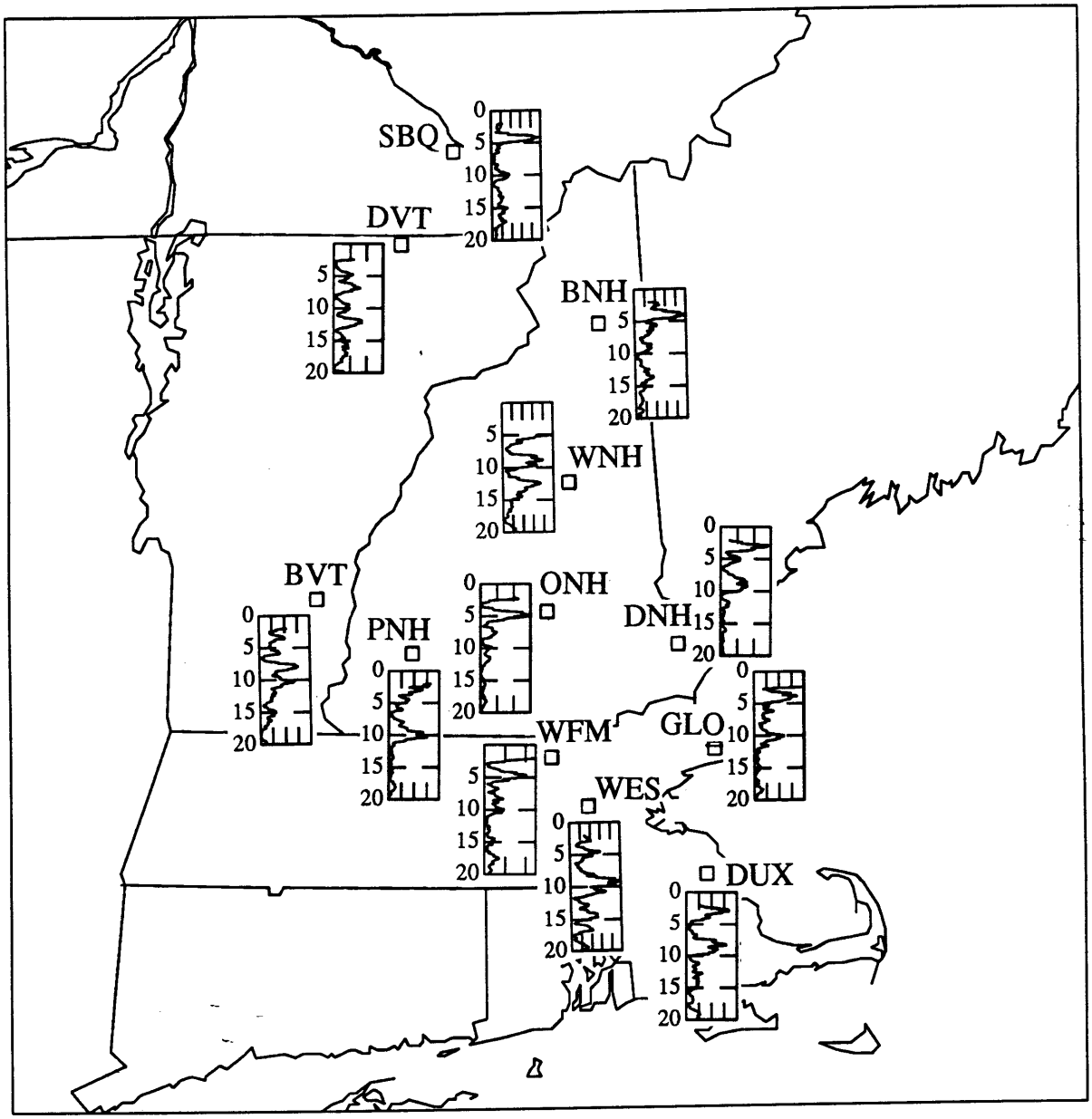

Figure 28: *Rpt* analysis results for the New England stations. Here we plot each stack power result on a map of the region. Travel time is plotted on the vertical axis from 0 to 20 seconds two-way vertical travel time. The horizontal axis is relative stack power.

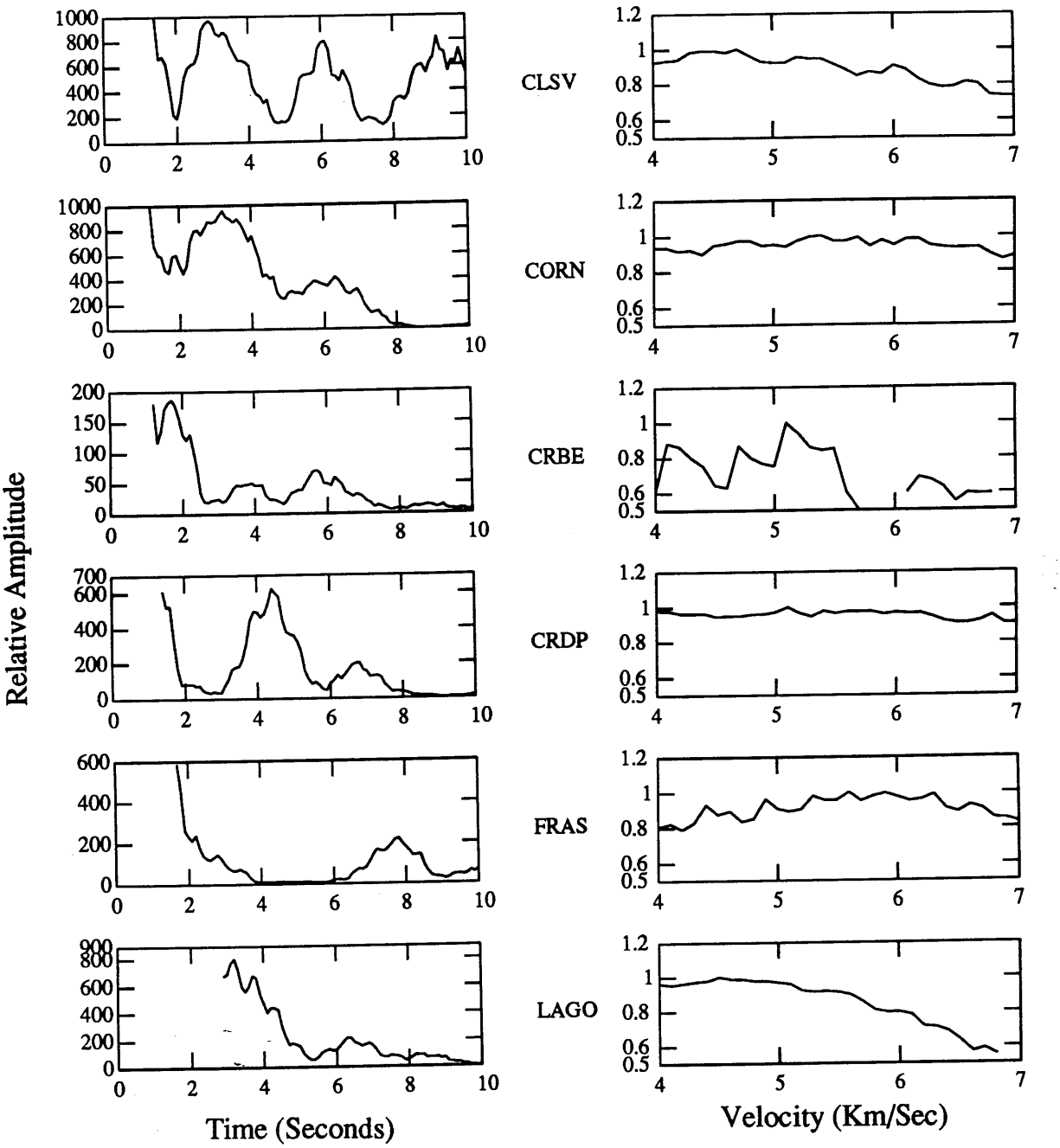

Figure 29: Results of the *rpt* analysis in Larderello. For all stations we plot the P-wave travel time analysis (left) and the P-velocity analysis (right). The phase used in the velocity analysis is indicated with an arrow.

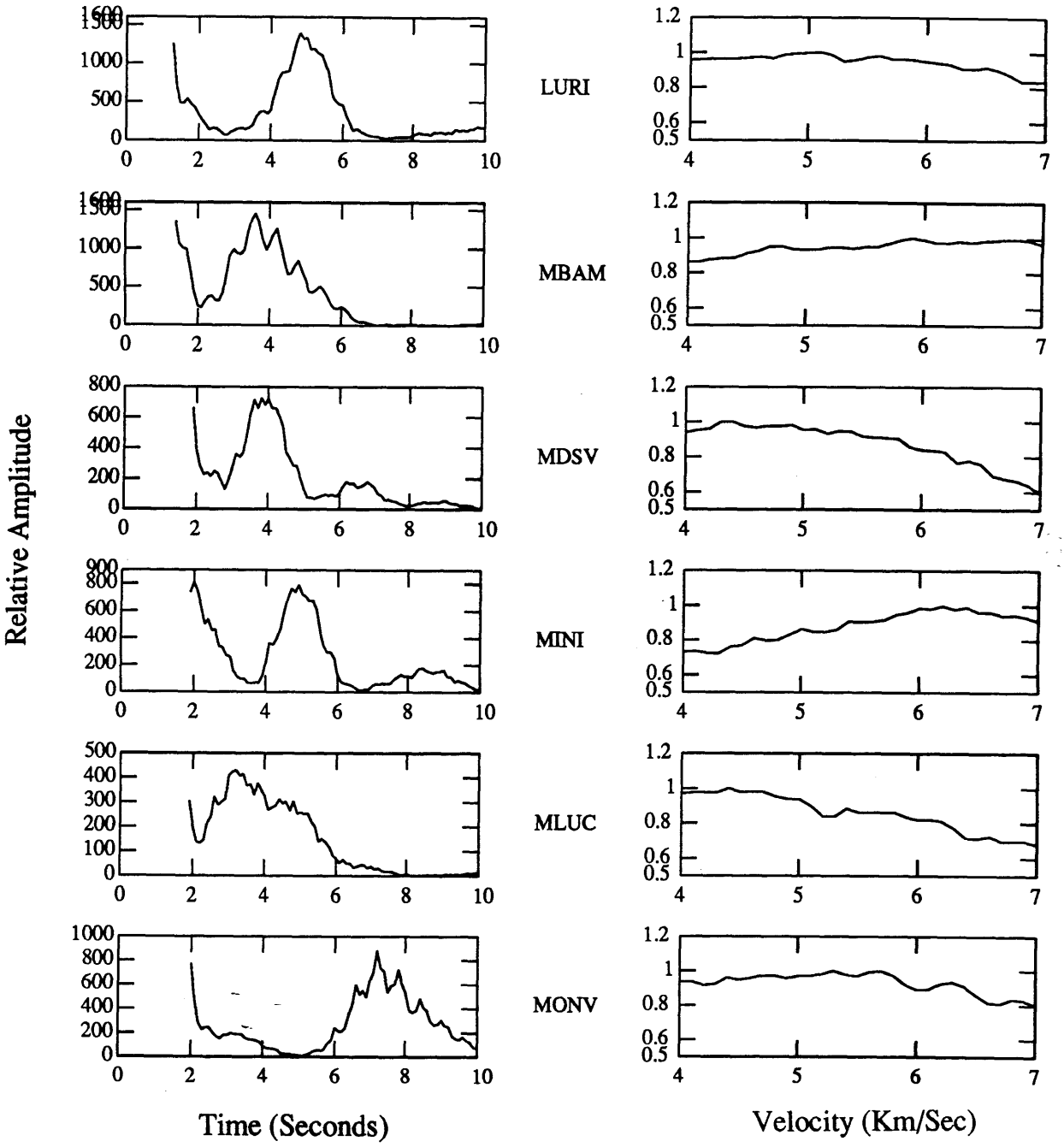

Figure 29: (Continued)

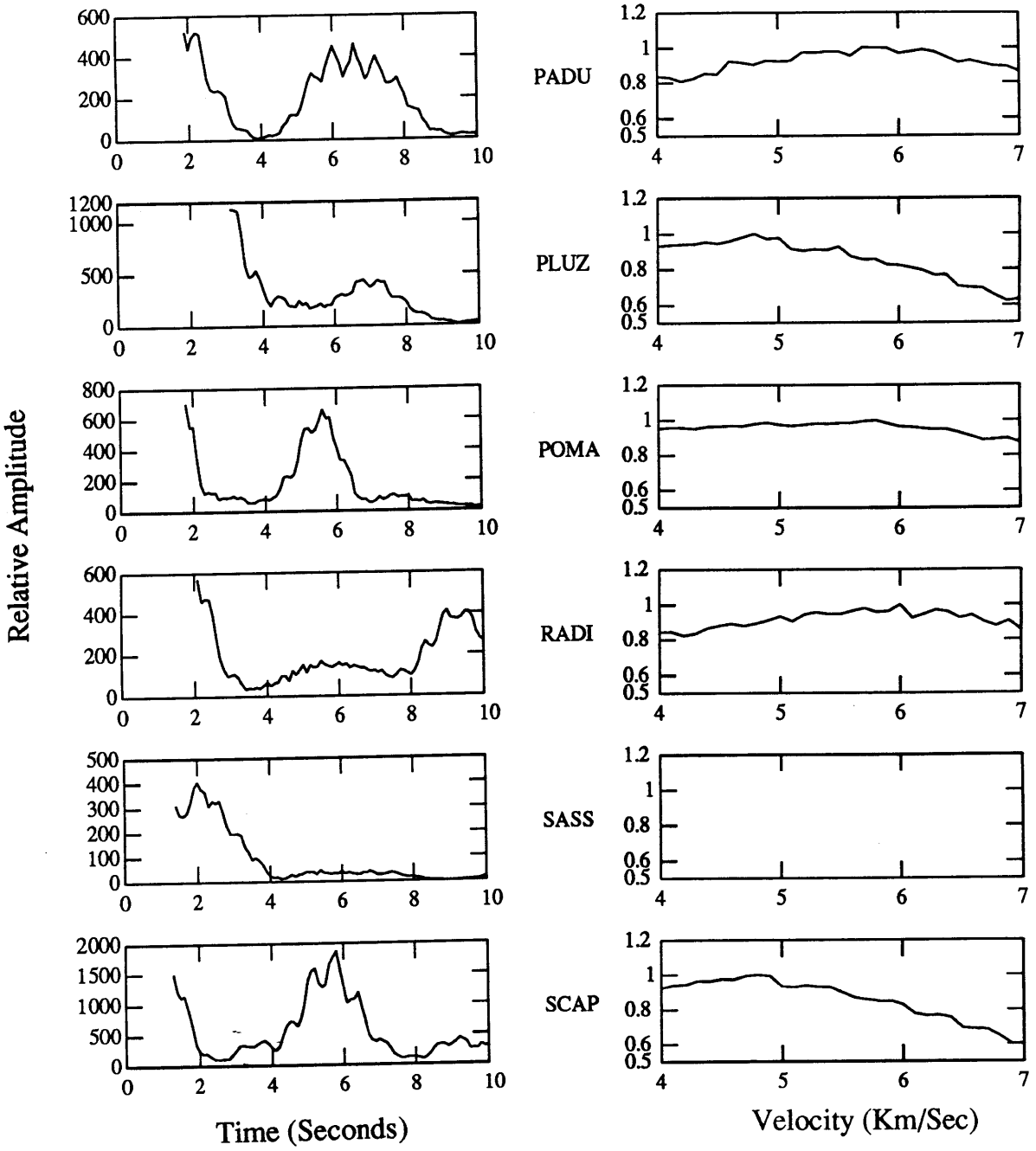

Figure 29: (Continued)

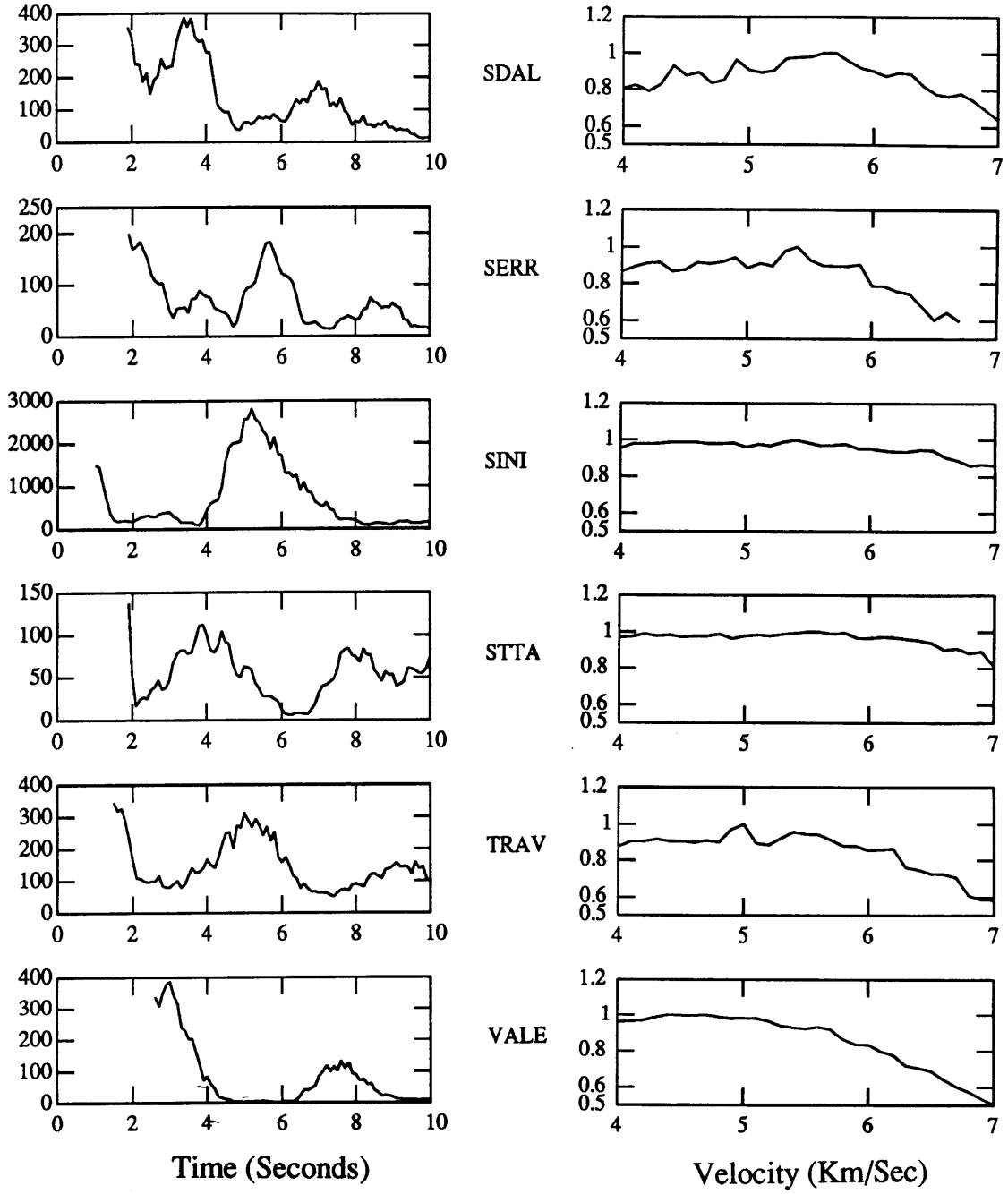

Figure 29: (Continued)

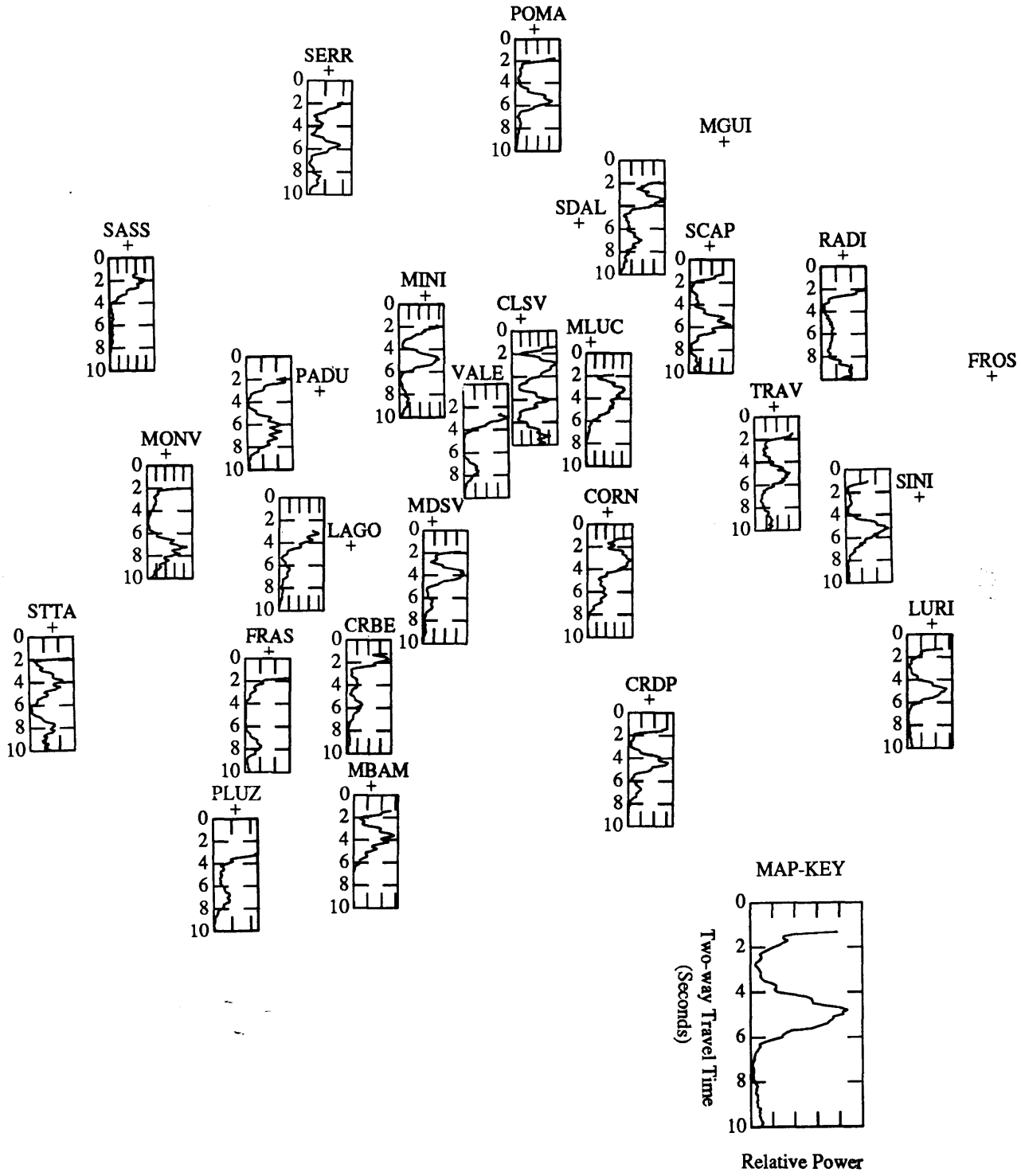

Figure 30: Regional distribution of the *rpt* analysis. We plot the relative stack power verse vertical two-way travel time for each station at the actual station location.

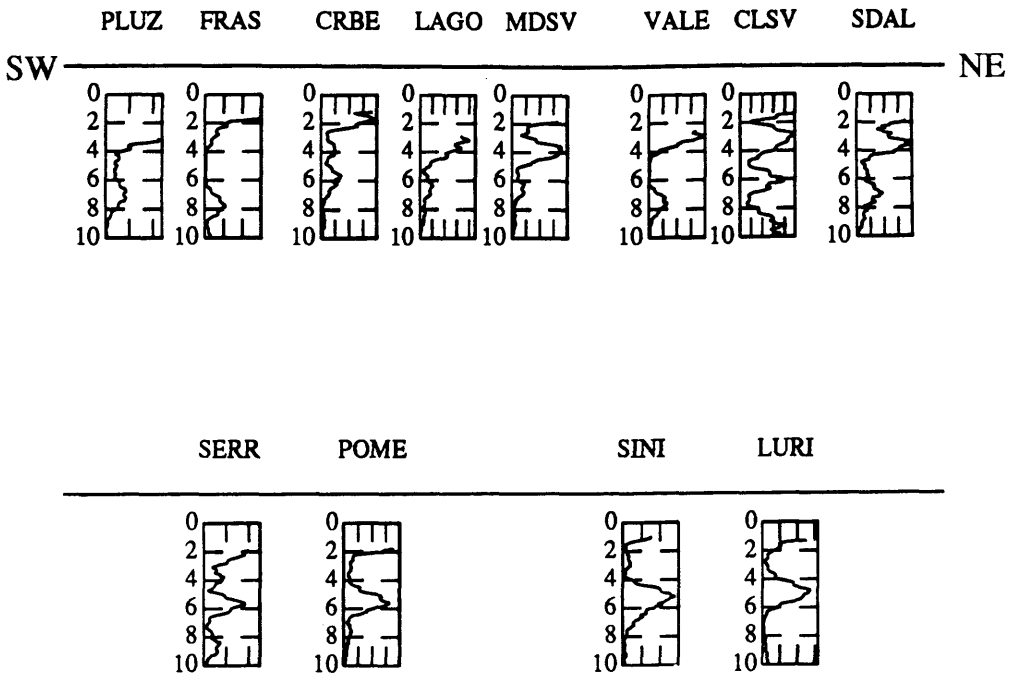

Figure 31: Cross-sectional view of the *rpt* results (top) along a SW-NE trending strike which passes through PLUZ and SDAL, other stations are less than 5 km from this line. Bottom figure is a collection of 4 peripheral stations; SERR and POMA are the 2 most northerly stations, LURI and SINI are the most westerly.

Chapter 6

TELESEISMIC WAVEFORM MODELING

6.1 Introduction

In order to determine all of the available information about the velocity structure of the crust from recorded teleseismic P-waveforms, one must incorporate the entire waveform into the analysis. We showed in Chapter 2 that reflections present in the coda of the direct P-wave, common to a number of stations in a network, can be used to further characterize the velocity structure of the crust using the simulated annealing method. In Chapter 3, we demonstrated that the relative travel time delays of direct P-wave arrivals can be used to determine the general locations of relative high and low velocity areas beneath a network, and in Chapter 5 we showed that local velocity profiles of the crust can be determined by applying the *rpt* stacking method to source transformed teleseismic waveform data. In this chapter, we present a method of non-linear waveform inversion which uses information present in the entire waveform to determine more detailed crustal velocity models. With this waveform inversion method we utilize all parts of the seismogram from the direct arrival to the first multiple reflection from the deepest crustal interfaces.

Both forward and inverse modeling of teleseismic waveforms has been used successfully in the past to determine the velocity structure of the earth. Phinney (1964) and Kurita

(1973) used frequency domain forward spectral matching techniques to determine broad low-frequency features of the crust. From time domain observations on WWSSN long period data Jordan and Frazer (1975) and Burdick and Langston (1977) determined crust and upper mantle structural features. Langston (1979) devised a means of isolating radial impulses of the earth (receiver functions) through a procedure of vertical/radial deconvolution and modeled these functions for crustal velocity structure (Langston, 1979; Langston, 1981). Mellman (1980) posed the technique of teleseismic waveform matching as an inverse problem and determined features of the crust-mantle transition zone in the Bering Sea. Owens (1984) and Owens et al. (1986) were successful in using inverse modeling of time domain broadband teleseismic radial receiver functions to determine crustal structure at broadband 3-component stations, and we follow a formulation similar to theirs in this study.

In Section 6.2 of this chapter we describe the stacking procedure which is essential to inverse teleseismic waveform applications. We also outline the forward waveform matching procedure used to determine starting models for the inversions. The inversion procedure is described in Section 6.3 and applied to the New England data in Section 6.4 and to the Larderello data in Section 6.5

Section 6.2 Waveform Stacking and Forward Modeling

Geometry

The geometry of the teleseismic waveform modeling problem is described in Chapter 1 and sketched in Figure 1-2. Teleseismic P-waves travel from the source through the earth's mantle to the base of the crust beneath the recording station, then interact with the structure under investigation. The resulting waveforms recorded at a surface station contain numerous reflected and converted phases which originate from the structure beneath the station and can be used to determine the crustal velocity structure in the vicinity of the station.

Data Gathers

In both forward and inverse waveform matching methods, synthetic seismograms are calculated for various crustal models in an iterative scheme until a waveform is found which

best matches the observed data. The observations consist of teleseismic P-wave seismograms recorded at an individual station. These seismograms have had their natural source signatures transformed into a common source pulse using the process described in Chapter 4. This transformation removes from the seismograms all effects which are common to all stations in the network and leaves in the trace only the effects of the earth's velocity structure in the region near the station. In addition, the source transformation method converts the natural source pulse into a simple zero phase wavelet which has been well defined (Chapter 4). Once the seismograms have been source equalized, they are sub-divided into groups of similar event back azimuth and incidence angle. In our analysis these *data gathers* are stacked to produce the final traces to be modeled. We refer to this collection of seismograms as the data gather stack. The gathering and stacking process, which is essential to the success of either forward or inverse modeling (Owens et al., 1986), serves three purposes. First, it collects together seismograms with very similar ray geometries, ensuring that each trace in the data gather stack samples a similar portion of the crust. Second, strict data gathering bounds (in back azimuth and incidence angle) ensure that reflections add constructively in the gather stack to enhance their amplitudes. Third, by allowing small variability in the raypaths within the data gathers, the stacking process helps to eliminate the abundant incoherent arrivals observed in the data which are attributed to local isolated scattering phenomena. The stacking process helps to limit the 3-dimensional velocity structure effects in the inversion which cannot be modeled with the 1-dimensional parameterization used in this analysis. With this process, arrivals originating from horizontal reflectors with appreciable regional extent are contained in the *data gather*. For the inversion used in this study 15 to 30 seismograms comprise a gather.

Forward Modeling

To produce the starting models for the inversions we use a time domain waveform matching procedure which is conceptually straightforward and computationally simple. As we saw in Chapter 4, the equation for the synthetic seismograms used in the analysis is:

$$SS(t) = E(t) * S(t) * I(t) * A(t), \tag{6.1}$$

where $SS(t)$ is the synthetic seismogram, $E(t)$ is the impulse response of the model, $S(t)$ is the source pulse arriving into the model, $I(t)$ is the instrument responses and $A(t)$ is the Futterman attenuation filter (Langston, 1979; Owens et al., 1986). As shown in Chapter 4, we can characterize $S(t)*I(t)*A(t)$ as an *effective* source S_e, which can be readily calculated for teleseismic events recorded on the NEUSSN and ENEL networks. We can also convert *effective* source pulse to a simpler source shape S_g^0 which is zero phase and common to all of the study events. With these simplifications, the stacking and forward modeling process becomes quite simple and proceeds as follows:

1. Gather common source-transformed data at a single station, sub-divide traces by azimuth and incidence groups, and produce data gather stacks to be modeled.
2. When available, estimate a starting model for the station under investigation from reflection and refraction or *rpt* results.
3. Calculate an impulse response of the current model for incidence angles corresponding to the *data gathers* being used and convolve the response with the common source pulse S_g^0.
4. Shift seismograms to align the direct P-wave of the model prediction with the direct P-wave of the observed trace and calculate a misfit function.
5. Through visual inspection of the misfit between synthetic and observed seismograms, update the model. Continue the process in steps 3 through 5 until the misfit is minimized.

The process of forward modeling seismic waveforms is tedious and difficult because of the very complicated model parameter interdependence. To keep the forward problem manageable we model the seismograms with only a few free parameters (fewer than 10). We maintain a simple parameterization of the earth so that we can model the seismograms with this straightforward waveform matching scheme. However, since we allow only a few parameters to vary (thickness and velocity of a small number of layers) we impose limitations on the range of possible data predictions. One aspect of this approach is that forward modeling with simple forward methods can never satisfy all of the observations. However, if the forward method is made overly complicated to allow for more exact waveform matches, the procedure becomes unwieldy due to complicated model interdependences and requires the

implementation of more powerful inverse techniques. We conclude that this forward modeling procedure can provide the rudimentary features of the crustal model and that inverse methods we must used to determine more accurate model estimates.

Section 6.3 Inverse Waveform Modeling

Like forward modeling, waveform inversion is a search for a model which produces a waveform that in some sense best fits some observed seismograms (Tarantola, 1987). The key element of waveform inversion, as it is posed here, is the development of a technique which uses the misfit to the data as a means of updating the model. The updated model creates a new prediction and the process continues iteratively until some minimization criteria are met. Essentially, with the inversion method we are automating the forward process outlined above. An iterative inversion procedure can be implemented by calculating the sensitivity of each point in the seismogram to each model parameter. This is a partial derivative function which contains information about how the seismogram is changed when each model parameter in perturbed and is the basis of the model update. There are several difficulties involved when partial derivative based inversions are applied to seismic waveform problems. Some of these problems are associated with the source representations, bandwidth limitations and numerical noise issues (see Tarantola, 1987; Tarantola et al., 1985; Pica et al., 1990; Narcissen et al., 1984; Nolet, 1988, for example). Furthermore, there are a number of specific problems and limitations related specifically to teleseismic inversions (Owens, 1984). Generally, additional information about the problem posed as a priori model information and a priori data information is required to produce reliable results in teleseismic waveform inversions.

The first step of waveform matching procedures, posed as forward or inverse problems, is to establish a function which can be optimized to yield the best possible estimate of the properties of the media (Mellman, 1980; Tarantola, 1987). We represent the waveform misfit function using the form

$$S(\mathbf{m}) = \frac{1}{p}\int_{T_0}^{T_f} (d(\tau) - g(\mathbf{m}, t))^p \, dt, \tag{6.2}$$

where p is the norm under which the optimization occurs and where the range of integration

is from the direct arrival time T_0 to T_f, the length of the data vector. $d(\tau)$ represents the data vector shifted by the amount needed to align the direct arrivals of the data to the model prediction. Since in our teleseismic waveform inversion all misfit measurements are made relative to the direct P-wave, no information about the absolute travel time of the direct phase is used. The lack of absolute direct P-wave information forces us to incorporate various additional constraints into the inversion when applying the method to actual data. In order keep the objective function in simple quadratic form, we set $p = 2$, (least squares) which makes the subsequent mathematics needed to design optimization schemes straigtforward and intuitive (Mellman, 1980; Owens, 1984). If we set $p = 2$ and introduce data and model covariance terms, Equation 2 can be written as

$$S(\mathbf{m}) = b^t C_d^{-1} b + (\mathbf{m} - \mathbf{m}_0)^t C_m^{-1} (\mathbf{m} - \mathbf{m}_0) \tag{6.3}$$

where b is the misfit vector $(d(t) - g(\mathbf{m}, t))$, C_d is a data covariance matrix which is introduced to weight the data vector and to incorporate a priori information about data variances, and C_m is a model covariance operator used to impart a priori model information. It is generally difficult to determine the variance of individual seismograms, but in this application we stack many seismograms to produce one data vector and we use the variability of each point in the stack as a measure of the experimental data variance.

The quadratic form of this equation leads to straightforward multi-parameter optimization methods. Since our problem is a non-linear one, we must solve it in a iterative scheme where a local linearized portion of the system is analyzed at each iteration. Provided that the non-linear nature of the problem is not too severe (the function $S(\mathbf{m})$ is smoothly varying), we can approach the global minimum in steps. The difficulties of this procedure are three-fold: first, we must develop an optimization scheme that reaches the global minimum of Equation 3 and not a secondary minimum; second, we must be able to analyze the error and resolution of the solution; and third, we must be able to reach our optimization point with a non-prohibitive amount of computing effort.

The most useful information about the nature of $S(\mathbf{m})$ comes from calculating its first and second partial derivatives with respect to perturbations in the models parameters. Most iterative optimization routines require knowledge about the shape of $S(\mathbf{m})$ (Tarantola, 1987

Nolet, 1987). The gradient and Hessian of $S(\mathbf{m})$ are defined as

$$F = \nabla_{\mathbf{m}} S(\mathbf{m}) = \frac{\partial S}{\partial \mathbf{m}} = G^T C_d^{-1} b + C_m^{-1}(m - m_0) \tag{6.4}$$

and

$$H = \nabla_{\mathbf{m}} \nabla_{\mathbf{m}} S(\mathbf{m}) = \frac{\partial^2 S}{\partial \mathbf{m}_i^2} = G^t C_d^{-1} G + C_m^{-1} + \xi. \tag{6.5}$$

Here G is the gradient of $g(\mathbf{m}, t)$ which holds the forward problem sensitivity information and ξ are the terms of order $\nabla_{\mathbf{m}} \nabla_{\mathbf{m}} g(\mathbf{m}, t)$. To estimate the update direction from the i^{th} step in an iterative procedure, one can use the Gauss-Newton algorithm

$$\mathbf{m}_{i+1} = \mathbf{m}_i + (H)^{-1} F \tag{6.6}$$

and when the second order terms of (5) are dropped, we get

$$\mathbf{m}_{i+1} - \mathbf{m}_i \simeq \left[G^T C_d^{-1} (G)T + C_m^{-1}\right]^{-1} \left[G^T b C_d^{-1} + C_m^{-1}(\mathbf{m} - \mathbf{m_0})\right], \tag{6.7}$$

which is equivalent to the form of Tarantola (1987) and Nolet (1988). This is the form we use in the applications below. Equation 7 is not the only way to optimize $S(\mathbf{m})$; Nolet (1988), Tarantola (1987) and Menke (1984) provide details on various gradient methods as applied to geophysical problems.

Implementation Issues

There are six key implementation issues important to this teleseismic waveform inversion problem: forward calculations, partial derivative calculations, convergence, noise, model parameter resolution and model parameter error.

- Forward Calculations

  To use Equation 7 as the solution of our inverse problem, the efficient and accurate calculation of synthetic seismograms is essential. Since we assume flat lying layers, a variety of efficient forward methods are available to us. We have chosen to use a ray tracing method to calculate model impulse responses which are convolved with a generic zero phase wavelet ($S_g^0(t)$) to create the synthetic seismograms. The layer thicknesses in the plane-layered crustal model remain constant in the inversion to

keep the number of free parameters manageable. We use two different approaches to establish the thickness of each layer. When initially modeling the crust for major features we use a small number of layers (about 10) with thickness of about 4 km each. Later, we increase the number of layers to about 20 and decrease the thickness of each layer to determine small scale features and to facilitate the representation of gradational velocity changes in the crust (Owens, 1984). We solve for the compressional velocity only in each layer, establishing the shear velocity using the assumption of a Poisson solid. The densities are derived from it using the relation $\rho = 0.32\,V_p + 0.77 \frac{gm}{cm^3}$ (Berteussen, 1977).

- Partial derivative calculations

  The matrix G contains the sensitivity information about the forward problem and is the most important function to be calculated as part of the optimization of S. The iterative scheme employed here (Equation 7) utilizes the curvature of S to select the best direction to change the model. To determine the gradient and Hessian terms, derivatives of the seismogram (prediction) with respect to the layer velocities (parameters) are required,

$$G(t) = \nabla_{\mathbf{m}}\, g(\mathbf{m}, t) = \frac{\partial g}{\partial \mathbf{m}}. \tag{6.8}$$

  G is calculated numerically in this study using a central difference approach, requiring two synthetic seismogram calculations per layer per iteration. Velocity perturbations are set to create a uniform travel time perturbation of 0.02 seconds for each layer in the model (five times the sampling rate) when taking the numerical derivatives. Examples are shown below.

- Convergence improvement

  Non-linear inversions work on the premise that linearized subsystems can be realized at each iterative step (Tarantola, 1987). Through extensive testing we have found that this assumption varies in validity at each iteration and depends on many qualitative issues such as the model parameterization, source representation, data complexity, current model estimate and noise. The function S has regions which are fairly linear

and areas which are highly non-linear. Equation 7 provides the optimal step to be added to the present model estimate in order to minimize S in the vicinity of the model. However, a full step in the prescribed direction does not always yield the best possible result (smallest value of S). To increase the convergence rate and to help proceed through regions of S which have difficult topographies (ie, strong non-linearities), we calculate S at various step lengths in the direction of the update and then interpolate to find the best step length. By inspection of the shape of S along the update direction, we can get a good qualitative feel for the degree of nonlinearity of the problem.

We have found in tests of the inversion procedure on synthetic data that we can usually recover the correct vertical travel time and magnitude of the velocity discontinuities of the model. However, the inversion procedure oftentimes has difficulty determining the correct absolute velocities in the model. Two techniques are readily available to overcome this deficiency of the method. First, we can constrain the total travel time through the model to some predetermined value (derived from the methods described in previous chapters). This constraint is incorporated into the inversion as an extra equation to be satisfied in Equation 7. We adjust C_d^{-1} to control the relative importance of this additional equation in the system. Second, we can constrain the lowest mantle velocity to a predetermined value (derived from either refraction results or the travel time residual inversion results). We have found that if we pin the mantle velocity to a specific value, the non-uniqueness of the problem is significantly reduced. This constraint is easily implemented by setting the covariance term associated with the mantle velocity parameter in Equation 7 to a very small value.

In addition to these travel time and velocity constraints, we have tested the effects of constraining the level of model smoothness of the velocity profile. This is accomplished by incorporating a second difference smoothing operator into C_m^{-1} which minimizes the roughness of adjacent model parameters. We control the relative importance of this term in Equation 7 with a scale factor on the $(m-m_0)^t C_m^{-1}(m-m_0)$ term. In general, we find that a very small smoothness term reduces the complexity of the final model

without degrading the fit to the waveform.

- **Noise**

  Noise is the single largest problem in teleseismic time domain waveform modeling. The inversion process itself cannot discriminate between the signal and noise in the waveforms and therefore it attempts to fit all of the data. Tests on noise-contaminated synthetic waveforms have revealed that when the inversion model is far from the true model, the misfit is dominated by the differences between the prediction and the signal. However, since the data contain both signal and noise, when the inversion gets close to the solution the misfit between the prediction and signal is small and the noise becomes very important in controlling the model changes. We conclude from synthetic tests that when noise levels above 5% of the direct arrival are present in the data, we cannot recover the true model without starting close to the solution. When noise levels above 10 % exist in the data, the procedure generally fails to converge.

- Resolution and Error

  The ability of this method to determine individual model parameters is characterized by the a posteriori model resolution matrix (Tarantola, 1987; Menke, 1984)

$$\mathcal{R}_n = G_n^{-g} G_n, \tag{6.9}$$

  where R is the resolution matrix, G_n^{-g} is the generalized inverse operator, and n is the index number associated with the final model. If $\mathcal{R}$ is the identity matrix, then the model parameters are perfectly resolved whereas if it is not the identity matrix, then we are resolving combinations of the model parameters with the off-diagonal terms representing the model interdependence. Since we order our model parameters by increasing depth, the rows of the resolution matrix show us the relative resolution of various part of the crust. We see from the resolution plots that follow in the application sections (Figures 4b, 5b, 9 and 10) that the model parameters generally trade off with neighboring layer velocities. Velocity contrasts are well resolved, but individual layer velocities are really localized averages over a few layers.

To determine the posterior covariances of the final model estimates due to contributions of both noise in the data as well as imperfect resolution, we calculate model covariance matrices using the relation

$$\mathcal{E}(m^{est}) = G_n^{-g}\, C_d^{-1}\, G_n^{-gT} + (I - \mathcal{R}_n)\, C_m^{-1}\, (I - \mathcal{R}_n)^T, \tag{6.10}$$

where $\mathcal{R}$ is the resolution matrix, C_d a priori data covariance matrix, and C_m is the a priori model covariance matrix (Menke, 1984). This operation provides a means of estimating the relative covariances of the model parameters. The diagonal terms of $\mathcal{E}(\mathbf{m})$ provide a measure of the relative error associated with each individual parameter estimate.

Section 6.4 New England Applications

As a means of demonstrating the techniques described above, forward and inverse waveform matching methods are applied to two NEUSSN stations: GLO, located in Glouchester, Massachusetts, and BVT located in Baltimore, Vermont. These stations were selected because they are characteristic of two separate tectonic regimes found in New England and because they are representative of stations within the NEUSSN with average data quality (GLO) and above average data quality (BVT). A high *quality* station is defined here as one which records a number of teleseismic signals from similar azimuths and incidence angles and with clear strong and repeatable phases. These characteristics facilitate data enhancement through stacking, a data requirement essential to both forward and inverse modeling. At many stations in the NEUSSN there is a large amount of incoherent energy on a majority of the seismograms as well as phases which have large amplitudes but which are not common to all seismograms from events with similar back azimuths and incidence angles. Figure 1 shows one such set of observations for station DVT, located in Derby, Vermont. On the left of this Figure we plot 12 traces from events arriving at DVT within 9 degrees of the same back azimuth and 4 degrees of the same incidence angle. Each traces has had the natural source function transformed into a simple wavelet (see Chapter 4). We see from this plot that there are a number of common features in the seismograms including strong

near surface arrivals as well as mid- and lower crustal phases at about 10 seconds after the direct P-wave. However, dissimilar waveform features dominate the data, and although each trace has roughly the same character (similar number of arrivals at similar times), the higher amplitude phases in the data are not repeatable. The relatively small number of traces in this gather (11) is not sufficient to enhance coherent isolated arrivals through stacking. In Figure 1b (right) we plot 5 traces from DVT, all seismograms coming from events with nearly identical back azimuths and incidence angles (these 5 seismograms come from nuclear detonations from the same area within the USSR). Again, numerous high amplitude arrivals exist on each trace, but now we see a repeatable waveform pattern in all the data. When we compare the relative similarity in this second data gather to the strong dissimilarities in the first data gather at this station, we can speculate that a high degree of scattering is occurring in the crust near the receiver and that the wavelengths of the scatters must be less than the average difference in the raypaths represented in the first gather, or about 10 km. Many stations in the NEUSSN exhibit similar phenomenon, and we must be selective when choosing stations for analysis with forward or inverse waveform matching applications based on plane layer parameterization. Station BVT represents an example where the crust appears to be less heterogeneous than the average station, and consequently, the data are highly repeatable. GLO represents a more typical station for New England.

WAVEFORM MODELING BVT

BVT is located at Baltimore, Vermont (see Figure 1-3) and is located in the Connecticut Synclinorium. The P-wave *rpt* analysis at BVT (Figure 5-23) revealed a primary Moho P reflection with two-way travel time of 10.5 seconds and a converted phase Moho arrival at about 18 seconds (the two-way vertical S-time). Crustal P and S velocity estimates made from the velocity analysis (Figure 5-23) yield an average P-wave crustal velocity estimate of 6.3 $\frac{km}{sec}$, an S-wave velocity of about 4.2 $\frac{km}{sec}$, and the Moho to be at a depth of about 33 km. At shallower depths we see numerous arrivals in the *rpt* analyses which indicate a more complicated than average crustal structure with numerous velocity discontinuities in the top 30 km. Using a starting model derived from the *rpt* results we can match some

simple features in the waveform data with forward modeling. In Figure 2 we show three data gathers from BVT from the north-northeast, south and northwest. We see a good level of repeatability in these data. To demonstrate the waveform matching techniques, we applied the forward and inverse waveform matching schemes to the northwest data gather for this station. This gather has a back azimuth 12.3° and an incidence angle of 22.4° and includes 16 traces. Figure 3 shows the best waveform match for this gather which could be achieved with forward modeling. On top is plotted the stack of the 12 traces in the gather along with the best synthetic waveform, and below we show the velocity model which produced the synthetic waveforms. The model in Figure 3 defines the basic features of the crust: a low velocity upper-crustal layer, a strong velocity inversion at about 15 km and the Moho at about 33 km.

Next, the inversion procedure is applied to the BVT data. As a test of the ability of the inversion procedure to reach an accurate final model from starting models distant from the solution, we ran the inversion *without* incorporating the forward modeling information and began the inversion from a halfspace starting model. The results of the inversion run are shown in Figure 4. Here we see that the velocity model is similar to that of the forward modeling, but now we satisfy much more of the data with our prediction, particularly from the mid-crust (at 7 seconds) and Moho (12 seconds). The waveform inversion took 12 iterations to converge or 3 minutes of Cray-2 supercomputer time. The forward modeling took about 2 man-hours of analysis.

As we discussed above, with the waveform inversion method we are able to assess the reliability of the final models. The model resolution and covariance and sensitivity information are plotted in Figure 4b. The sensitivity matrix shows us which parts of the data are most sensitive to changes in the model, and we see that the first few seconds (essentially the observed source wavelet) of the seismogram are controlled by the top few layers. The mid-crust reflection phase (7 seconds) is sensitive to changes in the velocities of all layers above the discontinuity causing the arrival. This analysis also reveals that the Moho arrival at about 12 seconds is complicated by a multiple reflection of the mid-crustal feature; we can determine this from the observation that model sensitivity (at 12 seconds) is strongly dimin-

ished below layer 11. The model resolution matrix (Figure 4b) show us how uniquely each model parameter is being determined. The trade-off between successive model parameters indicates that we can resolve velocity contrasts well but that individual velocity estimates must be considered to be localized averages. The covariance matrix reveals the way in which data errors and imperfect resolution are mapped into the model, and from the relative size of the diagonal terms we see that each parameter has roughly the same variance.

WAVEFORM MODELING GLO

GLO is located in Glouchester, Massachusetts on Cape Ann. This station lies on the Avalon Terrane which is a tectonic province in New England demonstrated to have fundamental differences in velocity structure from terranes further inland (Doll, 1987; Foley, 1984). From the *rpt* analysis (Figure 5-25) we determine that the Moho at GLO has a two-way vertical travel time of about 10.1 seconds. Using the velocity analysis results (Figure 5-26) we estimate the Moho to be at a depth of about 28 km. We also detect near surface discontinuities which produce phases arriving about 2 and 5 seconds after the direct arrival.

Forward and inverse techniques were applied to a data gather at GLO where the data have an average back azimuth of 182° and an average incidence angle of 30°. The results of this inverse modeling are shown in Figure 5. We see from the results from this station that the deep crust at GLO is quite simple with the only major velocity discontinuity being the Moho at 28 km. The upper crust is also relatively uncomplicated, with a slight velocity inversion in the upper 10 km.

The waveform inversions at GLO and BVT are primarily undertaken as a means of testing the inversion procedure and assessing the usefulness of the waveform inversion applications to *typical* seismic network stations which are quite abundant around the world. Until this study, inversion of teleseismic P-waveforms has been limited to broadband three component data (Owens, 1984; Owens et al., 1987). We show with these two examples, along with some data from Larderello shown in the next section, that inversion of single channel vertical component teleseismic data can yield very important information about the seismic structure of the crust. We also conclude that the most important factor which dictates the overall success of the method is the signal-to-noise ratio of the traces used in the inversion. The

source equalization method gives us a very convenient and effective way to produce reliable data with generic source functions which can be used to improve the signal-to-noise ratio of the data.

Section 6.5 Larderello Applications

In this section we present the results of the waveform inversions of the teleseismic P-wave data recorded on the Larderello Seismic Network. In this study we have a large amount of near vertically incident seismograms and use these data exclusively to model the crust. The use of vertically incident data has important advantages to off-vertical data: 1) The stacking assumptions are most valid for vertically incident rays; rays travel in similar parts of the crust, and therefore stack in phase. 2) The effects of 2-dimensional and 3-dimensional structures in the vicinity of the station are minimized with vertically incident data, and 3) Vertically incident seismograms are simpler; in a truly 1-dimensional earth no shear waves are present on vertical component seismograms for vertically incident events. For each application of the waveform inversion method in this section, we stack 10 or more seismograms to produce each data gather. Before stacking the natural source wavelet of each seismogram is transformed into a common zero-phase wavelet.

We have focused our attention on 12 stations from the ENEL network (Figure 6) which represent a good sampling of the geologic setting of the region. Seven of these stations lie roughly along a NE-SW line through the center of the area. This is the same strike direction we looked at in the travel time residual inversion study (Chapter 3) and the *rpt* application (Chapter 5). It will also be utilized in Chapter 7 where we discuss the findings of all of the Larderello applications.

To demonstrate some of the important issues in this application, we present the results at two stations (LAGO and POMA) in detail before all of the results are shown. Geologically, these two stations are situated in very different provinces of the region and have the most variation in crustal structure observed in the area. LAGO is in the center of the network in the area of strong geothermal production. This locality has a strong local negative gravity anomaly (-20 mGals), very high temperatures (above 300° C at 2 km), a high rate of shallow

seismicity (less than 4 km) and an elevation of the **K** reflection horizon which is proposed to represent a petrophysical marker of the top of the late Apline contact aureole (Batini et al., 1983). POMA is about 30 km north of LAGO and is located in an area which has much weaker geophysical observations. Earthquakes are less abundant, the 2 km temperatures less elevated (about 150° C), and gravity measurements are not strongly anomalous.

Figures 7 and 8 show the inversion results for LAGO and POMA, respectively. On the left of the figures, we show the seismograms which went into the vertical incidence data gather (0 to 6 degrees) and present the stack of the data below. To the right, we present the best waveform fit from the inversion (actual data is solid line) and the model producing the fit. The errors for each model parameter represent one standard deviation from the best estimate of the layer velocity. In Figures 9 and 10 we present additional information for these two stations, namely the partial derivative matrix for the final iteration (top), model resolution and covariance (bottom) matrices for stations LAGO and POMA, respectively. For the remainder of the stations (Figure 11) we present the best model and fit to the data only.

From a review of the waveform fits (Figure 11), we conclude that this procedure can adequately determine models which best satisfy the observations in Larderello. The fits to the data are generally excellent, with none of the misfits greater than 2 standard deviations of the data vector, which are determined during the data gathering and stacking procedure. We were able to reach the final models without introducing model penalty functions or strong model smoothness constraints into the inversion. The only model constraint needed to produce rapid convergence was on the velocity at deepest mantle layer. The velocity of these layers is constrained by the results of the travel time residual inversion of Chapter 3. These velocities range from 8.2 $\frac{km}{sec}$ on the periphery (in agreement to the refraction results of Giese et al., 1980) to 7.6 $\frac{km}{sec}$ in the central regions.

The procedure we follow to reach the final model is generally divided into two stages. In the first stage we we invert the data for a coarse model of about 5 to 10 layers. The starting models for this first stage are derived from the *rpt* results (Chapter 5), but we have found that we can get to the final *coarse* model from nearly any starting model, including

a layer over a halfspace. The best model estimate of the first stage is made into a model with thinner layers for the second stage inversion, where the finer details of the media are determined. We generally use 5 to 15 iterations per stage to reach the final model.

We show resolution matrices for stations LAGO and POMA in Figures 9 and 10. We can see from these plots that there is some trade-off between the parameters. In the LAGO case for example, (Figure 9) we see that Parameter 5 (depth 5.5 km) is functionally related to Parameter 8 in a positive sense and negatively with Parameter 4. The cause of these relationships is evident from the sensitivity analysis. Layers 5 and 8 affect the seismogram in a a similar sense (equivalent changes in these parameters cause similar differences in the predicted seismogram) and Layers 4 and 5 in an opposite sense (a positive change in Parameter 4 and a negative change in Parameter 5 will have similar effects on the seismogram). In general, the sensitivity analysis (Figures 8 and 9) shows that the final seismogram (from direct P-wave onward) is approximately related to the depth of the model parameter; early parts of the trace are sensitive to upper layers, the middle of the seismogram is sensitive to the mid crust, and so on.

In addition to this quantitative analysis of the final models, there are a few qualitative observation that can be made to increase our confidence in the results: 1) The velocities of the final models fall within reasonable physical bounds and are derived without the addition of penalty functions or strong smoothness constraints. 2) By calculating the travel times through all of the final inversion models, we can calculate travel time residuals predicted by the waveform inversion method. In Figure 12 these residuals are plotted against the travel time residuals derived in Chapter 3. We see from this comparison that the inversion procedure is accurately reproducing the general velocity trends found in the direct P-wave travel time study. The stations which fall below the line representing equivalent travel time residuals (CRBE, FRAS, LAGO, PADU and MDSV) are all located in the same area within 8 km of each other (see Figure 6). We conclude from this pattern and from the cross-sectional view of the travel time residual results of Chapter 3 (Figure 3-11) that the low velocity anomaly in Larderello extends below the crust and continues to exist into the mantle. 3) The models produced in the inversion compare well with the results of the *rpt* results. In

Figure 13 we plot the inversion results on a map of the network. We superimpose the *rpt* results on this graph as arrows at depths predicted by that stacking procedure. We see from this figure that the inversion can reproduce the majority of the features derived in the *rpt* analysis. We put these results in a more general context in Chapter 7.

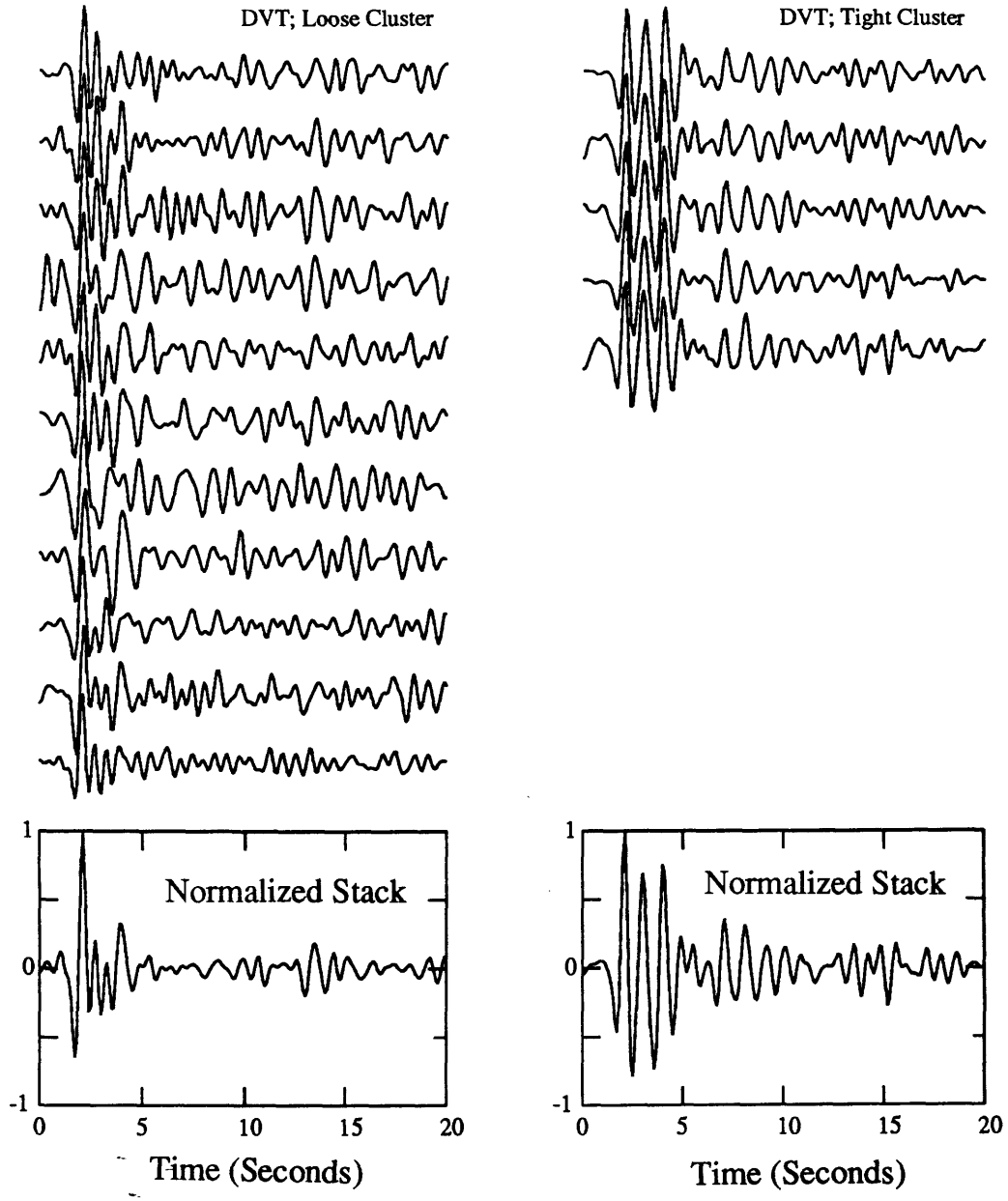

Figure 1: Source equalized seismograms for Station DVT, located in Derby, Vermont. On left we plot 12 traces all coming from events within 9 degrees of back azimuth and 4 degrees of incidence angle; average back azimuth is 182 degrees, and average incidence angle is 22 degrees. On right are 5 events from the same USSR nuclear test site; back azimuth is 23.3 degrees incidence angle is 20.4.

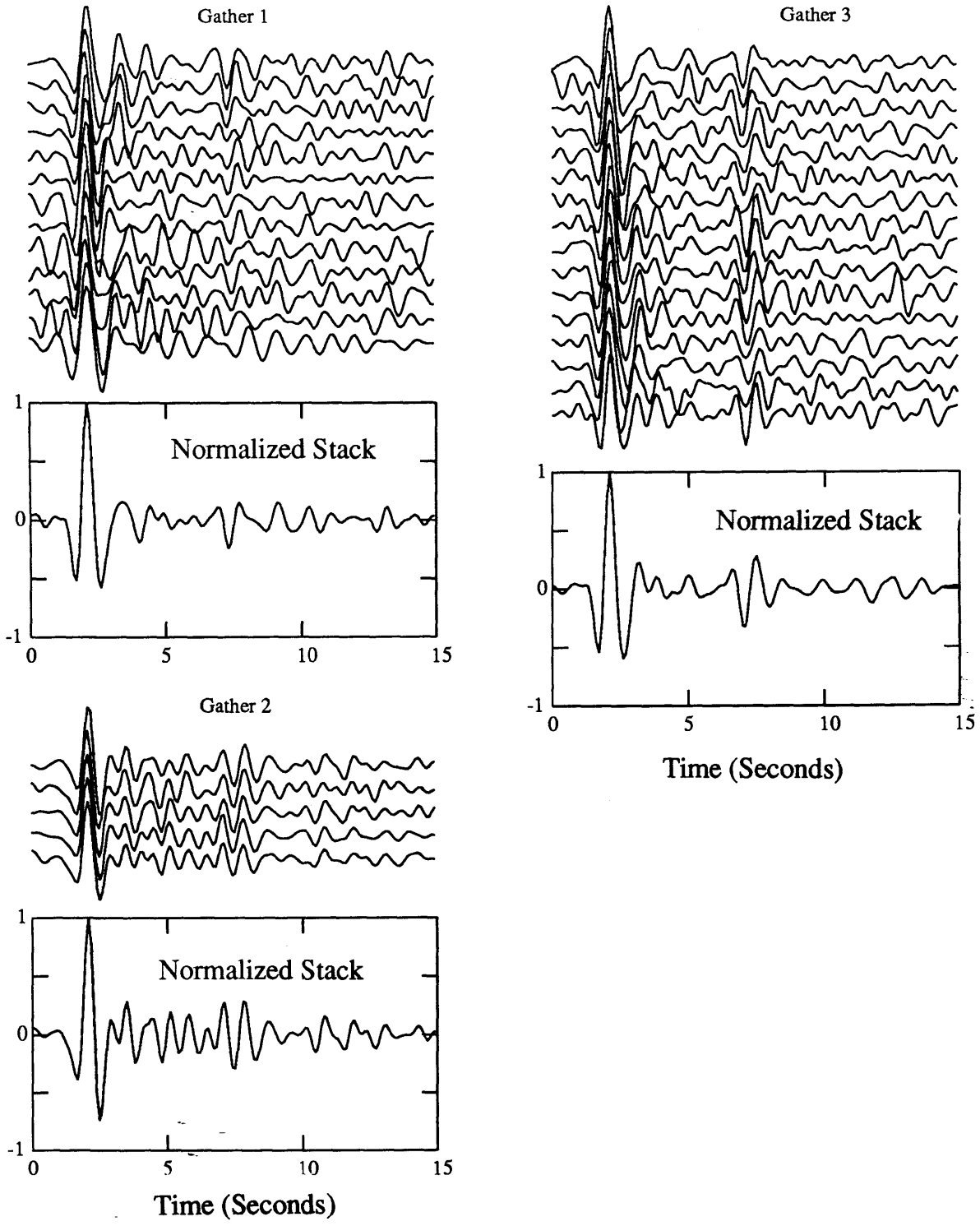

Figure 2: Data Gathers from the Station BVT, located in Baltimore, Vt. Gather 1 is from the South, Gather 2 from the north-northeast and Gather 3 from the northwest. All traces are normalized and have had their natural source function converted into a common wavelet.

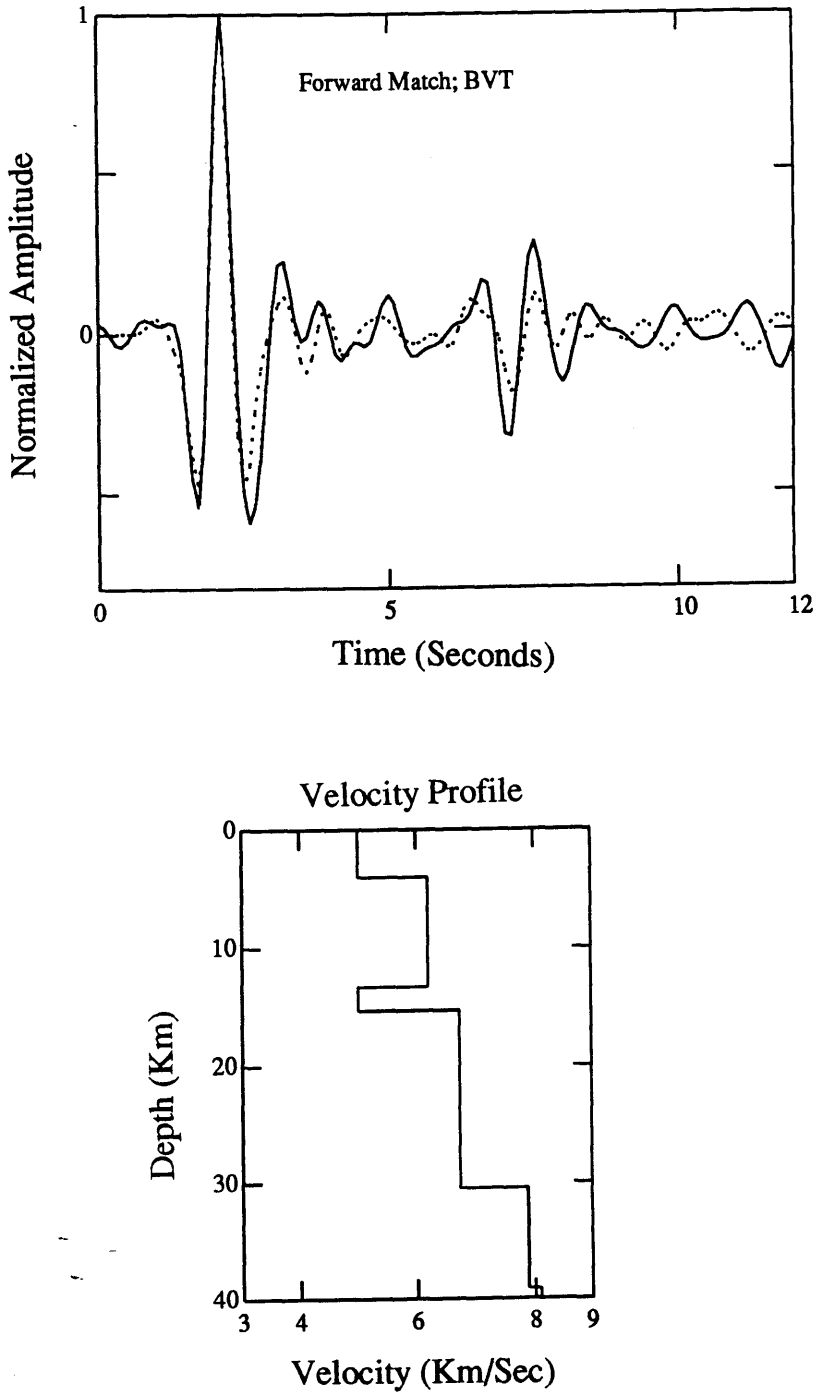

Figure 3: Best forward waveform match for BVT station gather 3. On top we plotted the stack of the 12 traces in the gather (solid) and the best fit to the data. Below is the model derived via forward modeling.

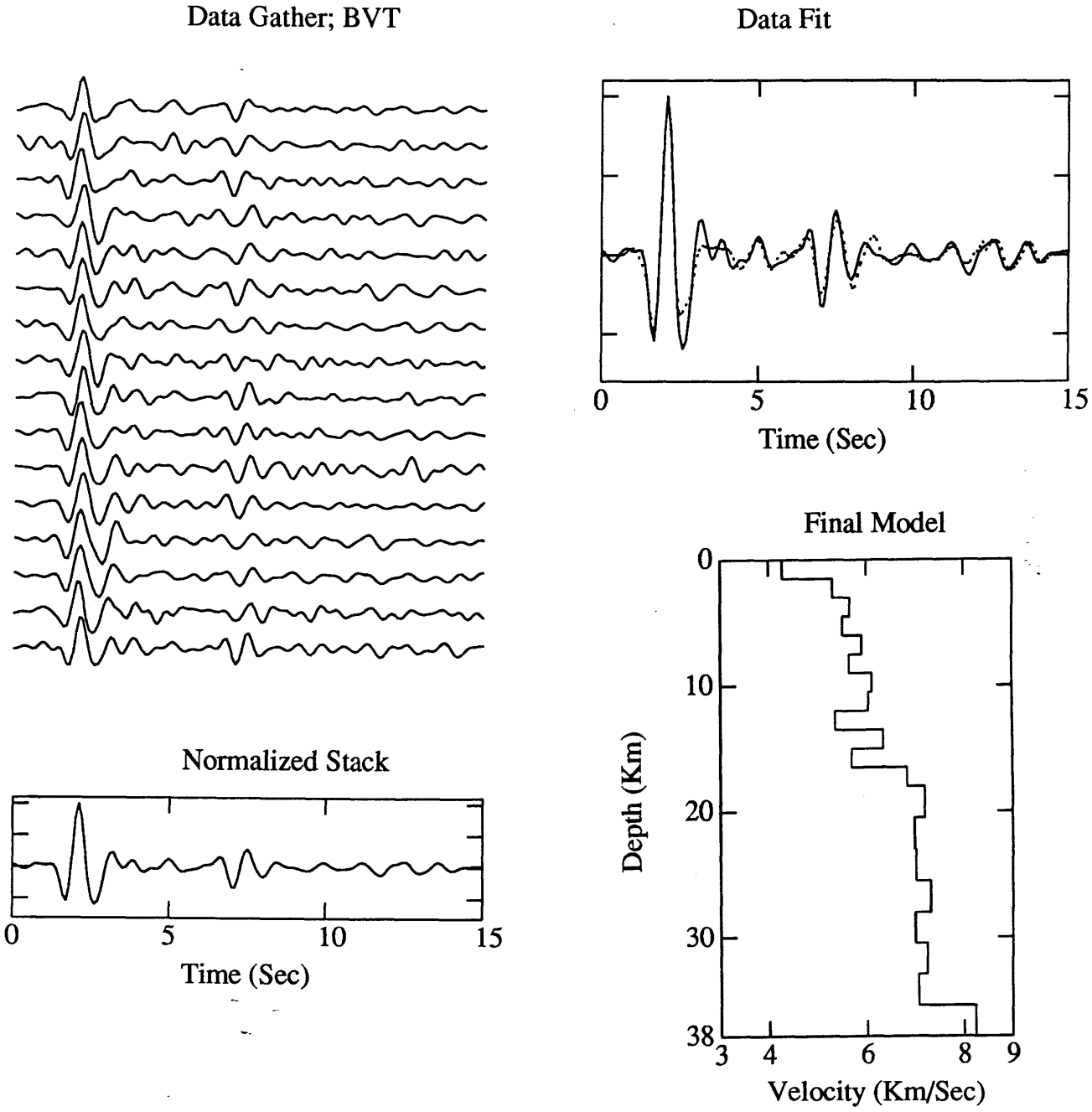

Figure 4: Waveform inversion results from BVT for the data gather of Figure 3. On left are traces in the gather, with the stack below, on the right is the best fitting prediction and the derived model.

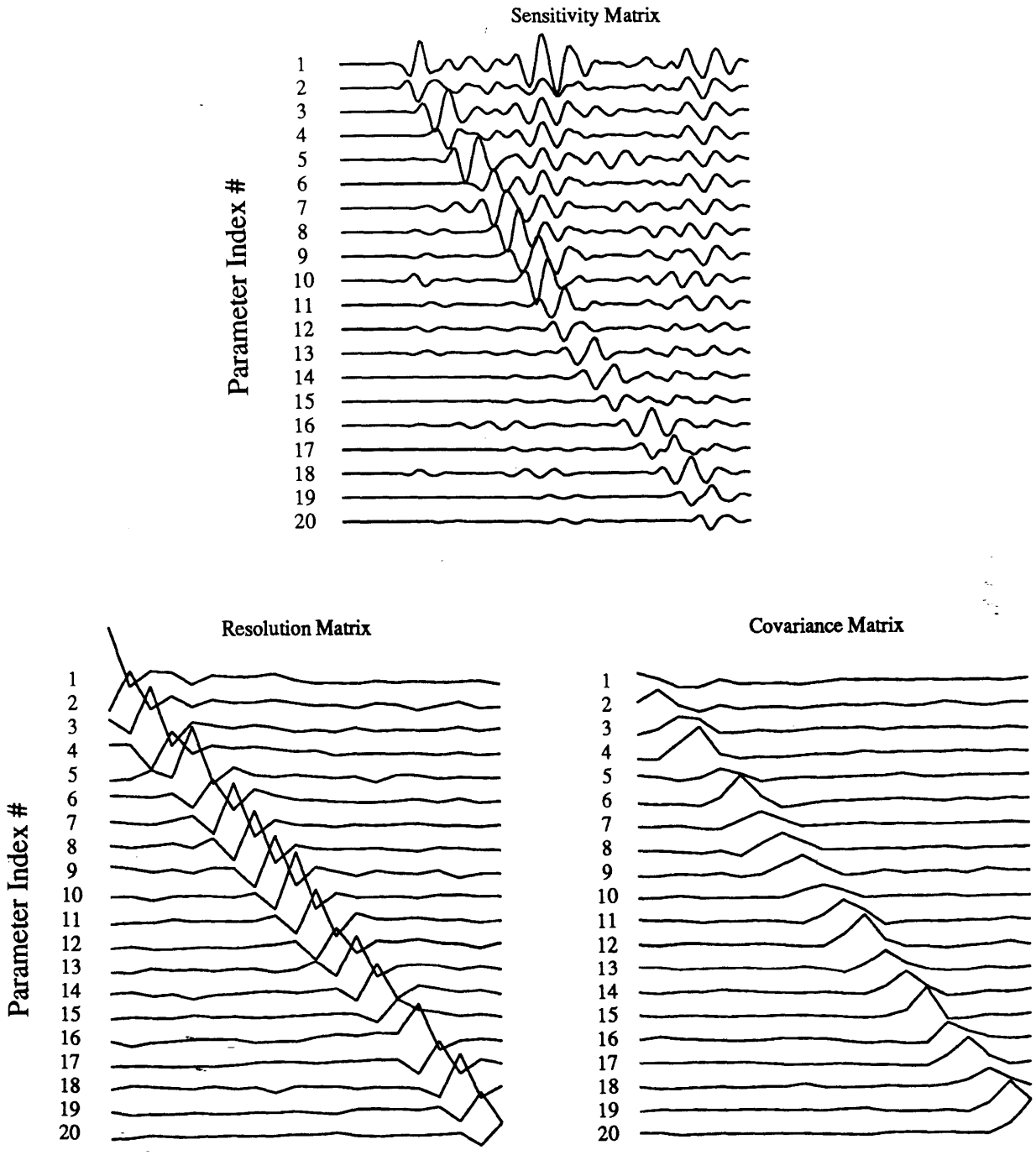

Figure 4b: Addition information from the waveform inversion for BVT data gather-3. On top is the sensitivity matrix of the final prediction, and below are the model resolution and covariance operators.

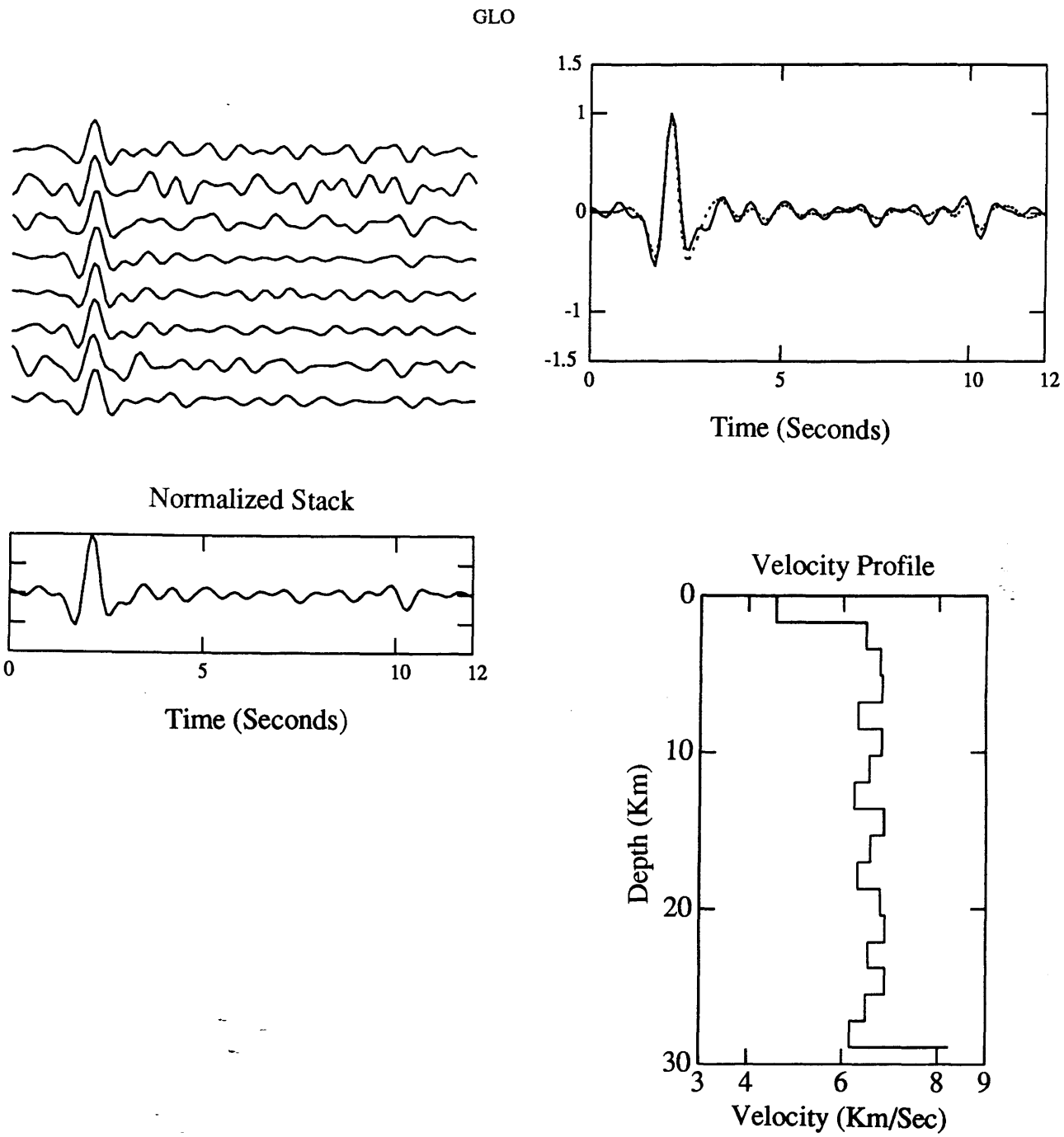

Figure 5: Waveform inversion results from GLO. On the left are the traces in gather, with the stack below, on the right is the best fitting prediction and the derived model.

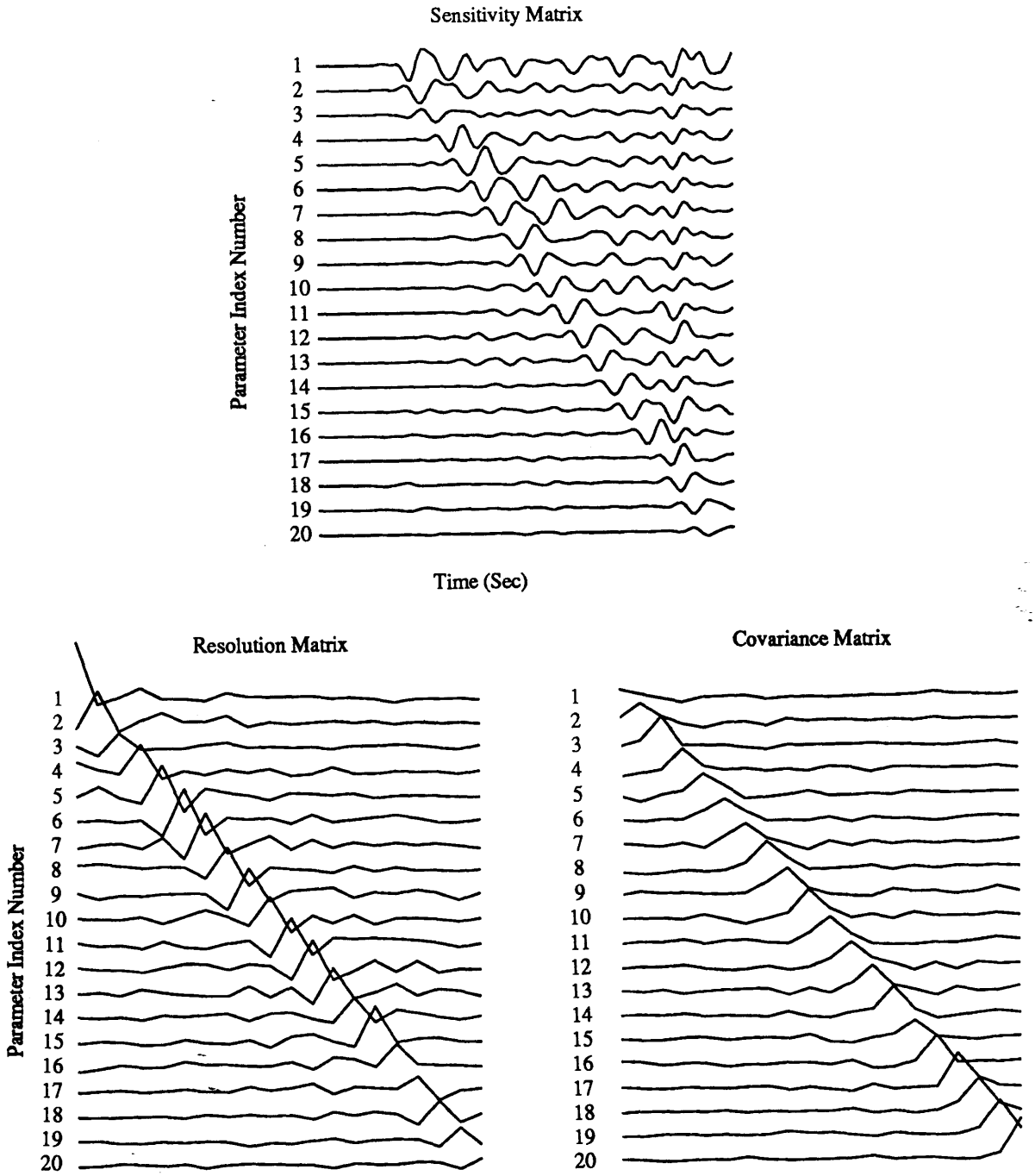

Figure 5: Addition information from the waveform inversion for GLO data gather. On top is the sensitivity matrix of the final prediction, and below are the model resolution and covariance operators.

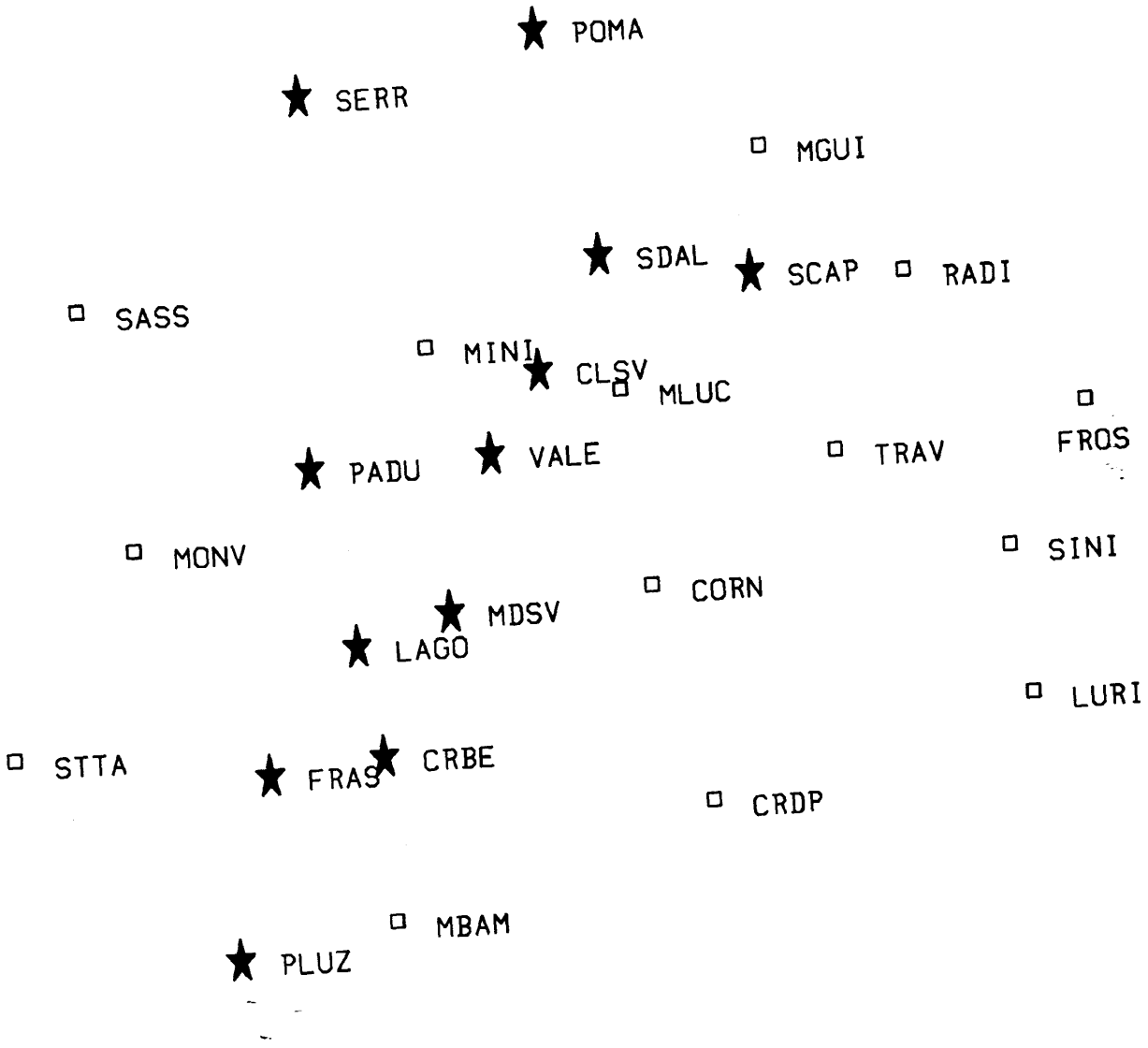

Figure 6: Stations in the ENEL network where waveform inversions were performed (stars). See Table 2 for station information.

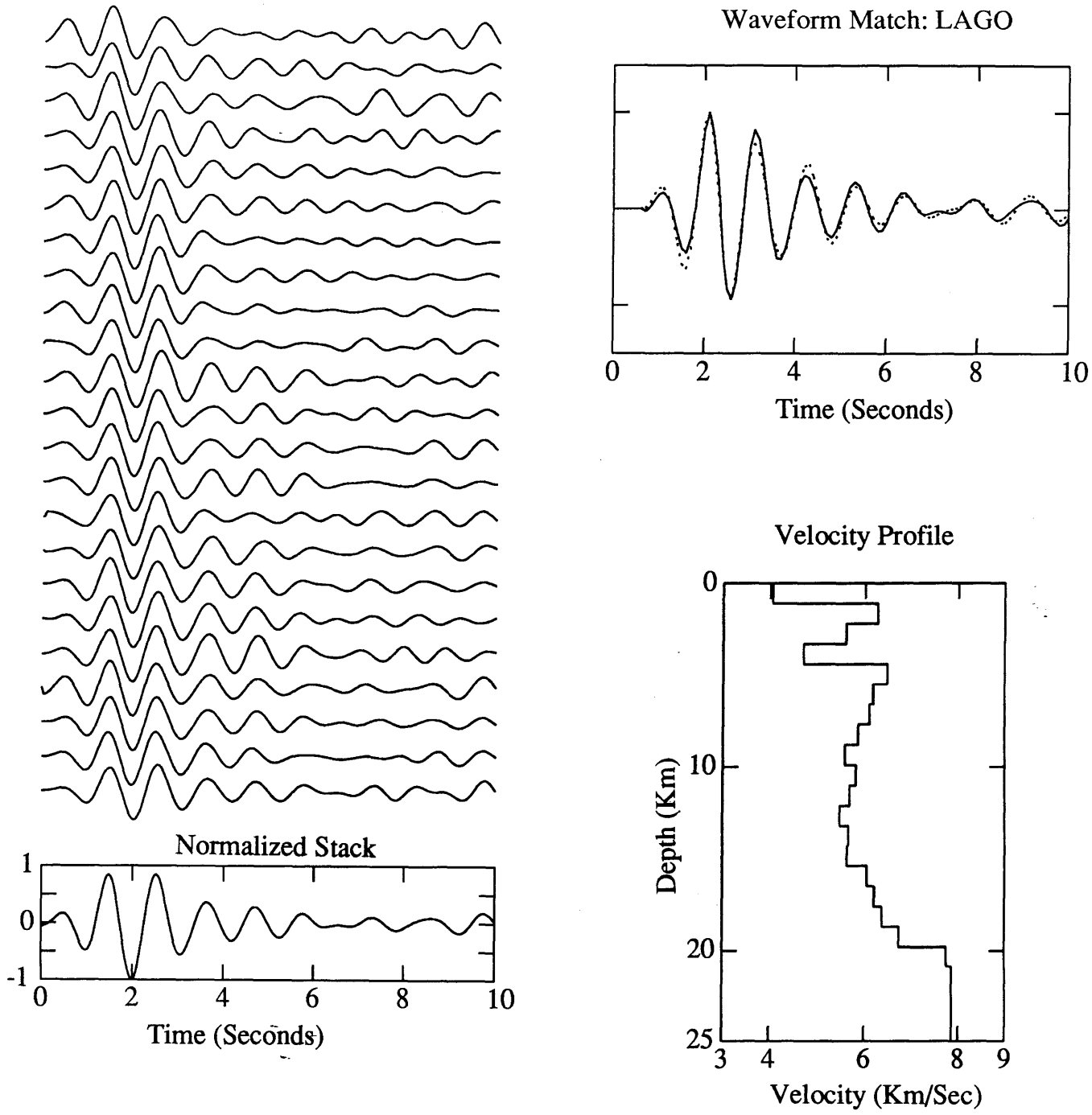

Figure 7: Waveform inversion results for ENEL Station LAGO. On the left are the vertically incident source equalized data which went into the data gather. On the right is the waveform comparison (top) with the actual data (solid line), and the model which produced this best fit.

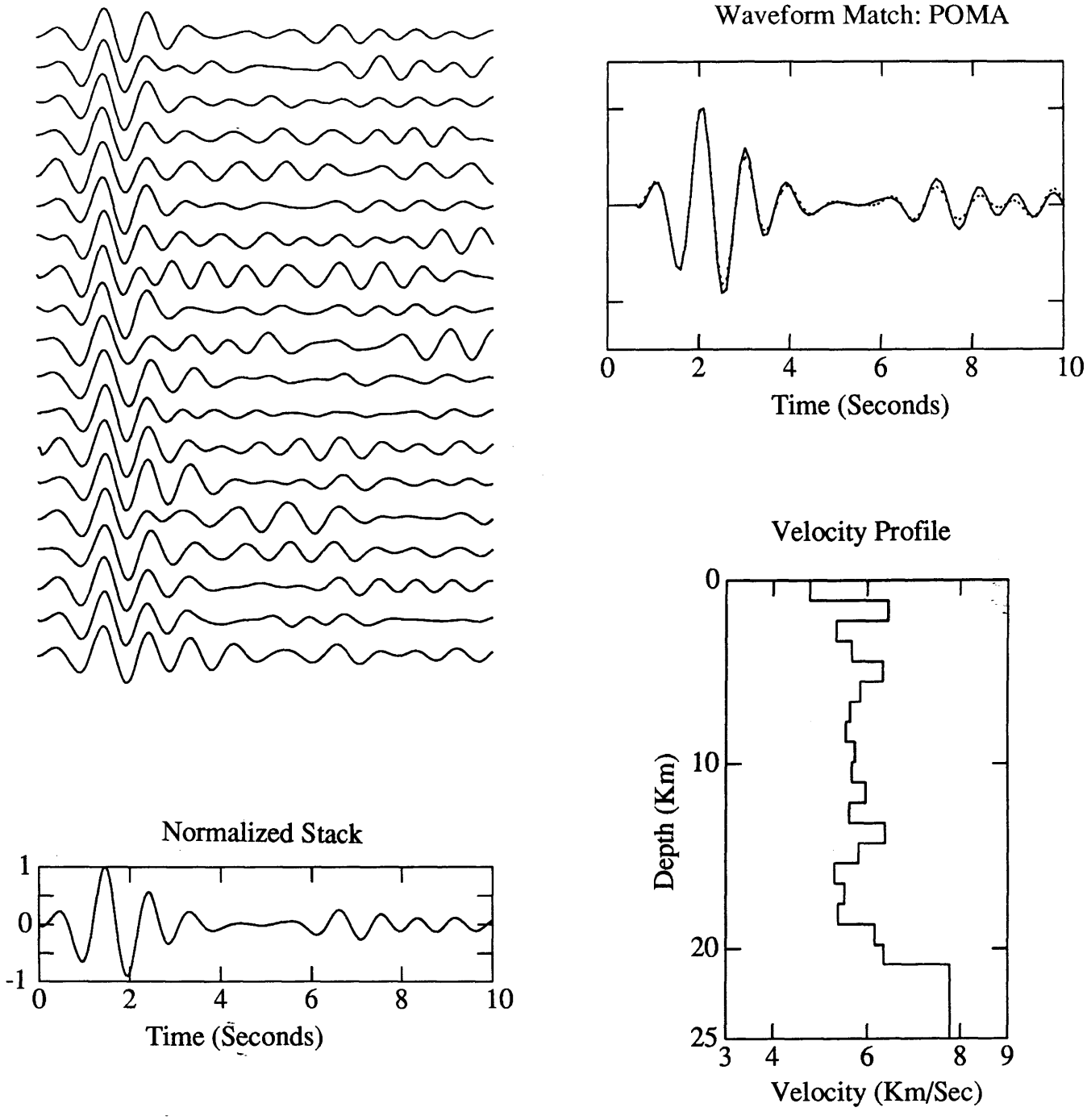

Figure 8: Waveform inversion results for ENEL Station POMA. On the left are the vertical incident source equalized data which went into the data gather. On the right is the waveform fit (Top) with the actual data a solid line, and the model which produced this waveform.

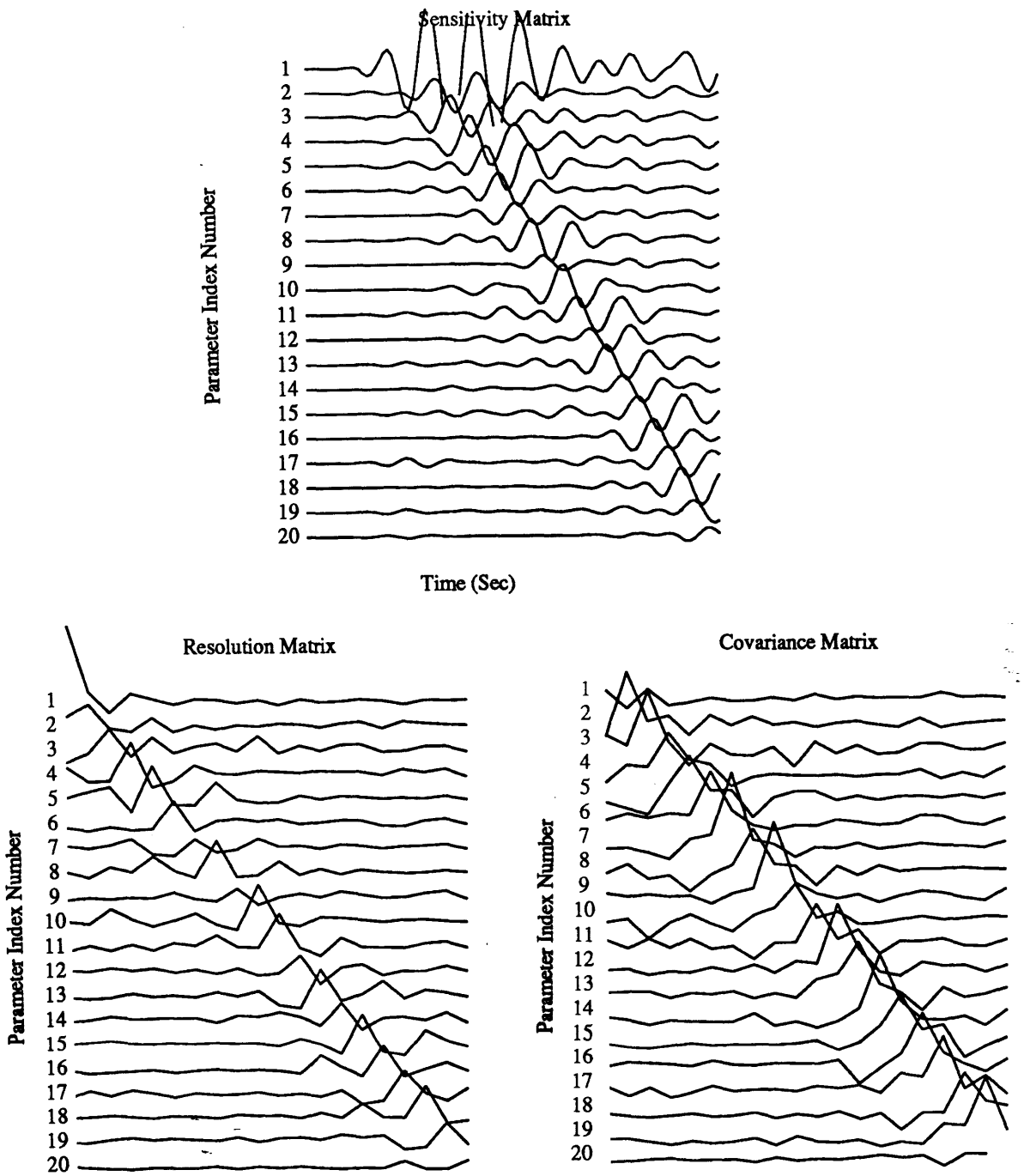

Figure 9: Additional inversion information for Station LAGO. Top: sensitivity matrix of the final model (see Figure 7), each trace represents the sensitivity of the seismogram to perturbation in the P-wave velocity of the layer. Bottom: Resolution matrix for the final model (left) and covariance matrix for the final model (right). See text for discussion.

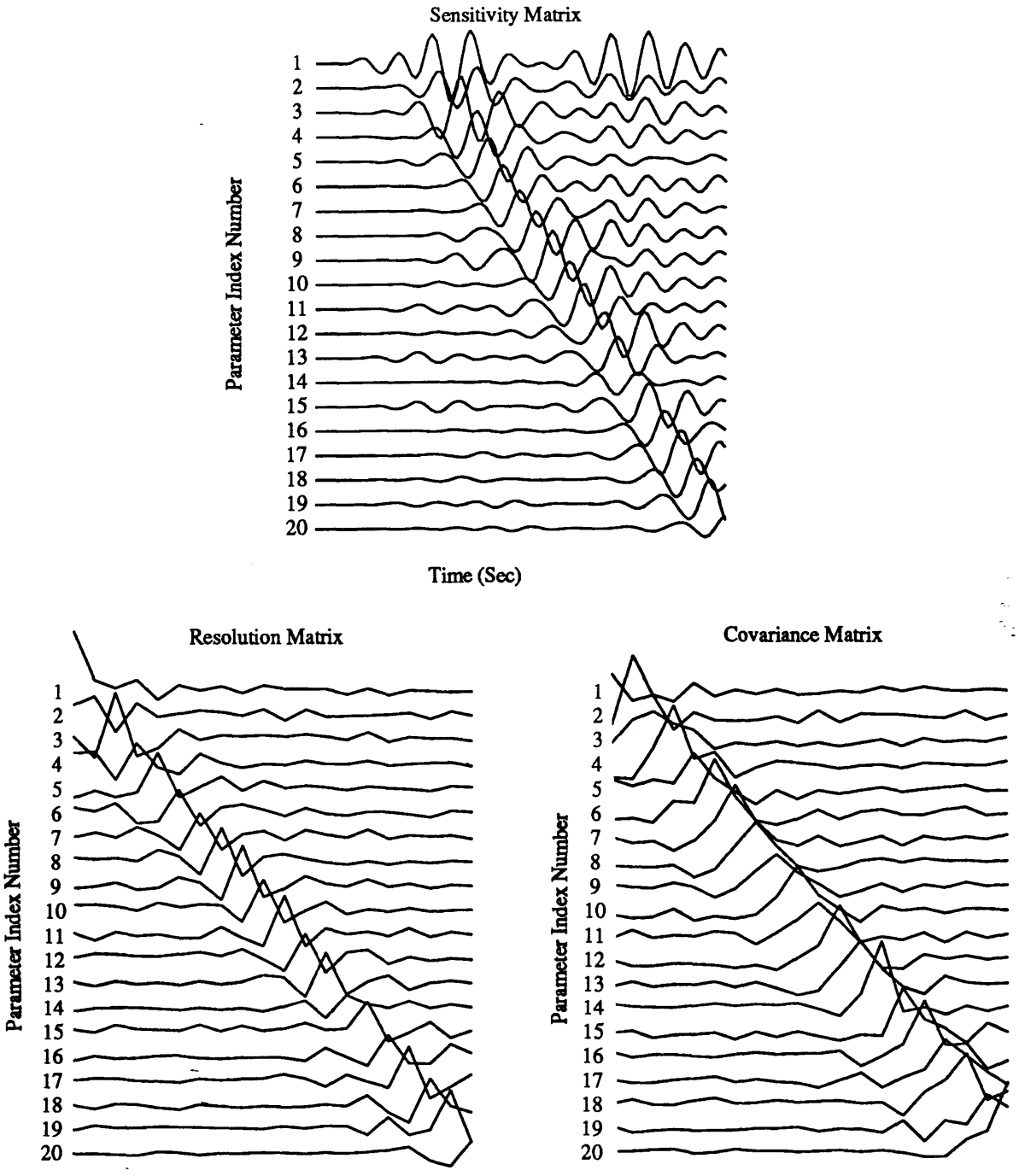

Figure 10: Additional inversion information for Station POMA. Top: sensitivity matrix of the final model (see Figure 8), each trace represents the sensitivity of the seismogram to perturbation in the P-wave velocity of the layer. Bottom: Resolution matrix for the final model (left) and covariance matrix for the final model (right). See text for discussion.

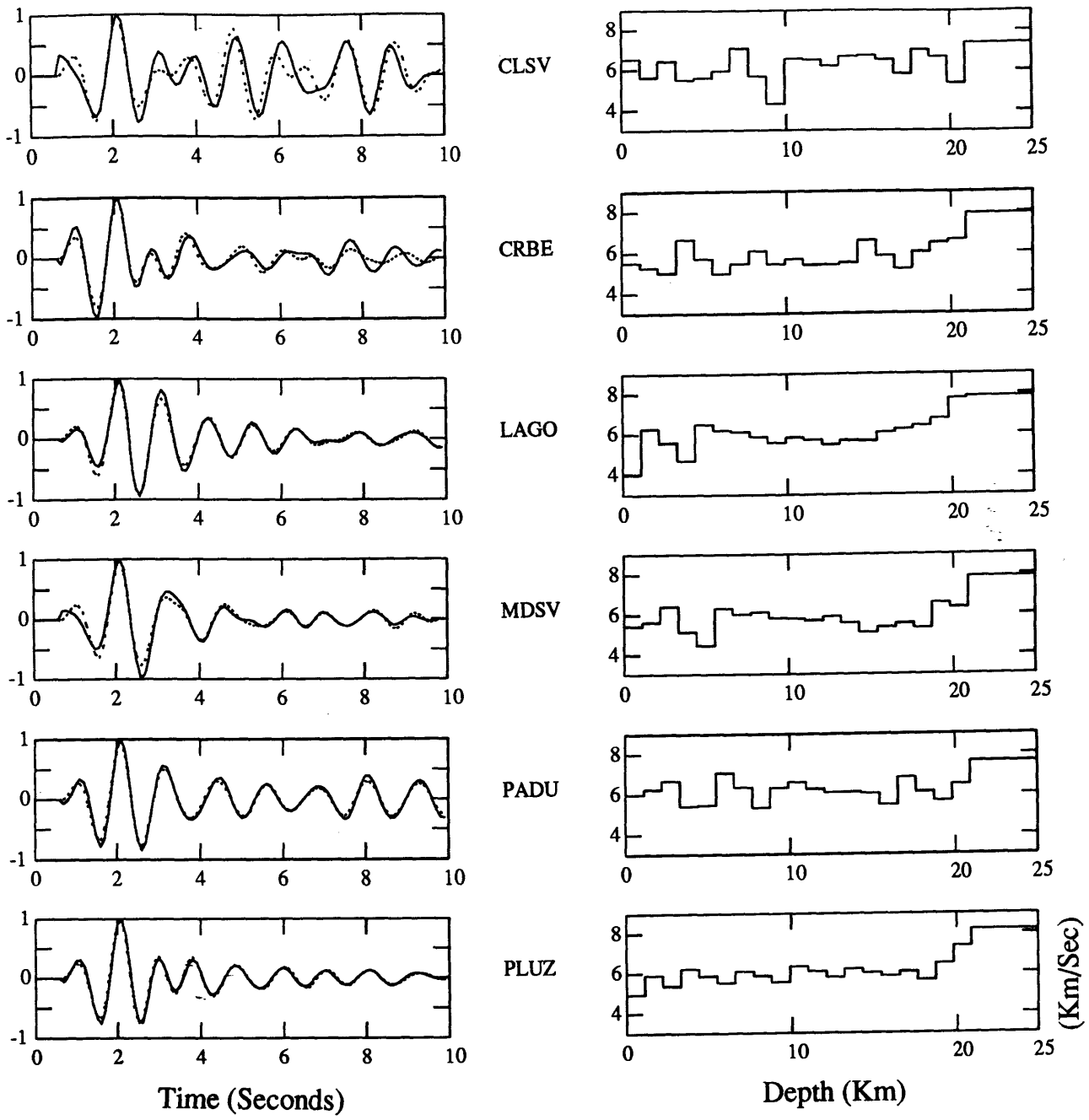

Figure 11: Inversion results from the ENEL data. On the left is the match to the data with the final prediction dashed. On the right is the final velocity model.

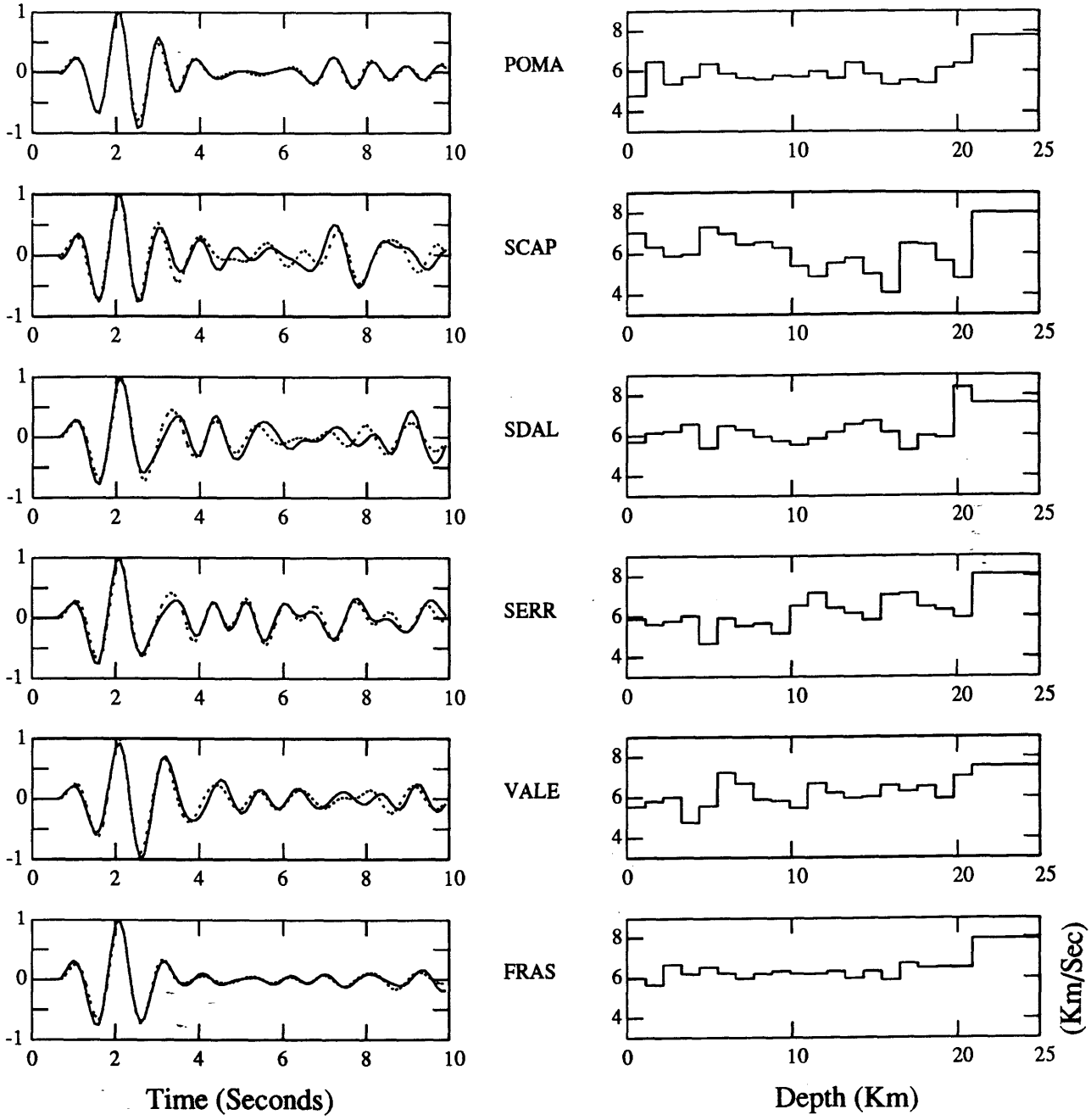

Figure 11 (Continued): Inversion results from the ENEL data. On the left is the match to the data (final prediction dashed). On the right is the final velocity model.

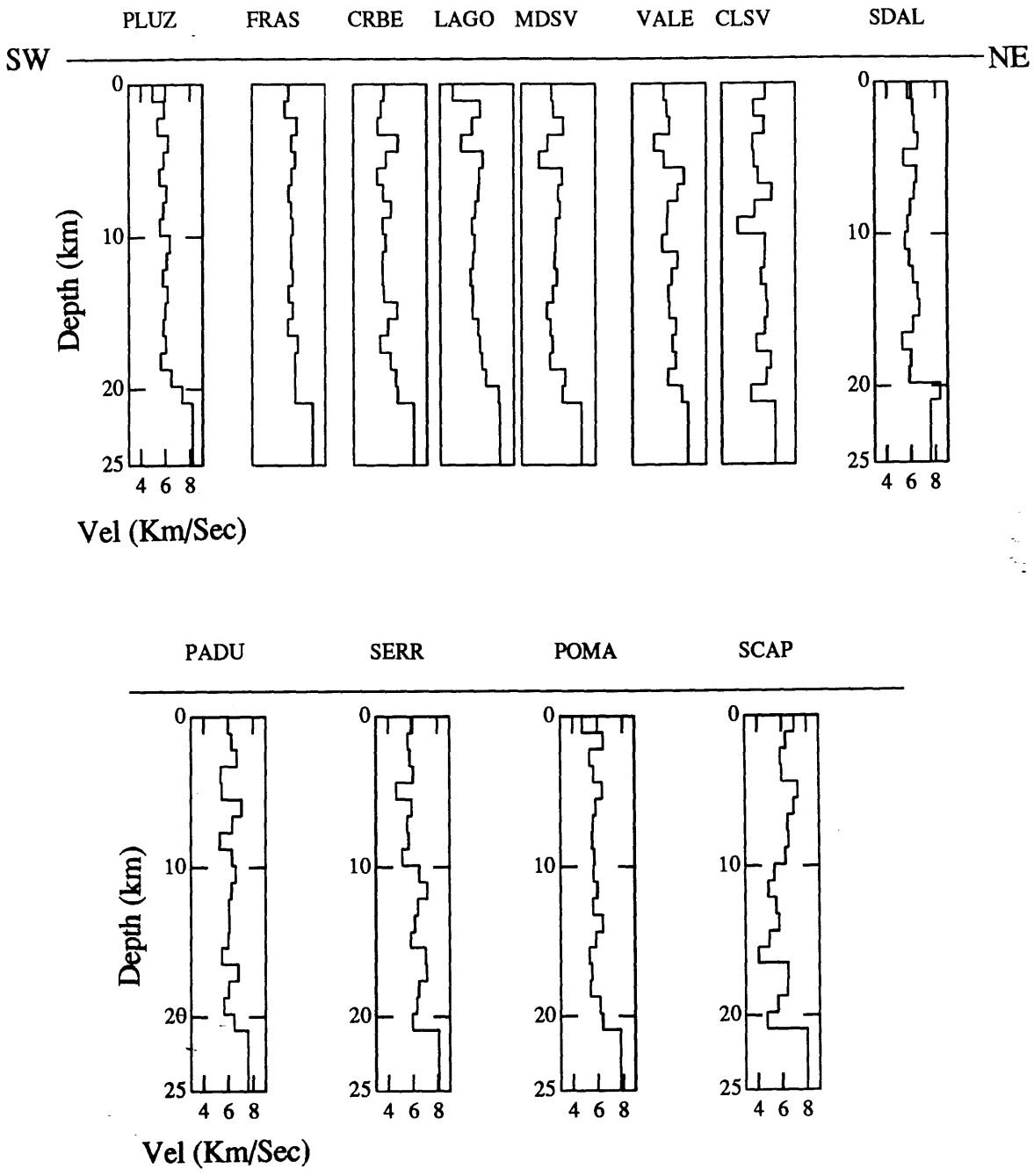

Figure 12: Cross-section of waveform inversion results along a strike SW NE through the center of the network.

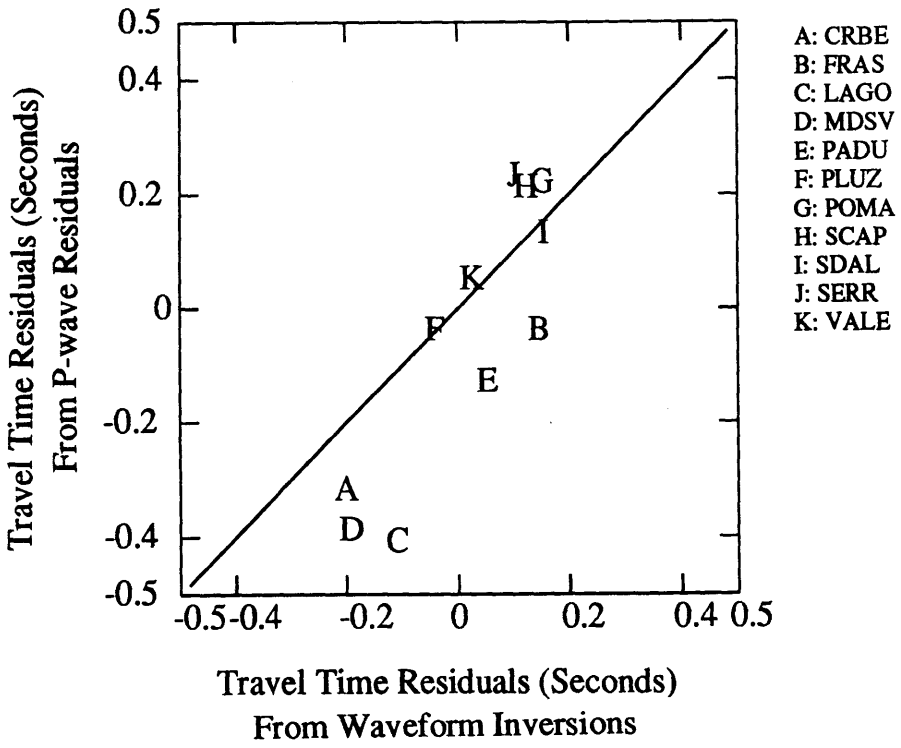

Figure 13: Travel time residuals for the inversion derived models plotted against the travel time values derived in Chapter 2.

Chapter 7

Discussion and Conclusions

7.1 Introduction

The Larderello geothermal field is located in southwest Tuscany about 100 km south of Florence, Italy and is situated within the complicated geologic and tectonic setting of the Inner Appennines (Bagnoli et al, 1979; Puxeddu, 1984; Boccaletti et al., 1985). One of the main objectives of this thesis is to examine the seismic velocity structure of this area by developing and implementing various techniques of teleseismic waveform analysis. We supplement what is currently known about the regional crustal characteristics, explore a part of the crust (below 6 km) which has not previously been significantly imaged with seismic methods, and formulate a model of this dynamic geophysical environment. A second goal of this project is to determine the overall usefulness of teleseismic body wave observations as applied to the problem of crustal velocity structure analysis. We investigate the inherent qualities and limitations of vertical component teleseismic P-waveforms and develop techniques to take full advantage of these data.

Two new tools are developed to enhance the usefulness of teleseismic P-waveform data. The first is an optimization scheme based on the simulated annealing approach and is used to determine accurate measures of teleseismic phase arrival times (see Chapter 2). The second technique (described in Chapter 4) is used to determine the source function for each teleseismic event and to re-shape the event-dependent wavelet into a common and repeatable

function. The proper application of this source equalization scheme makes a number of analysis techniques available to us because we are able to process data recorded at a single station from *different* events without contaminating the results with the ambiguity of source, raypath and crustal effects. The fact that we have shown these data enhancement techniques to effectively improve the usefulness of vertical component teleseismic data assures us that these methods have a wide base of application.

In this chapter we first review geologic and tectonic background of the Larderello geothermmal area as well as some of the geophysical observation made in this region in Section 7.2. The results of the three separate studies carried out in Larderello which utilize the data enhancement techniques described above and the high quality teleseismic P-wave data collected on ENEL's 26 station seismic monitoring network are presented in Section 7.3. In Section 7.4 we discuss our teleseismic waveforms results within a general tectonic framework of the Larderello region, compare our findings with other geological and geophysical data and develop a geophysical model of this area. In Section 7.5 we present our final comments and conclusions about vertical component teleseismic P-wave data as well as the methods we have developed to determine crustal velocity characteristics.

7.2 GELOGIC AND GEOPHYSICAL BACKGROUND OF LARDERELLO

The Larderello geothermal field is located within the complex structure of the Apennines Mountains which run down the center of the Italian Peninsula. Most Italian geothermal settings lie in the inner Apennines (toward the Tyrrhenian Sea) and are characterized by a complicated tectonic history. Larderello is in southwest Tuscany and has had a tectonic history similar to that of other geothermal areas which exist in the NW-SE trending tectonic belt (Mt Amiata, Mt. Cimino, Mt. Vesuvious, Mt. Etna, for example). This area is characterized by 3 main geologic units (see Figure 1-5): the cap rocks comprise a sequence of clayey flysch and conglomerates which is underlain by a series of folded sedimentary nappes, which are in turn underlain by a metamorphic basement composed of phyllites and

quartzites strongly corrugated during the Hercynian orogeny. A brief description of the geologic and tectonic background of the Tuscan region as well as a description of other geophysical observation made in Larderllo follows below. A more complete discussion of the Tuscan region can be found in Puxeddu (1984) and Boccaletti et al. (1985).

During the Mid-Triassic to Lower-Miocene a thick layer of carbonate rocks was deposited in the shallow Ligurian-Piedmontese Ocean basin. Collectively referred to as the Tuscan Series, these sedimentary rock were deposited as a series of basal evaporites and anhydrites, followed by dolomites, limestones and finally marls and sandstones and lie directly above an older (Paleozoic) metamorphic basement complex. To the west of the Tuscan carbonate deposits was a Jurrassic to Mid-Miocene Ligurian flysch depositional regime (Puxeddu, 1984). This facies consists of 700 to 1000 m of clayey limestones and sandstones. Both the Tuscan Series to the east and the flysch deposits to the west were strongly deformed and mobilized during the last phase of the Alpine Orogeny (Upper Miocene). The Tuscan Series was detached from the the basement rocks and thrust eastward forming the Tuscan Nappe. Basal evaporites served as the slip plane for these events. The more westerly flysch sequence also slid eastward forming a complicated series of nappes and folds which overlay the Tuscan Series and the Paleozoic basement where the younger sediments were removed. Some basement metamorphics were mobilized during this phase and moved to the east as well.

The metamorphic basement rocks can be characterized by two units; the uppermost one is variable in age (Triassic to Paleozoic) and thickness (0 to 1000 meters) and can generally be thought of as metamorphozed terrigenous wedges. The lower unit is characterized by an increasing degree of metamorphism from top to bottom: phyllites and quartzites which give way to micaschists and gneisses. These basement rocks are of Ordivician to Silurain age and were strongly deformed and mobilized during the Hercynian Orogeny. Together, these crystalline rocks are referred to as the Paleozoic metasediment basement (Puxeddu, 1984).

By the end of the Miocene the long period of compressional deformation which produced the folded and thrusted nature of the sedimentary pile gave way to extensional tectonics in the Pliocene and Quaternary which continues to exist today (Batini et al., 1987). The

extensional regime is characterized by normal faulting, horst and grabben formations and rapid terrigenous depositions as well as the introduction of intrusive igneous rocks. Volcanics were extruded to surface levels at several locations to the south of Larderello, most notably at the Mt. Amiata Geothermal Field, which is another area of geothermal exploitation less than 100 km SSE of Larderello (Batini et al., 1988).

There are numerous geophysical data to support this simplified picture of the tectonic and geologic evolution of the region that include seismic reflection, seismic refraction, gravity magnetics, heat flow, well logging, and core analysis. An extensive seismic reflection program was established by ENEL in this geothermal area (Batini et al., 1983; Batini et al., 1984) in an attempt to understand the nature of the structure in the Larderello area as well as to gain insight into the mechanisms which produce the steam itself. In addition to detailing the subtle changes in the velocity structure of the upper 3 km in Larderello, Batini et al. (1984) have found an important seismic marker which exists within the metamorphic basement on nearly all reflection lines and which occurs at depths between 3 and 6 km. They interpret this feature (called the **K** Horizon) as a petrophysical anomaly which delineates the top of the contact aureole associated with the intrusive body. The zone which represents the **K** horizon appears to be highly fractured and may be filled with steam or hot fluids as well as authigenic mineral assembleges (Cavarretta et al., 1982; Del Moro et al., 1982; Batini et al., 1984). This feature is also seen on reflection data collected at the Mt. Amiata geothermal Field (Gianelli et al., 1988) where volcanics have been extruded to the surface. There has been little success in imaging the crust below this petrophysical marker; extensive scattering from the highly fractured metamorphic rocks higher in the crust make imaging deep arrivals difficult (Batini et al., 1983). The lack of penetration of seismic waves from surface sources to depths greated than 5 km in the crust makes conventional reflection techniques ineffective in Larderello for modeling the deep structure.

Many of the recent wells drilled for steam production in the Larderello area have been cored and extensively logged using appropriate wireline logs (Batini et al., 1983, Batini et al., 1984). Well depths of 4 km have been reached, and over 1000 core samples have been gathered (Puxeddu, 1984). These data have been instrumental in the interpretation of

surface seismic data as well as the petrophysical description of the mid-crust. The discovery of granitic-aplitic dikelets (Batini et al., 1983) have been used to support the hypothesis of high temperature granitic intrusions as the heat source in the area. The timing of the emplacement of the intrusion is estimated to be about 2.5 mybp (Batini et al., 1983) from the Rb-Sr and K-AR ages of minerals cored in deep wells in Larderello (Del Moro et al., 1982). The temperature gradient generally exceeds 1 $°C/10$ m, with a maximum of about 3 ° C/10 m recorded near station SDAL. Temperatures in excess 300 $°C$ at 2 km are common in most areas with a maximum of about 400 $°C$ at 4 km in a well near station LAGO.

Two seismic refraction experiments have been carried out in the Tuscan region; one in 1974 (Morelli et al., 1977) and the second in 1978 and 1979 (Giese et al., 1980). One recording line in the more recent experiment came close to the production area in Larderello. From these data, Giese et al. (1980) determined V_p to be in the range of 2.6 to 6.5 km/sec from 3 to 8 km, and V_p of 6 to 6.3 at depth of 3-8 to 14-25 km, and V_p of 7.4 to 7.9 to the Moho. Giese et al. (1980) find the Moho to exist at a ranges of depth from 20 to 32 km in SW Tuscany. They also observed very few S-waves from the lines which passed near Larderello, which led Puxeddu (1984) to suggest the existence of partially molten material in the area at the depth ranges of 10 to 17 km and molten material where the Moho may normally be expected. Giese et al. (1980) report a dominant lower crust low velocity zone existing over broad region of SW Tuscany with V_p reduced to about 4 to 6 $\frac{km}{sec}$ for thicknesses of about 5-8 km. They also report that strong variations in Moho depth can be seen in the Larderello area with a thinner crust to the southeast (to about 20 - 25 km depth) and a deeper Moho to the northwest (depths to about 30-35 km). The rapid Moho depth variation could be interpreted as an important fault feature affecting the entire crust (Puxeddu, 1984). Landsat image analysis has led to the observation that geothermal regions in Italy are predominantly located in areas where strong NE linearments intersect the dominant NW/SE tectonic grain of the Apennines.

Morelli et al. (1977) postulated a doubling of the Tuscan crust through the subduction of the Corsician continental crust beneath the Adriatic Plate (Apennines) from the interpretation of low velocities (6.8 $\frac{km}{sec}$) observed at depths in excess of 60 km. Calcagnile and

Panza (1979) reject this model, and Giese et al. (1980) find no evidence to support it in the Larderello area.

In 1978 ENEL established the first seismic recording stations in the Larderello area to monitor the seismic effects of a reinjection program at some of the geothermal production sites (Batini et al., 1985). These stations also provide important information about natural seismic activity which have been correlated with areas of geothermal interest. The spatial and temporal of distribution of seismic activity reveals that in the center of the region earthquakes occur more frequently and at shallower depths than on the periphery. This pattern roughly follows the **K** horizon and is discussed below. In addition, Batini et al. (1985) have determined focal mechanism solutions for many of the 1000 events detected between 1978 and 1982 (M_L between 0.0 and 3.2) and find that normal faulting predominates in the region with an axis of maximum tension along a NW-SE direction. This trend is in general agreement with the geologic features observed in the area (Batini et al., 1985).

Gravimetric surveys have revealed that a regional Bouguer gravity low exists over central and southern parts of Tuscany (Cataldi et al., 1978) which suggest that a low density intrusive body may have regional extent in this area. Within the geothermal regions of Larderello and Mt. Amiata negative Bouguer anomalies are correlated roughly with areas of high heat flow (Calamai et al., 1977). The negative anomaly of about 25 mGal in Larderello has been explained by the presence of granitic plutonic intrusions (Monton, 1969). At the Mt. Amiata geothermal area two-dimensional gravimetric modeling has revealed a low density body at depth of 6 to 11 km associated with a gravity low of about 20 mGals (Gianelli et al., 1988).

7.3 REVIEW OF RESULTS FROM LARDERELLO

The teleseismic studies of the Larderello region include: travel time residual inversions (Chapter 3), ray parameter dependent trajectory stacking (Chapter 5) and waveform inversions (Chapter 6). We show in this section the usefulness of each method, explain which aspects of the velocity structure each method is targeted to explore, and demonstrate a high level of agreement in the results among the three separate applications.

Travel Time Residuals

The analysis of teleseismic travel time residuals observed on the Larderello Seismic Network has revealed a sharp low velocity zone in the center of the geothermal area. Residuals from 101 teleseismic events, automatically determined with the implementation of a simulated annealing optimization procedure, are inverted to produce an image of the anomalous low velocity zone. The top of this region is constrained to be below 6 km depth from local earthquake seismicity patterns. The low velocity zone exists to a depth of greater than 20 km, extends into the upper mantle and broadens with increasing depth. The results of this study are comparable to those from other geothermal areas where the Aki et al. (1977) block inversion method was used: The Geysers – Clear Lake Geothermal field in California (Oppenheim et al., 1981); Yellowstone (Zandt, 1978; Iyer et al., 1981); Eastern Snake-River Region (Evans, 1982): Hawaii (Ellsworth, 1977); Long Valley, California (Sanders, 1984); The Coso Geothermal Area (Reasenberg et al., 1980); Roosevelt Hot Springs, Utah (Robinson and Iyer, 1981); and San Francisco Mt., Arizona (Stauber, 1982). See Iyer (1988) for a review of these studies.

Figure 1 shows the average station travel time residuals for all 101 events used in the analysis. We see from this map that the strongest low velocity area is concentrated in the center of the network. Strong positive residuals (slow) of up to 0.6 second are observed, in contrast to the negative (fast) residuals up to -0.4 second on the periphery. The contour of zero residual is aligned to the northeast with dimensions of approximately 25 by 40 km. The total travel time differences of about 1.0 second represent a very strong travel time anomaly for a small region (approximately 25 km between average extremes). To produce a relative P-wave delay time of one second for a PKIKP event (near vertical ray) from crustal effects requires about a 35% velocity decrease along the entire 20-25 km crustal raypath. Velocities of rhyolite melts (Murase and McBirney, 1973) and dacite melts (Hayakawa, 1957) of about 4 $\frac{km}{sec}$ would represent a 38% velocity reduction of a 6.5 $\frac{km}{sec}$ velocity unmelted country rock. This indicates that the low velocity anomaly exists either as a large region of melted material concentrated entirely in the crust or, more likely, that the zone penetrates the crust into the mantle to depths below 20 km. From the analysis of refraction data, Giese et al. (1980) have

found crustal P-wave velocities about 4 $\frac{km}{sec}$ in the deep crust and have observed a dramatic lack of shear waves in the lower crust in correspondence to the LVZ (at about 20 km). This has led Giese et al. (1980) and Puxeddu (1984) to conclude that a zone of melted or partially melted material exists at the base of the crust over appreciable regions of southwest Tuscany. Our findings from the travel time residual patterns reinforce this interpretation.

Figure 2 shows the results of the Larderello travel time residual inversion. These plots show the velocity perturbation for each of the five layers established to represent the crust and upper mantle in percent of the background velocity as contours of equal velocity perturbation. For the crustal layers (1, 2 and 3; from 6 to 21 km) the region of relative low velocity is confined to the center of the network in an area 25 by 40 km in extent with an elongate pattern to the northeast. This pattern coincides with the region of low amplitude teleseismic P-waves, high heat flow, negative Bouguer gravity anomaly and elevation of the **K** reflection horizon. The total lateral extent of the LVZ (about 1000 km^2) is similar to the region of uplift in the area of the Mt. Amiata volcano, located about 60 km to the SE of Larderello, which is associated with the intrusion of a large batholith at the end of the Apline orogenic episode (Gianelli et al., 1988). Layers 4 and 5 of the inversion model (depths from 21 to 41 km) also have a distinct low velocity pattern in the center of the network with relative velocity perturbations are still quite large at these depths (10% in the center). The zone of maximum low velocity migrates to the northeast at greater depths and increases in area. Since we have no stations outside the Larderello geothermal area in this analysis, we cannot scale our velocity perturbation results to absolute velocity levels in the crust. The contour of zero velocity perturbation cannot be used as a delineation of regions in the crust without deep-seated low velocity zones. In fact, from the gravity and temperature observations made in the area, it is likely that the entire region has locally reduced crustal velocities. Slices through the final model based on the travel time residual inversion (Figure 3) show the pattern of the strong LVZ vertical cross section. The SW to NE slice (Figure 3a) shows that strong velocity reductions (up to 18%) from depths of about 6 to 16 km are necessary to satisfy the travel time residual observations. The LVZ in the upper part of the crust is about 20 km wide. Deeper in the crust and in the upper mantle the perturbations in velocity

are smaller and cover a larger region. However, the velocity results in the lower part of the model may be corrupted by smearing effects in the inversion. This technique distributes travel time residuals into the model by back propagating the residuals equally along each raypath, and when criss-crossing ray coverage is not sufficient in an area artificial velocity anomalies can be created. An insufficiency in the ray coverage may be accentuating the deep and widespread low velocity area of Layers 4 and 5 where velocity reductions of up to 10% are required by the data and where the LVZ covers an area about 35 km wide. Given the strong variations in travel times observed in the data and the level velocity reductions required if all of the velocity anomaly exists in the crust, we believe that the low velocity zone predicted by the travel time inversion is reasonable. The NW to SE slice through the Larderello area (Figure 3b) shows a similar pattern of low velocity as the previous slice, with velocity reductions of about 10% existing from the top layer (6 km) to a depth of 41 km. The width of the LVZ is about 15 km in the crustal layers and increases in width at depth. In the mantle (Layers 4 and 5 at depths of 21 to 41 km) we see that the LVZ does not exist continuously from NW to SE but rather is interrupted by an area of relatively higher velocities. This pattern indicates that the deep LVZ does not exist as a large continuous body but instead as a series of intermittent low velocity regions.

Ray Parameter Trajectory Stacks

In order to refine the picture of the crust derived from the travel time residual inversion, we implement the *rpt* stacking method to all but 2 stations of the Larderello Geothermal Field Seismic Network. Stations FRAS and MGUI were removed from the analysis because they recorded very few usable events during the period of interest and do not have adequate ray parameter coverage. The results of this analysis are shown in Figure 4, where the stack power profiles are displayed on a map of the Larderello Seismic Network to illustrate the regional distribution of these results; stack power is plotted against vertical two-way travel time. There are a number of key points that are evident from this figure.

1. In general, we see that there are very strong reflections coherent across most stations. This indicates that nearly horizontal features exist under most stations in the region.

2. The stations in the central and southwest part of the network have a more complicated

upper-crustal reflection pattern than stations on the periphery (two-way travel times of less than 5 seconds or depths to about 12 km). This is indicated by the presence of numerous peaks in the *rpt* plots arriving at different two-way vertical travel times at different closely spaced stations. There are several stations with a weak arrival at about 6-8 seconds indicating that a reflective region of the crust exists between 16 to 22 km in depth. These stations are plotted in cross-section in Figure 5a.

3. The stations on the periphery of the network (SINI, LURI, POMA, SERR; Figure 5b) are dominated by very clear, strong and isolated arrivals at about 5.5 seconds after the direct P-wave arrival and are primary P-wave reflections from discontinuities at 16 to 18 km in depth. In Figure 6 we show the stack of the vertical incident seismograms for 2 of these stations (SINI and LURI) and we see coherent and repeatable high amplitude reflections in the waveforms. Giese et al. (1980) and Puxeddu (1984) suggest that a region of partially or fully melted material exist at the base of the crust over an extended portion of Tuscany. In Figure 7 we show the refraction model presented by Giese et al. (1980) for this region and a synthetic seismogram derived from this refraction model (from a vertically incident teleseismic plane wave). In general, the synthetic waveform is similar to waveforms observed at stations located on the periphery of the network. These repeatable high amplitude arrivals at about 6 seconds after the direct arrival indicate that a strong low velocity zone must exist deep in the crust. We plot a map of arrival times of coherent deep crustal arrivals derived from the *rpt* method in Figure 8. We can see from this map that all peripheral stations have a common arrival between 5.5 and 7 seconds, or approximately 15 to 20 in depth. This feature is interrupted in the center of the network where no clear and coherent deep crustal reflector is present. From our *rpt* travel time results and from the observation of anomalously high amplitude reflections observed at the peripheral stations we confirm the existence of a regional scale lower-crustal LVZ beneath Larderello.

4. Of all the stations in the network, only three (SASS, MBAM and MLUC) have no observable peaks in the stack power plots after 4 seconds two-way vertical travel time (about 10 km depth). From a visual review of the seismograms recorded at these

stations, we conclude that deep reflectors may exist at each of these stations, but they are not imaged with this technique due to steep dip of the interface. This conclusion is drawn from the observation of numerous high amplitude arrivals in the waveforms which do fall along trajectories predicted with horizontal layers.

Waveform Inversions

In this section we present the teleseismic P-wave waveform inversion results from data recorded on the Larderello Seismic Network. Waveform inversions represent an important improvement over both the travel time residual and *rpt* analyses in determining the crustal velocity structure in Larderello Geothermal Field. With this method we utilize the entire waveform to determine the structure, which improves the resolution in depth and velocity of crustal velocity structure features. The analysis of the first few seconds of the waveforms, which cannot be made with *rpt* method due to source wavelet considerations, provides well controlled information about the seismic velocities of the upper 5-6 km of the crust. Information about the seismic velocity at these shallow depths is particularly important for geothermal production considerations.

We have focused our attention on 12 stations from the ENEL network which represent a good sampling of the geologic setting of the region. Seven of these stations lie roughly on a NE-SW strike through the center of the area, which is the strike used in Figures 3 and 5 above and is further utilized below. From a review of the waveform fits (presented on a map of the area in Figure 9 and in cross-section in Figure 10), we see that this procedure adequately determines models which satisfy the waveform observations. The match between the observed and predicted waveforms is generally excellent and in all cases the differences in the waveshapes (the misfits) fall within 2 standard deviations of the data vector. This measure of the stacked waveform standard deviation is determined during the data gathering procedure and represents the degree of variability in the seismograms comprising the data vector.

We were able to reach the final models from a wide variety of starting models without constraining the velocities of the crust. The only model constraint needed to produce rapid convergence was on the velocity of the deepest mantle layer. The velocity at this level is

constrained by the results of the travel time residual inversions of Chapter 3.

We superimpose the *rpt* results on the the plot of final inversion models (Figures 9 and 10) with arrows at the depths of discontinuities predicted by the *rpt* procedure. We see from these figures that the waveform inversion can reproduce most of the velocity features of the mid- and lower- crust determined with the *rpt* analysis. By calculating the travel times through all of the final inversion models, we can calculated travel time residuals predicted by the waveform inversion method. In Figure 11 these residuals are plotted against the travel time residuals derived in Chapter 3. We see from this comparison that the inversion procedure accurately reproduces the general velocity trends found in the direct P-wave travel time study. The stations which fall below the line representing equivalent travel time residuals (CRBE, FRAS, LAGO, PADU and MDSV) are all located in the same area within 8 km of each other (see Figure 6-6). We conclude from this pattern and from the cross-sectional view of the travel time residual results of Chapter 3 (Figure 3) that the low velocity anomaly in Larderello extends below the crust and continues to exist into the mantle .

The waveform inversions reveal important additional information about the crust not determined by either the travel time inversion or the *rpt* analysis. The first main finding comes from the initial 3-4 seconds of the data. This part of the seismogram is most sensitive to the upper 10 km of the media (see Figure 6-23, for example), and this region of the crust includes the **K** horizon, which is an important marker used in geothermal exploration in this region (Batini et al., 1984). The similarity of each trace in the data gathers (see Figure 6-7, for example) for the first few seconds confirms that the stacking criteria are best satisfied early in the waveforms and indicates that the results of the inversion in the upper-crust are the most reliable in the analysis. Later in the waveforms the variability in the seismograms is greater than in the first few seconds, and subsequently, the image of the deep crust is less reliable. From Figure 9, we see that the central 7 stations (from southwest to northeast we plot CRBE, LAGO, MDSV, PADU, VALE, CLSV and SDAL) all show distinct strong discontinuities at shallow depths (3 to 7 km) which strongly alter the shape of the first few seconds of the P-waveform. We correlate the depth estimates of this velocity discontinuity with variations in the depths of the **K** horizon along this profile (Batini et al., 1988) in Figure

12. We see from this plot that we are able to image the **K** horizon with the application of the waveform inversion technique. The peripheral stations (POMA, SERR, PLUZ and SCAP) show velocity discontinuities in the upper 8 km but these discontinuities are less strong than those of the central region. The station coverage on the edges of the network is not sufficient to infer a common interpretation of these features.

7.4 GENERAL DISCUSSION

The present geophysical setting of the Larderello Geothermal Field is the product of a long and complicated tectonic evolution. The basement rocks (below 2-3 km) are highly metamorphosed sediments of Paleozoic and Mesozoic age which have experienced intense periods of deformation, mobilization and fracturing over the last 200 million years. These rocks are overlain by a sedimentary pile of younger terrigenous and shallow ocean deposits of Triassic and Jurassic ages which were strongly folded and thrusted during the Alpine orogeny. At the end of the Alpine event hot granitic intrusions were emplaced into this regime. The modern expression of these events is complicated and numerous geological and geophysical studies have been carried out to investigate this region (Puxeddu, 1984). In this section we review our finding within this tectonic framework and develop a model of this dynamic region.

The anomalous region of the crust and upper mantle beneath Larderello which give rise to the low velocity features in the crust observed on teleseismic data in this area have strong effects on many other geophysical observations made in the region. The observed travel time residual anomaly, determined from the direct P-wave arrivals, correlates with observed gravity lows, heat flow highs, the shallowing of a dominant upper-crustal reflection (the **K** horizon) and diminished teleseismic P-wave amplitudes. A series of intrusive bodies in the crust have elevated the temperature of the region to over 350 $^{\circ}C$ at 2 km and is the origin of the geothermal energy (Batini et al., 1984). Various geophysical parameters are shown in Figure 13. We plot the temperature field measured at 2 km (Figure 13a), Bouguer gravity field (Figure 13b), average teleseismic body wave amplitudes (Figure 13c) and the depth to the **K** reflection horizon (Figure 13d) are strongly variable across the network. Average

PKIKP travel time residual (13e) are shown for comparison against the other observations. See Table 1 for parameter estimates for each station. At 2–km depth temperature values vary from about 150 to 350 $°C$ with the highest values in the center of the geothermal field corresponding with an area of very active geothermal production (near station LAGO). The Bouguer gravity anomaly (Cataldi et al., 1978) is also greatest in the center of the geothermal field, with a gavity low of 25 mGals. A low density, granitic magmatic intrusion has been proposed to be the source of this gravity feature (Puxeddu, 1984) and the magnitude of this gravity feature compares well with gravity lows of 30 mGals at The Geysers (Iyer et al., 1981) and 50 mGals at Yellowstone (Ellsworth, 1977), both sites of shallow magmatic intrusions. The depth of the **K** reflection horizon (Batini et al., 1983) which varies in depth from about 3 to 8 km across Larderello, is deepest on the periphery of the network and shallowest in the center of the network, coincident with the area of high geothermal activity.

Teleseismic P-wave amplitude patterns can be used to help understand the structure beneath seismic arrays (Thompson and Gubbins, 1982). For our study relative average amplitudes are calculated for all events used in the travel time residual study using the formula

$$A(i) = \frac{1}{N}\left(\sum_{i=1}^{N} \frac{SWP}{AWP}\right) \tag{7.1}$$

where SWP is the station window power for an individual event, AWP is the average window power for the event and N is the number of events recorded at the station. Window power is defined as the sum of the squared amplitudes in the first 1.0 second of the raw data. The average amplitude variations for the PKIKP events (Figure 13d) show a complicated pattern with generally smaller window power values in the center of the network and to the southeast and larger values to the north.

To view the correspondence of the various geophysical parameters measured in the Larderello region, we calculate non-dimensionalized product maps (Davis, 1973). These maps are made by first converting single parameter maps (such as temperature, gravity etc.) into *standard* maps via the formula

$$Z_i = \frac{P_i - P_i^{ave}}{S} \tag{7.2}$$

Here Z_i is the standardized map parameter, P_i is the input parameter and S is the standard

deviation of the data. Maps of standard temperature and standard PKIKP travel time residual maps are shown in Figure 14. Each point in the standard map now represents the parameter variation from the average weighted by the data standard deviation. Product maps are made from point–by–point multiplication of the non-dimensionalized parameters of two standard maps. Two non-dimensionalized product maps are shown in Figure 15. The first shows the correspondence between travel time residuals and temperature, with only PKIKP events used in the calculations to reduce the effect of gaps in the azimuthal data coverage. Two phenomena are visible on this map, the first of which clearly shows that the highest temperatures directly correspond with the most delayed PKIKP travel times with the major peak in the plot centered near station VALE. The second observation is that directly to the west and east of the peak correspondence we see distinct lows in the non-dimensionalized product. This comes from high temperature areas which correspond geographically with areas that have PKIKP travel times faster than average (near TRAV and MONV). This tells us that the anomalous body, which gives rise to the travel time delays and high temperatures in the center of the network, only strongly affects the temperature observations on the periphery and does not effect the travel times significantly. This is an important result because it indicates that outside the center of the network the crust is hot but may not be melted; the rocks maintain their competence, have a higher average P-wave velocity, and generally retain significant stress levels to produce small earthquakes (Batini et al, 1985). We find that the use of temperature data from depths of 2 km does not adequately predict strong low velocity zones deep in the crust. Results from Christensen (1979) on the change in velocity of rocks with increased temperature indicate that an increase in temperature from 0 to 200° C decreases the the compressional velocity of granites by about 1.5% and an increase to 400° C reduces velocities by about 4.5%. In Larderello we find temperatures in excess of 200° C at 2 km in many areas, even where we observe negative relative travel time residuals.

The product map between PKIKP travel times and averaged relative PKIKP amplitude anomalies (Figure 15) shows a complicated pattern of correspondence of these two parameters. Here, the sense of the amplitude anomaly is reversed to produce a positive value

when reduced amplitudes and delayed arrivals match. From this map we see that in the center of the network smaller than average amplitudes and low velocity regions coincide. To the northwest, larger than average amplitudes and relative high velocities correlate. This leads us to believe that the emplaced body and subsequent effects it had on the media are scattering and attenuating seismic energy in the crust. We observe this effect as diminished average window power values from seismograms recorded in the region of low velocity. Very low Q values may exist in partially or fully melted regions of the crust (Roberts, 1989) and may significantly reduce amplitudes provided that ray travels in the material for a few wavelengths (about 10 to 15 km). A high degree of scattering may also exist in the region due to the large velocity and density contrasts between the competent country rock and partially of fully melted material.

We examine the structure of the Larderello Geothermal Field in cross-section and present our final schematic model of this region in Figure 16. The strike used in this figure (SE to NW) is the same strike as in Figures 3, 5 and 10 above. In cross-section we plot following parameters: 2 km temperature profile derived from deep wells (Batini et al., 1984), Bouguer gravity anomaly (Cataldi, 1978), teleseismic P-wave travel time residual profile (Chapter 3) and teleseismic P-wave amplitude anomalies. Below these plots we show 2 depth dependent profiles, the first is the seismicity pattern along the SW - NE strike and the second shows the velocity profiles derived from teleseismic waveform inversions of Chapter 6. On the bottom of this figure we present our final schematic model which explains these geophysical data.

We see in the first 3 plots (temperature, gravity and travel time residuals) that there is a strong similarity in the pattern of these observations. Each of these parameters is a low-frequency measure of the anomaly and can only be used to infer broad features of the crust. The travel time measurements have the most rapid decay from the peak value in the center, indicating that the rocks can be hot (above 200° C) without appreciably affecting the P-wave velocity (Christensen, 1979). Anomalous gravity and temperature observations decrease more gradually towards the periphery and are less indicative of specific features in the crust. The pattern of teleseismic P-wave amplitudes is more strongly affected by localized velocity anomalies. In general, the amplitude residual pattern is in agreement with

the temperature, gravity and travel time pattern, with low amplitudes observed in the center of the network and larger amplitudes to the southeast and northwest. In addition to this broad feature we also see that distinct relative high amplitude zones exist adjacent to the region of strongest amplitude reduction and that the area of lowest amplitude corresponds clearly with the zone of highest seismic activity. We infer from these patterns that the broad features of the velocity structure are focusing rays into the center of the region, and thus the amplitudes of the far periphery are reduced from that of more internal areas. In the center of the network opposite effects dominate where regions of highly attenuating melted material exist which reduce P-wave amplitudes. Strong seismic activity in the central area indicates that the crust is highly fractured which in turn increases scattering and additionally lowers amplitudes of the direct teleseismic arrivals in the center of the area. We also see from the seismicity pattern that the majority of the earthquake activity lies above the **K** horizon (Batini et al., 1984) particularly to the northeast. This distribution indicates that the **K** horizon marks a rheological change in the crust, a change from a region of competent rock able to build up the stresses released in small earthquakes (generally less the M_L=3) to a region of where the regional stresses in the rocks are released aseismically. In the center of the network we see numerous earthquake hypocenters below the **K** horizon. These events may be caused by thermal stresses induced by the emplaced bodies in this area.

Below the seismicity plot of Figure 16 we show the velocity profiles derived from the waveform inversion application. The position of the **K** marker is superimposed on the plot for reference. We see that the inversion procedure has located this petrophysical feature and that the marker represents a strong negative impedance contrast in the crust. In each case where the **K** is isolated, a low velocity zone exists in the crust as two 1.1 km thick layers of the final velocity profile each with a reduced velocity up to 35%. Batini et al. (1984) interpret the **K** as a the top of a contact aureole: a region which is highly fractured and possibly filled with hot fluids or steam. In general, our waveform results support this model of the **K** horizon, and we additionally conclude that the **K** is underlain by a 1-3 km thick region of low velocity material which is probably partially or fully melted. The lateral dimension of this body is interpreted to be about 20 km and is inferred from the anomalies

K horizon depths, teleseismic travel times and teleseismic P-wave amplitudes. A number of isolated and less well imaged low velocity zones exist throughout the crust as evidenced by the *rpt* and waveform inversion results. These features are interpreted to be sills of emplaced low velocity material which in many cases are lying near horizontal.

The bottom panel of Figure 16 shows our final schematic model for this the Larderello Geothermal Field. We see a number of up-welled low density intrusive bodies which collectively reduced the travel time of teleseismic P-wave in the central area. This model is similar to that of Baily (1980) who describes the setting in Long Valley. Many of these low density dikes and sills are partially of fully melted and are probably fed from below from a large scale batholith which exists beneath the entire area. This regional feature causes strong reflections from the deep crust which are evident in teleseismic waveforms and seismic refraction data (Giese et al., 1980) and elevates the temperature of the entire region (Fanelli, 1974). The observation of a regional scale gravity lows supports the idea of a zone of partially of fully melted material at the base of the crust (Puxeddu, 1984). The magmatic activity in Larderello has probably elevated the surface topography as a similar batholith has done at the Mt. Amiata region about 60 km to the SE. Normal faulting is common to many earthquakes in Larderello (Batini et al., 1985) and indicates that tensile stresses are still prevalent in the area.

In the center of the network we have a deep rooted low velocity zone. The travel time inversion results predicts up to 10% velocity reduction to a depth of 31 km and a 5% reduction below 40 km. The waveform inversion profiles calculated at some central stations indicate that a gradational increase in velocity with depth exists. The travel time residuals calculated from the waveform inversion velocity profiles also suggests that the deep crustal low velocity zone penetrates into the mantle. From the Rb-Sr and K-AR ages of minerals cored in deep wells in Larderello the emplacement of low density granitic intrusive material into the upper crust is constrained to have occurred 2.5-3.7 Ma (Del Moro et al., 1982). These Late Alpine intrusive materials upwelled from the mantle never reached the surface of the earth as was the case at Mt. Amiata and numerous other locations along the Appennines (Giovanni et al., 1988) but instead have remained below the surface. This series of intrusions has collectively

delayed teleseismic P-wave arrivals by nearly 1 second and reduced their peak amplitudes by up to a factor of 4. This anomaly has caused a distinct negative gravity anomaly to exist has elevated temperatures in the area to very high levels, today measuring over $350°C$ at 2 km, and is the source of intense geothermal activity.

7.5 GENERAL CONCLUSIONS AND RECOMMENDATIONS

The analysis of teleseismic P-waveforms, collected on vertical component seismic stations can yield important information about the velocity structure of the earth in the vicinity of the receiver. Our general conclusions follow:

- Travel time residuals of the direct P-wave arrival are easy to determine and are very useful data. As an integral of the slowness along the entire raypath, the travel time of a ray is not strongly effected by small scale features of the velocity structure, and this data provide a good measure of the broad features of the crust. The accurate determination of travel times is very important and the simulated annealing method (Chapter 2) provides a straightforward technique to measure the relative travel times of targeted phases as well as a means to determine a measure of the *quality* of each travel time selection.

- Most of the information in teleseismic P-wave data about the crustal velocity structure near a receiver lies in the waveforms after the direct arrival. Within in the coda of the direct P-wave we generally have a number of reflected and converted phases, and the amplitude and timing of these arrivals can provide important information about the velocity structure of specific regions in the crust. With the careful application of the techniques introduced in this study, this information can be extracted from the waveforms.

- The common theme that runs through of all the applications of this study represents a fundamental principle of data processing: signal enhancement through stacking. The simulated annealing method is an automated means to find the best set of trace shifts which maximize the power of a stack of waveforms. Source equalization is a method of wavelet shaping developed to allow us to compare traces at a single station from different events. The subsequent comparisons are based on stacks of waveforms. In the *rpt* technique we stack traces along trajectories predicted by the event incident angle, and in the waveform inversion application we find the best model to fit a set of seismograms stacked to produce a single waveform. With stacking we can boost

the generally low signal in the data and apply a variety of methods to the problem of velocity structure determination. Without stacking, generally we are left with the analysis of the direct arrival.

- Source equalization, essential to most methods which use waveforms recorded at a single station from different events, is possible with vertical component teleseismic P-wave data. The key element in this procedure is the design a wavelet with a frequency response which is common to most of the data recorded on a seismic network. With this approach we can transform most of the natural source functions of teleseismic waveforms to a common and repeatable shape.

- With source equalized data numerous applications to determine the velocity structure of the earth are possible and the *rpt* method (Chapter 5) and waveform inversion (Chapter 6) represent two examples. Reflections from coherent velocity discontinuities within the crust arriving in teleseismic data after the direct arrival can provide important specific information about the crust. The *rpt* method takes advantage of the incident angle dependence of the travel times of reflected arrivals and can be applied to determine the vertical two-way travel time to reflectors existing beneath a station. When ray coverage is good this method can also provide a measure of the average velocity of the crust above the discontinuity.

- Waveform inversions can be implemented to determine the fine details of the structure of the earth. We developed and implemented a 1-D waveform inversion which utilized the *rpt* results as a starting model and an abundance of vertical incidence waveforms in order to determine the velocity structure beneath various stations. With the waveform inversion applications we showed that we can effectively automate the forward waveform trial-and-error matching procedure by calculating the Frechet derivatives of the current model prediction. The final models are quite reliable and produce a good picture of the crust when station coverage is adequate.

- In this thesis vertical component teleseismic data is used exclusively in the analyses. Generally, these waveforms are abundant from any digital seismic network. In the

New England case, where the station spacing is generally on the order of 5 to 10 wavelengths, we demonstrated that we can determine structural information in the vicinity of individual station (via *rpt* or waveform inversion) as well as regional trends of deep features (via simulated annealing for Moho depths of deep velocity trends from travel time inversion (Taylor and Toksoz, 1979)). In the Larderello case, where the spacing is much better (about 1 wavelength) teleseismic modeling applications with vertical component data reveal important crustal velocity information with greater resolution.

Recommendations for Future Analysis

- As we mentioned above, the methods we have utilized have been successful because we are able to enhance the signal-to-noise of the data through stacking. The first improvement we can make upon the present results will come from increasing the amount of data used in the analyses. Specifically, we can easily improve the ray parameter coverage for the *rpt* analysis, back azimuth and incidence angle coverage for the travel time residual inversions and number of traces which comprise each data vector in the waveform inversion. These simple improvements to the study should significantly improve the results in Larderello.

- We need to extend the travel time residual study to more regional distances and include stations from outside the Larderello geothermal area. This will help us to reference the *relative* velocity perturbations derived from the inversions to a more well controlled background velocity structure.

- The simulated annealing technique has numerous applications in seismic waveform analysis. Whenever a set seismograms can be windowed to contain a targeted arrival and the wavelet of the arrival can be assumed to be the same in each window, we can apply this method to the data. One immediate improvement to teleseismic tomographic imaging based on travel time residuals will come from the incorporation of the final correlation levels (derived from the simulated annealing process) as data weights in the inversion.

- Source equalization allows us to use modern methods of analysis with teleseismic data after the direct arrival. However, for regional and global travel time tomography problems we can significantly improve the quality of direct P-wave (and S-wave) travel time residual determinations if we convert the earthquake source time function into simplified wavelets. This procedure will require special consideration to account for the directivity of the source and the position of each station on the focal sphere, but the improvements in the travel time data brought forward by the application of this technique should be significant.

- To further advance the results of the waveform inversions in Larderello two steps should be taken. First we should increase the amount of data in the inversion and include the inversion of waveforms from obliquely incident events. Waveforms from additional incidence angles (inverted separately and simultaneously) will introduce shear waves into the analysis and help to further resolve the lower crust where we believe partially of fully melted material exists. Second, we can collect more closely spaced data in areas where particular interest exists. For example, if we need to know about the nature of the **K** horizon in a particular isolated region of the network, we can deploy a number of temporary recording instruments in that area for 6 months to develop a data base sufficient model this feature of the crust. The lateral resolution of detail is mainly dependent on the station spacing.

Table 1: Parameter Values for Larderello Seismic Network Stations

Station Name	Lat	Lon	Elev (Meters)	Resid (Sec)	Temp $^{\circ}C$	**K**-depth (Meters)	Grav (mGals)	Amplitude Residuals
MINI	43.23	10.85	444	0.37	260	4600	19	0.33
SERR	43.31	10.79	223	-0.23	150	–	26	2.60
POMA	43.33	10.90	231	-0.19	150	–	33	1.94
SDAL	43.26	10.93	380	-0.13	225	5000	23	0.22
SCAP	43.25	11.00	360	-0.25	175	8000	24	0.21
MGUI	43.29	11.01	341	-0.26	150	–	31	0.44
RADI	43.25	11.07	489	-0.30	150	8500	29	0.22
MLUC	43.22	10.94	572	0.83	240	4200	21	0.10
FROS	43.20	11.15	432	-0.38	150	–	26	0.92
SINI	43.16	11.11	350	-0.03	150	–	16	1.08
LURI	43.12	11.12	458	-0.08	150	–	18	1.09
TRAV	43.19	11.03	472	-0.05	300	7000	17	1.12
CORN	43.16	10.94	886	-0.03	250	4400	24	0.64
VALE	43.20	10.87	782	0.63	320	3800	20	2.01
CRDP	43.09	10.97	816	-0.21	150	–	18	0.62
MDSV	43.15	10.85	754	0.51	300	3600	19	0.56
CRBE	43.11	10.82	442	0.08	300	3200	25	0.99
MBAM	43.06	10.82	342	-0.03	250	3400	32	0.80
LAGO	43.15	10.81	319	0.40	300	3000	15	2.21
PADU	43.20	10.79	439	0.16	250	4600	22	0.26
SASS	43.25	10.69	438	-0.33	150	–	40	1.11
MONV	43.18	10.71	445	-0.20	255	5000	29	0.68
FRAS	43.11	10.76	220	0.00	200	4000	30	0.64
STTA	43.12	10.65	361	-0.28	150	–	37	0.55
PLUZ	43.05	10.74	156	0.00	150	4000	33	1.04

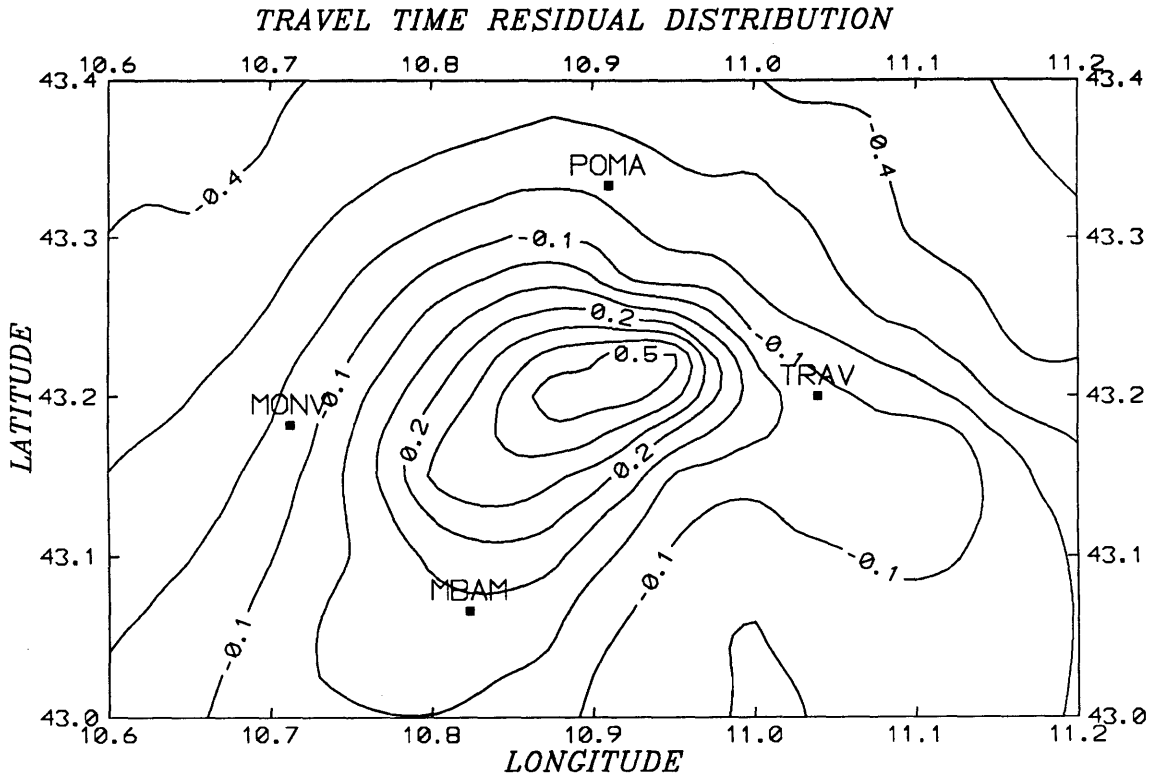

Figure 1: Average travel time residuals of all direct P-waves. Contour interval is 0.1 seconds, with four stations are plotted for reference. Maximum travel time difference is about one second.

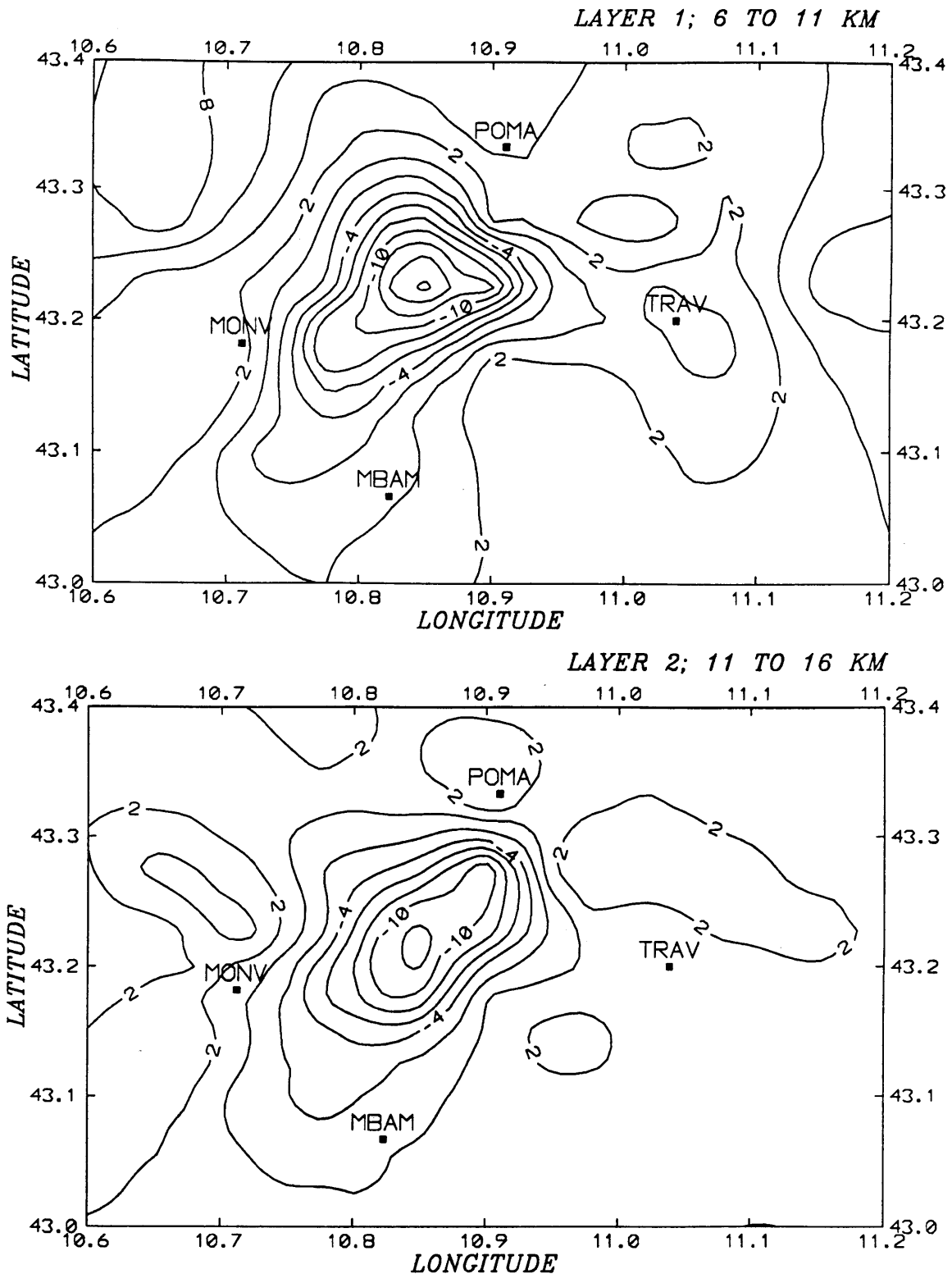

Figure 2: Inversion results for Layer 1 (6 to 11 km) and Layer 2 (11 to 16 km). Contours are lines of equal velocity perturbation in percent with interval of 2%.

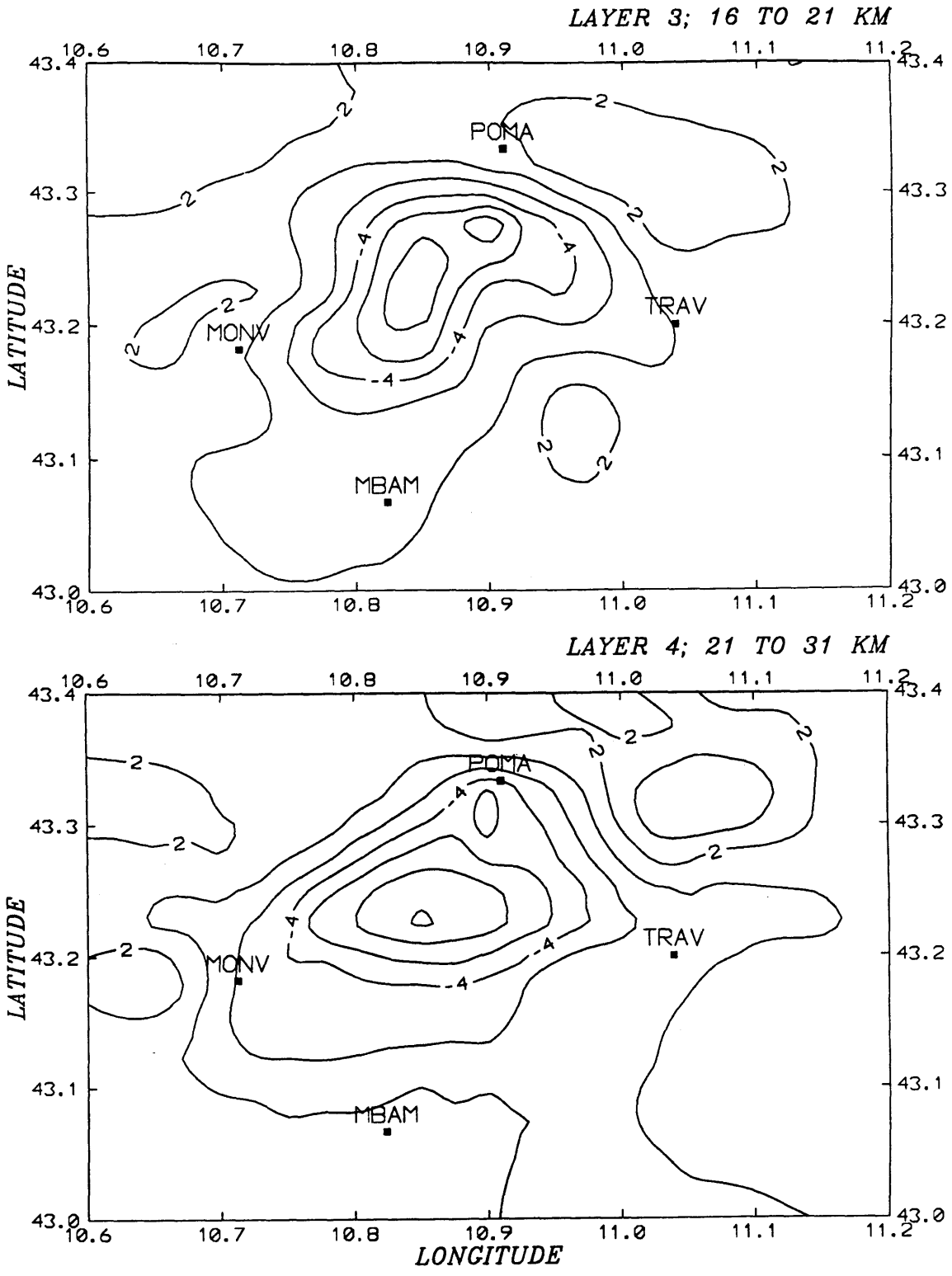

Figure 2: Inversion results for Layer 3 (16 to 21 km) and Layer 4 (21 to 31 km). Contours are lines of equal velocity perturbation in percent with interval of 2%.

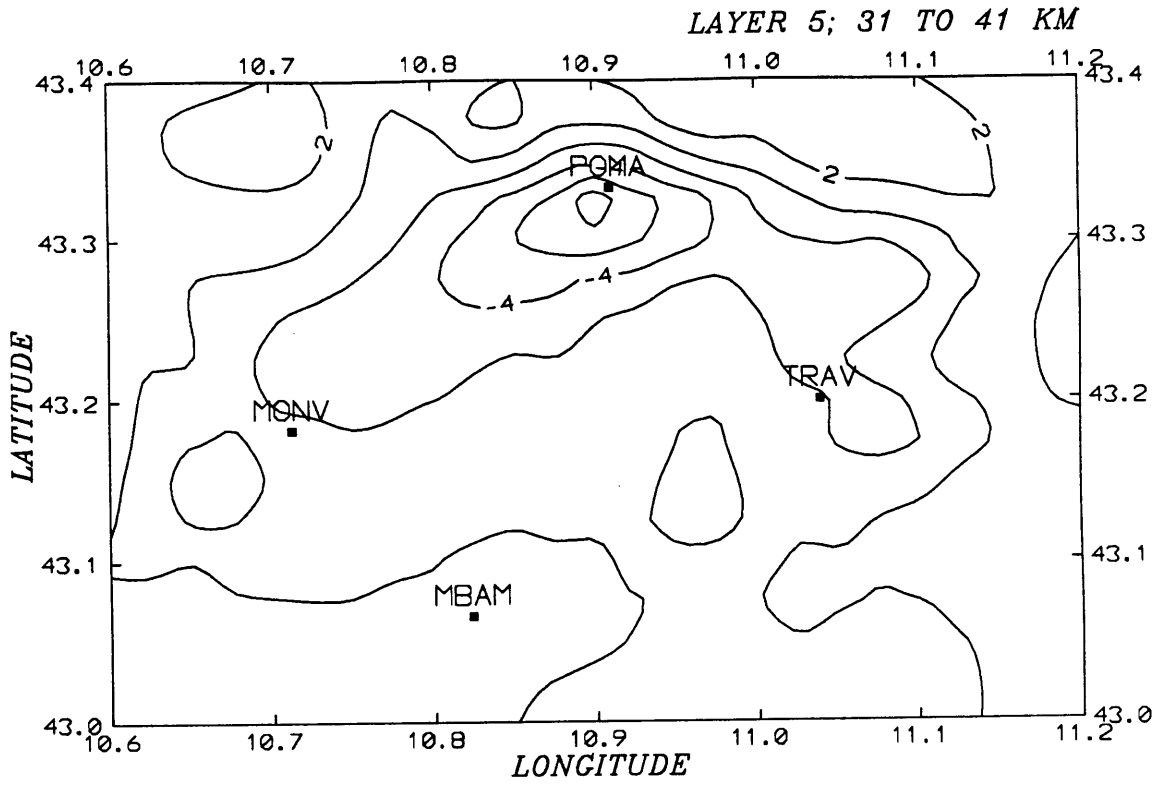

Figure 2: Inversion results for Layer 5 (31 to 41 km in depth). Contours are lines of equal velocity perturbation in percent with interval of 2%.

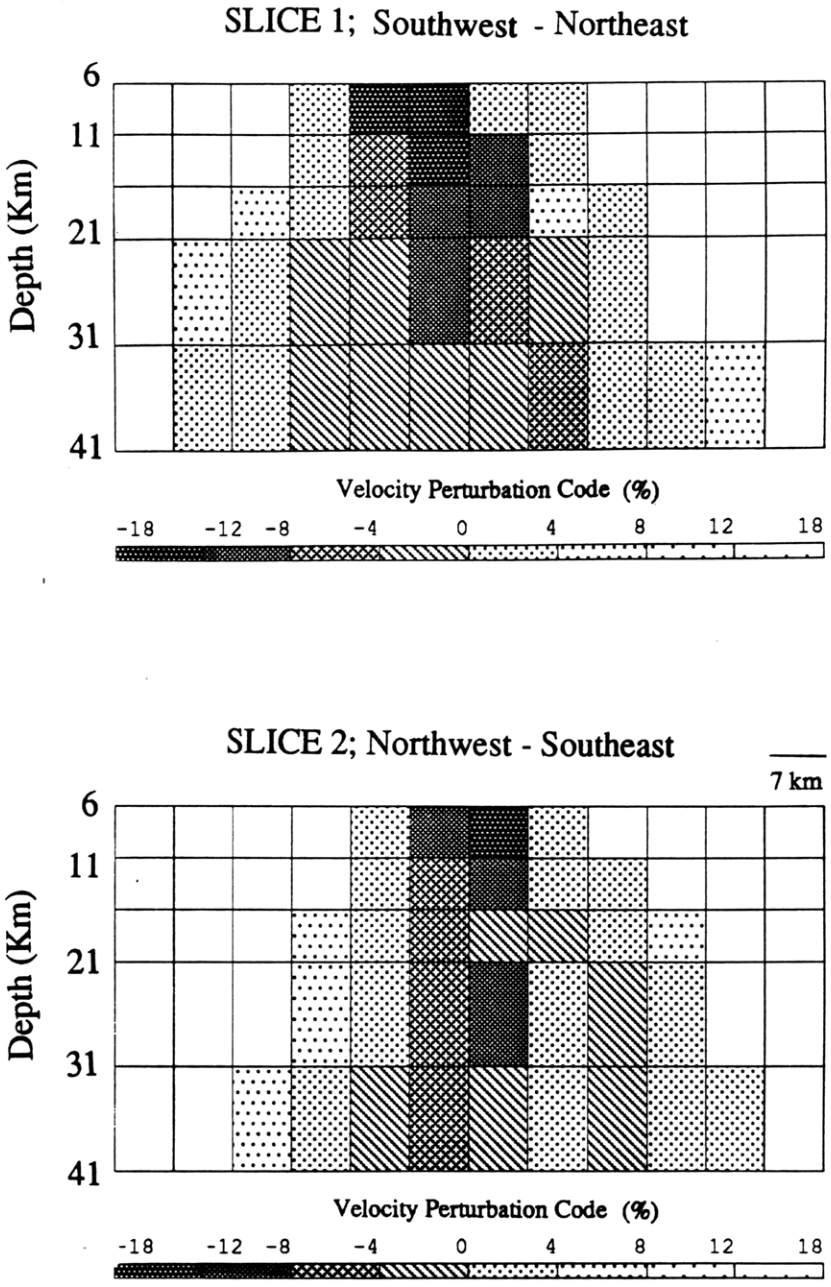

Figure 3: Vertical cross sectional slice through the Larderello Geothermal Field from SW to NE through the network. Each block is 7 km in width. Velocity contrasts are depicted with different shade patterns with cross hatched blocks representing velocity decreases and stippled blocks representing regions of increased velocity. Blocks without any pattern represent regions not sampled densely enough (at least 10 rays) for a parameter estimate to be made.

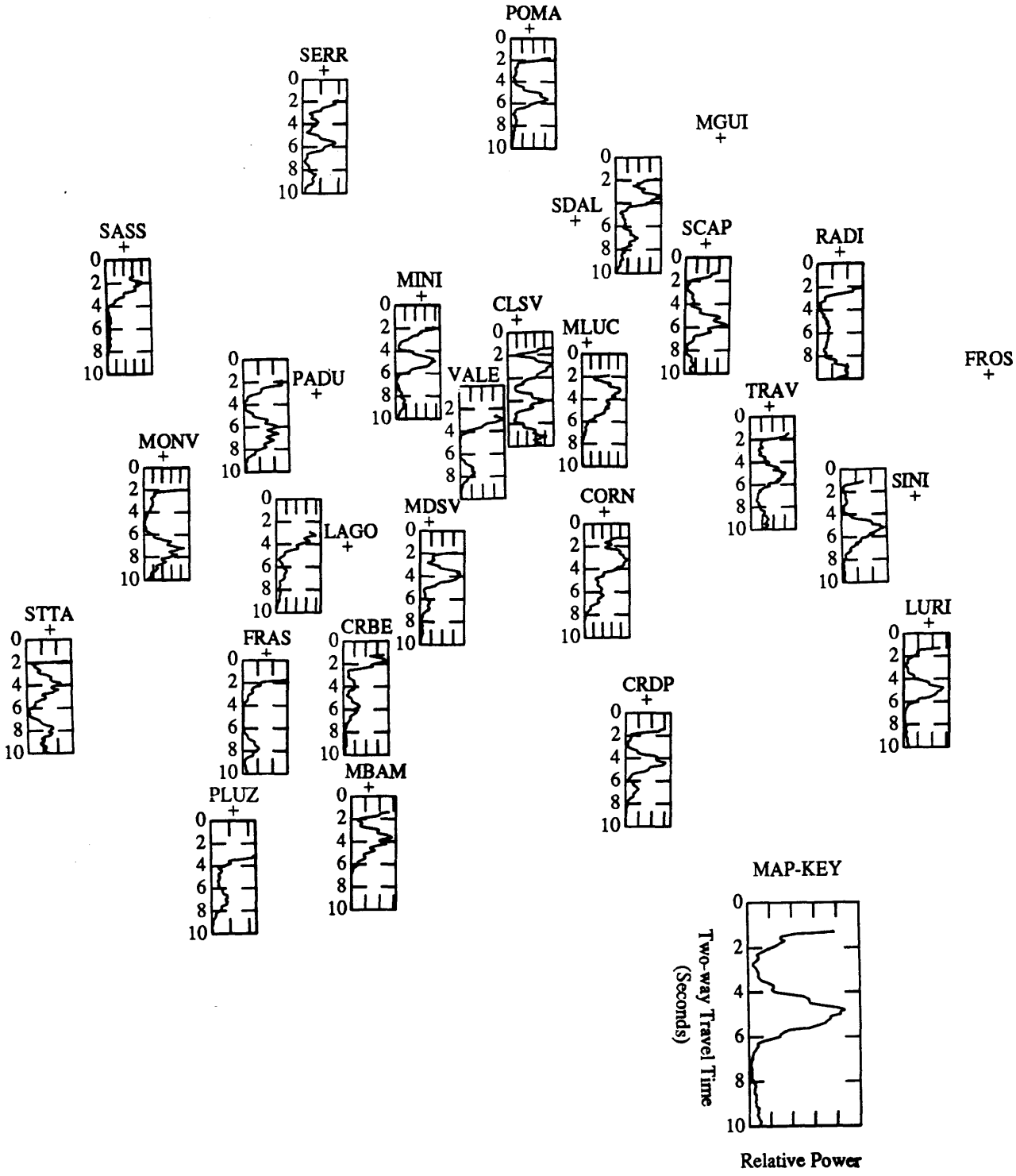

Figure 4: Map of the *rpt* results. Each plot shows relative stack power (X) versus vertical two-way travel time (Y).

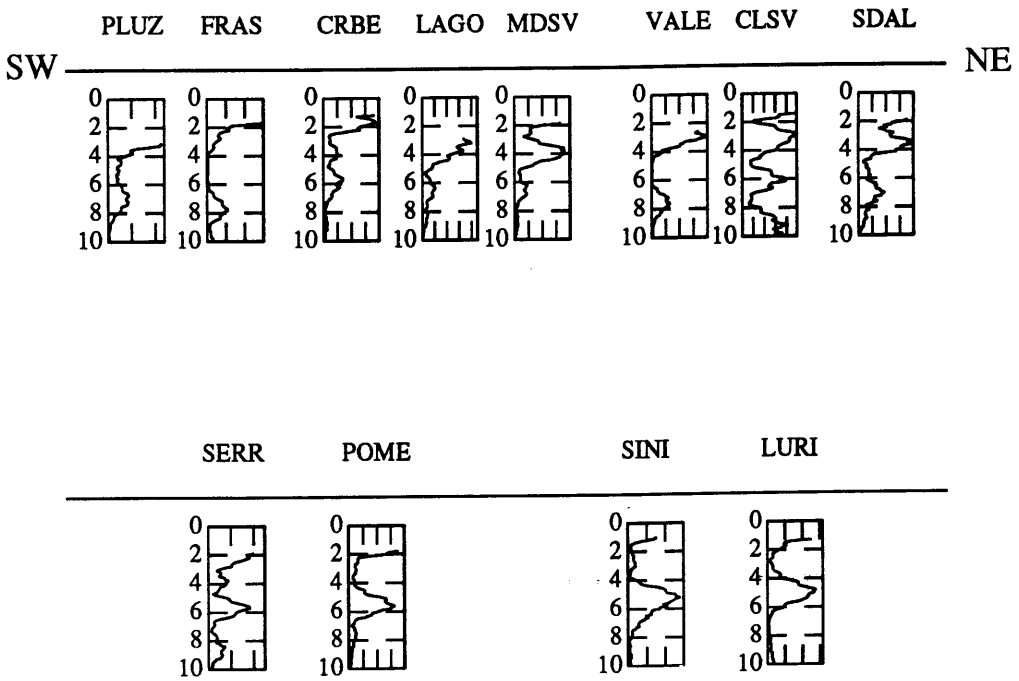

Figure 5: (Top) *Rpt* results in cross-section, same slice as in the travel time residuals: SE to NW. (Bottom) Peripheral stations with common coherent reflection between 5 and 6 seconds.

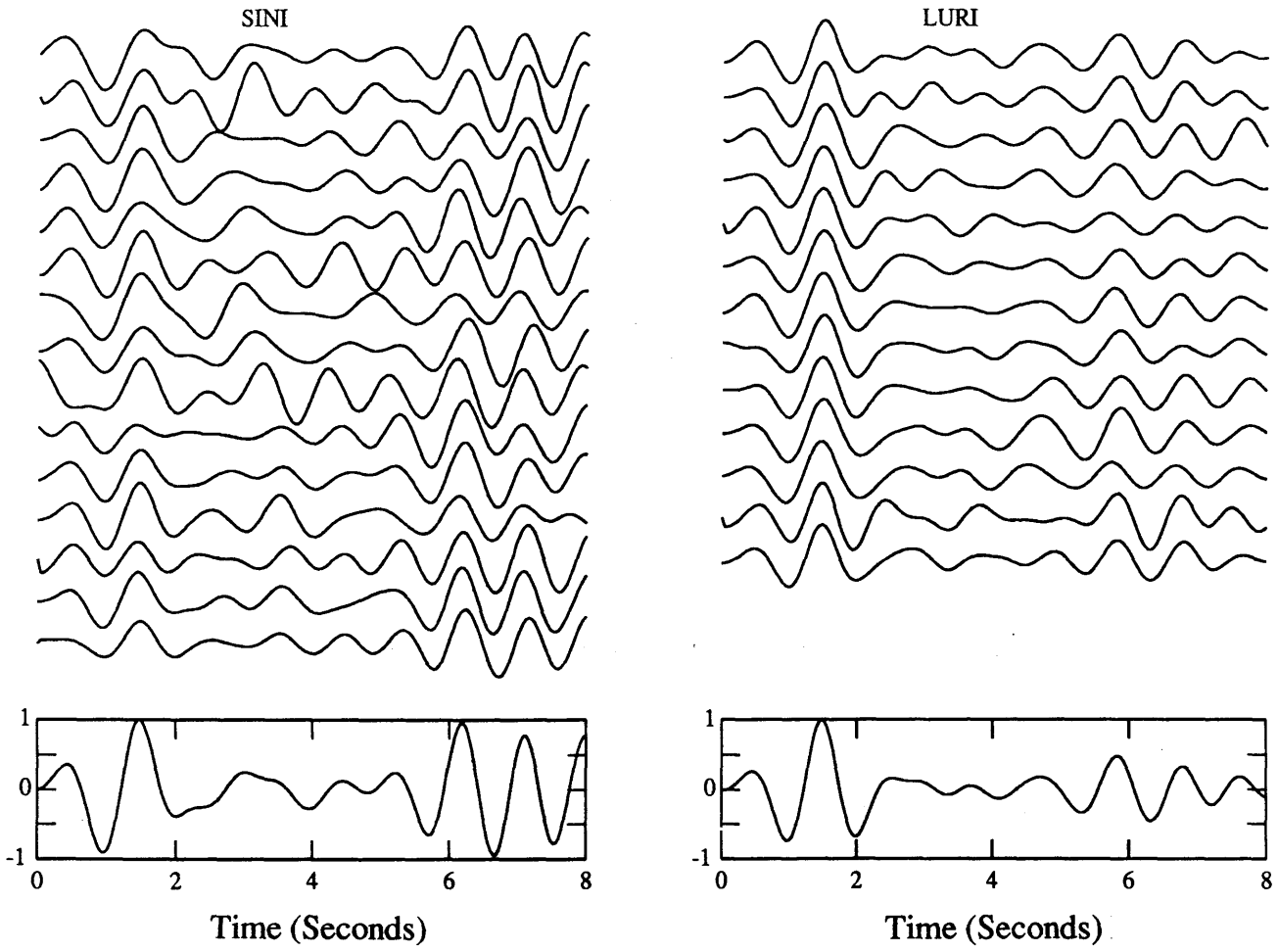

Figure 6: Vertically incident seismograms (source equalized) from stations SINI and LURI, both on the eastern edge of the network. On top are all data received at the stations with incidence angles less the 6 degrees, and on bottom is a normalized stack of the above data. These observation indicate a very strong low velocity zone at depth.

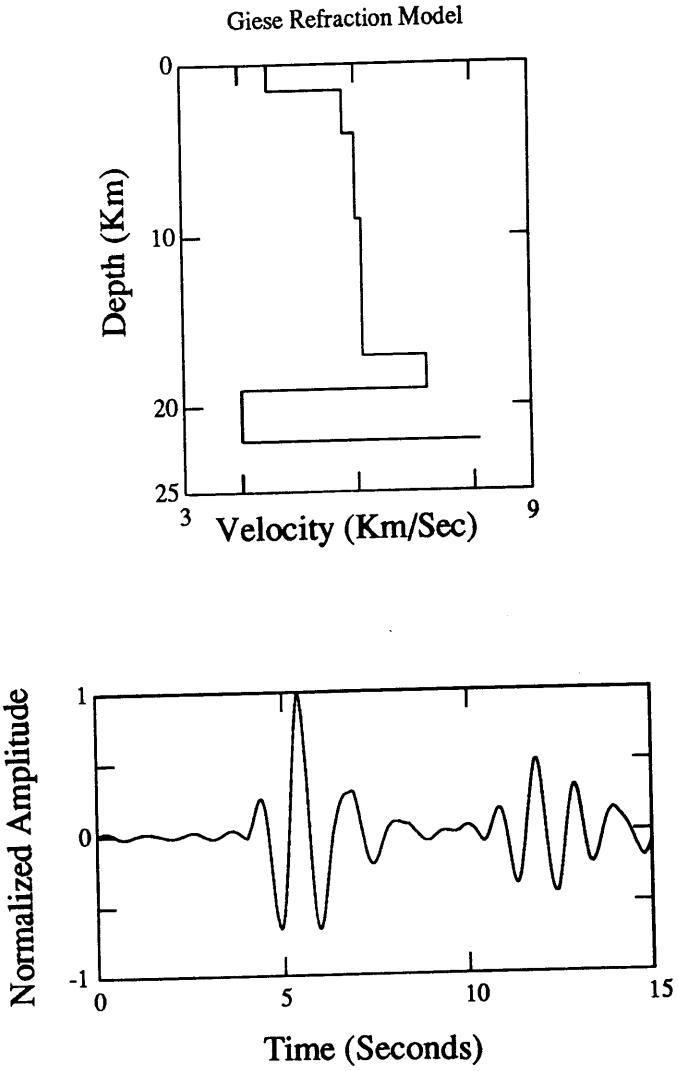

Figure 7: Crustal velocity model (Top) from Giese et al. (1981) from refraction data near Larderello and a vertical component synthetic seismogram for a vertically incident plane wave. This refraction model prediction is similar to the observations shown in Figure 6.

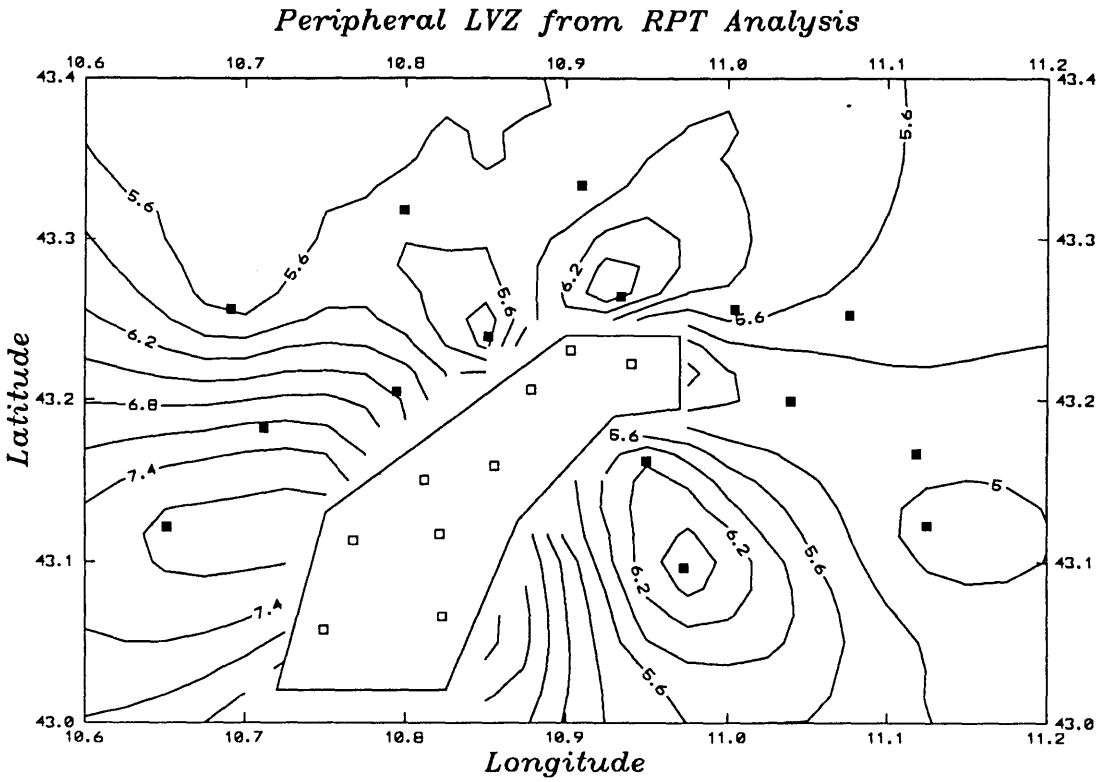

Figure 8: Map of the two-way vertical travel times of deep coherent crustal reflections derived from the *rpt* analysis. Stations excluded from this plot which did not exhibit clear isolated arrivals are indicated with open boxes.

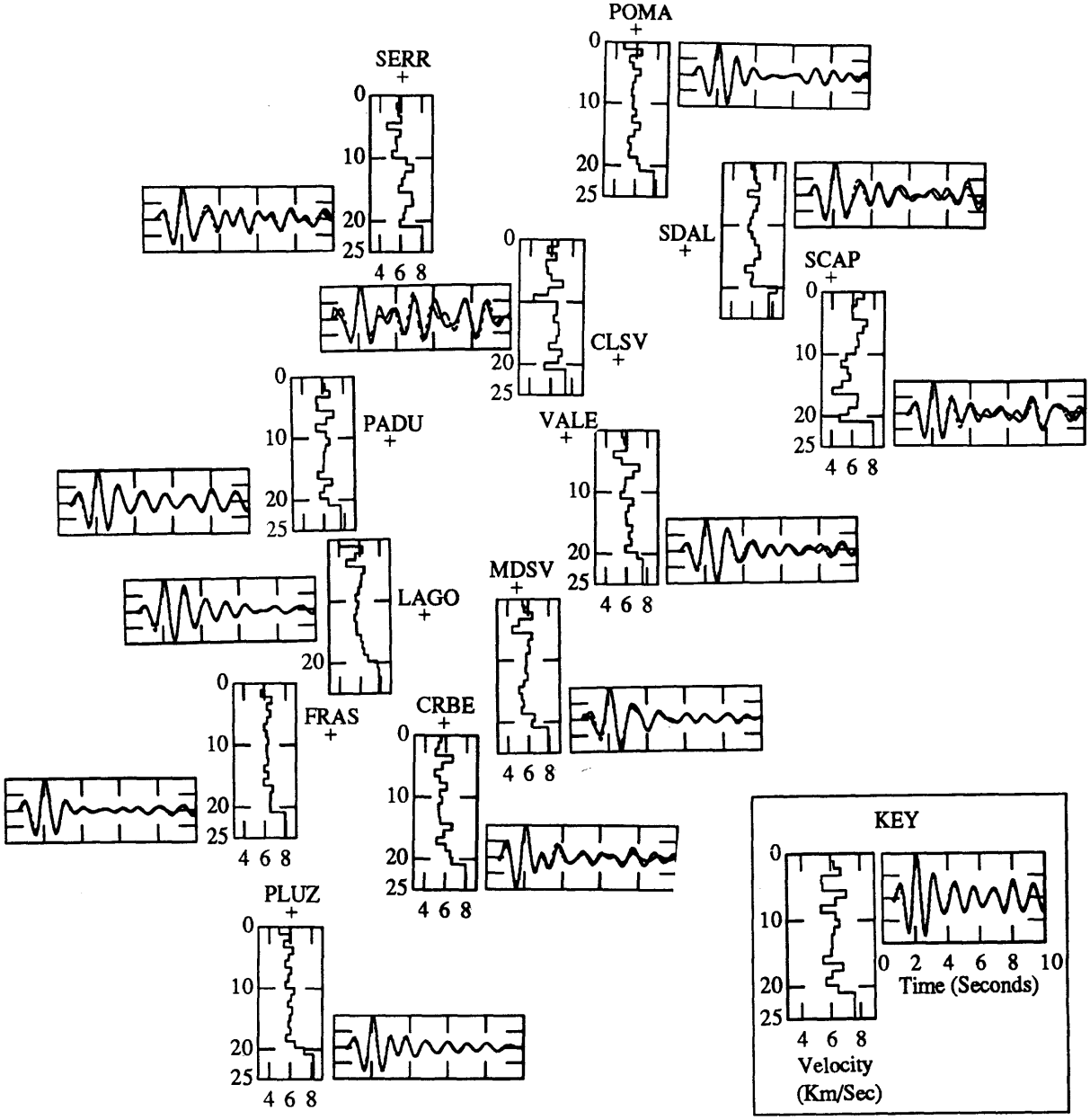

Figure 9: Map of the Larderello waveform inversion results. We plot ten seconds of the predicted and observed waveforms (predicted dashed) calculated from the final model. Final models are shown with depth as the vertical axis (0 to 25 km in each case). The velocity range for each profile is from 3 to 9 $\frac{km}{sec}$ (See key).

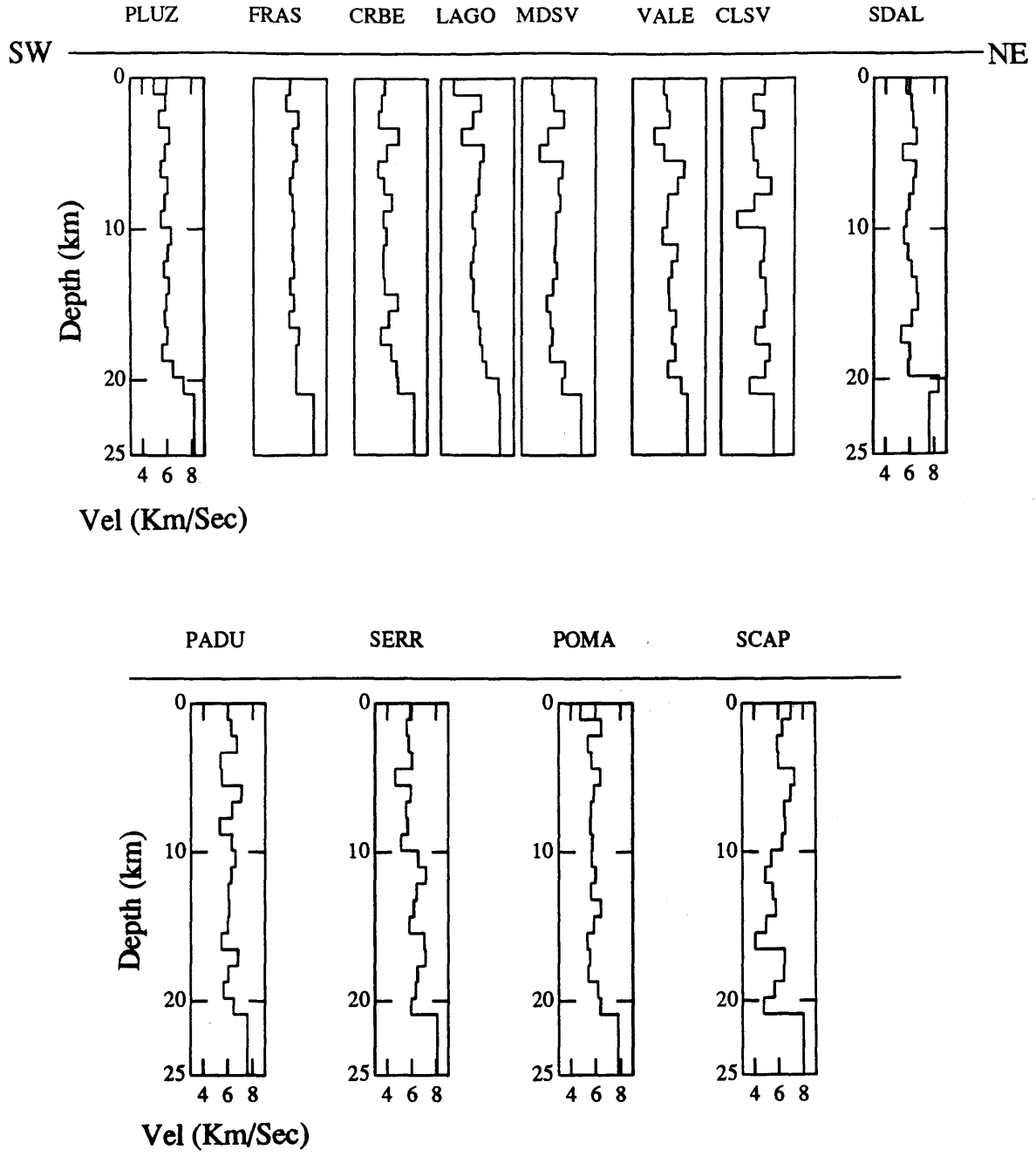

Figure 10: Waveform inversion results in cross-section from southwest to northeast. Same cross-section as previous figures.

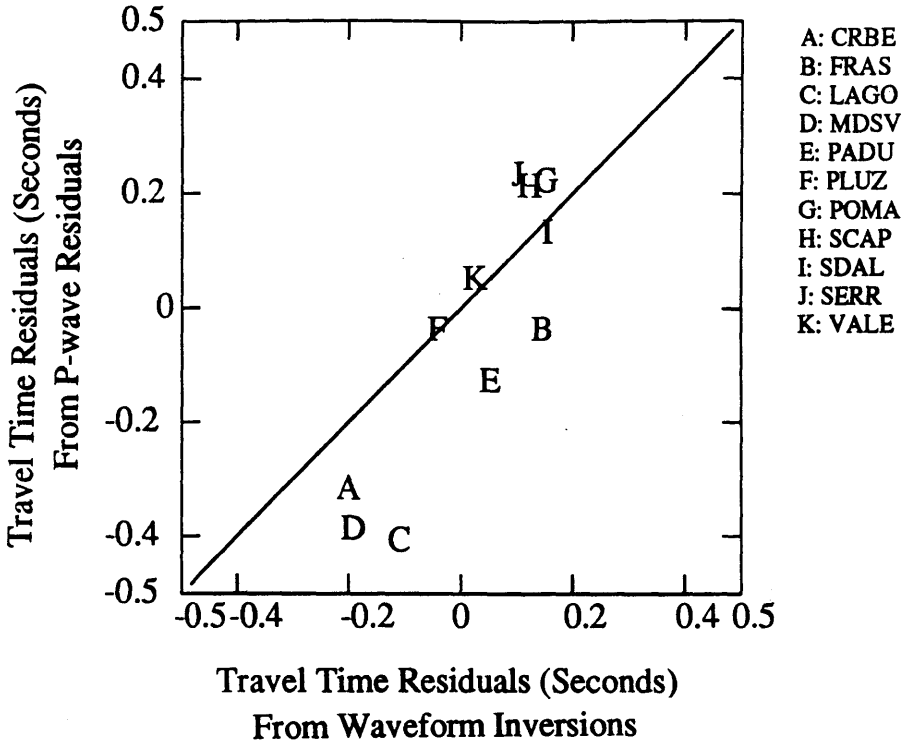

Figure 11: Travel time residuals derived from the direct P-wave analysis of Chapter 3 versus the travel time residuals of the 11 stations models with waveform inversions.

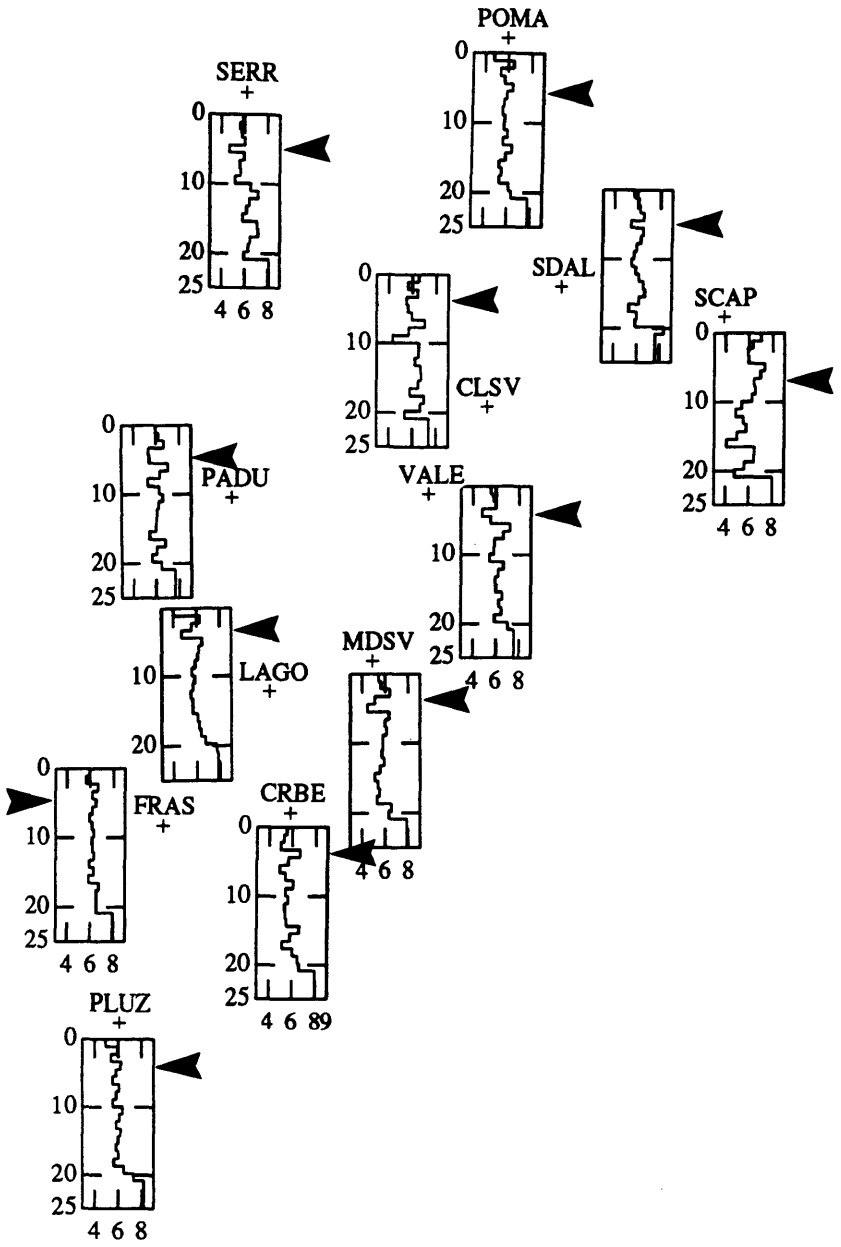

Figure 12: Correlation of the **K** horizon depth estimates derived from the inversion of stacked vertical incident P-wave data and the estimates of the **K** derived from seismic reflection interpretations (Batini et al. 1984).

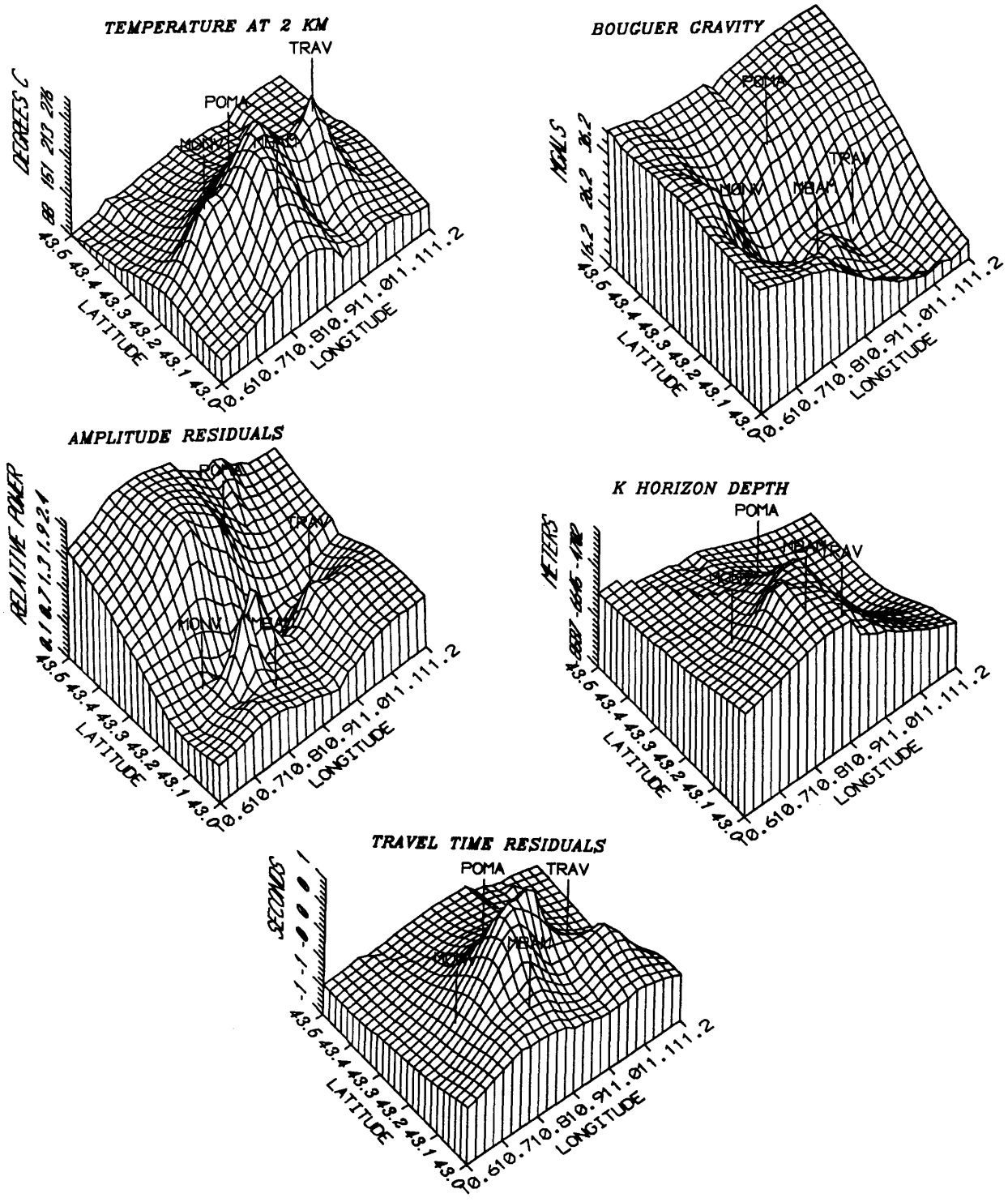

Figure 13: Other geophysical observations from Larderello: temperature at 2 *km* (13a), gravity (13b), direct P-wave amplitude residuals (13c) **K** horizon depth (13d), travel time residuals of PKIKP arrivals (13e). Four stations are plotted for reference.

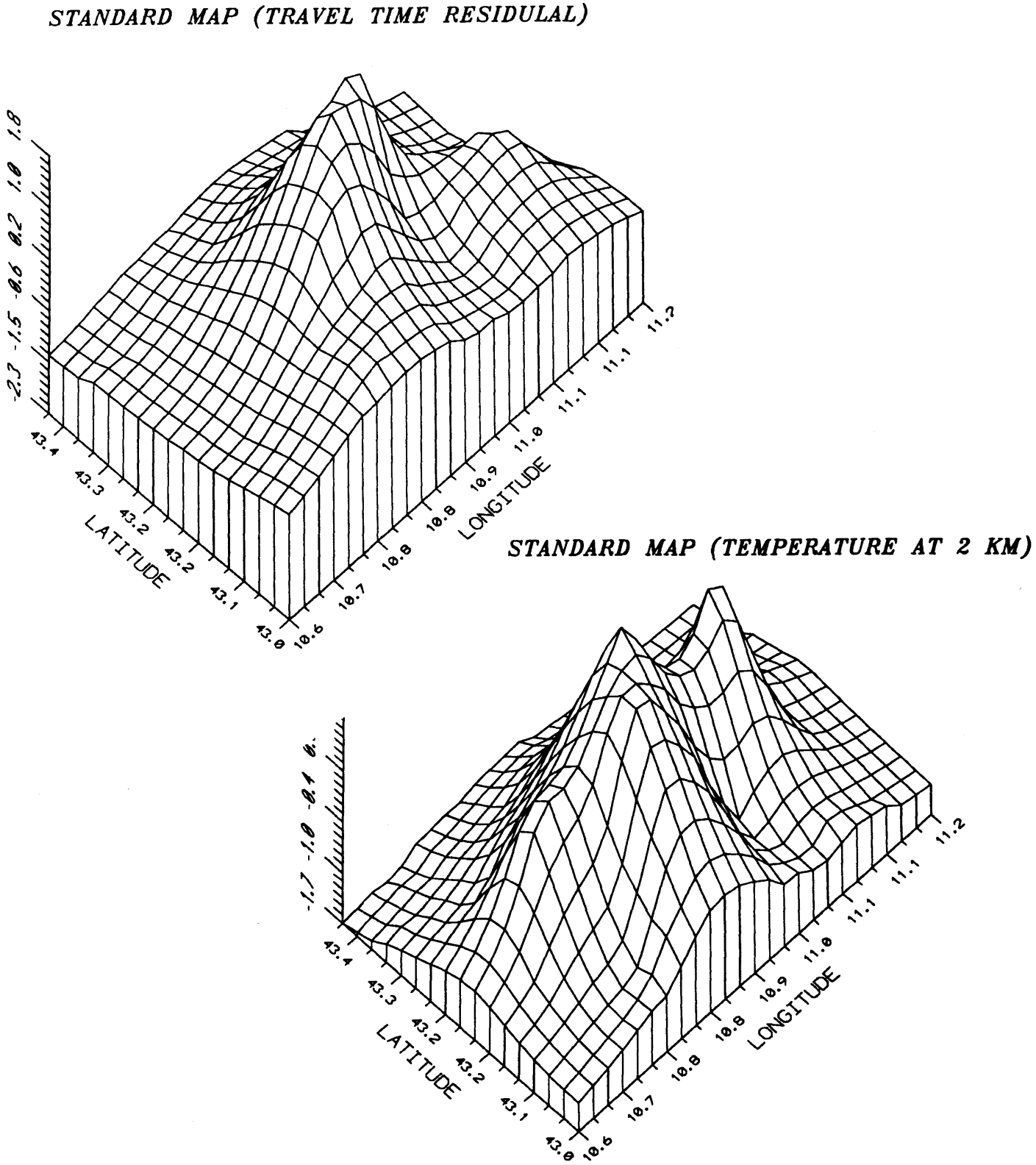

Figure 14: *Standard* temperature and *Standard* PKIKP travel time residual maps for the Larderello region.

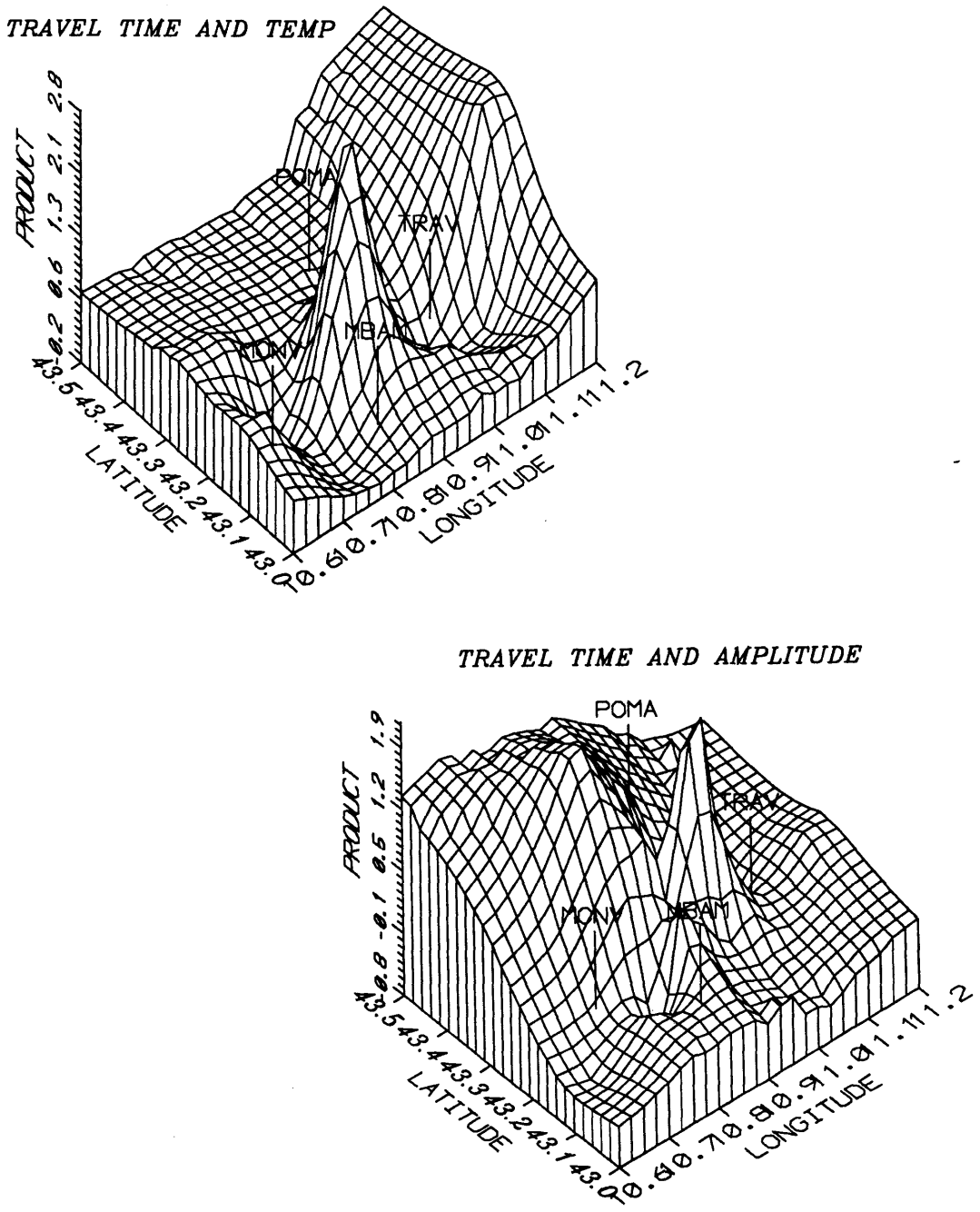

Figure 15: The product map between PKIKP travel times and temperature (Top) and product map between PKIKP travel times and average relative PKIKP amplitude (Bottom). Four stations are shown for reference.

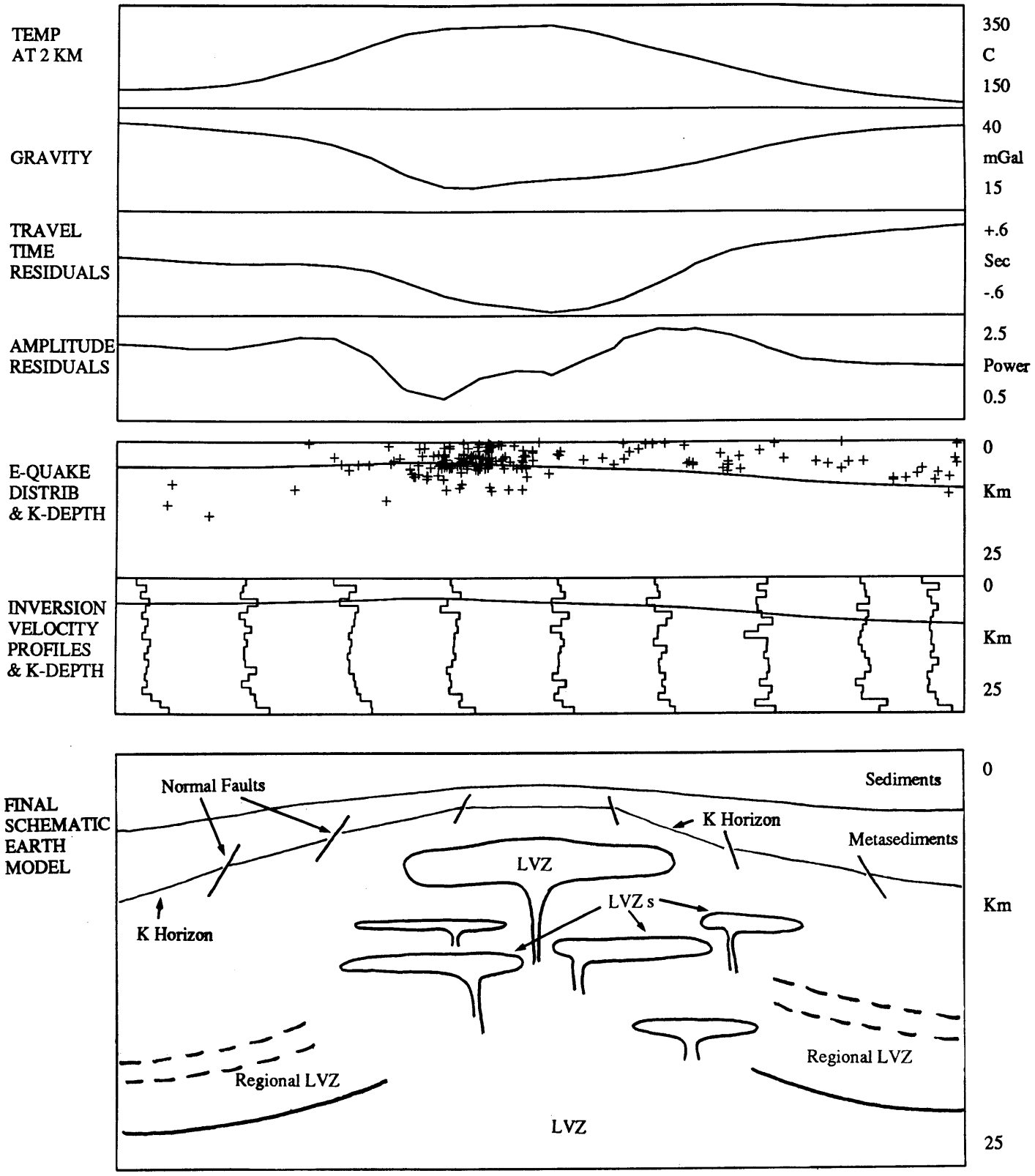

Figure 16: Cross-sectional view of the various geophysical observations along a strike trending SW to NE (same strike as previous Figures). See text for discussion.

References

Achauer, U., L. Greene, J. Evans, and H. M. Iyer, Nature of the magma chamber underlying the Mono Craters area, eastern California, as determined from teleseismic travel time residuals, *J. Geophys. Res., 91,* 13873–13891, 1986.

Aki, K. and P. Richards, *Quantitative Seismology – Theory and Methods,* W. H. Freeman, San Francisco, 1980.

Aki, K., A. Christoffersson, and E. S. Husebye, Determination of the three-dimensional seismic structure of the lithosphere, *J. Geophys. Res., 82,* 237–296, 1977.

Ando, C. J., B. Czuchra, S. Klemperer, L. D. Brown, M. Cheadle, F. A. Cook, J. E. Oliver, S. Kaufman, T. Walsh, J. B. T. J. B. Lyons, and J. L. Rosenfeld, A crustal profile of a mountain belt: COCORP deep seismic reflection profile in the New England Appalachians, *Amer. Assoc. Petrol. Geol., 68,* 819–837, 1984.

Bagnoli, G., G. Gianelli, M. Puxeddu, A. Rau, A. Squarci, and M. Tongiorgi, A tenative stratigraphic reconstruction of the Tuscan Paleozoic basement, *Mem. Soc. Geol. Ital., 20,* 99–116, 1978.

Baily, R. A., G. B. Dalrymple, and M. A. Lanphere, Volcanism, strucutre, and the geochronology of Long Valley caldera, California, *J. Geophys. Res., 81,* 725–744, 1976.

Basham, P., J. Lyons, J. Drysdale, W. Shannon, F. Andersen, B. Haymen, and R. Wetmiller, *Canadian Seismic Agreement,* NRC Technical Report, Canadian Commercial Corporation, 1985.

Batini, F., *Rete Sismica Larderello - Travale Caratteristiche e curve di calibrazione,* Internal Report, Unita Nazionale Geothermica, 1987.

Batini, F. and R. Nicolich, The application of seismic reflection methods to geothermal exploration, *Seminar on Utilization of Geothermal Energy for Electric Power Production and Space Heating, 11–17 May, Florence, Italy,* 1984.

Batini, F., P. D. Burgassi, G. M. Cameli, R. Nicolich, and P. Squarci, Contribution of the study of the deep lithospheric profiles: deep reflecting horizons in the Larderello Travele geothermal field, *Mem. Soc. Geol. Ital., 9,* 477–484, 1978.

Batini, F., G. Bertini, G. Gianelli, E. Pandeli, and M. Puxeddu, Deep structure of the Larderello field: contribution from recent geophysical and geological data, *Mem. Soc. Geol. Ital., 25,* 219–235, 1983.

Batini, F., R. Console, and G. Luongo, Seismological study of Larderello-Travale geothermal area, *Geothermics, 14,* 255–272, 1985.

Berteussen, K. A., Moho depth determinations based on spectral ratio analysis of NORSAR long period P waves, *Phys. Earth Pl. Int., 15,* 13–27, 1977.

Berteussen, K. A., E. S. Husebye, R. F. Mereu, and A. Rau, Quantitative assessment of the crust-upper mantle heterogeneities beneath the Gauribidnaur seismic array in southern India, *Earth Planet. Sci. Lett., 37,* 326–332, 1975.

Boccaletti, M., M. Coli, C. Eva, G. Ferrari, G. Giglia, A. Lazzarotto, F. Merlanti, R. Nicolich, G. Papani, and D. Postpischl, Considerations on the seismotectonics of the northern Apennines, *Tectonics, 47,* 7–38, 1985.

bohachecsky, I., M. Johnson, and M. Stein, Generalized simulated annealing for function optimization, *Technometrics, 28,* 209–217, 1986.

Brown, L. D., C. J. Ando, S. Klemperer, , S. Kaufman, B. Czuchra, T. Walsh, and Y. W. Isachsen, Adirondack-Appalachian crustal srtructure: the COCORP nartheast traverse., *Bull. Geol. Soc. Amer., 94,* 1173–1184, 1983.

Burdick, L. J. and C. A. Langston, Modeling crustal structure through the use of converted phases in teleseismic body waveforms, *Bull. Seis. Soc. Am., 67,* 677–691, 1977.

Calamai, A., R. Cataldi, P. Squarci, and L. Taffi, Geology, geophysics and geohydrology of the Monte Amiata geothermal fields, *Geothermics, Special Volume,* 1–9, 1970.

Calcagnile, C. and G. F. Panza, Crust and upper mantle structure beneath the Apennines region as inferred from the study of Rayleigh waves, *J. Geophys., 45,* 319–327, 1979.

Cataldi, R., A. Lazzarotto, L. P. Muffler, P. S. Squarci, and G. C. Stefani, Assessment of geothermal potential of central and southern tuscany, *Geothermics, 7,* 91–131, 1978.

Cavarretta, G., G. Gianelli, and M. Puxeddu, Formation of authigenic minerals and their use as indicators of the physicochemical parameters of the fluid in the Larderello-Travale geothermal field, *Bull. Soc. Econ. Geol., 77,* 1071–1084, 1982.

Chiburis, E. R., R. Ahern, and T. Graham, Prelimanary travl time model of southern New England, *Earthquake Notes, 48,* 3, 19.

Christensen, N. I., Compressional wave velocities in rocks at high temperatures and pressures, crutical thermal gradients and crustal low velocity zones, *J. Geophys. Res., 84,* 6849–6857, 1979.

Clayton, R. W. and R. A. Wiggins, Source shape estimation and deconvolution of teleseismic bodywaves, *Geophys. J. R. Astr. Soc., 47,* 151–177, 1976.

Dainty, A., Studies of coda using array and three-component processing, *Pure Appl. Geophys., 132,* 221–244, 1990.

Davis, J. C., *Statistics and Data Analysis in Geology,* John Wiley and Sons, San Francisco, 1973.

Doll, C., *Crustal seismic structure beneath New England Seismic Station WES in Weston Massachusetts determined from modeling short period teleseismic P-waveforms,* Master's thesis, Boston College, 1987.

Ebel, J. E., NRC Technical Report, Weston Observatory of Boston College, 1985.

Ellsworth, W. L., *Three dimensional structure of the crust and upper mantle beneath the island of Hawaii,* PhD thesis, Massachusetts Institute of Technology, 1977.

Evans, J. R., Compressional wave velocity structure of the upper 350 km under the eastern Snakle River Plane near Rexburg, Idahoe, *J. Geophys. Res., 87,* 2564–2670, 1982.

Fanelli, M., M. Loddo, F. Mongelli, and P. Squarci, Terrestrial heat flow measurements near Rosignano Solvay (Tuscany), Italy, *Geothermics, 3,* 65–73, 1974.

Foley, J., *The crustal receiver structure beneath Weston Observatory from long period synthetic seismogram analysis,* Master's thesis, Boston College, 1984.

Foley, J. E. and J. E. Ebel, Long-period synthetic seismogram receiver structure for WWSSN station WES, *EOS, Trans. Am. Geoph. Un., 65,* 1016, 1984.

Foley, J. E. and M. N. Toksoz, Crustal thickness in the northeastern u. s. from pmp moho reflections, *EOS, Trans. Am. Geoph. Un., 68,* 347, 1987.

Futterman, W. I., Dispersive body waves, *J. Geophys. Res., 67,* 5279–5291, 1962.

Gianelli, G., M. Puxeddu, and P. Squarci, Structural setting of the Larderello - Travale geothermal region, *Mem. Soc. Geol. Ital., 19,* 469–476, 1978.

Gianelli, G., M. Puxeddu, F. Batini, G. Bertini, I. Dini, and E. P. R. Nicolich, Geologic model of a young volcano-plutonic system: the geothermal region of Mount Amiata (Tuscany, Italy), *Geothermics, 17,* 719–734, 1988.

Giese, G., P. Wigger, C. Morelli, and R. Nicolich, Seismic studies for the determination of the crustal in the area of the geothermal anomaly in Tuscany, in *Advances in European Geothermal Research,* E. C. Geothermal Energy Research, Strasbourg, 4-6 March , 1980.

Hale, L. D. and G. A. Thompson, The seismic reflection character of the continential mohorovicic discontinuity, *J. Geophys. Res., 87,* 4625–4635, 1982.

Haskell, N. A., Crustal reflection of plane p ans sv waves, *J. Geophys. Res., 67,* 4751–4767, 1962.

Hayakawa, M., Prospecting of the underground structure at Showa-Shinzan by various geophysical methods, particularly seismic survey, *Japan J. Geoph., 1,* 13–20, 1957.

Helmberger, D. and R. A. Wiggins, Upper mantle structure of the midwestern United States, *J. Geophys. Res., 76,* 3229–3245, 1971.

Herrin, E., Seismological tables of p-phases, *Bull. Seis. Soc. Am., 58,* 1193–1241, 1968.

Hutchinson, D. R., J. A. Grow, K. D. Klitgord, and R. S. Detrick, *Moho reflections from the Long Island Platform, Eastern United States,* pp. 173–188, vol. 14 of *Geodynamics Series,* American Geophysical Union, Washington, D.C., 1986.

Iyer, H. M., Anomalous delays of teleseismic P-waves in Yellowstone National Park, *Nature, 253,* 425–426, 1975.

Iyer, H. M., Geophysical evidence for the locations, shapes and sizes and internal structures of magma chambers beneath region of Quaternary volcanism, *Phil. Tran. R. Soc. London, A310,* 473–510, 1984.

Iyer, H. M., *Seismological detection and delineation of magma chambers beneath interplate volcanic centers in western U. S. A., Modeling of Volcanic Processes,* Friedr. Vieweg and Sohn, New York, 1988.

Iyer, H. M., D. H. Oppenheimer, T. Hitchcock, L. N. Roloff, and J. M. Caokley, Large teleseismic P-wave delays in the Geysers Clear Lake geothermal area, *U. S. Geol. Surv. Prof. Pap., 1141,* 97–116, 1981.

Jordan, T. H. and L. N. Frazer, Crustal and upper mantle structure fron sp phases, *J. Geophys. Res., 80,* 1504–1518, 1975.

Kane, M. F., G. Simmons, W. Diment, M. Fitzpatrick, W. Joyner, and R. Bromery, Bouguer gravity and generalized geologic map of New England and adjoining areas, *USGS Geoph. Invest. Map Ser., GP-839,* 1972.

Kirkpatrick, S., C. Gelatt, and M. Vecchi, Optimization by simulated annealing, *Science, 220,* 671–680, 1983.

Kissling, E., W. L. Ellsworth, and R. S. Cocherham, Three-dimensional structure of the Long Valley caldera, California, region by geotomography, *U. S. Geol. Surv. Open-File Rep., 84-939,* 118–220, 1984.

Kurita, T., A procedure for elucidating fine structure of the crust and upper mantle from seismological data, *Bull. Seis. Soc. Am., 63,* 189–204, 1973.

Landa, E., W. Beydoun, and A. Tarantola, Reference velocity model estimation from prestacked waveforms: coherency optimization by simulated annealing, *Submitted to Geophysics,* 1989.

Langston, C. A., The effect of planar dipping structure on source and receiver responses for constant ray parameter, *Bull. Seis. Soc. Am., 67,* 1029–1050, 1977.

Langston, C. A., Structure under mount rainier, washington, inferred from teleseismic body waves, *J. Geophys. Res., 84,* 4749–4762, 1979.

Langston, C. A., Evidence for the subducting lithosphere under southern vancouver island and western oregon from teleseismic p wave conversions, *J. Geophys. Res., 86,* 3857–3866, 1981.

Lawson, C. L. and R. J. Hanson, *Solving Least Squares Problems,* Prentice Hall, Englewood Cliffs, NJ, 1974.

Leblanc, G., Truncated transfer functions and fine crustal structure determinations, *Bull. Seis. Soc. Am., 57,* 719–733, 1967.

Leet, L. D., Travel times for northeast America, *Bull. Seis. Soc. Am., 31,* 325–324, 19.

Lehman, J. A., R. B. Smith, M. M. Schilly, and L. W. Braile, Upper crustal structure of the Yellowstone caldera from seismic delay time analysis and gravity correlations, *J. Geophys. Res., 87,* 2713–2730, 1982.

Luetgert, J. H., C. E. Mann, and S. L. Klemperer, Wide angle deep crustal reflections in the northern Appalachians, *Geophys. J. R. Astr. Soc., 89,* 183–188, 1987.

Mavko, G., Velocity and attenuation in partially molten rocks, *J. Geophys. Res., 85,* 5173–5189, 1980.

Mellman, G. R., A method of body-wave waveform inversion for determination of earth structure, *Geophys. J. R. Astr. Soc., 62,* 481–505, 1980.

Menke, W., *Geophysical Dta Analysis: Discrete Inverse Theory,* Academic Press, Orlando, 1984.

Mereu, R., W. Dapeng, and K. Oliver, *Evidence for an inactive rift in the Precambrian from a wide-angle survey across the Ottawa-Bonnechere Grabben,* pp. 127–134, vol. 14 of *Geodynamics Series,* American Geophysical Union, Washington, D.C., 1986.

Monton, J., Contribution des methodes de prospections geothermiques a letude des champs geothermiques de Toscane, Italie., *Bull. Volcanol., 33,* 165–190, 1969.

Morelli, C., P. Giese, M. Corrozzo, B. Colombi, I. Gurerra, A. Hirn, H. Letz, R. Nicolich, C. Prodehl, C. Reichert, P. Rower, M. Sapin, S. Scarascia, and P. Wigger, Crustal and upper mantle structure of the Northern Apennines, the Ligurian Sea and Corsica, derived from seismic and gravimetric data, *Boll. Geofis. Teor. Appl., 19:75-76,* 199–260, 1977.

Morgan, P., D. D. Blackwell, R. E. Spafford, and R. B. Smith, Heat flow measurements in Yellowstone Lake and the thermal structure of the Yellowstone area, *J. Geophys. Res., 82,* 3719–3732, 1977.

Moro, A. D., M. Puxeddu, F. R. di Brozolo, and M. Villa, Rb-Sr and K-Ar ages on minerals at temperatures of 300 400 from deep wells in the larderello geothermal field (Italy), *Contrib. Miner. Pertol, 81,* 340–349, 1982.

Murase, T. and A. R. McBirney, Properties of some common igneous rocks and their melts at high temperatures, *Bull. Geol. Soc. Amer., 84,* 3563–3592, 1973.

Nercessian, A., A. Hirn, and A. Tarantola, Three dimensional seismic transmission prospecting of the Monte Dore volcano, France, *Geophys. J. R. Astr. Soc., 76,* 307–315, 1984.

Nolet, G., *Waveform tomography,* pp. 301–322, *Mathematical Geophysics,* D. Reidel Pubilshing Co., 1988.

Oliver, J., H. Cook, and L. Brown, Cocorp and the continental crust, *J. Geophys. Res., 87,* 3329–3347, 1983.

Oppenheimer, D. H. and K. E. Herkenhoff, Velocity–density properties of the lithosphere from three-dimensional modeling at the Geysers-Clear Lake region, California, *J. Geophys. Res., 86,* 6057–6065, 1981.

Owens, T. J., S. A. Taylor, and G. Zandt, A look at deep crustal structure in the eastern basin and range using teleseismic body waveform analysis, *Earthquake Notes, 53,* 23, 1982.

Owens, T. J., G. Zandt, and S. A. Taylor, Seismic evidence for an ancienr rift beneath the Cumberland Plateau, Tennessee: a detailed analysis of broadband teleseismic P waveforms, *J. Geophys. Res., 89,* 7783–7795, 1984.

Phinney, R. A., Structure of the earth's crust from spectral behavior of long-period vody waves, *J. Geophys. Res., 69,* 2997–3017, 1964.

Phinney, R. A., *A seismic cross-section tof the New England Appalachians: the orogent exposed,* pp. 157–172, vol. 14 of *Geodynamics Series,* American Geophysical Union, Washington, D.C., 1986.

Pica, A., J. P. Diet, and A. Tarantola, Non-linear inversion of seismic reflection data in a laterally inveriant medium, *Geophysics, 55,* 284–292, 1990.

Puxeddu, M., Structure and late cenozoic evolution of the upper lithosphere in south-west tuscany (italy), *Tectonics, 101,* 357–382, 1984.

Rast, N. and J. W. Skehan, The evolution of the Avalonian Plate, *Tectonophysics, 100,* 257–286, 1983.

Reasenberg, P., W. Ellsworth, and A. Walter, Teleseismic evidence for a low velocity body under the Coso geothermal area, *J. Geophys. Res., 84,* 2471–1483, 1980.

Robinson, E. A., *Seismic Velocity Analysis and the Convolutional Model,* IHRDC, Boston, MA, 1983.

Robinson, R. F. and H. M. Iyer, Delineation of a low velocity body under the Roosevelt Hot Springs geothermal area, *Geophysics, 46,* 1456–1466, 1981.

Rothman, D., Automatic estimation of large residual statics corrections, *Geophysics, 51,* 332–346, 1986.

Ryall, A. and F. Ryall, Attenuation of P and S waves in a magma chamber in Long Valley caldera, California, *Geophys. Res. Lett., 1,* 557–560, 1981.

Sanders, C. O., Location and configuration of magma bodies beneath Long Valley California, determined from anomalous earthquake signals, *J. Geophys. Res., 89,* 8287–8302, 1984.

Stauber, D. A., Two-dimensional compressional wave velocity structure under the San Francisco volcanic area, *J. Geophys. Res., 87,* 5451–5459, 1982.

Steeples, D. W. and H. M. Iyer, Low velocity zone under long valley as determinedfrom teleseismic events, *J. Geophys. Res., 81,* 849–860, 1976.

Stuart, D. B., J. D. Unger, J. D. Phillips, and R. Goldsmith, *The Quebec-Westernm Maine seismic reflection profile: setting and first year results,* pp. 189–199, vol. 14 of *Geodynamics Series,* American Geophysical Union, Washington, D.C., 1986.

Tarantola, A., *Inverse Problem Theory,* Evsevier, New York, 1987.

Tarantola, A. and A. Nercessian, Three-dimensional inversion without blocks, *Geophys. J. R. Astr. Soc., 76,* 299–306, 1984.

Taylor, S. R. and M. N. Toksoz, Three dimension crust and upper mantle structure of the northeastern united states, *J. Geophys. Res., 84,* 7627–7644, 1979.

Taylor, S. R. and M. N. Toksoz, Crust and upper Mantle velocity structure in the Appalachian orogenic belt; implications for tectonic evolution, *Bull. Geol. Soc. Amer., 93,* 315–329, 1982.

Telford, W. M., L. P. Geldart, R. E. Sheriff, and D. A. Keys, *Applied Geophysics,* Cambridge Univ. Press, New York, 1982.

Thompson, C. J. and D. Gubbins, Three-dimensional lithospheric modeling at norsar: linerarity of the method and amplitude variations from the anomalies, *Geophys. J. R. Astr. Soc., 71,* 1–36, 1982.

Toksoz, M. N. and K. Kadinsky-Cade, *A study of New England seismicity with emphasis on Massachusetts and New Hampshire,* NRC Final Report, Mass. Instit. Tech., 1988.

VanDecar, J. C. and R. S. Crosson, Determination of teleseismic relative phase arrival times using multi-channel cross correlation and least squares, *Bull. Seis. Soc. Am., 80,* 150–169, 1990.

Williams, H. and R. Hatcher, Suspect rerranes and accretionary histoy of the Appalachian orogen, *Geology, 10,* 530–536, 1982.

Young, C. and R. W. Ward, Three dimensional Q model of the Coso Hot Springs known geothermal resource area, *J. Geophys. Res., 85,* 2459–2470, 1980.

Zandt, G., *Study of the three dimensional heterogeneity beneath seismic arrays in central California and Yellowstone, Wyoming,* PhD thesis, Massachusetts Institute of Technology, 1978.

Zelt, C. A., J. J. Drew, M. J. Yedlin, and A. M. Ellis, Picking noisy refraction data using semblance supplemented by a Monte Carlo procedure and spectral balancing, *Bull. Seis. Soc. Am., 77,* 942–957, 1987.